

33  
2  
DTIC FILE COPY

AFWAL-TR-88-2043

ION KINETICS IN SILANE PLASMAS



AD-A200 465

Pete Haaland, Capt., USAF  
Power Components Branch  
Aerospace Power Division

April 1988

Interim Report for Period August 1985 - March 1988

Approved for Public Release; Distribution Unlimited

DTIC  
ELECTED  
NOV 18 1988  
S E B H D

AERO PROPULSION LABORATORY  
AIR FORCE WRIGHT AERONAUTICAL LABORATORIES  
AIR FORCE SYSTEMS COMMAND  
WRIGHT-PATTERSON AIR FORCE BASE, OHIO 45433-6533

88 11 18 140

UNCLASSIFIED  
SECURITY CLASSIFICATION OF THIS PAGE

Form Approved  
OMB No. 0704-0188

REPORT DOCUMENTATION PAGE					
1a. REPORT SECURITY CLASSIFICATION UNCLASSIFIED		1b. RESTRICTIVE MARKINGS N/A			
2a. SECURITY CLASSIFICATION AUTHORITY N/A		3. DISTRIBUTION/AVAILABILITY OF REPORT Approved for public release: Distribution unlimited.			
2b. DECLASSIFICATION/DOWNGRADING SCHEDULE N/A					
4. PERFORMING ORGANIZATION REPORT NUMBER(S)  AFWAL-TR-88-2043		5. MONITORING ORGANIZATION REPORT NUMBER(S)			
6a. NAME OF PERFORMING ORGANIZATION Aero Propulsion Laboratory Aerospace Power Division		6b. OFFICE SYMBOL (if applicable) POOC-3	7a. NAME OF MONITORING ORGANIZATION		
6c. ADDRESS (City, State, and ZIP Code)  Wright-Patterson AFB OH 45433-6563		7b. ADDRESS (City, State, and ZIP Code)			
8a. NAME OF FUNDING / SPONSORING ORGANIZATION AFOSR		8b. OFFICE SYMBOL (if applicable) NP	9. PROCUREMENT INSTRUMENT IDENTIFICATION NUMBER  N/A		
8c. ADDRESS (City, State, and ZIP Code)  Bolling AFB DC 20332		10. SOURCE OF FUNDING NUMBERS			
		PROGRAM ELEMENT NO. 61102F	PROJECT NO. 2301	TASK NO. 2301S2	WORK UNIT ACCESSION NO. 04
11. TITLE (Include Security Classification)  Ion Kinetics in Silane Plasmas					
12. PERSONAL AUTHOR(S) P. D. Haaland					
13a. TYPE OF REPORT Thesis	13b. TIME COVERED FROM 08/85 TO 03/88		14. DATE OF REPORT (Year, Month, Day) 1988 April 20	15. PAGE COUNT 197	
16. SUPPLEMENTARY NOTATION Capt. Haaland's thesis was granted by Harvard University. He was graduated in May 1988. All experimental study and much of the theory was performed by Capt. Haaland at the Advanced Plasma Research Laboratory (AFWAL/POOC).					
17. COSATI CODES		18. SUBJECT TERMS (Continue on reverse if necessary and identify by block number)  Charge Transfer, Ionization, Attachment, Thin Film			
FIELD 20	GROUP 09	SUB-GROUP			
09	03				
19. ABSTRACT (Continue on reverse if necessary and identify by block number)  The kinetics of ion formation by electron impact and subsequent reaction in silane:noble-gas mixtures have been examined using pulsed ion cyclotron resonance (ICR) mass spectrometry with the objective of discerning the role played by ions in plasma reactors which deposit amorphous silicon films. Cross sections for ionization of the noble-gases and silane as well as dissociative attachment of electrons to silane are presented. The nascent ion species distribution formed by electron-impact in a plasma environment changes with time as a result of charge transfer reactions. Room-temperature rate constants for these reactions have been measured with the pulsed ICR techniques, and an anomalous trend in reactivity down the eighth period has been identified. The general departure from the Langevin limiting rate for ion-molecule reactions is examined with ab initio electronic structure calculations and a model is advanced which probes quantum mechanical constraints on electron transfer from silane to the noble cations. The model offers a consistent rationalization for the observed rate constants and product distributions and permits analysis of experimentally inaccessible processes such as ion-					
20. DISTRIBUTION/AVAILABILITY OF ABSTRACT <input checked="" type="checkbox"/> UNCLASSIFIED/UNLIMITED <input type="checkbox"/> SAME AS RPT <input type="checkbox"/> DTIC USERS			21. ABSTRACT SECURITY CLASSIFICATION UNCLASSIFIED		
22a. NAME OF RESPONSIBLE INDIVIDUAL Alan Garscadden			22b. TELEPHONE (Include Area Code) 513-255-2923	22c. OFFICE SYMBOL AFWAL/POOC-3	

19. radical reactions: Parametric variation of the homogeneous ion kinetics with gas mixture, pressure, and excitation variation are explored for conditions typical of commercial deposition reactors. The correlation of calculated silicon-hydride ion wall fluxes with observed film deposition rates is used to argue that SiH<sup>+</sup> ions are often the principal depositing species in these reactors. The competition<sup>n</sup> between deposition by charged and neutral free radicals is shown to be nonlinearly dependent on the neutrals' sticking coefficient. Radicals which fail to stick with high probability are rapidly ionized by plasma electrons. Another aspect of the ion reactions is the kinetic competition between hydride transfer and formation of new silicon-silicon bonds.

Insertion of an ion into the Si...H bond may provide nucleation sites for undesirable particulate formation. The competition, which is modified both by the gas-mixture and excitation conditions, places calculable constraints on the operating parameters which suppress dust formation.



Accession For	
NTIS GRA&I	<input checked="" type="checkbox"/>
DTIC TAB	<input type="checkbox"/>
Unannounced	<input type="checkbox"/>
Justification	
By _____	
Distribution/ _____	
Availability Codes	
Avail and/or	
Dist	Special

# Contents

<b>1</b>	<b>Silane Plasma Kinetics</b>	<b>1</b>
1.1	Motivation . . . . .	1
1.2	Experimental Scope . . . . .	3
1.3	<i>Ab Initio</i> Investigations . . . . .	6
1.4	Implications . . . . .	7
1.5	Outline . . . . .	9
<b>2</b>	<b>Noble Ion Formation</b>	<b>13</b>
2.1	Introduction . . . . .	13
2.2	Literature Precis . . . . .	13
2.3	Experimental Methods . . . . .	18
2.3.1	Pressure Determination . . . . .	20
2.3.2	Electron Beam Characterization . . . . .	22
2.3.3	Interaction Region . . . . .	29
2.3.4	Ion Signals . . . . .	30
2.4	Noble Gas Measurements . . . . .	31
2.5	Implications . . . . .	40
2.5.1	$Rg_2^{2+}$ Laser? . . . . .	40
2.5.2	$Rg^{n+}$ in PECVD? . . . . .	41
2.6	Conclusions . . . . .	42
<b>3</b>	<b>Silane Ionization</b>	<b>46</b>
3.1	Introduction . . . . .	46
3.2	The Molecular Silane Cation? . . . . .	48
3.2.1	$Rg$ versus $SiH_4$ . . . . .	48
3.2.2	Electron-impact Spectra . . . . .	49
3.2.3	Photoionization . . . . .	51

3.2.4	Electronic Structure . . . . .	53
3.3	Ionization Cross Sections . . . . .	65
3.3.1	FTMS Measurements . . . . .	65
3.3.2	$SiH_m^{n+}$ for $n > 1$ . . . . .	69
3.4	Conclusions . . . . .	71
<b>4</b>	<b>Negative Ion Formation</b>	<b>76</b>
4.1	Background . . . . .	76
4.2	ICR Measurements . . . . .	79
4.2.1	Experimental Techniques . . . . .	79
4.2.2	Results . . . . .	79
4.3	Theoretical Aspects . . . . .	82
4.3.1	$SiH_n^-$ . . . . .	82
4.3.2	$H^- + SiH_4$ . . . . .	88
4.3.3	Attachment to $H_2$ and $SiH_n$ radicals . . . . .	91
4.4	Conclusions . . . . .	91
<b>5</b>	<b>Ion Source Kinetics</b>	<b>95</b>
5.1	Positive Ion Sources . . . . .	95
5.1.1	$\mathcal{F}$ and ion formation . . . . .	95
5.1.2	$\mathcal{F}$ estimates . . . . .	97
5.2	Anion Sources . . . . .	98
5.3	Nonlinear Sources . . . . .	102
5.3.1	Radical Ionization . . . . .	102
5.3.2	Radical Attachment . . . . .	103
5.4	Conclusions . . . . .	105
<b>6</b>	<b>Ion Kinetics</b>	<b>108</b>
6.1	Introduction . . . . .	108
6.2	Silane Polarizability . . . . .	109
6.3	Silicon Hydride Cation Reactions . . . . .	112
6.3.1	$SiH_3^+$ Reactions . . . . .	115
6.3.2	$SiH_2^+$ Reactions . . . . .	119
6.3.3	$SiH^+$ Reactions . . . . .	121
6.3.4	$Si^+$ Reactions . . . . .	124
6.3.5	Summary of $SiH_n^+$ reactions . . . . .	126
6.4	$H_3^+$ Reaction . . . . .	130

**CONTENTS**

v

6.5	Noble-Gas Ion Reactions . . . . .	132
6.5.1	$He^+$ Reactions . . . . .	133
6.5.2	$Ne^+$ Reactions . . . . .	134
6.5.3	$Ar^+$ Reactions . . . . .	136
6.5.4	$Kr^+$ Reactions . . . . .	137
6.5.5	$Xe^+$ Reactions . . . . .	138
6.6	Conclusions . . . . .	139
<b>7</b>	<b>Theory for Charge Transfer</b>	<b>144</b>
7.1	Introduction . . . . .	144
7.2	Classical Features . . . . .	144
7.3	Electronic Structure . . . . .	148
7.4	Quantum Constraints . . . . .	154
7.5	Comments . . . . .	159
<b>8</b>	<b>Films and Ions?</b>	<b>163</b>
8.1	Ions or Radicals? . . . . .	163
8.2	The Wall . . . . .	166
8.3	Clusters and Dust . . . . .	173
8.4	Negative Ions . . . . .	176
8.5	Homogeneous Ion Losses . . . . .	179
8.6	Optimal Conditions . . . . .	181
8.7	Conclusions . . . . .	182

# List of Figures

2.1	$\sigma_t(Rg)$	14
2.2	$\sigma_1(Rg)$	15
2.3	$\sigma_n(Rg)n > 1$	16
2.4	$\sigma_1(Rg)$	17
2.5	ICR Trap Geometry	19
2.6	FTMS Schematic	21
2.7	UHV Leakup Rate	23
2.8	Pulsed Calibration	24
2.9	Transient Pressure	25
2.10	Ion Gauge Error	26
2.11	Beam current measurements	28
2.12	$\sigma_1(Ne)$	29
2.13	$He, Ne^{2+}$ Formation	32
2.14	$Xe^{n+}$ ?	33
2.15	$Ne + 2e \rightarrow Ne^{2+}$	34
2.16	$\sigma_{12}(Ne)$	38
2.17	$\sigma_{mn}(Kr^{2+})$	39
2.18	$Rg_2^{2+}$ energy diagram	41
3.1	$SiH_4 + e \rightarrow SiH_n^+, H_n^+$	47
3.2	FTMS of $SiH_4$	50
3.3	Orbital energy changes after ionization of silane	56
3.4	$SiH_4^+ \rightarrow SiH_3^+ + H$	57
3.5	$SiH_n^+$ Enthalpies	58
3.6	$SiH_4^+$ geometries	60
3.7	$SiH_4^+$ potential surface II	64
3.8	Silane and Neon gas puffs	67
3.9	Chemistry during $\sigma_i$ determination?	68

3.10	Scaled literature $\sigma_m(SiH_4)$ . . . . .	70
3.11	Recommended $\sigma_m(SiH_4)$ . . . . .	71
4.1	FTMS anion spectrum . . . . .	80
4.2	$H^- + SiH_4?$ . . . . .	81
4.3	$\sigma_a$ using FTMS . . . . .	83
4.4	$SiH_4^-$ geometry . . . . .	85
4.5	$SiH_4^-$ correlation diagram . . . . .	86
4.6	$H^- + SiH_4$ reaction coordinates . . . . .	89
5.1	$k_i$ for Maxwellians . . . . .	99
5.2	$k_i$ for Gaussians . . . . .	100
5.3	$k_a$ for Maxwellians . . . . .	101
5.4	Radical Ionization . . . . .	103
6.1	Polarization potentials . . . . .	113
6.2	$^{30}SiH_3^+ + SiH_4 \rightarrow$ . . . . .	117
6.3	$SiH_3^+ + SiH_4 \rightarrow Si_2H_n^+$ . . . . .	118
6.4	Hydride transfer from $SiH_4$ to $SiH_n^+ n = 2, 3$ . . . . .	120
6.5	$SiH_2^+ + SiH_4 \rightarrow Si_2H_n^+$ . . . . .	121
6.6	$SiH^+ + SiH_4 \rightarrow$ . . . . .	122
6.7	$Si^+ + SiH_4 \rightarrow$ . . . . .	125
6.8	Nascent ion evolution . . . . .	127
6.9	Disilane ionization . . . . .	129
6.10	$SiH_n^+ + SiH_4$ kinetic flow chart . . . . .	130
6.11	$D_3^+ + SiH_4 \rightarrow$ . . . . .	131
6.12	$D_2^+ + D_2 + SiH_4$ . . . . .	133
6.13	$He^+ + SiH_4 \rightarrow$ products . . . . .	135
6.14	$He^+$ rate plot . . . . .	135
6.15	$Ne^+ + SiH_4 \rightarrow$ . . . . .	136
6.16	$Ar^+ + SiH_4 \rightarrow$ . . . . .	137
6.17	$Kr^+ + SiH_4 \rightarrow$ . . . . .	138
6.18	$Xe^+ + SiH_4 \rightarrow$ . . . . .	139
6.19	$XeSiH_n^+ n = 2, 3$ . . . . .	140
7.1	Polarization potentials . . . . .	147
7.2	$SiH_n^+$ orbital energies . . . . .	149
7.3	Orbital correlation diagram . . . . .	151

7.4	Schematic potential for predissociation . . . . .	156
8.1	$\sigma_d$ and $\sigma_i$ . . . . .	168
8.2	Radical:Silane ratios . . . . .	170
8.3	Clustering nomograph . . . . .	175
8.4	$k_a/k_d$ . . . . .	178

# List of Tables

2.1	$\sigma_{12}(Ne^{2+})$	37
3.1	$SiH_4^+$ : History	48
3.2	Calculated masses: $SiH_n^+$	51
3.3	Electronic eigenvalues of silane	55
3.4	$SiH_4^+$ potential partitions	59
3.5	$SiH_n^+$ appearance potentials	62
3.6	$SiH_n$ ionization potentials	66
3.7	$\sigma_t$ and $\sigma_m$ of $SiH_4$	67
4.1	$SiH_n^-$ from $SiH_4$	78
4.2	Attachment data of Srivastava	78
4.3	$SiH_n$ electron affinities	84
6.1	$SiH_4$ refractivity	110
6.2	Errors in $\alpha(SiH_4)$	111
6.3	$\alpha$ from <i>ab initio</i> calculations	111
6.4	$SiH_n^+ + SiH_4$ literature rates	114
6.5	Hydride transfer thermochemistry	123
6.6	$^4Si^+ + SiH_4$ thermochemistry	124
6.7	$Rg^+ + SiH_4$ literature rates	134
6.8	Summary of $Rg^+ + SiH_4$ reaction rates	141
7.1	$Rg^+ + SiH_4$ rates	145
7.2	Thermochemical kinetic predictions	145
7.3	Thermochemistry for $Rg^+ + SiH_4$	147
7.4	Noble gas orbital energies	150
7.5	Electron tunneling prefactors	159

LIST OF TABLES

8.1	$N_e$ and $\Gamma$ in an R.F. reactor . . . . .	164
8.2	$SiH_n^+$ fluxes in Turban's RF reactor . . . . .	165
8.3	$k_d$ and $k_i$ estimates . . . . .	167
8.4	$\Lambda$ and $\lambda$ . . . . .	174

# Chapter 1

## Silane Plasma Kinetics

### 1.1 Motivation

Since the award of the 1956 Nobel prize in physics for the invention of the transistor, the influence of semiconductors has become pervasive. In particular the naturally abundant element silicon has formed the basis of an economically viable technology whose applications range from subatomic particle detectors to word processing. The principal methods for preparing thin films of silicon are chemical vapor deposition (CVD), in which a volatile silicon-containing gas at atmospheric pressure is pyrolyzed, and plasma enhanced chemical-vapor deposition (PECVD), in which electric current is passed through a low pressure, room-temperature gas mixture. A voluminous empirical literature on these processing reactors has evolved in response to economic driving forces. While the CVD process has attracted enormous investment for the production of solar cells, most silicon electronic devices are produced using variations on the PECVD theme.

What is responsible for film growth in plasma reactors? The vast literature on silane plasmas can be used to argue many mechanisms. Some authors claim that free radicals produced by electron impact dissociation of silane lead directly to film. Others propose that ions cause film growth. Still others argue that electron and ion fluxes catalyze decomposition of adsorbed silane. In some cases simple, gas-phase precursors are proposed. In others, complicated polysilicon-hydride cluster ions are in vogue. There is no consensus on which species lead to thin film growth.

Reactors for the production of high-quality amorphous silicon (*a*-Si:H) typically operate at total pressures of 10 to 1000 millitorr. The reagent gas contains

between one and fifty percent silane ( $SiH_4$ ), the silicon analogue of methane. The remaining components include a noble-gas buffer such as helium or argon, volatile hydrides of phosphorous or boron for doping, and sometimes molecular hydrogen. Excitation of the flowing reagent gas can be accomplished with d.c., microwave, or capacitatively coupled, radiofrequency electric fields. Alternatively, hollow cathode or electron beam approaches may be employed. In any event the gas breaks down and a fractional ionization<sup>1</sup> of  $10^{-6}$  is typically achieved. The energy of the applied electric field is coupled into the gas mixture primarily through inelastic electron collisions. It is this coupling, which depends sensitively on the chemical and charged-particle transport characteristics of a particular configuration, that ultimately determines the quality of and efficiency with which silicon circuits and solar cells are made.

Plasma-enhanced chemical vapor deposition differs fundamentally from higher pressure thermal deposition processes because of the presence of energetic electrons, ions, excited species, and free radicals in the low pressure discharges. This is not to say that pyrolysis of silane which leads to silicon films is an equilibrium or kinetically simple process. On the contrary, silicon is deposited from 1 atmosphere of silane at roughly  $450^{\circ}C$ . However molecular beam experiments [1, 34] clearly show that silane is not dissociated in a single collision with a silicon surface until the temperature is raised to over  $700^{\circ}C$ . Not enough energy is transferred to silane in a single collision with the  $400^{\circ}C$  surface to cause its dissociation. One concludes that pyrolytic deposition of silicon from silane at lower temperatures must occur by multiple collisions in which energy is transferred from the hot surface to impinging reagent molecules. The pooling of this energy at the surface and in the gas-phase boundary layer leads to silane dissociation and thin film deposition. While the separate roles of heterogeneous and homogeneous kinetics are not understood in detail, there is clear evidence that an important role is played by gas phase free radicals [3].

PECVD is considered attractive in part because the film is grown at reduced temperatures, typically less than  $200^{\circ}C$ . In plasma reactors the molecular mean free path is comparable to the reactor dimensions and the wall temperatures are well below  $700^{\circ}C$ . Therefore thermal pyrolysis of silane does not occur in plasma reactors. A silane molecule that strikes a  $150^{\circ}$  substrate will not be sufficiently excited in a single collision to dissociate at the surface or in the gas phase. The chance of its being reflected back to the substrate before having lost its

---

<sup>1</sup>ratio of positive ion to total gas densities

internal energy by collision with a room-temperature reactor surface is too small for pyrolysis to account for the observed angstrom per second deposition rates. In sum, the mechanisms by which energy is coupled into silane decomposition in pyrolytic and plasma reactors are qualitatively different.

The voluminous literature on silicon film deposition provides an indirect clue to the nature of the species which ought to be pivotal in PECVD. On intuitive grounds, it is remarkable that high quality films are grown from plasmas under such a broad range of gas mixture, pressure, and excitation conditions. The kinetics of both charged and neutral free-radicals are extremely diverse and would be expected to vary dramatically over the range of operating conditions under which good films have been produced. However the variation of the neutral kinetics is expected to be qualitatively greater, since the ion chemistry is additionally constrained by Maxwell's equations. That is, charged-particle formation and reaction are determined not only by the chemical reactivity but by the electrical properties of the plasma. Current continuity, impedance matching, and the coupling between total charged particle fluxes and power density require the global variation of ion chemistry to be less than that of the neutral free radicals, whose kinetics are constrained only by gas composition and heterogeneous boundary conditions. The robustness of plasma enhanced chemical vapor deposition therefore suggests, *but does not prove*, that ion chemistry plays an important role in the formation of amorphous silicon films.

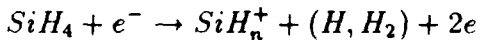
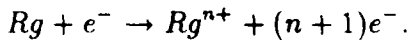
## 1.2 Experimental Scope

The objective of this investigation has been a quantitative understanding of the role played by ions in silicon deposition discharges. The formation of a nascent ion distribution by electron impact on the reagent gas and its evolution due to homogeneous ion-molecule reactions have been examined using pulsed ion cyclotron resonance (ICR) mass spectrometry. In these experiments ions are formed from energy-resolved electron impact at reagent pressures in the  $10^{-7}$  torr range. Ensembles of tens of thousands of ions are trapped in combined solenoidal magnetic and electrostatic fields. The mass spectrum of the ion ensemble is probed in the time domain by first coherently exciting the ions' cyclotron motion with a broad-band radiofrequency chirp. Next, the coherent ion motion is detected by an antenna formed from two conducting plates oriented parallel to the magnetic field axis. The image current induced in the antennae is a time domain signal which

contains fourier components corresponding to the ions' cyclotron frequencies. The mass spectrum of the ion ensemble is obtained by appropriate transformation of the antenna signal into the frequency domain. Although discrete Fourier transforms are often employed, maximum entropy spectral analysis techniques provide superior spectral resolution and are used to provide complementary analyses of the time domain ion cyclotron signals [4]. Straightforward calculations relate the observed frequencies to ion mass and the power spectral densities to ion number. This approach to ion cyclotron mass spectrometry, which was discovered by Comisarow and Marshall in 1974 [7], was chosen for the present investigation for reasons including:

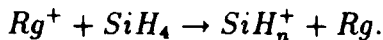
- Ions are formed and detected in the same space. No ion optic or transmission fudge factors are required.
- Ions are not actually collected, obviating multiplier gain uncertainties.
- Time domain experiments using resonance ejection permit examination of charged reactants and products of rapid ion molecule reactions at very low reagent pressures and manageable reaction times.

All three classes of phenomena which are important to the kinetics of ion formation and reaction in silane-containing discharges are amenable to the pulsed ICR experiments. First of these are the cross sections for cation formation from rare-gases,  $Rg$  and silane:



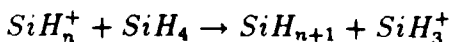
Accurate determination of the magnitudes and electron energy dependence of these cross sections can be used with experimental or theoretical descriptions of the electron energy distribution function to calculate the reactive ion sources and electron current amplification by which actual plasmas are maintained. Very high mass resolution capabilities of the pulsed ICR technique have been used to demonstrate that the ionization of silane by electron impact is exclusively dissociative. This observation has important mechanistic consequences, since heterogeneous reduction of  $SiH_n^+$  for  $n < 4$  at a reactor wall yields species that are coordinatively unsaturated; that is able to interact chemically with the surface. Noble-gas ions, by contrast, are reduced to form neutrals which are at most physisorbed to the wall.

The nascent distribution of ion species formed by electron impact on the reagent-gas mixture evolves in time by ion-molecule reactions whose kinetics form the second class of problems to be probed by the ICR techniques *e.g.*:



First-order theoretical treatment of these reaction rates is assessed using the approach pioneered by Langevin at the turn of the century [6] and couched in kinetic terms by Eyring [2] in the 1930's. The rate constant for charge transfer in this approximation is independant of the reactants' relative kinetic energy and increases linearly with the neutral's dielectric polarizability,  $\alpha$ . Examination of the dissociative charge transfer reaction of silane with all of the noble-gas ions provides an opportunity to test conventional kinetic theory. Since the chemical and physical properties of the noble-gases vary monotonically down the periods of Mendeleev's table, one might anticipate a deviation from the first-order Langevin rate, if any, also to vary monotonically from helium to xenon. ICR experiments show this is clearly not the case—the helium, neon, krypton and xenon reactions proceed at over half the Langevin rate, while the rate for  $Ar^+$  charge transfer is less than one tenth of the Langevin value.

In addition to details of rare-gas charge transfer the reactions of silicon-hydride and hydrogen cations with silane can be probed using resonance ejection techniques. For example the naturally abundant isotopes of  $^{29}Si$  and  $^{30}Si$  are used to ascertain the role of hydrogen versus hydride ion transfer in these collisions. Systematic examination of the reactions of  $SiH_n^+$  with silane illuminates the competition between hydride transfer:



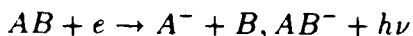
and formation of new silicon-silicon bonds:



This competition plays a pivotal role in the generation of heavy species which are nucleation sites for undesirable particulate formation.

Most literature with the phrase *ion chemistry* in its title is concerned only with the properties and reactions of positively charged species. Anions play a qualitatively different and important role in semiconductor deposition discharges. Therefore the third class of interaction which is analyzed experimentally with the

pulsed ICR techniques is the formation of negative ions by electron impact on silane. While the processes:



play no role in noble-gas plasmas, electron attachment has important consequences for both the electrical and chemical characteristics of silane-containing plasmas. Electrically, the large mobility difference between electrons and negative ions forces new boundary conditions on the steady state solutions of the plasma equations. The increased discharge impedance caused by attachment requires that the plasma be driven harder to obtain the same current densities as discharges without attachment. Additionally negative ion motion to the walls is restricted by the space-charge sheaths which are set up to insure equality of charged particle fluxes to dielectric boundaries. This means that negative ions are required to have long residence times in the gas phase, that is a near-zero sticking coefficient, which in turn accentuates the importance of their homogeneous reactions.

### 1.3 *Ab Initio* Investigations

To complement the experimental probes of the nascent ion distribution and its reactive evolution *ab initio* electronic structure calculations have been performed to provide mechanistic insight on a quantum mechanical level. These calculations are particularly useful for bounding the role of processes such as free-radical ionization and attachment, which are extremely difficult to probe accurately with experiment. The calculations also provide an internally consistent and complete description of the thermochemistry which constrains deposition. Finally, the *ab initio* calculations guide intuition in the interpretation of trends in the chemistry which occurs in silane-containing plasmas. For example the molecular silane ion, while not formed by electron impact, has been unambiguously observed in photoionization mass spectra. The interpretation of this dissonance is made possible by detailed calculations of the molecular ion's Jahn-Teller unstable potential energy surface.

The calculations also provide a tool with which hypotheses concerning the non-monotonic trend in noble-gas ion reactions may be probed. In the end, the anomalous reactivity of the argon cation can be described without *ab initio* methods, using a variation on the theme of Stark ionization and the Landau-Zener predissociation formalism. The slow reaction of the argon cation with

silane and the change in product ions with noble-gas reagent are shown to be a consequence of quantum mechanical constraints on electron transfer during the reactive collision. These constraints may be estimated using only the first and second ionization potentials of the reactants and, if available, the photoelectron spectrum of the neutral. For situations where the relevant electronic eigenvalues are not known spectroscopically, for example if one wanted to estimate the rate for the reaction of a noble cation with the  $SiH_3$  radical, the *ab initio* methods can provide the necessary information.

## 1.4 Implications

The combined experimental and theoretical investigations of microscopic processes in silane-containing plasmas permit useful predictions and rationalizations of the macroscopic performance and scaling characteristics of deposition reactors. For example, the reactivity of the noble cations affects the deposition process non-linearly. The empirical choice of argon as a preferred buffer can be understood in terms of its influence on gas-phase ion chemistry. Plasmas such as radiofrequency discharges, which are maintained in part by a fast, beam component of the electron energy distribution, produce noble as well as silicon-hydride ions in large numbers. Helium and neon cations react with silane to produce very reactive  $Si^+$  and  $SiH^+$ . These react further with silane at near-Langevin rates to produce unsaturated polysilicon-hydride cluster ions that are natural nucleation sites for undesirable silicon dusts often observed in plasma reactors. By contrast, the argon cation slowly forms only unreactive  $SiH_3^+$  in its reaction with silane, thus limiting the clustering channel even more effectively than electron impact ionization, which produces modest quantities of  $Si^+$  above 13.3 eV.

The microscopic evidence from the present investigation of homogeneous ion chemistry argues strongly for ion deposition of thin silicon films. The magnitude and composition of ion fluxes is calculable from the microscopic data and is of the same order as observed deposition rates. Further, the calculated (and very recently measured) ionization potentials of the silicon-hydride radicals are much less than that of silane itself but well above the work function of amorphous silicon. In the Born-Oppenheimer approximation, electron transfer from the silicon solid to an incoming ion occurs in a time which is short compared to that for nuclear motion. In other words, the distinction between radical flux and ion flux is blurred as one gets arbitrarily close to the surface. The difference

between ions and radicals impinging on the walls is that the former have higher, directed velocities due to their acceleration by the sheath electric field common to all dielectric boundaries in a plasma. This kinetic energy, which is of the order of that required to break silicon-silicon and silicon-hydrogen bonds, is available to overcome thermodynamic and kinetic barriers to surface chemistry which may preclude incorporation of radicals impinging with thermal velocities.

It has been argued that since the electron impact dissociation cross-section is larger than that for ionization of silane at all energies, the neutral radicals are responsible for film deposition [1]. Such a conclusion is only valid if the radicals have large sticking coefficients. For the authors' conditions, the radical sticking coefficient would have to exceed ten percent for deposition to be faster than radical ionization. In other words, unless the silicon-hydride radicals stick with probabilities of order unity, they are more likely ionized by plasma electrons than deposited as radicals. Furthermore, it is difficult to understand the stoichiometry of the films in terms of  $SiH_3$  and  $SiH_2$  deposition. The amorphous films typically contain 3–10 atom % hydrogen. With the ion fluxes, the proclivity for hydride transfer from silane to  $SiH_n^+$  and  $H_3^+$  have a natural analogy with a surface process which depletes hydrogen and returns either silane or a neutral silicon-hydride radical to the gas phase.

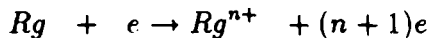
Careful measurement of relevant charged-particle formation and loss processes has provided a database from which parametric analysis of the kinetics in semiconductor deposition plasmas is possible. From these analyses it is concluded that silicon-hydride ion fluxes are the primary source of deposited film under many commercially useful operating conditions.

The synthesis of experimental and theoretical descriptions of ion chemistry for silane-containing plasmas which is the theme of the present work provides insight into a much wider class of industrially important processes. The parameter space which must be explored for optimization of a general plasma-enhanced deposition process is too large and too complex to permit Edisonian optimization. If one is to extend the successful techniques of silicon film deposition to amorphous diamond, silicon nitride, or III-V semiconductors such as GaAs the approach applied in the present work provides a larger and less expensive return on research investment.

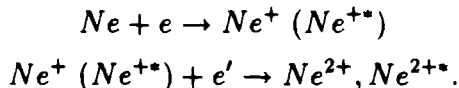
## 1.5 Outline

The eight chapters are organized to provide a systematic discussion of ion chemistry in silane-containing plasmas. As an aid to the reader a brief outline of the chapter contents is included below.

Chapter two introduces the experimental techniques developed for quantitative analysis of ionization cross sections using pulsed ion cyclotron resonance mass spectrometry. Measurement of the reagent gas pressure (in the  $\approx 10^{-8}$  torr range), electron beam characteristics, and ion trap physics are described. Application of these techniques to noble-gas ionization demonstrates a reason for the wide variance among literature cross-sections for the process:



for  $n$  greater than 1. The  $Ne^{++}$  concentration is shown to vary quadratically with the product of electron beam current and time as expected for the two step process:



Cross sections for this two step process are presented and discussed.

Chapter three is concerned with positive ions formed by electron impact on  $SiH_4$ . The electron impact ionization of silane is shown experimentally to be exclusively dissociative. Dissociation of the  $^2T_2$  ion and the thermochemistry of the silicon-hydride cations are analyzed using extensive *ab initio* electronic structure calculations. Very recent, unambiguous detection of a molecular silane ion by photoionization mass spectrometry contrasts with the equally unambiguous absence of  $SiH_4^+$  from the electron-impact mass spectrum. The relevance of this contrast to conventional analogies between the quantum constraints on electron versus photon induced ionization is assessed. Literature dissonance concerning the magnitude of the silane electron impact ionization cross sections is also reviewed and resolved by pulsed ICR measurement of silane ionization. Renormalization of extant literature data by these values brings the cross section data into plausible agreement over the energy range required for analysis of electron impact ionization in silane-containing plasmas.

Chapter four reviews negative ion formation from silane. Literature values for dissociative attachment to silane vary by over one order of magnitude. In addition, recent reports from the Jet Propulsion Laboratory suggest that  $H^-$  is

formed in significant quantities. Pulsed ICR techniques are applied to the measurement of silane dissociative attachment to yield cross sections in the  $10^{-19} \text{ cm}^2$  range for producing  $\text{SiH}_n^-$   $n = 1, 2, 3$ . No  $H^-$  is observed, a result which is also understandable on quantum mechanical grounds. Thermochemistry of the anions, the reaction of  $H^-$  with silane, and the attachment properties of the silicon-hydride free radicals are examined by *ab initio* electronic structure calculations. Nonlinear scaling of attachment in silane discharges is argued on the basis of the large electron affinities calculated for the  $\text{SiH}_2$  and  $\text{SiH}_3$  radicals.

Chapter five synthesizes the cross-section data for electron impact formation of anions and cations in mixtures of silane and noble-gases. A convenient form for parametric analysis of ionization and attachment rates in these plasmas is introduced which involves expansion of the electron energy distribution function,  $\mathcal{F}$ , in a series of normalized maxwellian and gaussian basis functions. Integral rates are tabulated from which the nascent ion species distribution produced by electron impact is simply evaluated for any  $\mathcal{F}$ . Estimates of neutral radical ionization rates and their implications for conclusions about the role of radicals and ions in thin film deposition are also presented.

Chapter six begins an analysis of the reactive evolution of the ion species distribution produced by electron impact on the silane:noble-gas mixtures. Literature values for silane's polarizability were too erratic to permit accurate discussion of the Langevin limiting rate for charge transfer with silane. Inference of this quantity from precise measurements of silane's refractive index at two wavelengths is described. The appropriate value for  $\alpha(\text{SiH}_4)$  is  $4.62 \pm 0.10 \text{ \AA}^3$ . The literature on reactions of silicon-hydride cations with silane is critically reviewed and outstanding controversies are resolved by pulsed ion cyclotron resonance experiments. Hydride transfer from silane to  $\text{SiH}_3^+$ ,  $\text{SiH}_2^+$  and  $\text{SiH}^+$  are all shown to be faster than condensation reactions which result in disilicon-hydride ion species. Hydride transfer to  $D_3^+$  is also examined, demonstrating a lack of hydrogen scrambling in the product  $\text{SiH}_3^+$ . Reaction kinetics and product distributions for the reaction of noble-gas ions  $\text{He}^+$ ,  $\text{Ne}^+$ ,  $\text{Ar}^+$ ,  $\text{Kr}^+$ , and  $\text{Xe}^+$  with silane are also presented. The reactivity trend is decidedly non-monotonic down the series, an anomaly whose theoretical implications are fully developed in chapter seven.  $\text{Kr}^+$  ion reactions occur at the Langevin limiting rate, He, Ne and Xe ions react at about half of this limiting rate, while  $\text{Ar}^+$  oxidizes silane at less than one tenth of the Langevin value. No  $\text{SiH}_4^+$  ion was observed as the product of any of these reactions, nor were proton or  $\text{H}_2^+$  detected.

Chapter seven is a detailed theoretical investigation of the reactivity trend

for the reactions of silane with noble-gas ions. Intuitive arguments based on the variation of the physical and chemical properties of the noble-gases are examined but found unable to account for the non-monotonic trend in the series of exothermic reactions. Similarly the thermochemical kinetic approach of Benson, which has been successful in understanding reactivity trends in radical-radical and radical-molecule kinetics, is shown to fail miserably for this problem. A paradigm is developed which is based on the changes in electronic structure of the reactants required for successful charge transfer. These changes are calculated using *ab initio* methods and, alternatively, spectroscopic data including photo-electron spectra. The paradigm, which is compared to the WKB treatment of Stark ionization and the Landau-Zener approach to predissociation, is successful in rationalizing differences in the rates and product distributions of the reactions between silane and rare-gas ions. Predictions for other ion-silane reaction rates and products based on this paradigm are presented.

Chapter eight concludes with a macroscopic description of kinetics in actual discharges. The importance of physical boundary conditions to the treatment of ion kinetics is reviewed. Specifically the fate of ions which diffuse to the reactor boundaries under the influence of plasma electric fields is assessed. Sample calculations for silane-containing plasmas are presented which examine the scaling of ion composition and wall fluxes with excitation, gas mixture, and total pressure variation. Silicon-hydride cations are shown to be the principal depositing species under typical PECVD reactor conditions. Calculation of the nascent ion distribution and its evolution by homogeneous reaction and diffusion permits useful parametric analysis of silicon deposition reactors. Estimates for the relationships between total silane pressure, buffer gas, reactor dimensions, gas residence time, deposition rate, and the formation of parasitic clusters are demonstrated as an illustration of the general methods advocated by and developed in this thesis.

## Bibliography

- [1] M. Farnhaam and D. Olander, *Surface Science*, **145**, 390 [1984].
- [2] C. DeJoseph, P. Haaland and A. Garscadden, *IEEE Transactions on Plasma Science*, **PS-14**, 165 [1986].
- [3] F. Ellis and R. Gordon, *Journal of Applied Physics*, **54**, 5381 [1983].
- [4] A. Rahbee, *Chemical Physics Letters*, **117**, 352 [1985].
- [5] M. Comisarow and A. Marshall, *Chemical Physics Letters*, **25**, 282 [1974].
- [6] M. Langevin, *Annales de Chemie et de Physique*, **8**, 245 [1905].
- [7] H. Eyring, J. Hirschfelder and H. Taylor, *Journal of Chemical Physics*, **4**, 479 [1936].
- [8] G. Turban, Y. Catherine and B. Grolleau, *Thin Solid Films*, **60**, 147 [1979].

æ

# Chapter 2

## Noble Ion Formation

### 2.1 Introduction

Electrical conductivity of low pressure plasmas is principally maintained by electron-impact ionization. The processes:



where  $A$  is a stable atom or molecule and the asterisk refers to charged products with internal electronic or vibrational energy, have been extensively investigated. A thorough and relatively recent review of the electron-impact ionization literature has appeared [1]. However the application of pulsed ion cyclotron resonance (ICR) techniques to cross-section measurement is new and yields results that have not been obtainable by other techniques. In addition to introducing the experimental methods on which the present work is based the examination of noble ion formation provides insight into the literature's dissonance over cross-sections for production of multiply charged ions by electron impact.

### 2.2 Literature Precis

The canonical reference for quantitative experimental measurement of noble-gas ionization is the 1965 work of Rapp and Englander-Golden [33]. These authors' ionization tube measurements of the total ionization cross-section  $\sigma_t$ :

$$\sigma_t = \sum_n (n \cdot \sigma_n)$$

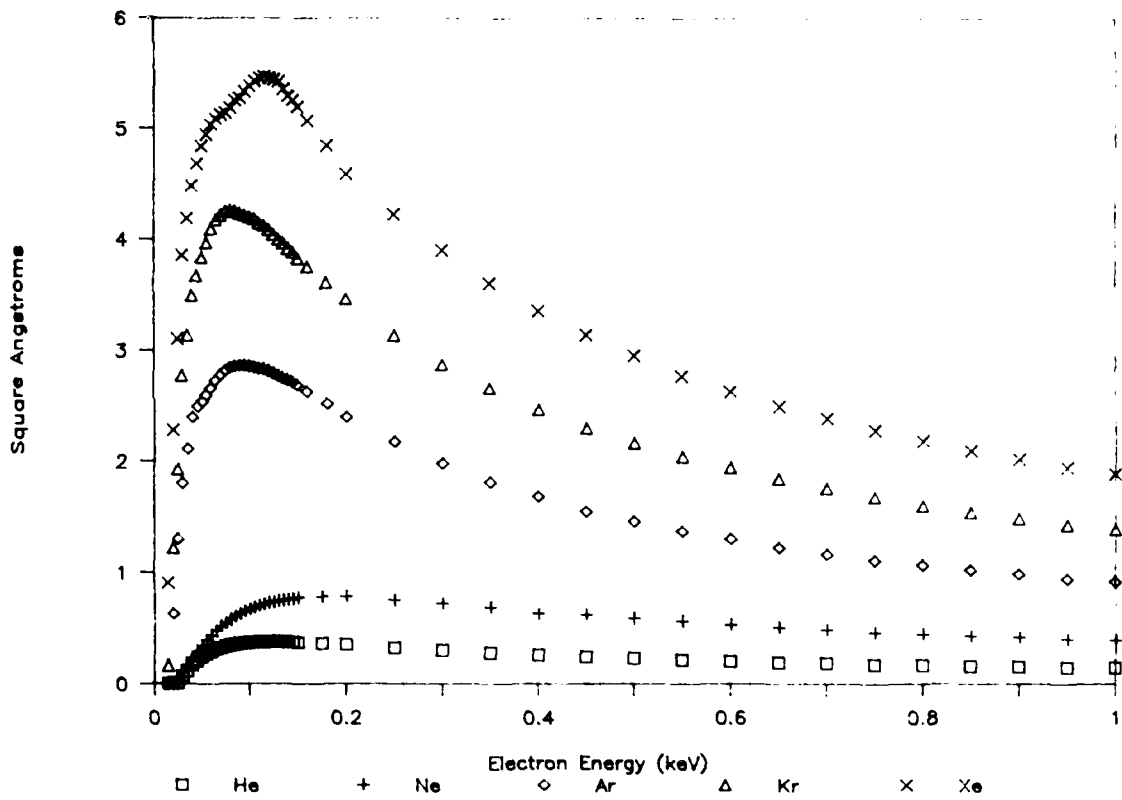


Figure 2.1: Total ionization cross-sections of Rapp and Englander-Golden.

are the principal benchmark against which more recent measurements of partial ionization cross-sections,  $\sigma_n$ , have been calibrated [1, 3, 22]. Figure 2.1 summarizes the experimental observations of Rapp. While there is substantial agreement on the total ionization of the noble-gases (e.g. references [1, 10]), the situation is less clear on the question of partial cross-sections; that is the extent to which multiply charged species contribute to the total ionization cross-section [11], [12], [13], [14], [15], [16], [17], [18], [19], [21], [22], [23], [24], [25], [26].

The 1987 measurements of partial ionization cross-sections reported by Wetzel *et al.* [35] are the best available experimental data for ionization of noble-gases. Using crossed beams of electrons and rare-gas atoms (formed by charge transfer from a mass-analyzed ion beam) the authors report  $\sigma_n$  for the noble-gases from threshold to 180 eV, as summarized in figures 2.2 and 2.3.

Pulsed ion cyclotron resonance mass spectrometry measurements to be de-

## 2.2. LITERATURE PRECIS

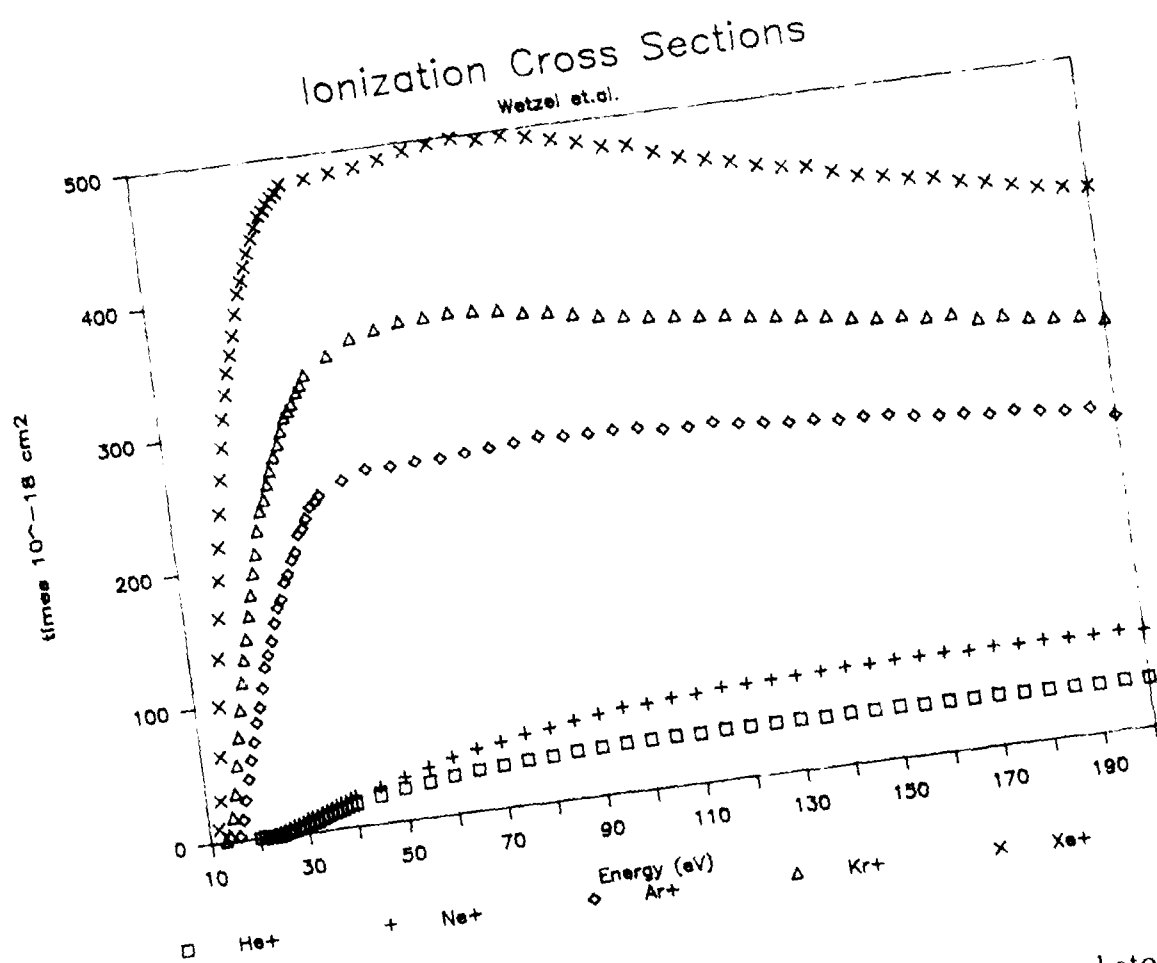


Figure 2.2: Partial cross-sections for  $Rg^+$  formation measured from crossed atom and electron beams by Wetzel et al. [35].

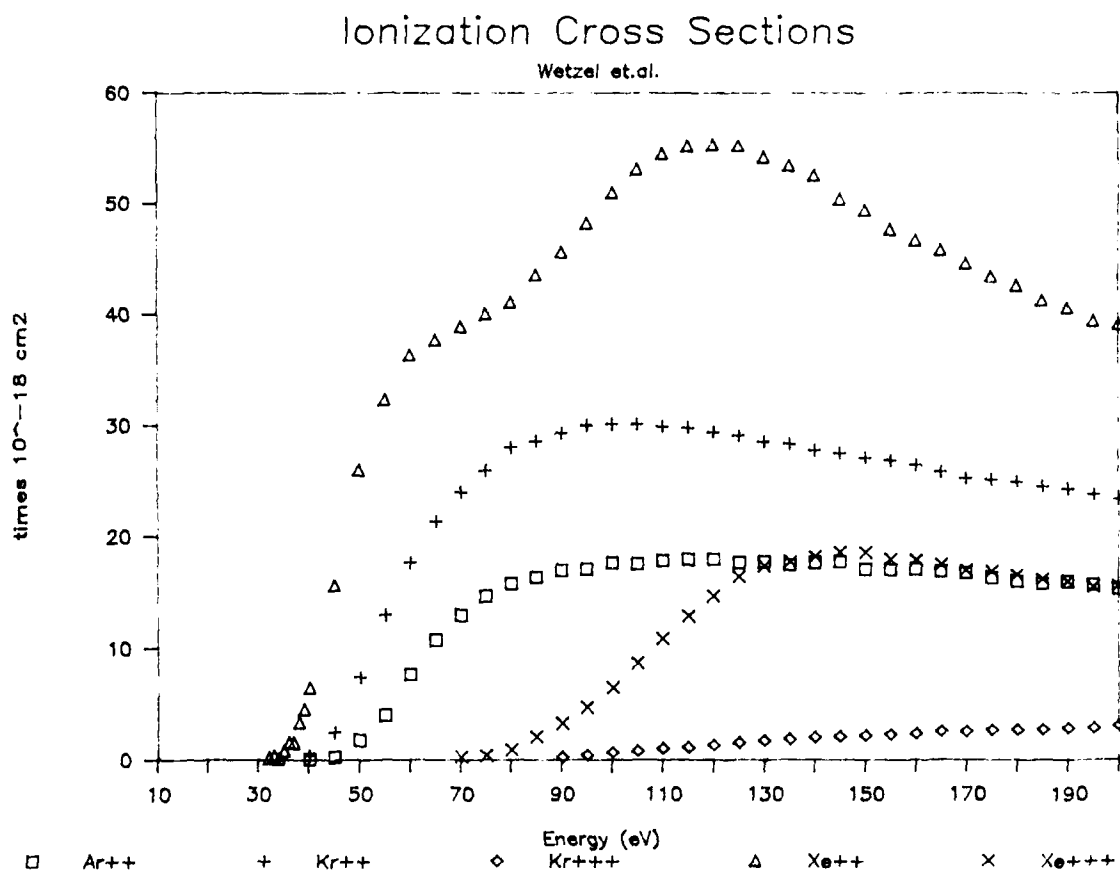


Figure 2.3: Partial ionization cross-sections for  $Rg^{n+}$  from crossed beam experiments of Wetzel *et al.* [35].

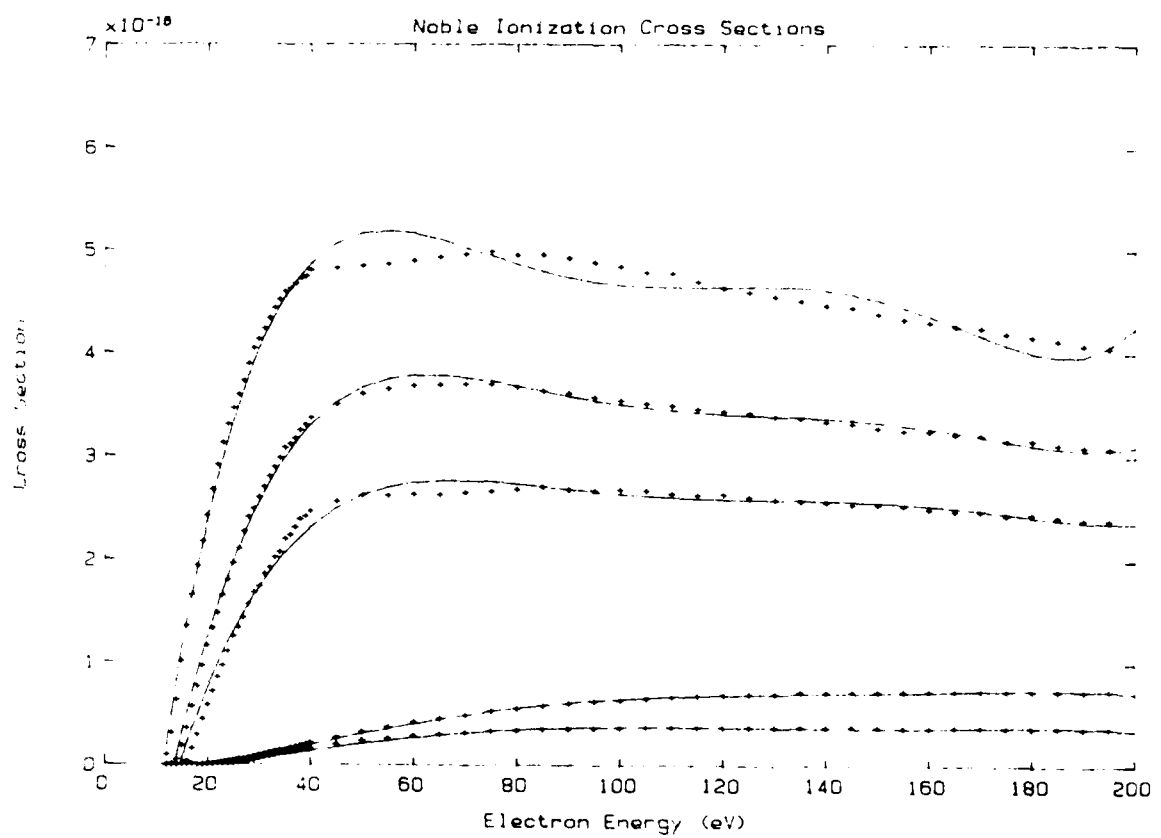


Figure 2.4: Polynomial fit (5th order) of cross-sections for production of singly charged noble cations by electron impact. The polynomial forms are used for ionization rate calculations described in chapter five.

scribed here complement the crossed-beam methods. Both experiments are performed under precisely controlled collision conditions. While atomic and selected radical species [5, 12] may be probed with the beam method, the internal electronic and vibrational energy of molecular species formed in the charge-transfer cell limits the technique's applicability. In the case of silane ionization this constraint is particularly severe—the molecular cation from which a fast neutral beam would be formed is not sufficiently hardy to survive collisional neutralization (chapter 3 and ref [20]).

## 2.3 Experimental Methods

Pulsed ion cyclotron resonance mass spectrometry (also called Fourier Transform Mass Spectrometry or FTMS) was discovered in 1974 by Comisarow and Marshall [7]. Since its introduction the evolution of FTMS hardware and techniques have been very rapid (e.g. ref [44]). The observable quantity in FTMS is associated with coherent ion motion in a cubic ion trap as sketched in figure 2.5 [9]. Ions are formed by pulsing a low current electron beam in a low pressure ( $\approx 10^{-7}$  torr) reagent gas along the axis of a strong magnetic field. The ions' motion is constrained radially by the magnetic field and longitudinally by a small (of order volts/cm) electrostatic field generated by trap plates oriented orthogonal to the magnetic field axis. The mass to charge ratio of the ion ensemble is probed in two steps. First, the ions are coherently excited by irradiating the trap with a radiofrequency chirp whose Fourier components include the cyclotron frequencies of the ions to be probed. Although linearly polarized sweeps ( $E(t) = \sin((\omega + c \cdot t) \cdot t)$ ) are most common, noise waveforms and Fourier synthesized excitation have also been employed [34, 35]. Second, the excite chirp is switched off and the coherent ion motion is detected as an image current induced in an antenna oriented parallel to the magnetic field and orthogonal to the excite plates. The image current is amplified, digitized, and Fourier analyzed to yield a spectrum of cyclotron frequencies associated with the ion ensemble.

Attributes of FTMS which are attractive for quantitative analysis of ionization include:

- Ion formation and detection occur in the same spatial volume, obviating ion optic transmission factors.
- The detected signal is derivable from the ion equations of motion and is

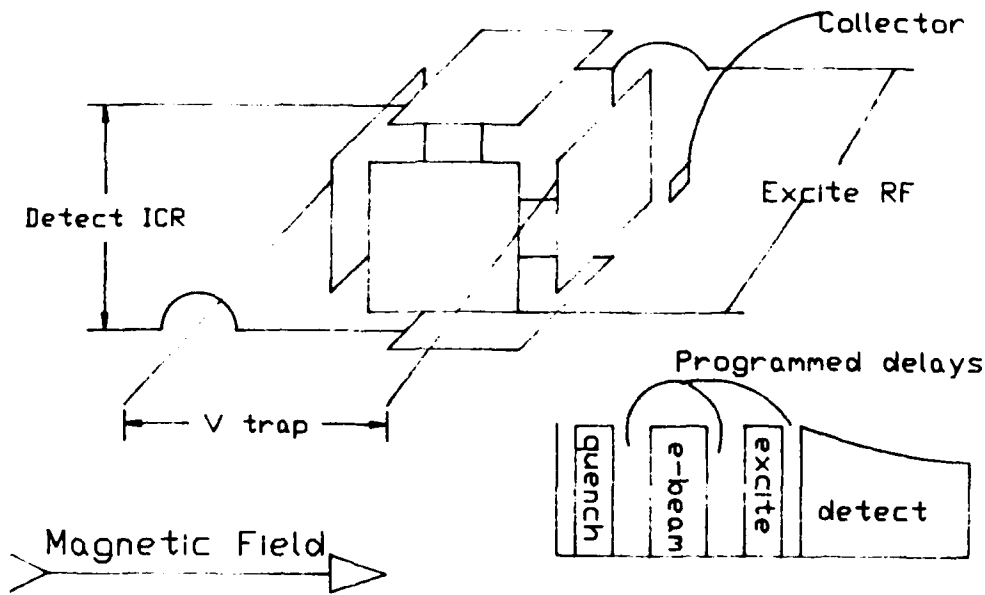


Figure 2.5: Pulsed ICR trap geometry illustrating the excitation, detection, and trapping plates and the current collector. Inset is a typical experimental timing sequence.

linear in ion number. As their electromagnetic influence is detected no ion collection is required, obviating collection or multiplier gain factors.

- Simultaneous detection of all mass to charge ratios obviates scanning.
- High mass resolution permits unambiguous identification of ion species in the presence of impurities and isotopic ambiguities.
- High sensitivity permits very low reagent pressure  $\approx 10^{-8}$  torr and rigorously single-collision operating conditions.

Beyond these features, which are common to all FTMS experiments, enhancements are required to permit quantification of ionization cross-sections and ion-molecule reaction rates. Measurement of ionization cross-sections using pulsed ion cyclotron resonance mass spectrometry requires observation of the following:

1. Reagent gas pressure.
2. Electron beam energy, current, and irradiation time.

3. Interaction volume.
4. Number of ions of each mass and charge.

### 2.3.1 Pressure Determination

Knowledge of the reagent gas pressure is central both to cross-section and ion-molecule reaction rate constant measurements. From the schematic drawing of the experiment (figure 2.6) it is clear that the observation of gas pressures in the  $10^{-8}$  torr range at the cell, immersed in a 30 kilogauss magnetic field, is experimentally difficult. The standard ion gauge provides only a qualitative estimate of gas pressure at the ICR cell because:

- Integrated conductance differs for the paths from ion-gauge to diffusion pump and ICR cell to diffusion pump.
- Under steady-state operating conditions the ICR cell is between the source and sink of reagent while the ion gauge is attached to the manifold at a dead end.
- Ion gauge calibration is complicated by the presence of fringe magnetic fields. Even with mu metal shielding the performance characteristics of nude ionization gauges in magnetic fields are decidedly nonlinear.
- The ionization gauge response is a sensitive function of gas composition—that is it must be scaled by the ionization cross-section which is the object of the measurement.

In some cases it is possible to discern the *in situ* reagent pressure using well-defined ion-molecule reaction rates [36]. Introduction of a temporal delay between ion formation and detection permits the pressure in the ion trap to be inferred from the observed  $d \log[X^+]/dt$ . To the extent that reaction conditions are analogous for the reference and FTMS measurements (i.e. ion internal and kinetic energy, etc.), the uncertainty of this measurement arises primarily from the experimental error of the reference rate constant measurement. However the approach is of limited utility since many systems of interest do not have reliable rate data from which to infer the pressure.

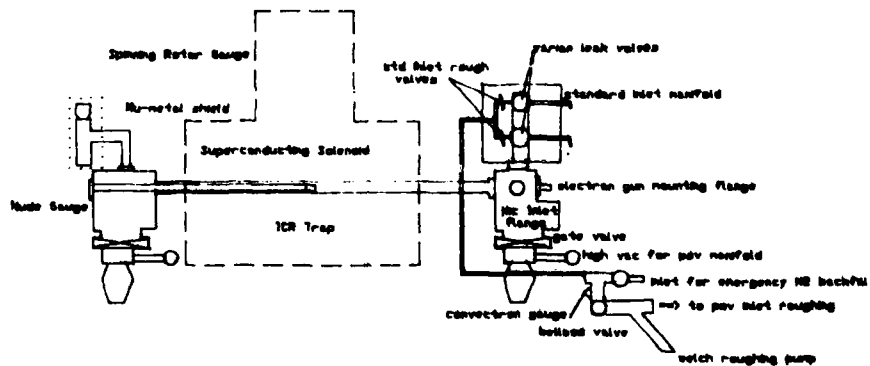


Figure 2.6: Schematic view of the Fourier Transform Mass Spectrometry system.

The present approach has been to apply Boyle's law, with two instrumental innovations, to the FTMS vacuum system. The innovations are pulsed supersonic piezoelectric gas valves developed by Lasertechnics [27] and the spinning rotor gas friction gauge developed by MKS instruments [28]. The pulsed valves are used to inject reproducible aliquots of reagent gas into the mass spectrometer vacuum system from a second manifold which is diagnosed with capacitance manometers. The spinning rotor gauge is a manometric probe which detects momentum transfer from low pressure gas samples to a magnetically suspended spinning ball. This gauge provides accurate and species independent pressure measurements down into the  $10^{-7}$  torr range. After measurement of the vacuum system leakup rate the mass spectrum of a small number,  $n_1$ , of gas puffs is measured with the chamber isolated from the pumps. A second mass spectrum is recorded with a defined delay between gas injection and spectrum acquisition while the high vacuum pump is connected. The ratio of ion signals,  $I_{\text{stat}}/I_{\text{dynam}}$ , is used to define the relationship between the gas pressure at the ICR cell under static and dynamic (actively pumping) conditions. The final step in the calibration is to isolate the manifold from its vacuum pumps and inject a large enough number of gas puffs,  $n_2$ , to provide reliable readings on the spinning rotor gauge. The spinning rotor pressure value is divided by  $n_2$  to yield the static pressure per

puff, that is the number of gas molecules in a puff divided by the total chamber volume. The relationship between mass spectral intensity and pressure is then inferred using  $n_2$ ,  $n_1$ , and  $I_{\text{stat}}/I_{\text{dynam}}$ .

Sample experimental data for the pressure calibration are shown in figures 2.7, 2.8, 2.9, and 2.10. Figure 2.7 illustrates a typical outgassing rate (all pumps isolated) of the vacuum system measured with the spinning rotor gauge. The principal contribution to the mass spectrum of the background gas is from  $H_2O$ . Note that the measured rate is almost an order of magnitude higher when the ionization gauge filaments are heated. With the nude ion gauge off the outgassing rate is less than  $2 \cdot 10^{-9}$  torr per second, a reasonable value for a diffusion pumped system considering the very large surface area of the manifold.

Figure 2.8 shows the response of the spinning rotor gauge to six bursts of ten, millisecond pulses of helium into the isolated chamber, after correcting for the measured leak-up rate. The quantity of injected gas as inferred either from the number of pulses or the spinning rotor measurement show good stability. Figure 2.9 is the helium pressure profile *at the ICR cell* calculated using the calibration procedure. For comparison, the relationship between this pressure and the reading of the nude gauge is illustrated in figure 2.10. The nude gauge is calibrated for nitrogen, so that a sensitivity correction which is the ratio of the nitrogen to helium ionization cross-sections is required for fair comparison. This ratio is 7.25 at 100 eV [33], so that an uncorrected reading of  $6 \cdot 10^{-7}$  torr in figure 2.10 corresponds to a helium pressure at the ion gauge of  $4.36 \cdot 10^{-6}$  torr, 67% larger than the correct value from the pulsed valve calibration.

### 2.3.2 Electron Beam Characterization

The second value for which quantitative measurement is required is the current of the electron beam. Conventional FTMS systems [31] provide ionizing electrons from a directly heated filament which is located on the magnetic field axis a few centimeters from the ICR trap. The entire filament is biased with respect to the trap to permit or preclude transmission of current through the cell. This design is inadequate for four reasons:

1. The energy spread of the electron beam is greater than or equal to the voltage drop across the directly heated filament (typically 2 volts).
2. The beam energy is constrained to be less than 90 volts due to Nicolet's power supply and high-vacuum feedthrough limitations.

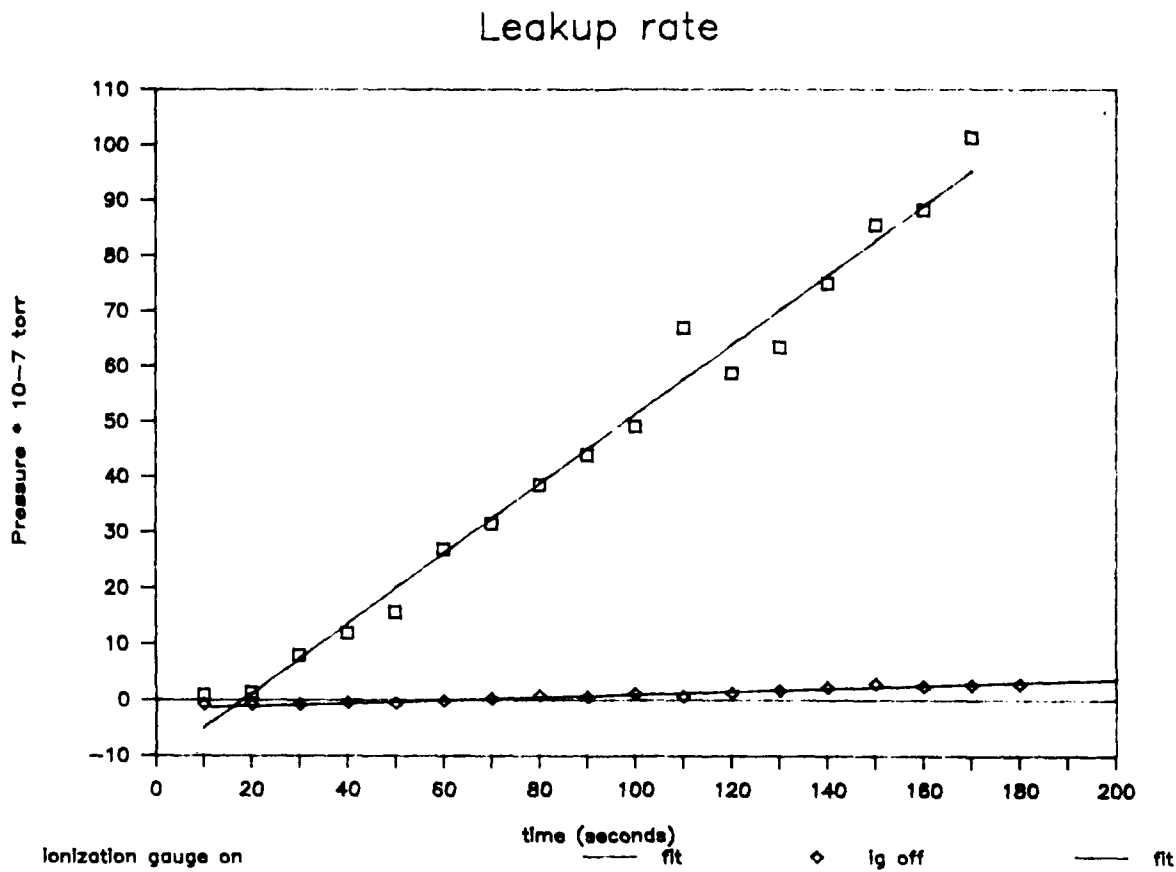


Figure 2.7: Vacuum chamber leakup rate with and without the nude ionization gauge turned on as measured with the spinning rotor friction gauge. The hot nude gauge acts as a source of gas.

## Spinning Rotor Calibration

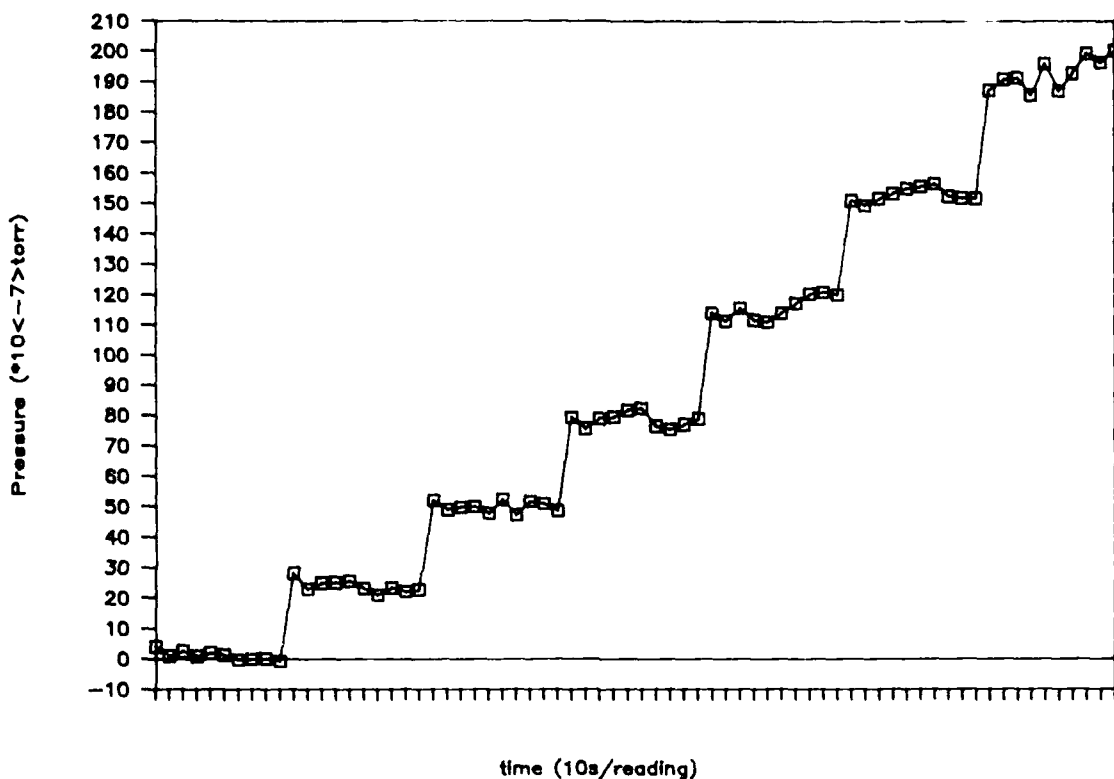


Figure 2.8: Multiple pulse response of the spinning rotor gauge. A series of six, ten-pulse (1ms/pulse) bursts of helium (from a manifold at 24.10 torr) were injected with pumps isolated from the vacuum chamber. Each square corresponds to the average of ten, one second rotor readings corrected for the finite outgassing rate shown in the figure 2.7.

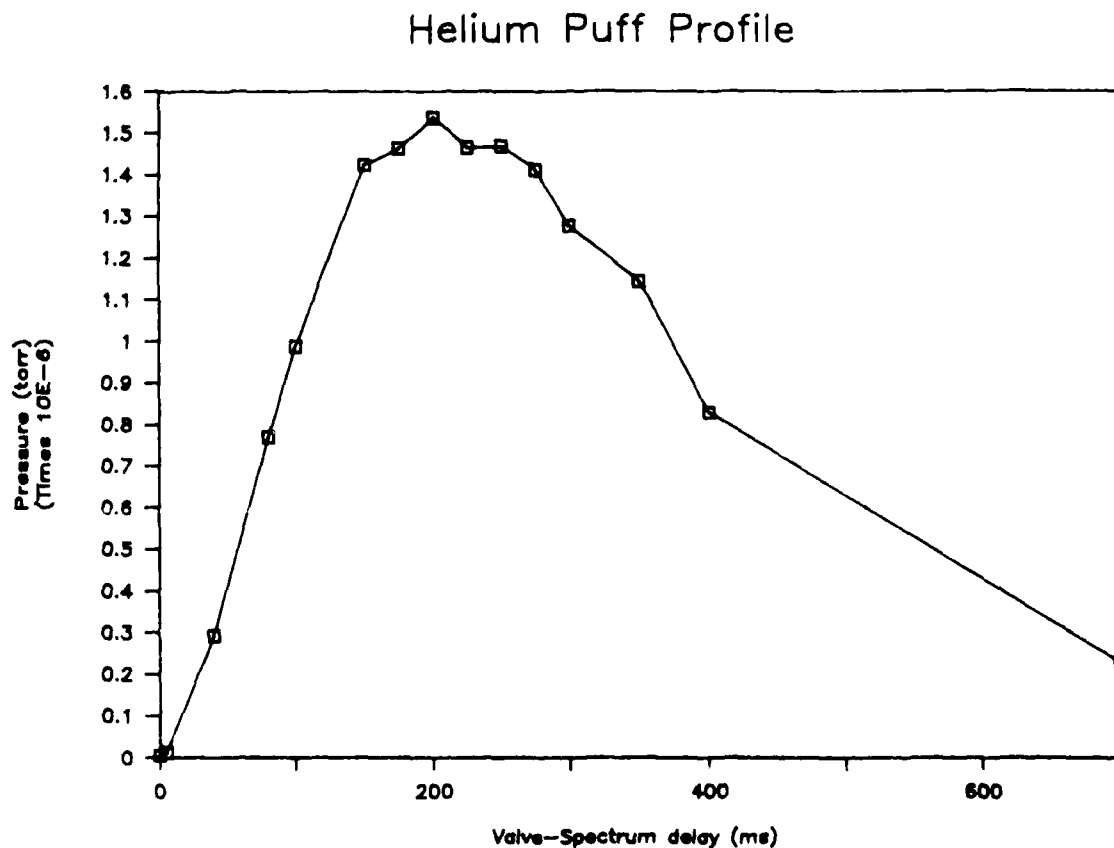


Figure 2.9: Helium pressure at the ICR cell as a function of delay between pulsed valve operation and spectrum acquisition using the pressure calibration procedure described in the text.

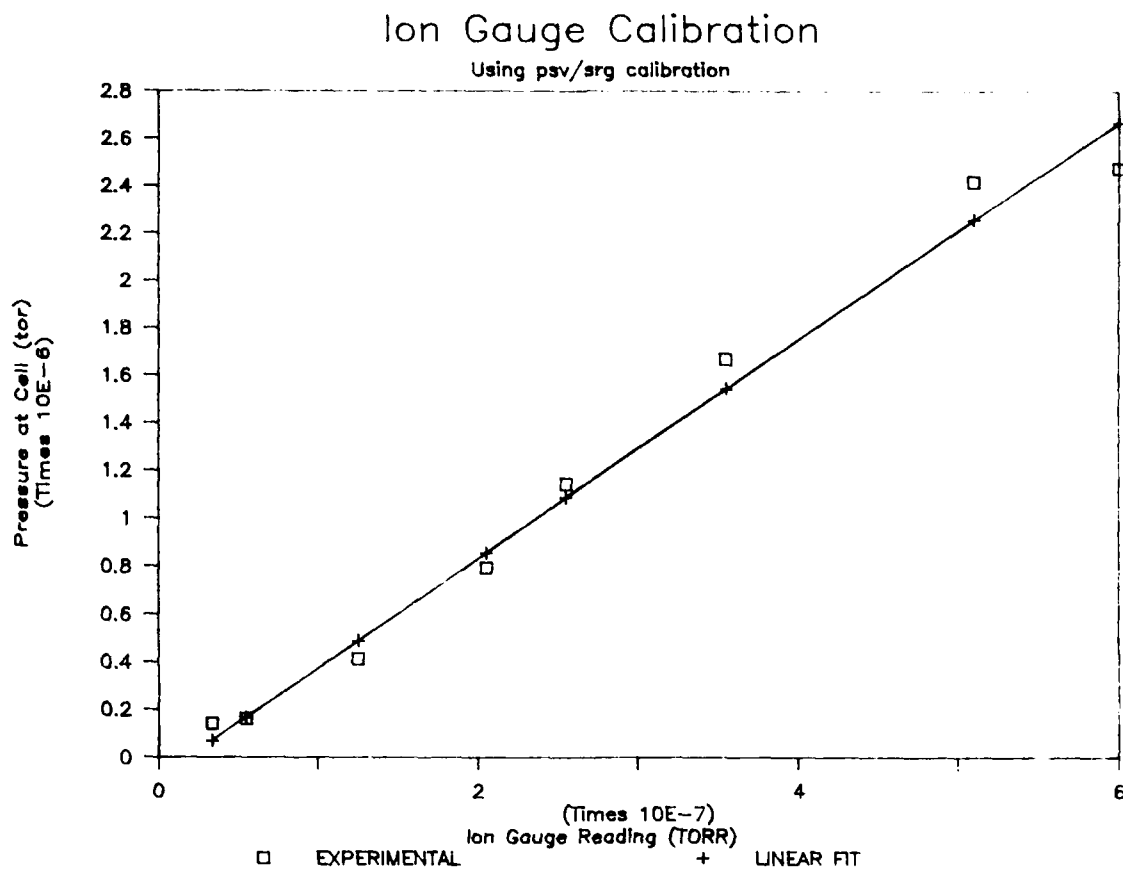


Figure 2.10: Comparison of uncorrected ion gauge pressures to those obtained with the pulsed-valve, spinning-rotor artifice. Corrected ion gauge readings are obtained by multiplying the x-axis values by 7.25; the total error of the ion gauge readings is +67%.

3. The proximity of the ionizer filament to the ICR cell provides a possible source of free radicals and photons which is difficult to define.
4. The proximity of the biased filament may influence the electric field profile inside the ion trap.

The solution to these difficulties was to incorporate a better electron gun with an indirectly heated cathode into the system on the magnetic axis far from the ICR cell, in a region of relatively low field. A Kimball Physics ELG-2 electron gun [29] was selected and integrated into the mass spectrometer system. This gun was capable of producing microampere currents over a range of energies from 10 to 1000 volts. A combination of zoom electron optics and an eccentric, rotatable, knife-edged flange facilitated alignment of the beam with the magnetic and geometric axes of the experiment. The low transverse energy of the beam, which is characteristic of indirectly heated cathodes, is essential since electrons with velocity transverse to the magnetic axis are very efficiently reflected by the magnetic mirror of the superconducting solenoid [32].

Electron beam alignment is accomplished by verifying zero current to the front and back trap plates<sup>1</sup> and a maximum current to an electrically isolated collector plate which is located on the geometric and magnetic axes of the experiment on the other side of the cell from the electron source. During operation, the beam current is usually measured by connecting this isolated plate to ground through a resistor and applying Ohm's law to the measured voltage. When preliminary measurements of ionization cross-sections of the noble-gases showed a peculiar electron energy dependence the *simple* beam current measurement was revisited. Cross-sections obtained from the ratio of the ion cyclotron resonance signals to the observed electron current displayed a discontinuous drop above 50 volts. After many careful experiments it was concluded that overestimation of the electron current at higher energies was responsible for the erroneous cross-sections. A special floating amplifier was designed [30] which allowed current measurement under conditions where the energy with which electrons strike the collector could be controlled.

It is well known that energetic electrons impinging on a metal surface can lead to secondary electron emission [33]. Figure 2.11 shows a comparison of beam current values measured alternately through a 100 kilohm resistor and with the floating amplifier where the impact energy of electrons was varied between 30

---

<sup>1</sup>The plates are actually molybdenum mesh supported on a stainless steel frame.

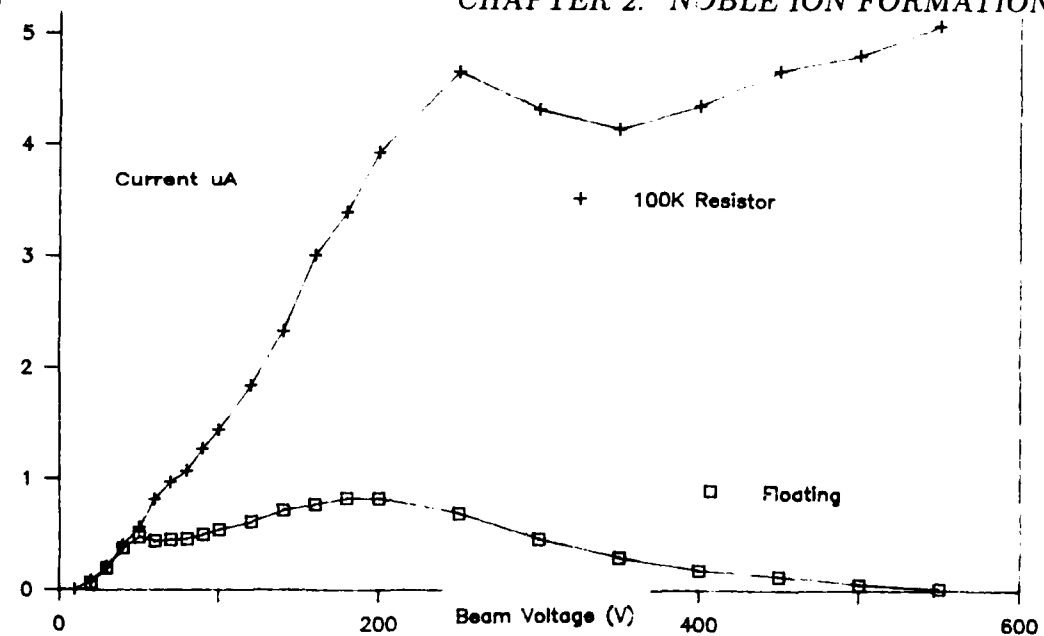


Figure 2.11: Electron beam currents measured alternately with a 100 kilohm resistor and the floating differential amplifier.

and 50 volts. Although the agreement between the two measures is excellent below fifty volts, the Ohm's law measurement substantially overestimates the beam current at higher energies. Beam electrons are tightly constrained by the magnetic field (any transverse velocity is filtered by the convergent magnetic mirror), but secondary electrons formed at the collector plate are not so constrained as they are generated in a region of uniform magnetic field. Their trajectories can intercept metal and insulator surfaces within the chamber and yield further secondaries which may be collected. In effect, the ICR cell behaves like a magnetic channeltron current amplifier. The details of this current amplification effect are expected to be influenced by individual system geometries, details of adsorbed gas, vacuum system materials, and alignment of the electron beam. Measurement of neon's ionization cross-section, that is the ratio of ion number to the electron current measured with the floating amplifier, scaled to Wetzel's value at 50 eV is shown in figure 2.12. The ratio of neon ion densities to measured electron beam current is smoothly varying, in contrast to what is obtained if the standard Ohm's law values illustrated in figure 2.11 were used for current diagnosis.

Large negative biases which are placed on the collector to inhibit secondary emission in the current measurement interfere with the electric fields of the ICR

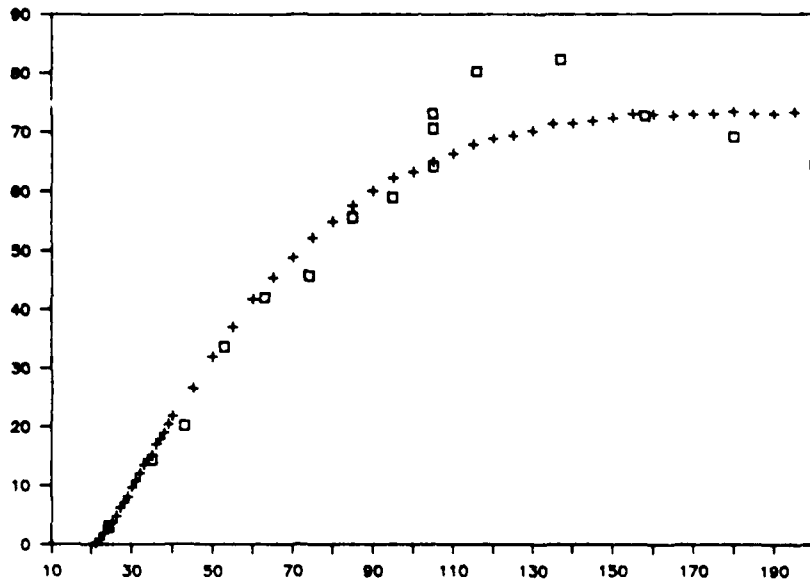


Figure 2.12: Ionization cross section,  $\sigma_1$ , from the ratio of FTMS signal to electron beam current (squares) scaled to the absolute values from the crossed-beam experiments of Wetzel at 50 eV.

trap, causing catastrophic perturbations to the ion motion. It is therefore necessary to perform the cyclotron excitation and detection with the collector close to ground potential, raising the possibility that secondary electrons may reenter the ICR trap and ionize reagent gas. Although the ICR volume is shielded by the rear trapping plate, the possibility of secondary electron interferences at high beam energies cannot be precluded in the present experimental configuration. For the measurements presented in this work the interference of secondaries is expected to be small since most data are acquired at energies below fifty volts, where the onset of this effect is indicated in figure 2.11. A new collector geometry is being designed which will eliminate this interference in future, high-energy experiments.

### 2.3.3 Interaction Region

The interaction volume in which ions are formed is a cylindrical string whose length is determined by the trap dimensions and whose diameter is related to the magnetically focused electron beam and the electron cyclotron radius at the field value inside the trap. For electrons generated two meters from the solenoid bore

the magnetic field at the cathode is roughly 100 Gauss. Magnetic focusing of the 1mm diameter beam is  $\approx 30,000/100$ , yielding a diameter of 3 microns from simple magnetic optic arguments. Confining a one microampere electron beam to this volume would give rise to enormous electric fields from Poisson's equation;

$$\nabla E = 4\pi\epsilon\rho$$

since  $\rho$ , the charged particle density, would be of order  $10^{12} \text{ cm}^{-3}$ . The actual radius of the electron beam represents the competition between magnetic focusing, on the one hand, and space charge defocusing on the other. Clearly a beam of infinitesimal current fired along the zero-magnetic field axis will propagate to the ion trap. Exact calculation of the beam radius for finite current beams depends on unmeasurable parameters such as the divergence of the electron beam, its geometric alignment with the magnetic field, and space-charge neutralization by ions formed in the experiment. However, a simple estimate of the interaction volume can be obtained from the electron cyclotron radius  $r$ :

$$r = 3.37 * \frac{\sqrt{v_{\perp}}}{B}$$

with  $B$  in Gauss and the velocity orthogonal to the magnetic axis,  $v_{\perp}$ , in cm/s. The convergent magnetic field acts as a transverse velocity filter, so that electrons with large  $v_{\perp}$  are reflected. The cyclotron trajectories with transverse velocity of  $10^7 \text{ cm/s}$  or less are constrained to radii of less than 3.35 mm at 3 Tesla. The interaction volume is therefore  $\approx \pi \cdot r^2 \cdot l$  where  $l$  is the distance between the electrostatic trapping plates (see figure 2.5) or  $\approx 1.7 \text{ cm}^3$  in these experiments.

### 2.3.4 Ion Signals

The relationship between ion number density and the signals recorded in FTMS has been extensively discussed in the literature [37], [38], [39], [40], [41], [42], [43] and the interested reader is referred to these references for details. Conceptually, the pulsed ICR experiment and its differences with classical ICR techniques are analogous to other Fourier transform methods as applied to absorption or nuclear magnetic resonance spectroscopies. From the classical equations of ion motion in a magnetic field the image currents and frequencies measured in the pulsed ICR experiment are linearly proportional to the number and mass, respectively, of ions in the ensemble. However care must be exercised if one is to retain this linearity in the presence of space charge, electrostatic potentials, cyclotron excitation, and collisional processes.

## 2.4 Noble Gas Measurements

As mentioned in the introduction there is substantial agreement on the magnitude and energy dependence of the total ionization cross-section:

$$\sigma_t = \sum_{i=1}^n (n * \sigma_n)$$

of the noble-gases ( $Rg = He, Ne, Ar, Kr, Xe$ ). At the same time there is significant variation in the literature values for partial ionization cross-sections,  $\sigma_n$ , of these same species:

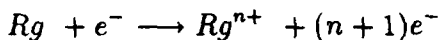
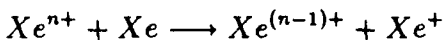


Figure 2.13 displays some of the reported partial ionization cross-sections for creation of multiply charged helium and neon by electron impact. Magnifying the obvious scatter in the experimental results is the failure of the recent crossed beam measurements [35] to observe either  $He^{2+}$  or  $Ne^{2+}$ . The probable cause for these variations is clarified by FTMS experiments on noble-gas ionization.

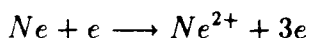
Early measurements of xenon and krypton ionization using FTMS revealed enormous signals at higher multiples of the monocation cyclotron frequencies. Figure 2.14 is typical of xenon spectra in the appearance of  $Xe^{n+}/Xe^+$  ratios which are over twice literature values [22]. After experimentally precluding harmonic distortion in the electronics and examination of the charge transfer reactions



it was clear that these were real signals from the multiply charged ions. Resolution of this curiosities was accomplished by examining the dependence of the ion signals on the product of electron beam current and irradiation time.

The literature values for multiple ionization of neon are widely scattered. Pulsed ICR measurements show that the intensity of the  $Ne^{2+}$  signal scales superlinearly with the product of electron beam irradiation time and current. Figure 2.15 is a plot of the  $Ne^{2+}$  signal arising from interaction of a 90 volt, 500nA electron beam for various times. The signal scales quadratically with the product of current and time, while that of the monocation varies linearly.

The interpretation is that production of the dication by the single collision process:



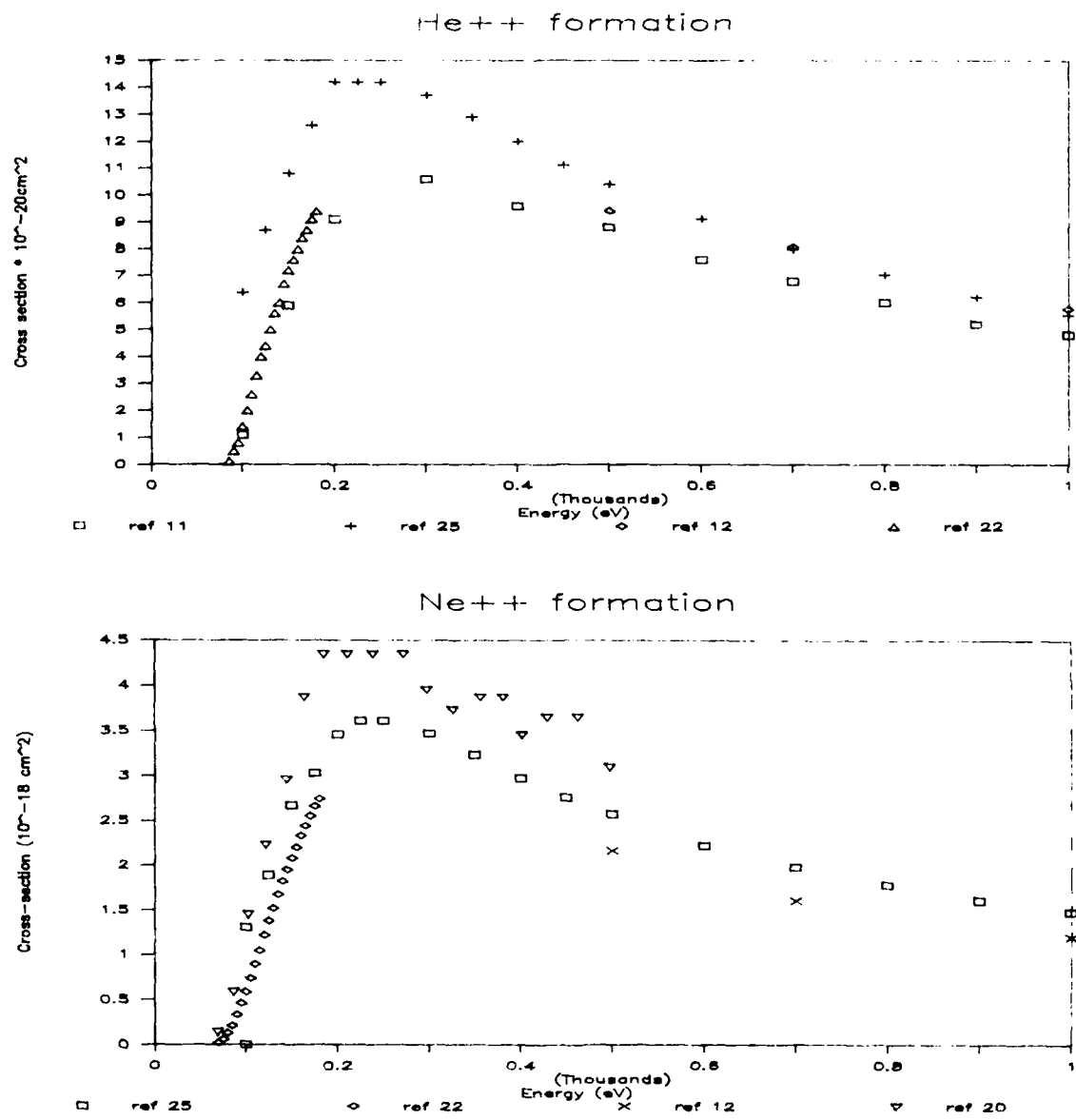


Figure 2.13: Literature cross-sections for helium and neon dication formation. Neither helium nor neon dications were observed in the recent crossed beam studies of Wetzel *et al.* [35]

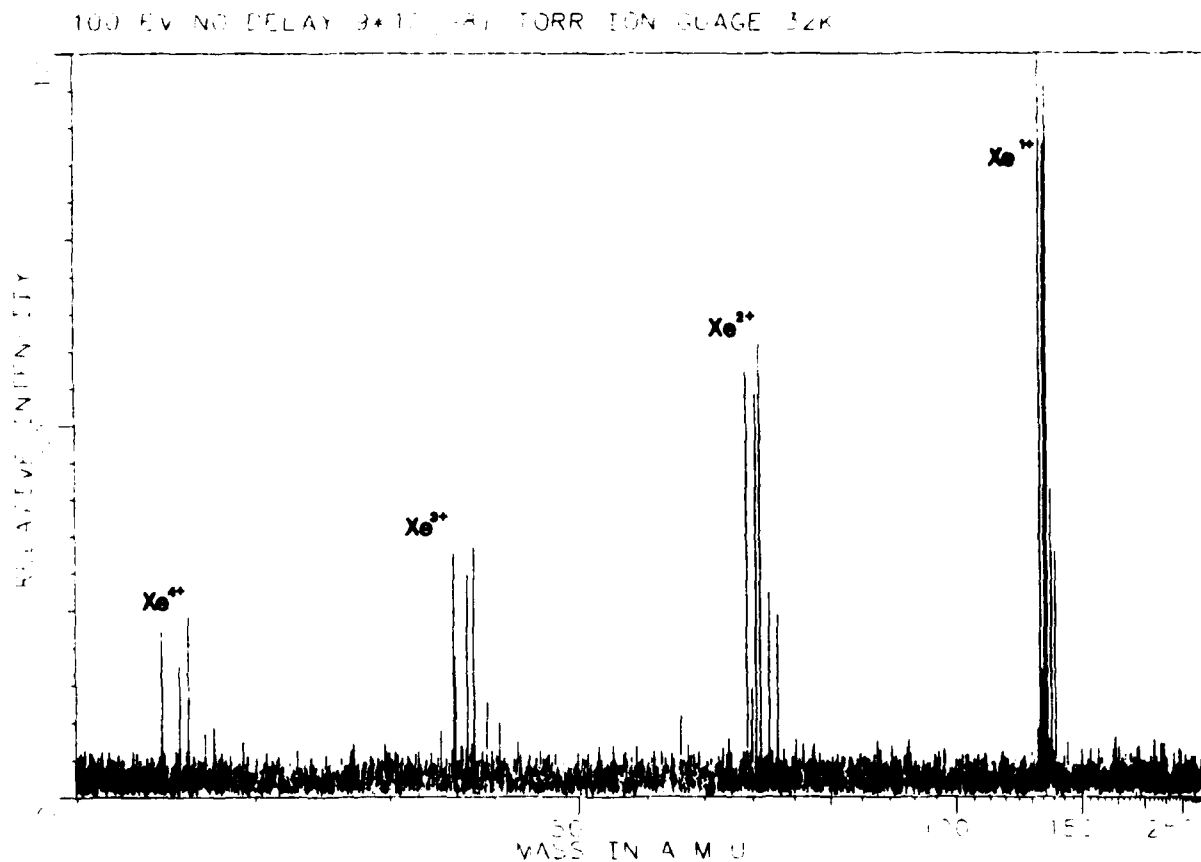


Figure 2.14: Typical xenon ion mass spectrum with exaggerated multiple ion intensities observed with an electron beam energy of 100 eV. According to the ref [22] the ratio of triple to double to single ionization cross-sections is .015:.108:1.0. Note that the observed intensities must be divided by the ion charge since the FTMS signal is proportional to the product of ion number and charge.

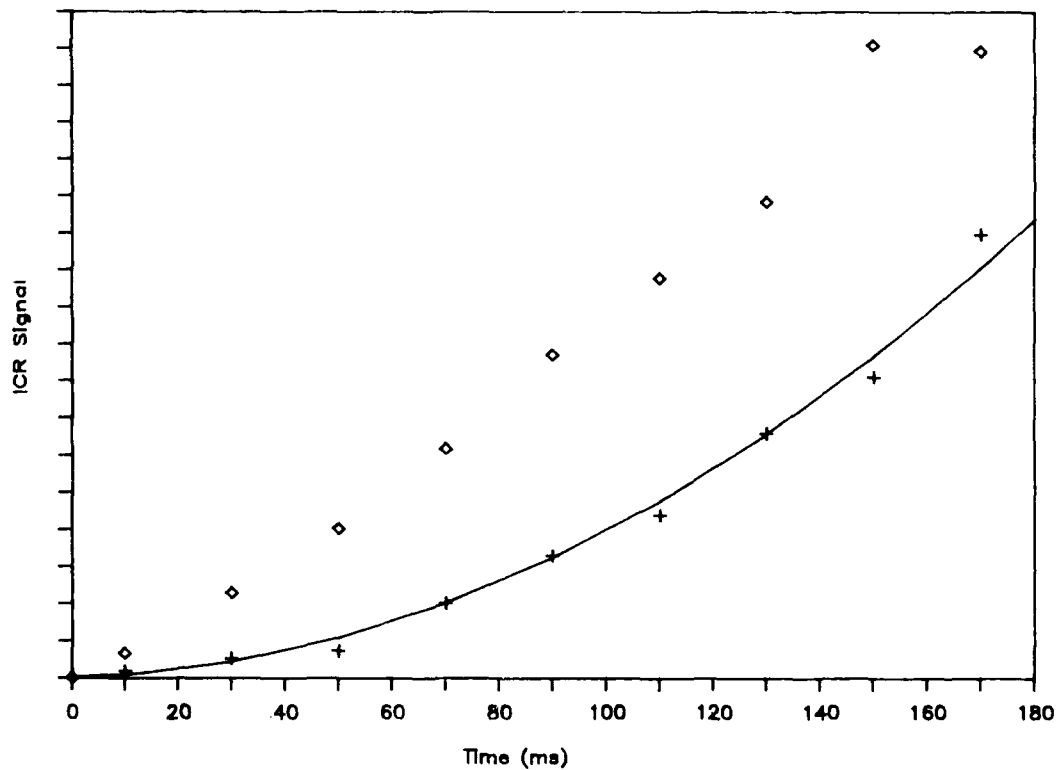
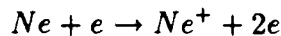
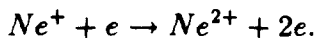


Figure 2.15:  $Ne^+$  (◊) and  $Ne^{+2}$  (+) ion signals as a function of electron beam irradiation time (ms) at constant, 500nA electron beam current. The  $Ne^+$  signals have been scaled by 1/13 to bring them onto the scale of the plot.

is less significant than two step ionization:



followed by



Multiple ion formation is ordinarily attributed to electron pair correlation in heavier atomic or conjugated molecular systems, and is therefore not anticipated to be important in neon [1]. Assuming the electron cyclotron radius defines the interaction volume these observations are made with current densities of order  $\mu\text{amps}/\text{cm}^2$  and total charges,  $I \cdot t$ , in the microcoulomb range. Singly charged rare-gas ions are constrained to a volume which is roughly coincident with the electron beam. Their transverse energy (from momentum transfer and trap electrostatic fields) is too small for the radius of their cyclotron orbit to be more than a tiny fraction of that of the electrons. (For dissociative ionization of a molecule from a strongly repulsive level this need not be true) A peculiar feature of the FTMS experiment is that higher order processes may be probed using long beam irradiation times; in conventional mass spectrometer ion sources the upper limit for  $I \cdot t$  is set by the relationship of the ionizer current to ion diffusion. Using the ion trap diffusion is constrained by the magnetic and electric fields; one must only satisfy the requirement that the total charge in the trap is not so large as to counteract the electrostatic trapping potential. A lower bound for the two-step process can be obtained by assuming 100% overlap of the electron beam and the ion cloud so that the rates for formation of  $Ne^+$  and  $Ne^{2+}$  are:

$$\frac{dNe^+}{dt} = \sigma_1 \cdot I \cdot N \cdot l$$

so that

$$Ne^+(t) = \sigma_1 \cdot N \cdot I \cdot l \cdot t$$

and

$$\frac{dNe^{2+}}{dt} = \sigma_2 \cdot N \cdot I \cdot l + \sigma_{12} \cdot \frac{Ne^+}{l} \cdot I \cdot l$$

so that

$$Ne^{2+}(t) = \sigma_2 \cdot N \cdot l \cdot I \cdot t + \sigma_{12}\sigma_1 \cdot N \cdot l \cdot I^2 \cdot t^2.$$

In these equations

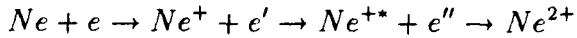
- $\sigma_1$  is the partial ionization cross-section for monocations

- $I$  is the electron beam current
- $N$  is the reagent gas number density
- $l$  is the path length of the cell (5cm)
- $\sigma_2$  is the partial ionization cross-section for dication
- $\sigma_{12}$  is the cross-section for further ionization of the singly charged species produced at a specific energy by another electron of the same energy. Note that generation of electronically excited or Rydberg states with  $\approx$  millisecond lifetimes may cause this number to exceed the ionization cross-section of the ground state monocation.

The ratio

$$\frac{[Ne^{2+}](t)}{[Ne^+](t)} = \frac{\sigma_2}{\sigma_1} + \sigma_{12} \cdot I \cdot t$$

is linearly proportional to the product of beam current and irradiation time if  $\sigma_2$  is zero. In fact this ratio provides an experimental lower bound on the cross-section  $\sigma_{12}$  since it is decreased by less than perfect overlap between the electron beam and ion cloud. Table 2.1 summarizes the value for  $\sigma_{12}$  measured by similar techniques at several electron energies. Note that doubly charged ions appear below the spectroscopic threshold (62.63 eV) for  $Ne^{2+}$  formation. This is thought to be a result of ionization of electronically excited ions formed by the first electron impact. Doubly charged ions with a quadratic  $I \cdot t$  dependence were not obtained at thirty-four volts, an energy lower than that of the first electronically excited state of  $Ne^+$  (48.46 eV). However weak signals of  $Ne^{2+}$  were observed at irradiation times over two seconds which are attributed to three electron processes:



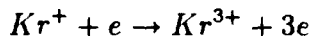
From table 2.1 and figure 2.16 it is clear that the magnitude of  $\sigma_{12}$  is enormous. While one expects this cross-section to be large from the long-range coulomb attraction between the electron and ion, cross-sections in the  $10^{-14} cm^2$  range are still remarkable. It is essential to distinguish the present values from crossed beam measurements of electron-ion ionization. In the present case one is probing ionization of an ensemble of ions by a second electron of the same energy as that which formed the singly charged species. Electronically excited ions and rydberg species with large scattering cross-sections which fail to decay radiatively will not

Energy (eV)	$\sigma_{12}$
34	no $Ne^{2+}$ observed
55	$5.4 \pm 2 \cdot 10^{-15} cm^2$
66	$6.2 \pm 3 \cdot 10^{-15} cm^2$
150	$2.0 \pm .9 \cdot 10^{-14} cm^2$

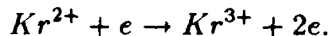
Table 2.1: Cross-sections for two step ionization ( $\sigma_{12}$ ) of neon. These values represent lower bounds on  $\sigma_{12}$  since complete overlap of the electron beam and ion cloud are assumed in their calculation.

have time to relax collisionally at the low ( $\approx 10^{-7}$  torr) pressures in the ion trap. Anything with a lifetime of millisecond order or greater is therefore vulnerable to sequential ionization. By contrast ion beams with which electron-ion ionization is probed [1] are generally formed by electron impact at energies low enough to avoid excited state formation, so that only the ionization of the ground electronic state is probed.

While careful analysis of the neon system at several energies led to no detectable value for  $\sigma_2$ , as expected from the crossed-beam measurements, the qualitative dependence of multiply charged ion formation on beam irradiation time for krypton gave different and intuitively comprehensible results. Figure 2.17 depicts the dependence of  $Kr^{n+}$  signals on the electron beam irradiation time. Since the ion signals for  $n=1$  and 2 are both linearly increasing in time, these appear to be direct processes as expected on the basis of the larger correlation of electron pairs in krypton. The signals for  $n=3$  and 4 are superlinearly dependent on irradiation time, suggesting a multiple step process for their formation. These data do not differentiate between the processes



and



There are plans to utilize selected waveform resonance ejection techniques [44] on these noble-gas systems to pinpoint the source of the highly charged species.<sup>2</sup>

On the basis of these measurements it is suggested that differences among the literature cross-sections for the formation of multiply charged ions by single electron impact, such as those illustrated in figure 2.13, are due to ionization of

<sup>2</sup>e.g. resonance ejection of  $Kr^+$  would not effect further ionization of  $Kr^{2+}$

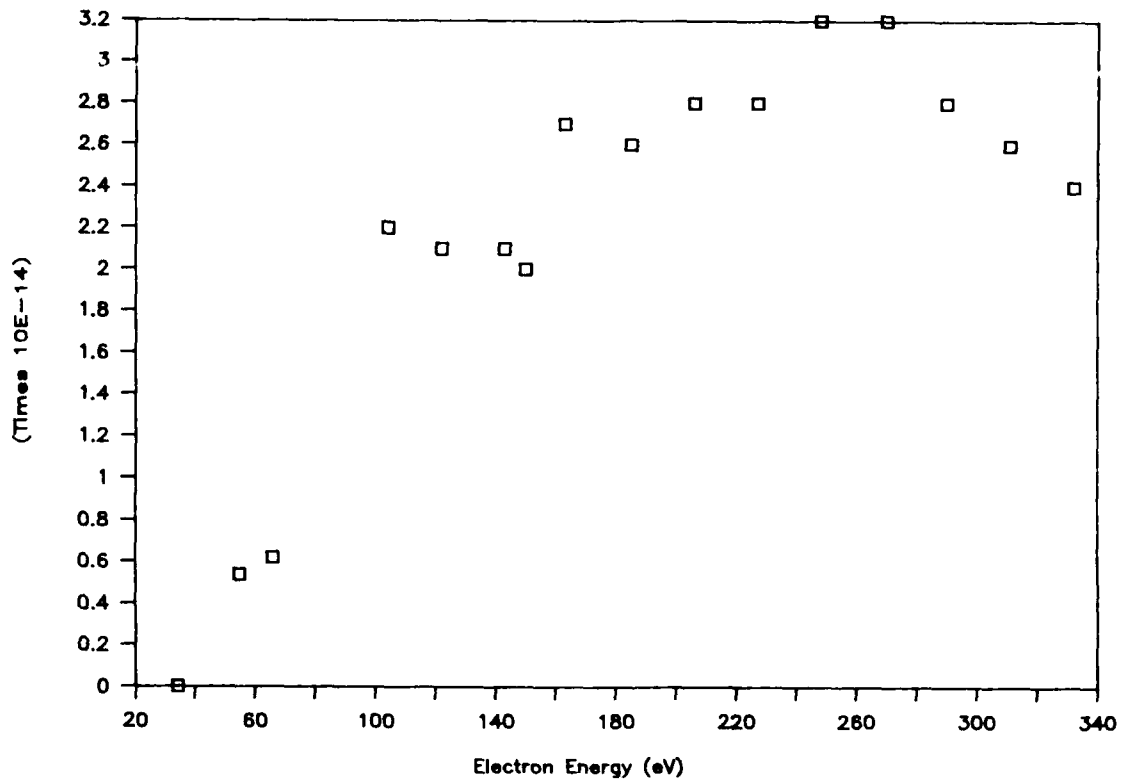


Figure 2.16:  $\sigma_{12}(Ne)$  inferred from the ratio of  $Ne^{2+}$  to  $Ne^+$  ICR signals at 150 millisecond irradiation times with various energies. Since the full  $(I \cdot t)$  dependence at each energy was not mapped the uncertainty is  $\approx \pm 10^{-14} \text{ cm}^2$ .

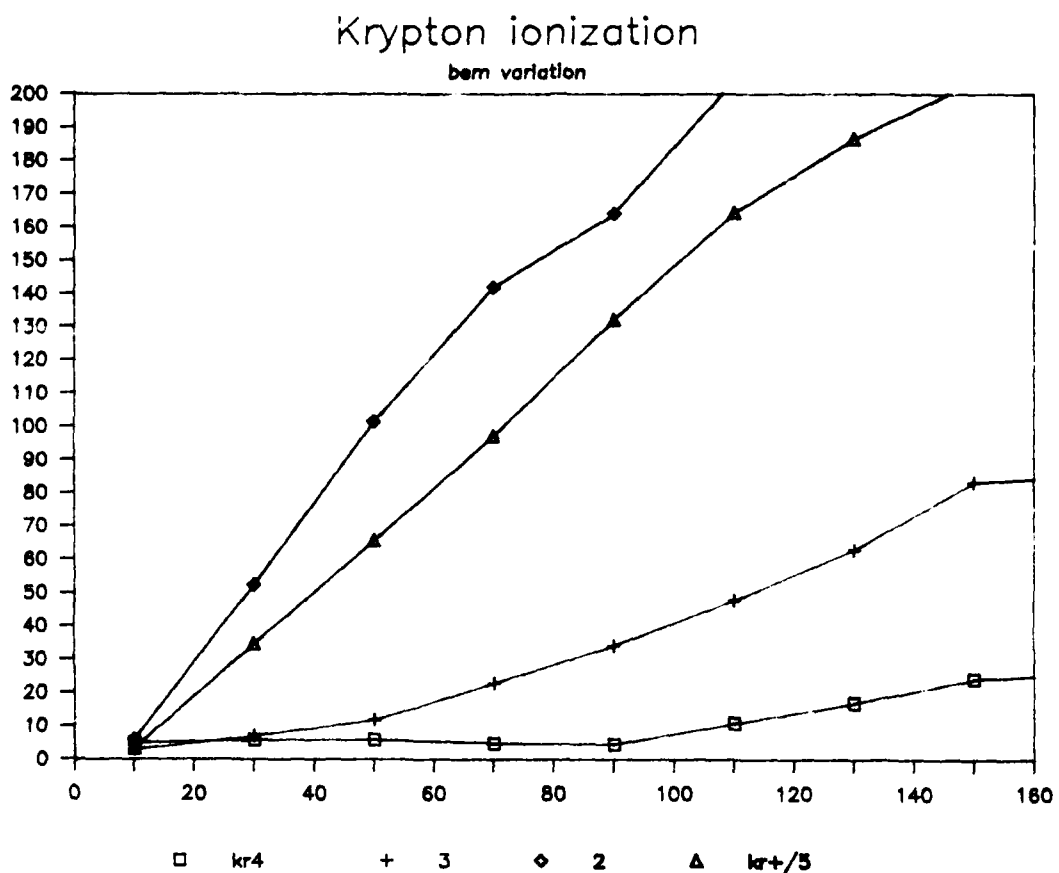


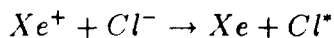
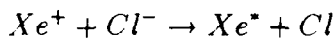
Figure 2.17: Variation of  $Kr^{n+}$  ICR signals with electron beam irradiation time for  $n=1,2,3$ , and 4 scaled by factors of 1, 10, 15, and 20 respectively.

the monocations and their excited states. The parameter with which these processes scale is a product of electron beam current and the time during which ions interact with the beam. This quantity, which has units of charge, is fractions of a microcoulomb for the presently observed  $Ne^{2+}$  formation at  $5 \cdot 10^{-7}$  torr. The very low pressure experiments, in which the time between ion-neutral collisions is long compared to the experimental observations, represent a limiting case for the sequential ionization of a gas. At higher pressures collisional quenching of ion charge and excited states can compete with sequential ionization, thereby reducing the influence of nonlinear terms such as  $\sigma_{12}$  on changes of the charge state ensemble with the product of beam current and interaction time. Both this product and collisional quenching have consequences for experimental determination of  $\sigma_2$  which depend in detail on the apparatus and method employed.

## 2.5 Implications

### 2.5.1 $Rg_2^{2+}$ Laser?

A novel aspect of the two-step ionization suggests a possible source of coherent x-ray and vuv radiation. Enhanced production of dication such as  $He^{2+}$  can be accomplished by maximizing the product of beam current and interaction time, for example by using 60 kV electron beam excitation of a very high pressure parent gas ( $\approx 10$  atmospheres). The resulting translationally cool dication are drawn to the parent gas by a long-range polarization potential. The presence of third bodies at high pressure facilitates formation of the complex  $Rg_2^{2+}$ . For example  $He^{2+}$  reacts rapidly ( $k = 4.8 \pm .5 \cdot 10^{-14} cm^3 s^{-1} + 2 \pm 1 \cdot 10^{-31} [He] cm^6 s^{-1}$ ) with helium to form a dimer,  $He_2^{2+}$ , [45] which is predicted to radiate at a wavelength of 60 nanometers ( $\approx 20eV$ ) [46]. The lower state is coulomb repulsive, so that its very efficient depopulation make it a natural candidate for stimulated emission.  $Rg_2^{2+}$  is then a classical excimer laser scheme which ought to apply generally to the homonuclear and heteronuclear rare-gas dimer dications. Beyond obviating the need for chemical fuel which characterizes such excimers as  $XeCl$ , the dimer dication scheme has qualitatively different competing mechanisms, for example charge transfer analagous to the process:



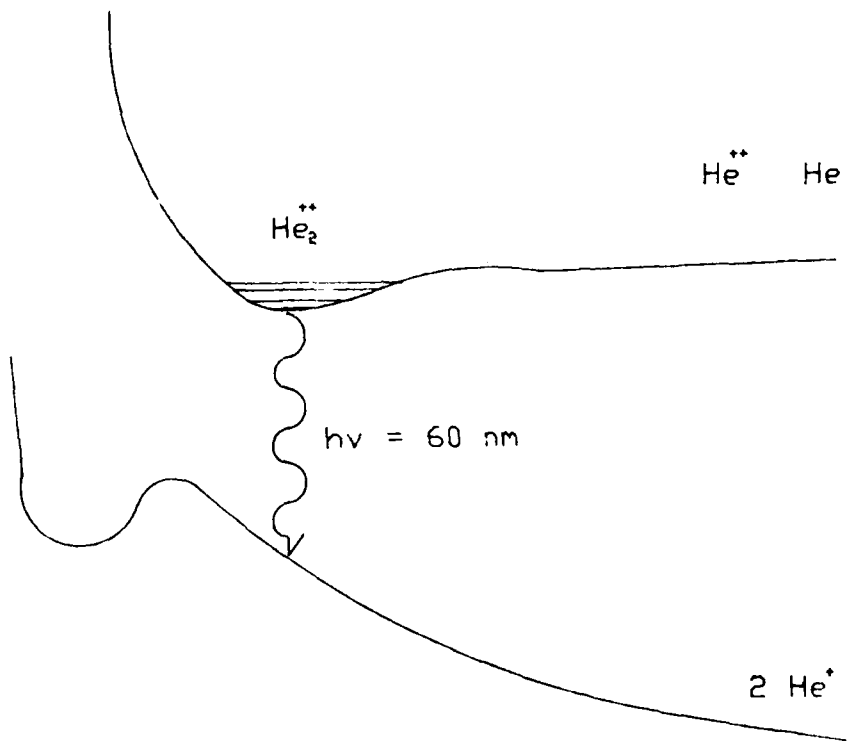


Figure 2.18: Schematic potential energy diagram for the  $\text{He}_2^{2+}$  radiation source.

is thermodynamically forbidden for all of the homonuclear  $Rg_2^{2+}$  species. Variations on this theme which involve higher charge states are also possible for the heavier rare-gases. However this dissertation is concerned with silicon deposition, to which we now return.

### 2.5.2 $Rg^{n+}$ in PECVD?

Discussion of multiply charged ion formation from noble-gases has been included primarily to illustrate the experimental methods with which ion chemistry in deposition discharges will be assessed in the present work. It is nevertheless fair to ask what role multiply charged ions play in these film reactors. The relevant quantity is the product of beam current and interaction time. In discharges ions are not trapped; the interaction time is governed by ion diffusion, which is on the order of tens of microseconds for plasma deposition reactors. The total discharge

currents are typically tens of milliamperes, so that the product of total current and interaction time is an order of magnitude less than that for which  $Ne^{2+}$  started to play a role in the ICR measurements. The fraction of electron current which is sufficiently energetic to play a role in multiple ion formation further reduces this contribution by several orders of magnitude. Whether one uses a monotonically decreasing electron energy distribution or one composed of a ballistic beam and low energy swarm (see chapter 5), the fraction of electrons which are high enough in energy to form  $Rg^{2+}$  is less than  $\approx 10^{-4}$ . The product of beam current and ion-electron interaction time therefore precludes the prospect of multiply charged ion formation playing a role in plasma deposition reactors.

## 2.6 Conclusions

The modifications to and application of pulsed ion cyclotron resonance mass spectrometry required for the measurement of ionization cross-sections have been described. In particular techniques for determining pressure and electron beam current have been developed. While the experimental literature concerning total ionization of noble-gases by electron impact is not controversial, dissonance is shown to remain on the question of multiple ion formation by single electron impact. The pulsed ICR technique is used to demonstrate the dominance of stepwise ionization of neon in the production of  $Ne^{2+}$  under conditions where the product of electron beam current and electron-ion interaction time is in the microcoulomb range. While of possible interest for the generation of coherent x-radiation or the charged particle kinetics of high pressure discharges, multiply charged ions are unlikely participants in PECVD reactor kinetics.

# Bibliography

- [1] T. D. Märk and G. H. Dunn **Electron Impact Ionization**, New York:Springer-Verlag [1985].
- [2] D. Rapp and P. Englander-Golden, *Journal of Chemical Physics*, **43**, 1464 [1965].
- [3] H. Helm and T. D. Märk, *Journal of Chemical Physics*, **73**, 7680 [1980]
- [4] R. C. Wetzel *et al.*, *Physical Review*, **A35**, 559 [1987].
- [5] T. Hayes, R. Wetzel and R. Freund, *Physical Review*, **A 35**, 578 [1987].
- [6] P. Haaland and A. Rahbee, *Chemical Physics Letters*, **114**, 571 [1985].
- [7] M. Comisarow and A. Marshall, *Chemical Physics Letters*, **25**, 282 [1974].
- [8] A. Marshall, *Accounts of Chemical Research*, **18**, 316 [1985].
- [9] S. Barlow *et al.*, *International Journal of Mass Spectrometry and Ion Processes*, **54**, 169 [1983].
- [10] K. Bell *et al.*, *Journal of Physical and Chemical Reference Data*, **12**, 891 [1983].
- [11] B. Adamczyk, *et al.*, *Journal of Chemical Physics*, **44** 4640 [1966].
- [12] P. Nagy, A. Skutlartz and V. Schmidt, *Journal of Physics B: Atomic and Molecular Physics*, **13**, 1249 [1980].
- [13] H. Drewitz, *International Journal of Mass Spectrometry and Ion Processes*, **19**, 313 [1976].

- [14] A. Crow, J. Preston and J. McConkey, *Journal of Chemical Physics*, **57**, 1620 [1972].
- [15] M. van der Wiel, F. deHeer and G. Wiebs, *Physics Letters*, **24A**, 423 [1967].
- [16] F. Fiquet-Fayard et M. Lahmani, *Journal de Chimie et de Physique*, **59**, 1050 [1962].
- [17] F. Fiquet-Fayard, *Journal de Chimie et de Physique*, **59**, 439 [1962].
- [18] R. Fox, *Journal of Chemical Physics*, **33**, 200 [1960].
- [19] D. Stevenson and J. Hipple, *Physical Review*, **62**, 237 [1942].
- [20] W. Bleakney and L. Smith, *Physical Review*, **49**, 402 [1936].
- [21] J. Tate and P. Smith, *Physical Review*, **46**, 773 [1934].
- [22] K. Stephan and T. Märk, *Journal of Chemical Physics*, **81**, 3116 [1984].
- [23] F. Egger and T. Märk, *Zeitschrift Naturforsch.*, **33a**, 1111 [1978].
- [24] K. Weismann, J. Puerta and B. Huber, *Journal of Physics D: Atomic and Molecular Physics*, **20**, 588 [1987].
- [25] A. Gaudin and R. Hagemann, *Journal de Chimie et de Physique*, **64**, 1209 [1967].
- [26] W. Bleakney, *Physical Review*, **36**, 1303 [1930].
- [27] Lasertechnics, Inc., Albuquerque, N.M.
- [28] Spinning Rotor Gauge SRG2, MKS Instruments, Inc., Burlington, MA.
- [29] ELG-2 electron gun and EG2PS power supply, Kimball Physics, Wilton, N.H.
- [30] J. Lobell, *Harvard Atmospheric Research Project*, [1987].
- [31] Nicolet FTMS-1000, Nicolet Analytical Instruments, Madison, WI.

- [32] L. Spitzer, *Physics of Fully Ionized Gases*, New York: Interscience Publishers [1956].
- [33] A. von Engle, *Ionized Gases*, Oxford: Clarendon Press, [1965].
- [34] A. Marshall *et al.*, *Journal of the American Chemical Society*, **107**, 7893 [1985].
- [35] A. Marshall and D. Roe, *Journal of Chemical Physics*, **73**, 1581 [1979].
- [36] W. Reents and A. Muisce, *International Journal of Mass Spectrometry and Ion Processes*, **59**, 65 [1984].
- [37] M. Comisarow, *Journal of Chemical Physics*, **69**, 4097 [1978].
- [38] D. Rempel, S.K. Huang and M.L. Gross, *International Journal of Mass Spectrometry and Ion Processes*, **70**, 163 [1986].
- [39] M. Riggin and I.B. Woods, *Canadian Journal of Physics*, **52**, 456 [1974].
- [40] T.F. Knott and M. Riggin, *Canadian Journal of Physics*, **52**, 426 [1974].
- [41] M. Bloom and M. Riggin, *Canadian Journal of Physics*, **52**, 436 [1974].
- [42] R.C. Dunbar, *International Journal of Mass Spectrometry and Ion Processes*, **56**, 1 [1984].
- [43] J.B. Jeffries, S.E. Barlow and G.H. Dunn, *International Journal of Mass Spectrometry and Ion Processes*, **54**, 169 [1983].
- [44] A. Marshall, T.C. Wang and T. Ricca, *Journal of the American Chemical Society*, **107**, 7893 [1985].
- [45] R. Johnson and M. Biondi, *Physical Review*, **A 18**, 996 and 989 [1978].
- [46] J. Cohen and J. Bardsley, *Physical Review*, **A 18**, 1004 [1978].

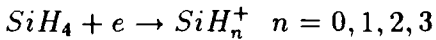
# Chapter 3

## Silane Ionization

### 3.1 Introduction

The processes by which silane is ionized in plasmas are characterized by qualitative differences from those by which rare-gas ions are formed. Although numerous articles whose objective has been analysis of silane ionization have appeared, there is a remarkable lack of consensus on features which are essential to a quantitative understanding of silane-containing discharges. Since the first measurements of silane ionization by Neuert and Classen [1] for example, the existence of the molecular silane cation,  $SiH_4^+$ , has been alternately 'confirmed' and 'precluded' in a variety of experiments. Table 3.1 summarizes reports of the molecular cation's observation.

A second open question concerns the extent to which silane is dissociatively ionized by electrons. While there is general agreement on the energy dependence of the partial ionization cross-sections:



the extent to which  $H^+$  and  $H_2^+$  are formed is less well-defined. Similarly, the agreement among published data for the magnitude of the electron-impact ionization cross-section, as illustrated in figure 3.1, is less than that required for quantitative modelling of ion kinetics in silane plasmas. These unresolved features of silane ion formation have been examined with pulsed ICR mass spectrometry and *ab initio* electronic structure calculations as described below.

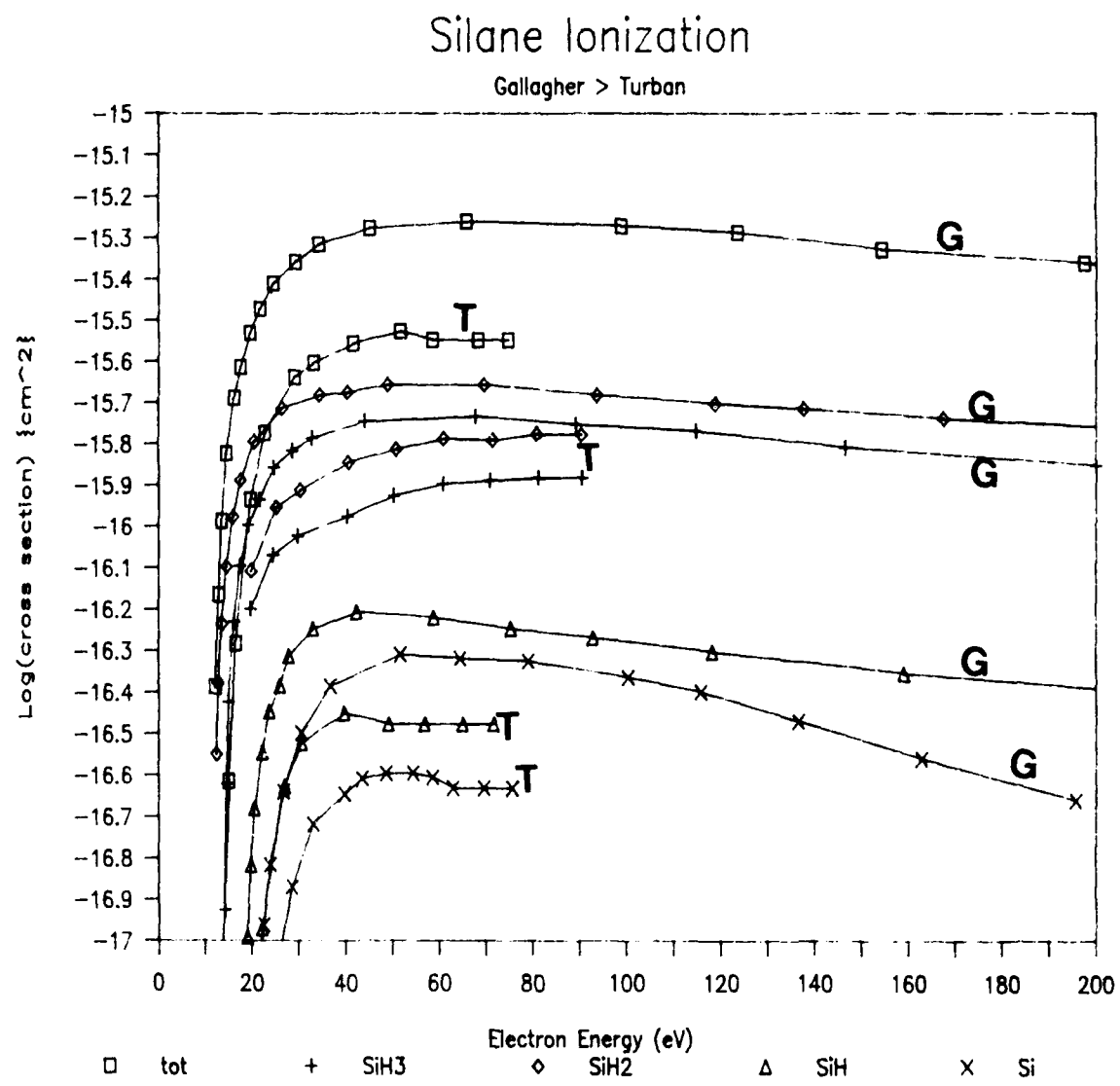


Figure 3.1: Logarithm of the partial and total electron impact ionization cross-sections of silane reported by Chatham and Gallagher (G) [12] and Turban (T) [12].

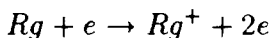
Date	$SiH_4^+$ ?	Excitation	Reference
1952	yes	electron	Neuert [1]
1963	yes	electron	Saalfeld [2]
1969	no	electron	Potzinger [3]
1973	no	electron	Morrison [4]
1980	no	electron	Turban [12]
1984	yes	photon	Genuit [11]
1984	no	electron	Chatham [12]
1984	yes	electron	Longeway [19]
1985	no	photon	Ding [14]
1985	no	electron	Haaland [20]
1986	no	photon	Borlin [17]
1987	yes	photon	Berkowitz [11]

Table 3.1: Experimental reports on the existence of the molecular silane cation.

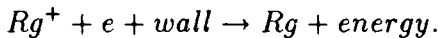
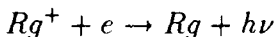
## 3.2 The Molecular Silane Cation?

### 3.2.1 $Rg$ versus $SiH_4$

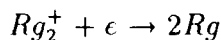
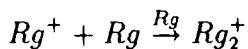
Ionization of noble-gases is reversible in a plasma environment in the sense that electron-ion recombination, charge transfer reactions, and wall loss yield the original noble-gas atom. The steady-state ion kinetics of a rare-gas glow discharge at low pressures are governed by the principal ion source:



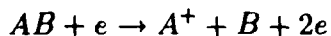
and ion losses:



As the gas pressure is increased above torr levels the rapid formation and dissociative recombination of dimer ions provides an important, homogeneous, two-step loss process for electrons:



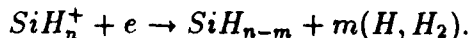
Ionization of molecular species is qualitatively different in three important ways. First, dissociative ionization:



is not easily reversible in the gas phase as was the regeneration of  $Rg$  in the rare-gas case. Second, reduction of  $A^+$  by electron transfer from a wall produces the  $A$ -free radical, which is capable of chemical bonding with a surface. The analogous reduction of  $Rg^+$  yields unreactive, physisorbed  $Rg$  atoms. Third, dissociative recombination of molecular ions and electrons:



which is typically five orders of magnitude more rapid than its radiative counterpart, can occur directly on the ions formed by electron impact:



This contrasts with the homogeneous loss process for electrons in noble gas discharges, in which the reaction  $Rg^+ + 2Rg \rightarrow Rg_2^+$  is the rate-limiting step which must occur to provide a species with which electrons may dissociatively recombine.

Definition of the ion kinetics in silane-containing plasmas therefore requires an understanding of the extent to which silane ionization is dissociative. Probing for the existence of  $SiH_4^+$  also raises some very basic questions, to be described below, about the collisional interactions which result in ion formation from molecular species.

### 3.2.2 Electron-impact Spectra

Measurement of the molecular cation is complicated by the natural occurrence of three stable silicon isotopes:  $^{28}Si$ ,  $^{29}Si$ , and  $^{30}Si$  whose relative abundances are 92.21, 4.70 and 3.09 % respectively [9]. The earliest observation of a large molecular ion signal by Neuert and Clasen [1] was later dismissed by Saalfeld and Svec [2] as an error in calibration of their spectrometer's mass scale. Nevertheless Saalfeld's 1963 work reports an appearance potential and a relative intensity for  $SiH_4^+$  of .44% compared to the principal  $SiH_2^+$  peak in the mass spectrum. Subsequent investigations using electron-impact excitation of silane have argued for or against the existence of the molecular cation. However these arguments

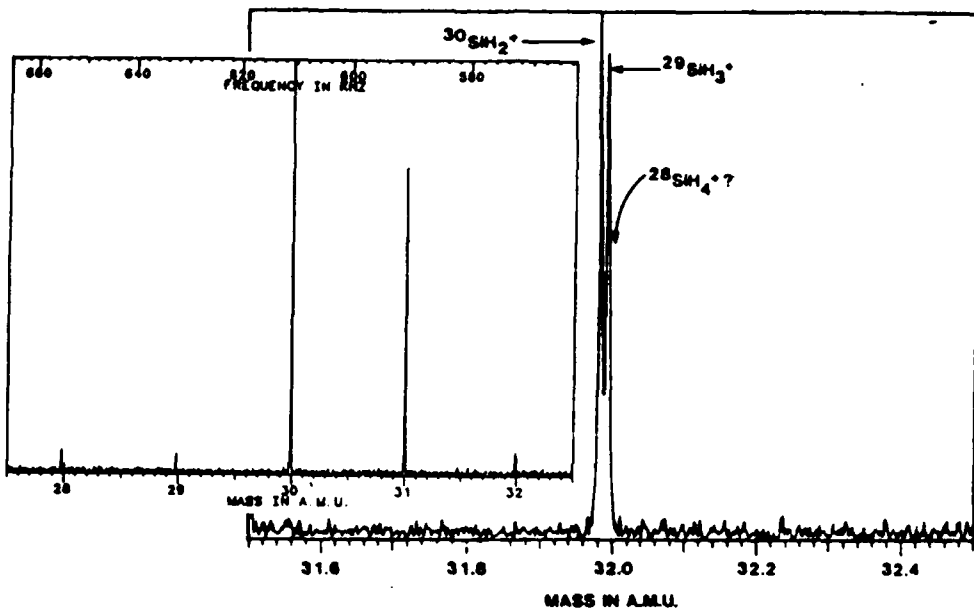


Figure 3.2: Pulsed ion cyclotron resonance mass spectrum of silane at 70 eV,  $\approx 10^{-9}$  torr. The two ions at  $m/e \approx 32$  correspond to  $^{29}SiH_3^+$  and  $^{30}SiH_2^+$  as summarized in table 3.2.

have been made on the basis of very small threshold signals which could not be resolved from isotopic contributions such as  $Si^{29}H_3^+$  and  $Si^{30}H_2^+$ .

Preliminary pulsed ion cyclotron resonance mass spectrometry of silane under single collision conditions was performed at the Air Force Geophysics Laboratory using a Nicolet FTMS-1000 instrument and has already been described in reference [20]. Ions with nominal mass to charge ratios 32 and 33 were shown to consist exclusively of di- and tri- hydride cations of the rarer  $Si^{29}$  and  $Si^{30}$  isotopes (Figure 3.2). The mass spectrum was measured over the electron energy range from threshold for appearance of  $SiH_2^+$  to ninety electron volts. No peak was evident at a mass to charge ratio of 34.

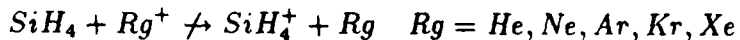
One possible objection to this early work is that infrared radiation from the proximal filament of the FTMS-1000 ionizer might dissociate the molecular cation [11, 11]. The experimental configuration described in chapter 2 overcomes this objection since the indirectly heated cathode is over two meters from the ion trap. Repeating the earlier measurements on the newer spectrometer yielded identical results. The most convincing evidence was the observation of only two peaks at 32 atomic mass units, since one should observe the principal isotope of the

Species	Calculated	Observed	error
<i>A</i> $^{29}SiH_3^+$	31.99942	31.99942	calibration
<i>B</i> $^{30}SiH_2^+$	31.98860	31.98867	0.00007
<i>C</i> $^{28}SiH_4^+$	32.00768	...	...
( <i>A</i> - <i>B</i> )	0.01082	0.01075	0.00007
( <i>C</i> - <i>A</i> )	0.00826	...	...
<i>A/B</i> intensity	1.07	1	...

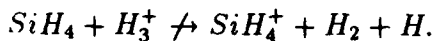
Table 3.2: Calculated and observed ion masses for the spectrum displayed in figure 3.2, which was recorded at 70 eV in  $\approx 10^{-9}$  torr silane as described in ref [20].

molecular ion,  $^{28}SiH_4^+$ , as a third signal in the high-resolution mass spectrum. Table 3.2 outlines the calculated and observed contributions to the ion spectrum near 32 atomic mass units.

Over the range of electron energies from the threshold for ion detection near ten volts to one kilovolt only two peaks were observed at 32 atomic mass units. Neither were isotopes of the molecular ion,  $^{29}SiH_4^+$  or  $^{30}SiH_4^+$  identified at 33 or 34 amu. Only a single peak was ever resolved at  $m/e=33$ , which arose from the  $^{30}SiH_3^+$  ion. In addition the molecular cation was not identified as a product of the reactions:



or



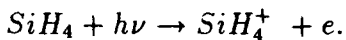
One is thus led to the conclusion that the ion  $SiH_4^+$ , if formed by electron impact, is not stable under collisionless conditions on a millisecond timescale. The earlier 'controversy' concerning observation of the molecular cation in magnetic sector and quadrupole mass spectrometers can only be understood on the basis of gas-phase impurities and nonlinearity of the ion detectors over the dynamic range required to simultaneously measure a weak parent peak in the presence of large signals from dissociative ionization of the heavier isotopes.

### 3.2.3 Photoionization

Formation of the molecular cation by photoionization of silane was first argued in 1982 [11]. Genuit *et al.* observed an ion signal at  $m/e=34$  using a quadrupole

mass filter with an argon resonance lamp (1066 and 1048 Å) as an ionization source. The room temperature measurements were performed with pressure in the ion source between  $10^{-2}$  and  $10^{-4}$  torr. Contamination by  $H_2S$  and  $PH_3$  was precluded from their observed spectra, however the possibility of  $Si^{28}H_5^+$  causing this signal was not discussed.  $SiH_5^+$  is formed by the reaction of proton donors such as  $NH_2^+$ ,  $C_2H_3^+$  or  $C_2H_6^+$ , which are common impurities in quadrupole vacuum systems, with silane [10]. The contribution of the molecular cation to the total ion signal was estimated at 4%, which would clearly be observable in the high-resolution electron-impact mass spectrum as a third peak at  $m/e = 32$  of comparable intensity to those shown in figure 3.2, a second at  $m/e = 33$ , and a single peak at  $m/e = 34$ .

Subsequent photoionization analyses using tunable radiation at low ( $10^{-4}$  mbar) pressure [17] and alternately in a supersonic expansion [14] observed no molecular ion signals. However a very recent report of photoionization of silane and its radicals provides compelling evidence for the process[11]:



Although the contributions of dissociatively ionized fragments were not resolved directly in the quadrupole mass spectrum, the observed correlation of the vibrational structure of the  $m/e = 32$  photoion peak with the photoelectron spectrum of silane [15] would be unlikely for an impurity signal. These photoion experiments were conducted under single-collision conditions, precluding collisional stabilization of the molecular cation by the  $120\text{ }^{\circ}K$  bath gas.<sup>1</sup> Observation of  $SiH_4^+$  was confined to the wavelength range between  $1100\text{\AA}$  and  $1000\text{\AA}$  (11.2 – 12.4 eV). The intensity of the molecular ion signal was consistent with the earlier work of Genuit if his argon lamp produced mostly  $1066\text{\AA}$  photons.

The molecular ion is reported over a relatively narrow range of photon energies. One might argue that failure to observe  $SiH_4^+$  in the electron-impact spectrum is a consequence of having too few electrons in the ionizing beam within the appropriate energy range. The full-width at half-maximum of the reported photoion at  $m/e = 32$  is approximately 0.5 eV, comparable to the expected energy spread of the electron beam in the ICR spectrometer. While spectra were recorded at increments of one volt or less near threshold, it is conceivable, but unlikely, that the overlap of the beam's energy distribution with the resonance reported in the photoion mass spectrum precluded significant formation of  $SiH_4^+$ .

<sup>1</sup>J. Berkowitz, Argonne National Laboratory, personnel communication, 9/87.

The overlap objection is also weakened by the fact that electron-impact excitation need not be resonant to satisfy energy and momentum conservation in its collision with silane. The energy with which silane is excited need only equal the energy *lost* by the incident electron, a condition which can be satisfied for any incident energy above threshold. By contrast photoexcitation must couple the ground state to a level equal in energy to the incident photon; as the density of states in the ionized continuum changes so must the photoionization cross-section. The generally more rapid decrease of photoion yields with increasing energy compared to analogous electron-impact ionization cross-sections is one tangible result of this constraint.

The conclusion drawn from the present experiments and a critical review of the recent literature is that  $SiH_4^+$  is not formed in detectable quantities by electron-impact on silane. However this species represents several percent of the photoionization mass spectrum between 11 and 12 eV. If ionization by photons and electrons were analogous, these observations would be inconsistent. Therefore a fundamental difference between ionization of silane by electrons and photons is indicated. While of considerable academic interest, this difference plays no role in PECD. Under plasma conditions, where ionization is performed by a broad range of electron energies, the integrated contribution of  $SiH_4^+$  to the ion distribution would be undetectable, according to the pulsed ICR measurements.

### 3.2.4 Electronic Structure

The commercial significance of simple silicon-hydrides has not escaped the notice of the computational chemistry community. Although early *ab initio* calculations of silanes focused on general descriptions of bonding [24] with emphasis on formation of multiple silicon-carbon bonds [25], more recent investigations have elucidated the thermochemistry [26] and reaction mechanisms [27] of silicon-hydride radicals. The first detailed *ab initio* investigation of the  $SiH_n^+$  ions was performed by Gordon in 1978 [6]. His unrestricted Hartree Fock (UHF) calculations found the  $^2T_2$  molecular ion to be Jahn-Teller unstable [16] to distortions away from  $T_d$  symmetry, as one would expect from the triply-degenerate, highest occupied molecular orbital (HOMO) of neutral silane. Gordon found three potential energy minima, the most stable having  $C_{3v}$  symmetry with one bond stretched by 50% of its original length. The remaining  $C_{2v}$  and  $D_{2d}$  configurations were found to be 0.47 and 1.03 eV less stable than the  $C_{3v}$  geometry.

As part of the present investigation *ab initio* electronic calculations for all of

the silicon-hydride cations, anions, and neutral radicals have been extended by the use of larger basis sets and electron correlation estimates using Möller Plesset (MP) perturbation theory. The calculations have been performed using the Gaussian-82 self-consistent field programs of Pople *et al.*[28]. Unless otherwise specified all results are obtained using the standard 6-31g\*\* basis set, which for silane employs 39 basis functions formed from 80 primitive gaussians. Geometry optimizations and frequency calculations have been performed using analytic MP2 gradients <sup>2</sup>. Potential energies at the optimized geometries are corrected by single-point calculations of electron correlation at the MP4 level. Enthalpies presented are obtained using the zero-point energies associated with the MP2 frequency calculations. Although these calculations ignore the anharmonicity of the potential and are often corrected by a 10% fudge factor, no such correction is applied in the present work, in the spirit of the phrase *ab initio*.

During the preparation of this thesis two articles by Pople and Curtiss [31] appeared with the more ambitious objective of calculating thermochemical properties for all of the  $AH_n^+$  species using large bases and Möller Plesset correlation estimates. The level and detail of the present calculations is slightly higher, for example MP2 gradients are used for the geometry optimizations and frequency calculations and pertinent reaction coordinates have been examined. However the scope of Pople's published results provides a more detailed check on the validity of the *ab initio* methods since his results are comparable to a broader range of experimental data.

The geometry of silane was optimized using analytic gradients at the MP2/6-31g\*\* level. As expected,  $SiH_4$  is in the  $T_d$  point group with a Si-H bond length of 1.474 Å. The calculated unrestricted Hartree-Fock (UHF) orbital eigenvalues are displayed in table 3.3. The Koopman's theorem ionization potential <sup>3</sup> from this calculated wavefunction is 13.1 eV. However removal of an electron from the system frozen into this geometry has a radically different self-consistent field solution. Figure 3.3 shows the change in the eigenvalue spectrum for the tetrahedral ion. The mean drop in the one electron eigenvalues is over 7 eV, which is logical since the effective nuclear charge felt by each electron is increased after ionization. It is remarkable that this energy drop of 127 eV is compensated by the increased coulomb and exchange interactions of the electrons to yield a potential energy difference which is within an eV of the Koopman's ionization potential. Using

<sup>2</sup>The number following MP refers to the order of perturbation theory used for estimation of electron correlation.

<sup>3</sup>Defined as the binding energy of the highest occupied molecular orbital (HOMO).

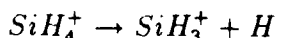
Orbital	Binding Energy (eV)
1a <sub>1</sub>	1864.8
2a <sub>1</sub>	166.0
1t <sub>2</sub>	114.7
3a <sub>1</sub>	19.8
2t <sub>2</sub>	13.1

Table 3.3: UHF binding energies for silane electrons at the MP2/6-31g\*\* optimized geometry.

fourth-order correlation energies and zero-point energy corrections the calculated vertical ionization potential of silane's ground vibrational state is 12.45 eV.

$SiH_4^+$  is non-linear and orbitally degenerate, so it distorts from  $T_d$  symmetry as predicted by the Jahn-Teller theorems [16]. The steepest gradient in the total potential energy changes the geometry smoothly over into a  $C_{3v}$  structure with one bond stretched to 1.95 Å and the other three slightly contracted to 1.46 Å. The silicon-hydrogen distances found were less than those originally reported in Gordon's 1978 paper, 1.63 and 1.47 Å, and the total energies are about half a hartree (13.6eV) lower than his results, a natural consequence of the improved basis sets and correlation estimates available for the present work. The enthalpy change associated with the distortion from the  $T_d$  geometry to the  $C_{3v}$  potential energy minimum is 1.16 eV. The  $C_{3v}$  ion is 0.12 eV lower in enthalpy than the optimized, dissociated fragments  $SiH_3^+$  and  $H$ . Three quarters of this calculated change, .08 eV, is due to the change in zero-point energy on moving from the  $T_d$  ion to  $SiH_3^+$ . For comparison, the potential energy associated with the polarization of the atom alone,  $-\alpha(H)e^2/(2r^4)$ , is 0.26 eV.

Two sets of calculations which gradually increase the longest Si-H bond distance while optimizing the geometry with respect to the remaining variables yield the potentials shown in figure 3.4. In one case the bond-length along the  $C_3$  axis was fixed and the geometry was optimized at the MP2/6-31g\*\* level. In the second case the optimized  $SiH_3^+$  geometry was utilized and the remaining silicon-hydrogen bond was incrementally stretched while maintaining  $C_{3v}$  symmetry. Permitting geometric displacement of hydrogens in the  $SiH_3$  moiety lowers the total energy by  $\approx 0.3$  eV at distances of less than 5 Å. The dissociation process:



is therefore viewed as involving more than a simple  $\sigma$ -bond interaction between

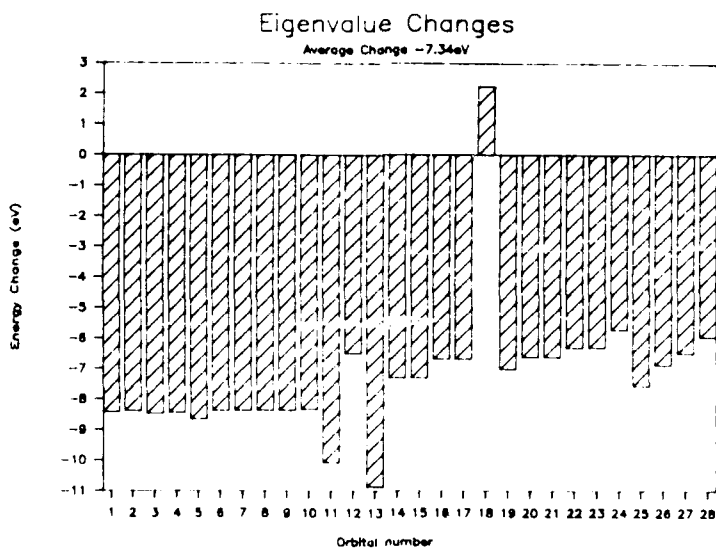


Figure 3.3: UHF eigenvalue spectrum changes on ionization of  $SiH_4$ .

the charged silicon center and the departing hydrogen; the remaining hydrogens participate in lowering the total energy along this dissociation coordinate.

Based on these calculations one expects the  $T_d$  molecular ion formed by vertical excitation of the molecule to adiabatically dissociate to  $SiH_3^+$  and  $H$  in the absence of a stabilizing collision or emission of infrared radiation. The vibrational frequency associated with this dissociation is calculated to be  $370\text{ cm}^{-1}$ , so that stabilization of the molecular ion on a  $10^{-13}$  second timescale is required for occupation of the  $C_{3v}$  potential energy minimum. A summary of the calculated enthalpies for silicon hydride cations relative to that for the tetrahedral molecular cation is provided in figure 3.5.

Additional insight from the calculations arises from a comparison of the eigenvectors for the unrestricted wavefunctions of the tetrahedral and distorted  $C_{3v}$  geometries. The one-electron eigenvalues and eigenvectors are nearly identical for the optimized  $C_{3v}$  and  $T_d$  structures—the average change in corresponding eigenvalues is less than 10 millihartrees (0.27 eV). The energy lowering on distortion is due primarily to changes in the nuclear-nuclear repulsion and the two-electron coulomb and exchange integral contributions. (Table 3.4).

While the above describes how the  $SiH_3^+$  ion is formed near threshold,  $SiH_2^+$  is the first and predominant ion observed in the electron-impact and photoionization

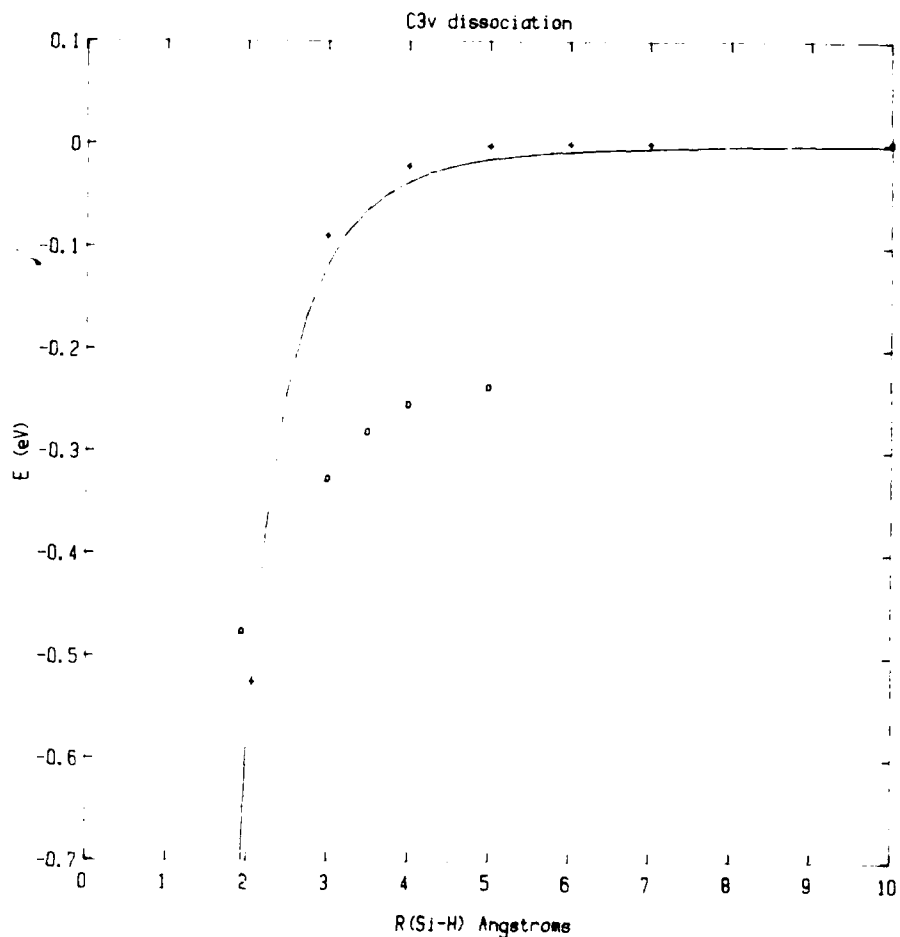


Figure 3.4: Potential energy for dissociation along a  $C_{3v}$  reaction coordinate.  $\circ$ 's represent fixing one Si-H bond distance and optimizing all remaining degrees of freedom at the MP2/6-31g\*\* level.  $+$ 's show the results using the fixed  $SiH_3^+$  optimized geometry while varying the last Si-H bond distance. The solid line is the calculated polarization potential for the ion-hydrogen atom interaction.

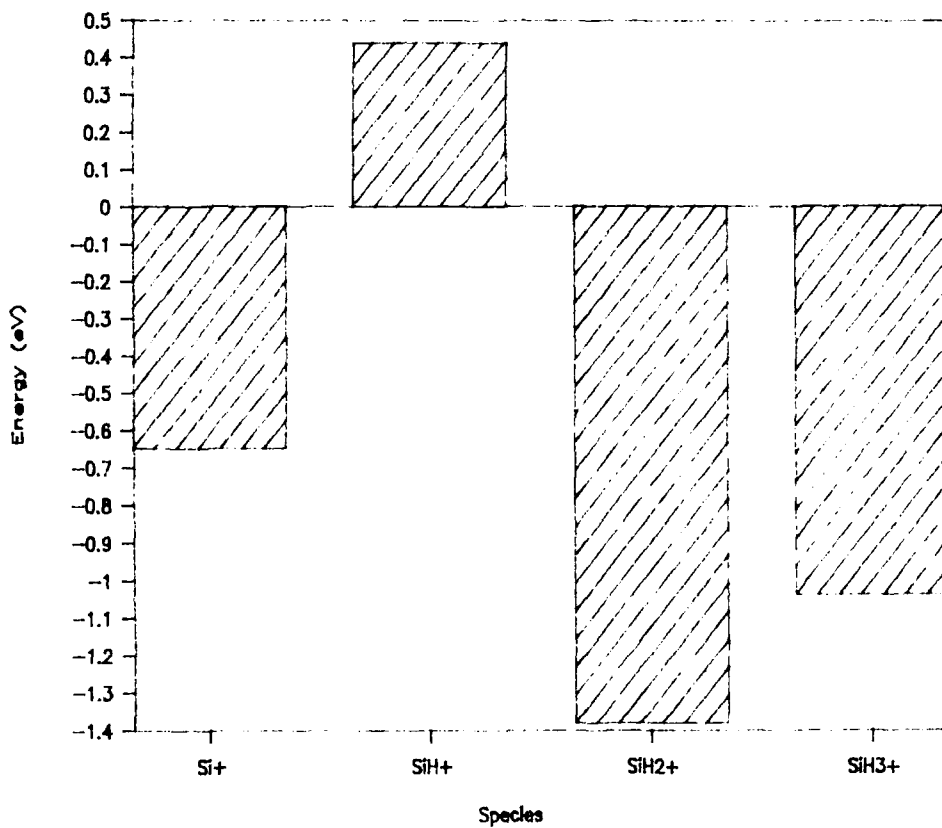
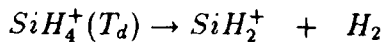


Figure 3.5: MP4/6-31g\*\* enthalpies for the silicon hydride cations at their MP2/6-31g\*\* geometries compared to those of the  $T_d$  cation whose geometry is identical to that of neutral silane. Zero-point energy corrections for the ions and hydrogen molecules are from MP2 frequency calculations for the silicon hydride species and exact values for  $H_2$ .

Energy	$T_d$	$C_{3v}$ opt	$\Delta_1$	$SiH_3^+, H$	$\Delta_2$
Electronic (HF)	-312.2119	-311.1652	+1.0467	-306.7092	+5.5027
Nuclear-Nuclear	+21.4235	+20.3276	-1.0959	+15.8752	-5.5483
Correllation (MP4)	-.1105	-.1039	+.0066	-.0999	+.0106
Zero-Point	.0267	.0267	.0000	.0234	+.0033
Total	-290.8722	-290.9148	-.0426	-290.9105	-.0383

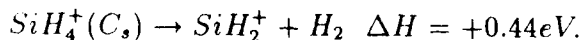
Table 3.4: Partitioning of the total energy (Hartrees) from *ab initio* calculations of  $SiH_4^+$  in  $T_d$  and the optimized  $C_{3v}$  geometries, as well as fully dissociated to  $SiH_3^+$  and  $H$ .  $\Delta_1$  and  $\Delta_2$  refer to energy changes from the  $T_d$  ion to the  $C_{3v}$  and dissociated structures, respectively.

mass spectral experiments. Formation of the dihydride cation and two hydrogen atoms is clearly endoergic near threshold, so the channel which produces  $SiH_2^+$  must have molecular hydrogen as the companion product. The enthalpy change calculated for the transformation:



is -1.39 eV. Pinching two of the hydrogen atoms from the  $T_d$  to a  $C_{2v}$  structure with an H-H distance of .7 Å, which is close to the distance in a hydrogen molecule, yields a potential energy which is .65 eV less than the  $T_d$  ion at the MP2/6-31g\*\* level. Although an adiabatic path between these two configurations was not identified, the latter geometry is unstable and, when optimized, converges to a  $C_{2v}$  structure with distances of 1.45 and 1.63 Å and angles of 142 and 33 degrees. This structure, sketched in figure 3.6, is marginally unbound ( $\Delta H \approx .01$  eV) with respect to  $SiH_2^+$  and molecular hydrogen, and is 1.40 eV lower in enthalpy than the  $T_d$  ion. Again for comparison, the classical polarization potential of molecular hydrogen at a distance of 1.6 Å is -0.74 eV.

Pople and Curtiss[31] reported a  $C_s$  structure of the molecular cation which they describe as a 'loose donor-acceptor complex' of  $SiH_2^+$  and  $H_2$  (figure 3.6) which is bound:



The energy difference between their  $T_d$  and  $C_s$  geometries is 1.93 eV at the HF/6-31g\* level. Using their  $C_s$  structure as a starting point, geometry optimization and frequency calculations were performed at the MP2/6-31g\*\* level. The MP4

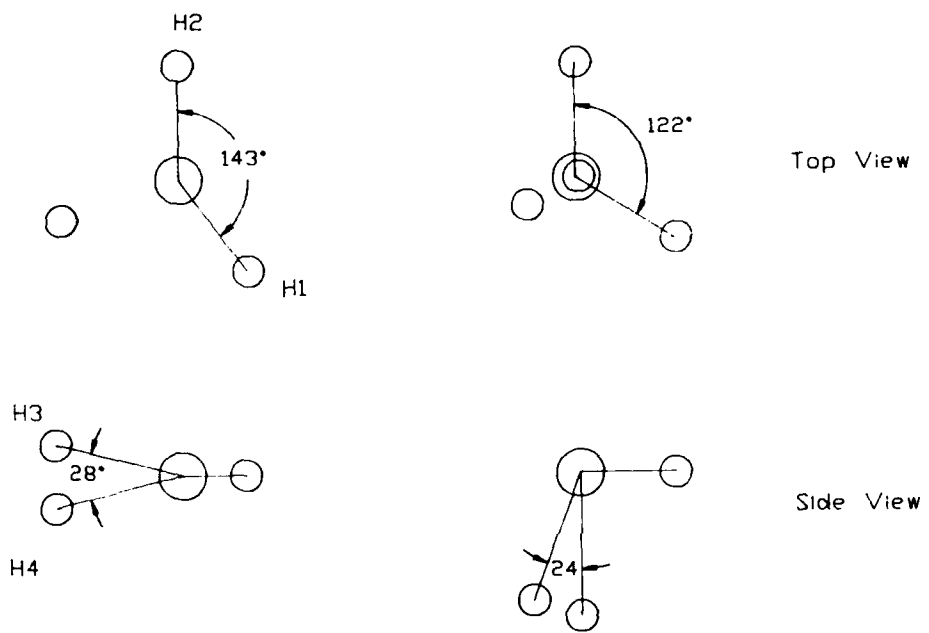
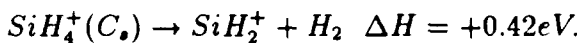


Figure 3.6: Two geometries of the molecular silane cation (see text). Both were obtained from MP2/6-31g\*\* geometry optimizations, the first by pinching the H-H distance on one side, and the second using the  $C_s$  structure of Pople and Curtiss [31] as a starting point.

energy difference between the  $T_d$  and  $C_s$  structures was reduced to 1.80 eV. The improved treatment of  $SiH_2^+$  at this level changes the calculated dissociation enthalpy by only 0.02 eV:



Although the  $C_{2v}$  structure described earlier and shown in figure 3.6 satisfied the force constant and displacement criteria for a potential energy minimum, the MP2 frequency calculations revealed a negative eigenvalue whose eigenvector characterized motion in the direction of Curtiss' "donor-acceptor complex." While the steepest gradient at the  $T_d$  geometry correlates with  $SiH_3^+$  and H, analysis of the analytic MP2 gradients at the  $T_d$  ion geometry revealed two, negative, orthogonal components with negative curvature. In other words, the nuclear rearrangement induced by changes in silane's electronic structure on ionization have access to channels which yield either  $SiH_3^+$  or  $SiH_2^+$ . Using the Born-Oppenheimer approximation, the partitioning between these two channels is constrained by the product of appropriate Franck-Condon factors and the distribution of nuclear configurations which characterize the silane molecule. The very modest rearrangement of light hydrogen nuclei required for access through the  $C_{2v}$  and  $C_s$  configurations on the way to  $SiH_2^+$  suggests an important role for tunneling in the dissociative ionization process. As first observed by Zener in the early 1930's [9]:

... even a very small transition probability, per oscillation, may give a high probability that the molecule will dissociate before returning, by radiation, to the normal state.

As the electron or photon energy is raised above 10.65 eV (the energy difference calculated for  $SiH_4^+(C_s) - SiH_4$ ) the production of Rydberg or virtual states with lifetimes long enough to permit tunneling to the  $C_s$  potential energy surfaces outlined in figure 3.7 becomes possible. Between 10.65 and 11.07 eV, nuclear rearrangement yields a bound molecular ion with the  $C_s$  geometry. By contrast a bound  $C_{3v}$  ion is theoretically possible only for excitations in the narrow range from 11.29 to 11.41 eV. With further increases in the electron or photon energy these states are permitted progressively greater amounts of internal energy. Therefore hydrogen tunneling is expected to permit observation of the dissociative ionization products in the order of their thermodynamic stability as the excitation energy increases. From figure 3.5 the calculations predict that the ions should

Source	$SiH_4^+$	$SiH_3^+$	$SiH_2^+$	$SiH^+$	$^2Si^+$	Reference
Electron	...	12.2	11.8	14.7	13.3	Morrison [4]
Electron	...	12.2	11.6	15	13.5	Chatham [12]
Electron	...	12.3	11.9	15.3	13.56	Potzinger [3]
Photon	...	12.10	11.05	13.8	12.65	Borlin [17]
Photon	11.00	12.09	11.54	...	...	Berkowitz [11]
Photon	...	12.23	11.67	...	...	Ding [14]
Average	11.00	12.18 $\pm$ .08	11.59 $\pm$ .27	14.7 $\pm$ .6	13.3 $\pm$ .4	...

Table 3.5: Appearance potentials (eV) for the silicon hydride cations. The general trend is clearly  $SiH_2^+ < SiH_3^+ < Si^+ < SiH^+$ . Errors on the averages are simply one standard deviation; no explicit inclusion of the experimental uncertainties is implied.

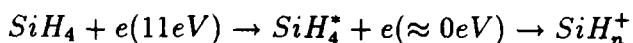
be observed in order of increasing threshold:  $SiH_2^+ < ^2Si^+ < SiH_3^+ < SiH^+$ , as found experimentally. Table 3.5 summarizes experimental values for the appearance potentials of the various silicon hydride cations from silane.

*Ab initio* calculations predict formation of  $SiH_3^+$  by adiabatic dissociation of the molecular ion at a potential of 12.45 eV, in reasonable agreement with the average experimental value of 12.18 eV. While  $SiH_2^+$  formation is also predicted at this energy, non-classical barrier penetration of an electron or hydrogen molecule from a Rydberg state of silane above 11.07 eV should also dissociate to  $SiH_2^+$  and  $H_2$  according to the calculations, a value close to the experimental average appearance potential of  $11.59 \pm .27(1\sigma)$  and in perfect agreement with the most recent value of 11.05 eV for the dihydride cation. Observation of  $Si^+$  in its electronic ground state is thermodynamically allowed for tunnelling from states above 13.10 eV, in excellent agreement with its observed appearance potential of  $13.25 \pm .36$  eV. Finally, the *ab initio* calculations suggest that  $SiH^+$  can be accessed by tunneling only from states above 12.89 eV, which is significantly below the experimental average of  $14.7 \pm .56$  eV. The first triplet state of  $SiH^+$  occurs at a calculated energy of 15.08 eV, suggesting its formation as the likely channel in electron-impact measurements near threshold.

What do the *ab initio* calculations say about the observations of the molecular silane ion? Consider the times required for the electron and photon excitation processes. For a 3 Å electron-silane interaction length an 11 eV electron passes by in about  $10^{-16}$  seconds. Photons travel much faster, so that the interaction time for photoion formation, assuming the same interaction length, is in the  $10^{-18}$

second range. While both of these times are small compared to silane's longest vibrational period,  $\approx 10^{-14}$  seconds, the electron impact process may actually take longer for two reasons. First, the momentum, i.e. velocity, of the electron wave-packet is decreased as the interaction occurs. Second, silane's other electrons have a chance to respond to the electric field induced by the incoming electron, an opportunity which is more severely constrained by time in photoionization.

The classical slowing of the incoming electron finds a more precise mathematical and experimental description in the literature on electron-impact resonances [23]. Specifically, one may formulate a compound state composed of the slowed, incoming electron and a Rydberg state of the target molecule.



Electron-energy loss experiments on silane argue for the importance of Rydberg states formed at energies above 7.8 eV [5]. The observation of vibrational structure in the electron-energy loss experiments from threshold to twenty volts argues for the existence of excited states with lifetimes that are longer than a vibrational period. The participation of these relatively long-lived states permits more extensive nuclear rearrangement in the electron-impact ionization process than is possible in photoionization, where the invariance of photon velocity and the inflexibility of Franck-Condon factors pose more exacting boundary conditions.

Finally, the calculations suggest that a molecular ion remains bound in the  $C_s$  geometry only if formed from a state whose energy is in a narrow range between 10.65 and 11.07 eV above neutral silane. A stable form of  $SiH_4^+$  with the  $C_3$  geometry is accessible only over a twelve millivolt energy range above 11.29 eV. The possibility of the  $C_3$  isomer rearranging to a conformation which correlates with  $SiH_2^+$  is not precluded by the present results. If this occurs, no stable  $C_3$  form would be possible, since its total energy is above that required for adiabatic dissociation to  $SiH_2^+$  and  $H_2$ .

Summarizing, the *ab initio* calculations provide important insight into quantum mechanical and energetic constraints on dissociative ionization. A summary of inferences concerning the potential energy surface of silane near its ionization threshold is sketched in figure 3.7. Careful measurements of thresholds and relative cross-sections for silane and deuteriosilane may provide quantitative insight into the role of tunneling in dissociative ionization, and are planned as part of a future series of experiments.

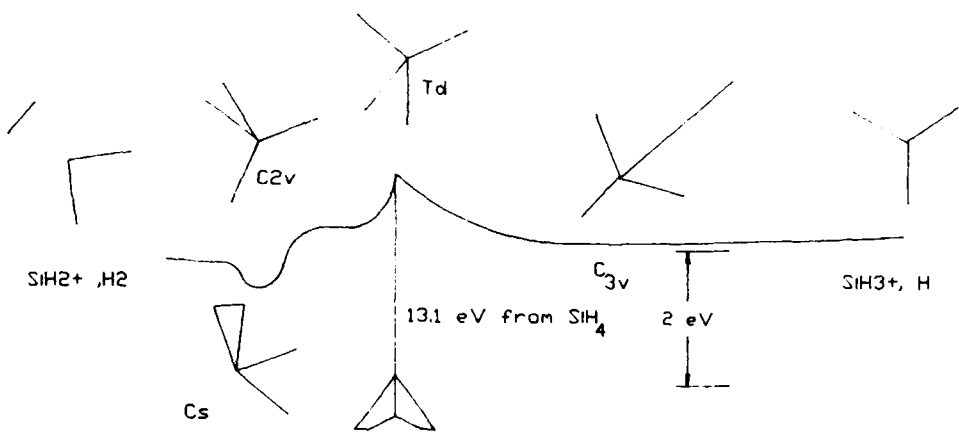


Figure 3.7: Schematic view of electronic states associated with ionization of silane inferred from *ab initio* electronic structure calculations. The reaction coordinate correlating H and  $\text{SiH}_3^+$  with the  $T_d$  molecular ion has been clearly identified.

### 3.3 Ionization Cross Sections

The total and partial ionization cross-sections of silane are pivotal elements in any quantitative description of silicon deposition discharges. The early work of Saalfeld and Svec [2] reported an integrated cross-section for  $SiH_n^+$  which was .459 times that for methane at sixty electron volts. While several publications concerning the appearance potentials of the silicon hydride ions appeared in the interim, it was not until 1980 and the thesis of Turban [12] that another quantitative measure of the silane ionization cross-section was reported. Turban's data were normalized to the total ionization cross-section of ethylene, for which the calibration derived from the work of Rapp and Englander-Golden [33]. At 50 eV the integrated silane cross-section was found to be .717 times that of ethylene. Using Rapp's measurement's for methane and ethylene <sup>4</sup> the total ionization cross-section is  $1.63\text{\AA}^2$  (60eV) according to Saalfeld but over twice this value,  $3.70\text{\AA}^2$  (50eV) according to Turban.

In 1984 Chatham *et al.*[12] reported on the ionization of silane by electron impact using both ionization tube and quadrupole mass spectrometric techniques. Their reported total ionization cross-section for silane is  $5.7\text{\AA}^2$  at fifty volts, half again as large as that reported by Turban. In addition, over five percent of their total cross-section is ascribed to  $H^+$  and  $H_2^+$ , an observation which is qualitatively different than the earlier measurements. The extent to which these light species influenced earlier measurements is ambiguous, perhaps reflecting limitations in the dynamic mass range of the quadrupole and magnetic sector spectrometers employed. From the Born-Oppenheimer approximation it is rather surprising that charge would reside on hydrogen rather than silicon since the ionization potentials of the radicals are all substantially lower than those of either atomic or molecular hydrogen (Table 3.6).

#### 3.3.1 FTMS Measurements

In order to resolve dissonance among reported values for the silane ionization cross-sections a series of pulsed ICR measurements were performed under well-defined collision conditions. As techniques with energy resolution better suited to threshold determination had achieved reasonable agreement on the electron-impact and photoionization thresholds and rough energy dependence of the cross-

---

<sup>4</sup>4.05 and  $5.46 \pi a_0^2$

Species	MP4	Isogyric [31]	Experiment [11]
$SiH_3$	7.78	7.80	8.01
$^1SiH_2$	8.63	9.16	9.15
$SiH$	7.49	7.80	7.91
$Si$	7.76	8.08	8.15
$H_2$	**	**	15.4
$H$	13.56	13.56	13.56

Table 3.6: Radical ionization potentials calculated from MP4 energies using MP2/6-31g\*\* optimized geometries and frequencies, using the isogyric artifice of Pople *et al.* [31], and photoionization mass spectrometry measurements by Berkowitz [11].

sections, the present work was confined to an accurate, quantitative measurement of the total and partial ionization cross-sections at fifty volts.

Reagents were injected using both pulsed supersonic beam valves, one backed by 2 torr of silane and the other research grade neon. The pressure of gas *in situ* was determined separately for each gas using the spinning rotor gauge artifice described earlier in chapter 2. A plot of the silane and neon pressures as a function of the delay between valve opening and spectrum acquisition is displayed in figure 3.8.

Figure 3.9 provides confirmation that silane chemistry was not occurring on the time scale of the experiment by illustrating the independence of the mass-spectral relative intensities over the pressure range of the silane pulses. Analogous spectra were acquired with neon as the reagent gas, permitting an absolute calibration of the abscissa with the carefully measured noble gas ionization cross-sections of Wetzel [35]. The resulting absolute silane ionization cross-sections at  $50 \pm 1$  eV are summarized in table 3.7.

Mass spectra were recorded over a wide range of electron energies from threshold to 1 kilovolt at low enough magnetic field to observe protons and the hydrogen molecular ion. Neither  $H^+$  nor  $H_2^+$  was observed. Although it is conceivable that these fragments are formed with substantial kinetic energy in the dissociative ionization process, no evidence for their generation using axial trapping potentials as high as ten volts was obtained. The observation of these ions by Chatham may be an artifact of quadrupole mass analysis. Measurements of silane pyrolysis using an Extranuclear Laboratories, modulated-beam quadrupole spectrometer had a *calibrated* sensitivity for  $H_2^+$  which was 2500 times that for the ethylene

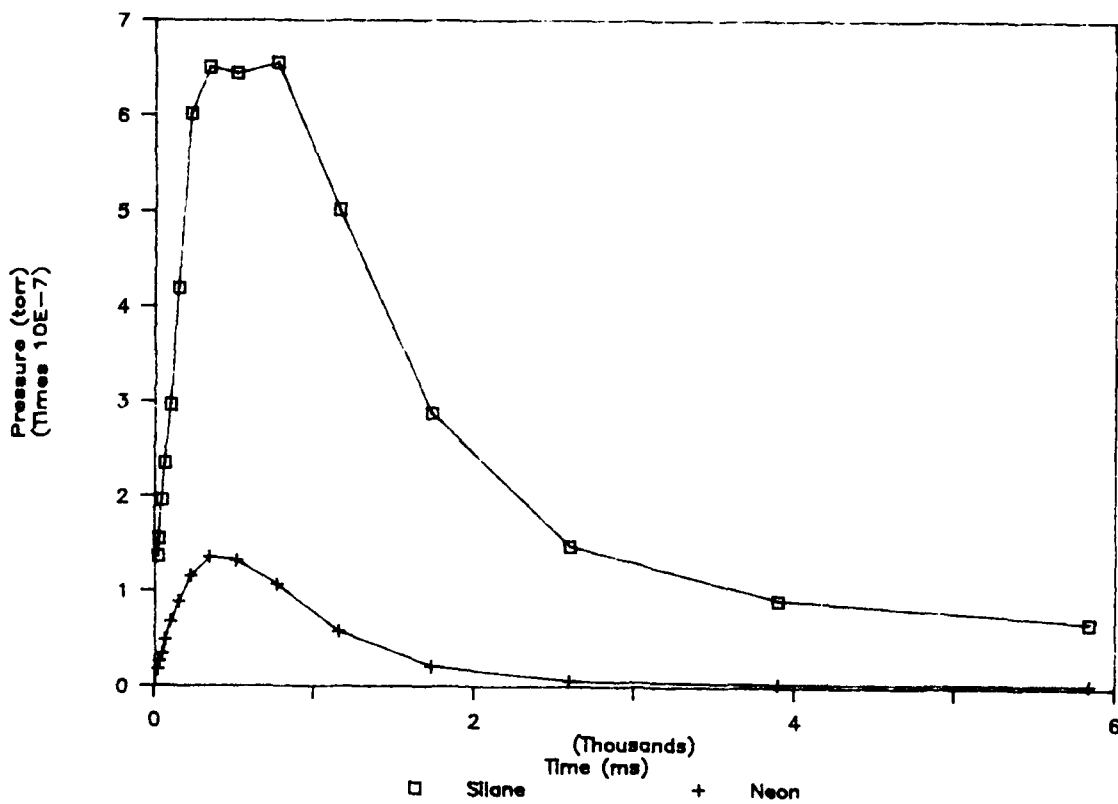


Figure 3.8: Transient silane and neon pressures measured by FTMS and calibrated using the spinning-rotor gauge, pulsed valve technique described in chapter 2.

Species	$\sigma_m \text{ \AA}^2(50\text{eV})$
$SiH_3^+$	0.50
$SiH_2^+$	0.74
$SiH^+$	0.21
$Si^+$	0.19
Total	1.62

Table 3.7: FTMS dissociative ionization cross-sections of silane at 50 eV. Confidence limits are  $\pm 15\%$ , principally from the uncertainty of  $\sigma_i(Ne)$ .

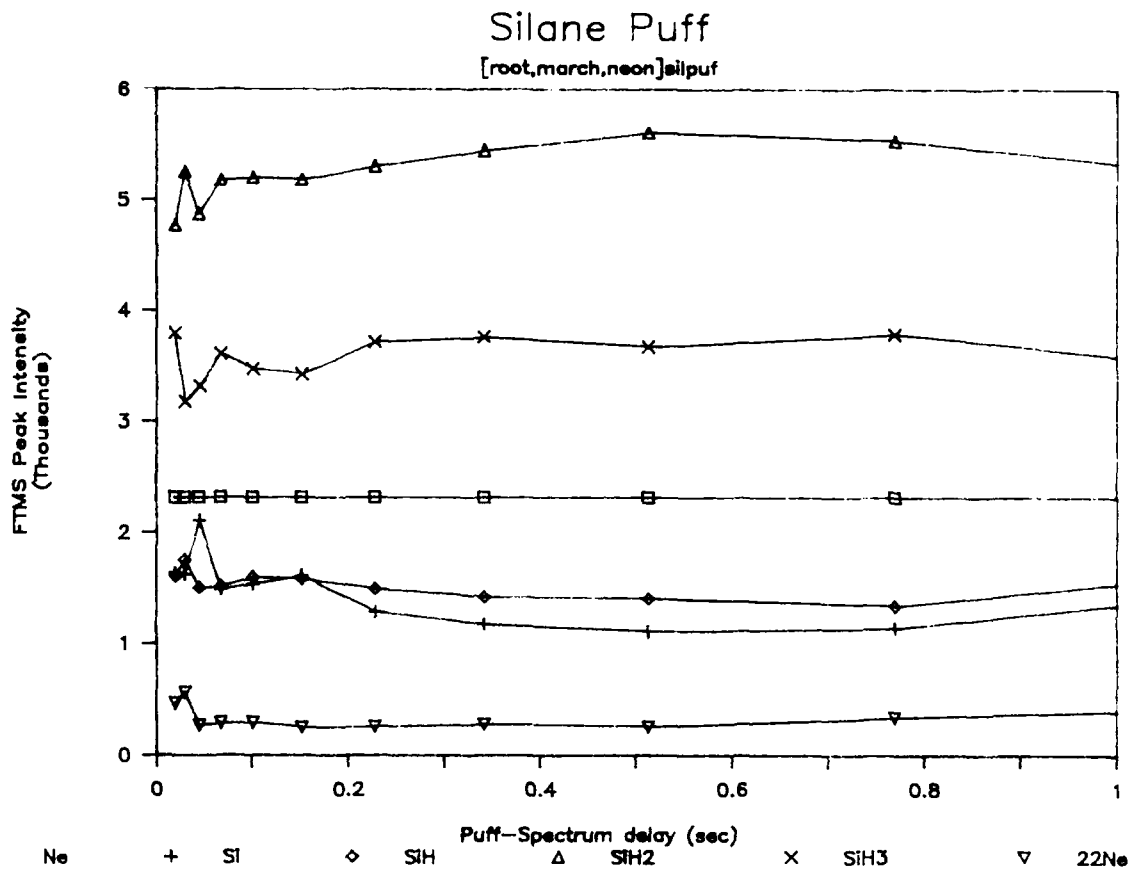


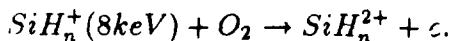
Figure 3.9: Silane cracking pattern as a function of the delay between pulsed gas injection and spectrum acquisition. The invariance of the relative amplitudes verifies that no charge transfer chemistry is occurring on the timescale of the measurements over the range of pressures at as read from figure 3.8.

cation [34]. It is therefore quite possible that the signals attributed to hydrogen cation formation from silane in reference [12] are in fact a consequence of impurity ionization.<sup>5</sup>

Although there are many plausible reasons for error in the total ionization cross-section of silane measured by techniques involving conventional mass spectrometers and ionization tubes, these errors are largely irrelevant for threshold information and the qualitative energy dependence of the cross-sections. Figure 3.10 illustrates selected literature values for partial ionization of silane scaled to the absolute total cross-section obtained above at 50 volts. The agreement among published values is seen to be much improved from the *status quo* illustrated in figure 3.1. The recommended ionization cross-sections have been synthesized from the careful differential measurements of Morrison [4] and the present absolute cross-sections at 50 eV. Figures 3.11 and 3.10 are plots of these partial ionization cross-sections.

### 3.3.2 $SiH_m^{n+}$ for $n > 1$

Recently there has been an experimental report of multiply charged silicon hydride ions formed by high-energy, charge-stripping collisions [36]:



As suggested from the observation of multiply charged rare-gas ions in the last chapter, evidence for production of  $SiH_n^{2+}$  by electron-impact ionization of the monocation has been observed in the pulsed ICR spectra at large products of beam current and irradiation time. While these species are of fundamental interest in their own right, they will not play a role in PECVD for the same reasons indicated in the last chapter concerning  $Rg^{2+}$ . The product of current, interaction time, and the electron energy distribution function integrated over a range where multiple ion formation is thermodynamically accessible is over four orders of magnitude smaller than monocation formation rates under PECVD reactor conditions. As was suggested for the rare-gas dications, the detailed sources of such species as  $SiH_3^{2+}$  merit investigation which is outside the scope of the present discussion.

---

<sup>5</sup>The use of a turbomolecular pump and a pyrolytic foreline trap as described by the authors would be expected to produce significant quantities of molecular hydrogen in the mass spectrometer.

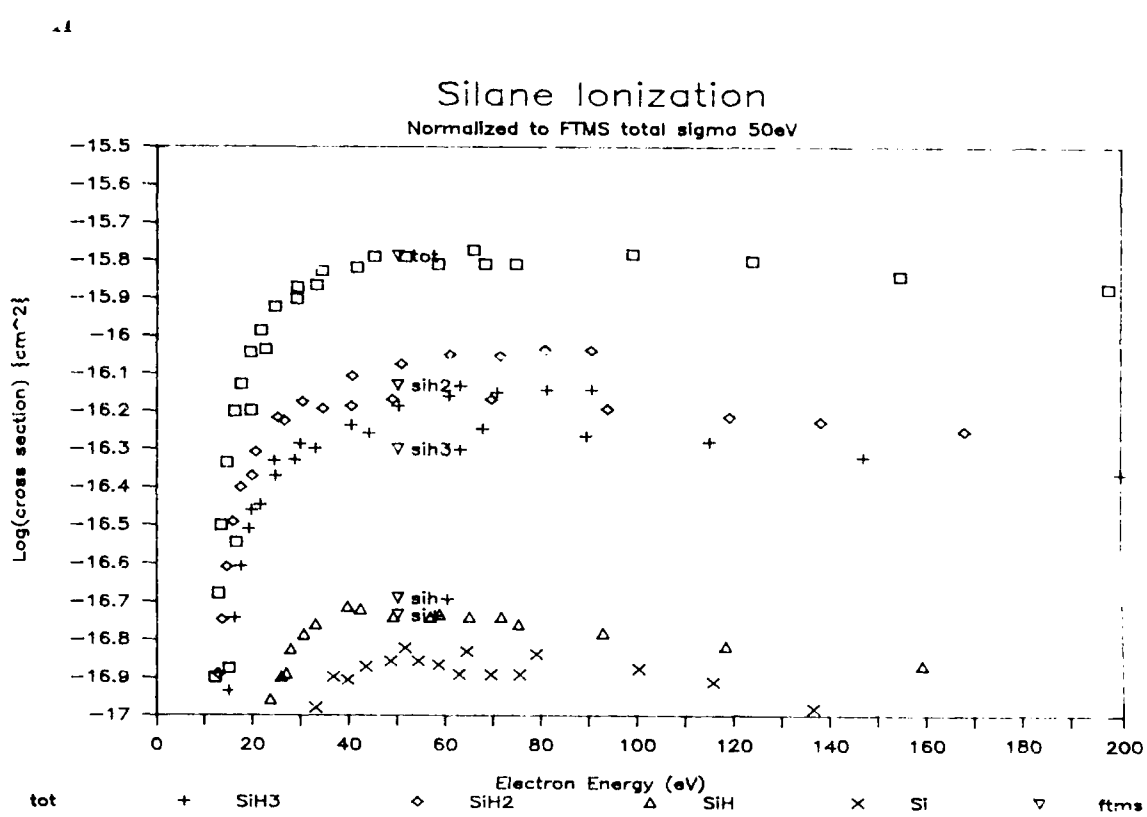


Figure 3.10: Partial ionization cross-sections of Chatham and Turban scaled by the present total cross-section observed at 50 eV.

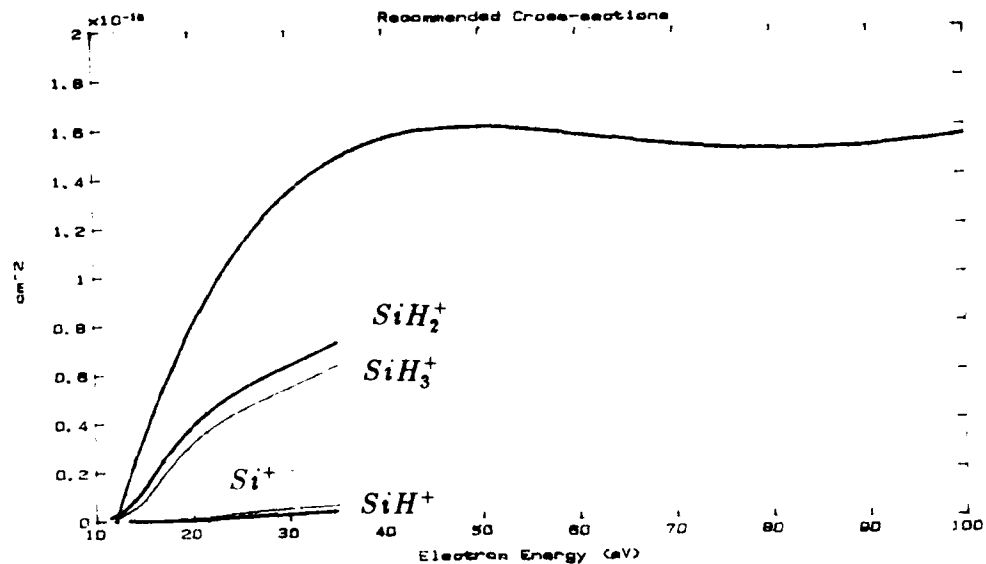


Figure 3.11: Recommended partial ionization cross-sections for electron impact dissociative ionization of silane synthesized from the present results at 50 eV and the differential measurements of Morrison (see text).

### 3.4 Conclusions

Resolution of disparate experimental and theoretical conclusions concerning silane ionization by electrons and photons has been addressed with a view to providing a consistent set of cross-section data from which the scaling of ion generation rates in realistic plasma situations may be calculated. The following conclusions are drawn:

1. Ionization of silane by electron impact is exclusively dissociative.
2. Photoionization of silane can generate small yields of a molecular silane cation. The absence of this species in the electron impact mass spectrum provides a challenge to conventional notions of the correlation between the two ionization processes. Although photons in the 11.2 - 12.4 eV energy range may be present under plasma conditions, their contribution to the total ionization rate will be orders of magnitude smaller than the electron impact effects. The molecular ion is therefore unimportant in silane plasma chemistry.

3. *Ab initio* electronic structure calculations provide useful guidance for the thermochemistry and quantum physics of dissociative ionization. Appearance potentials inferred for the silicon hydride cations are in excellent agreement with experimental values. Formation of  $SiH^+$  observed experimentally is predicted to be in the first excited triplet electronic state, which is 2.2 eV above the singlet ground-state.
4. The difference between electron-impact and photoionization in production of a molecular cation is ascribed to the different time-scales which characterize the ionizing collisions. The participation of Rydberg states of silane in the electron impact case suggests ample time for nuclear reorganization, including dissociation of  $SiH_4^+$ .
5. Pulsed ion cyclotron resonance mass spectra of silane reveal no channels for production of  $H^+$  or  $H_2^+$ , as one expects from the ionization potentials calculated (and recently measured) for the silicon hydride radicals and the Born-Oppenheimer approximation.
6. Absolute partial ionization cross-sections for the silicon hydride cations have been established at an energy of 50 electron volts, permitting renormalization of the historically disparate reported values for silane ionization.

## Bibliography

- [1] H. Neuert and H. Clasen, *Z. Naturforsch.*, **7A** 410 [1952].
- [2] F. Saalfeld and H. Svec, *Inorganic Chemistry*, **2** 46 [1963].
- [3] P. Potzinger and F. Lampe, *Journal of Physical Chemistry*, **73** 3912 [1969].
- [4] J. Morrison and J. Traeger, *International Journal of Mass Spectrometry and Ion Physics*, **11** 289 [1973].
- [5] H. Bock *et al.*, *Journal of the American Chemical Society*, **98** 668 [1976].
- [6] M. Gordon, *Chemical Physics Letters*, **3** 410 [1978].
- [7] G. Turban, PhD thesis, University of Nantes [1980].
- [8] G. Turban, Y. Catherine and B. Grolleau, *Plasma Chemistry and Plasma Processing*, **2** 61 [1982].
- [9] Chemical Rubber Company Handbook of Chemistry and Physics, **65** [1985].
- [10] T.M. Chen and F.W. Lampe, *Chemical Physics Letters*, **19** 532 [1973].
- [11] W. Genuit, A. Boerboom and T. Govers, *International Journal of Mass Spectrometry and Ion Processes*, **62** 341 [1984].
- [12] H. Chatham *et al.*, *Journal of Chemical Physics*, **81** 1770 [1984].
- [13] M. Hayashi, 'Electron collision cross-sections for molecules determined from beam and swarm data,' *Proceedings of the Joint Symposium on Swarm Studies and Inelastic Electron-Molecule Collisions*, Granlibakken [1986].

- [14] A. Ding *et al.*, *Journal of Chemical Physics*, **83** 3426 [1985].
- [15] A. Potts and W. Price, *Proceedings of the Royal Society, London*, **A 326** 165 [1972].
- [16] H. Jahn and E. Teller, *Physical Review*, **49** 874 [1936] and *Proceedings of the Royal Society*, **161a**, 220 [1937].
- [17] K. Borlin, T. Heinis and M. Jungen, *Chemical Physics*, **103** 93 [1986].
- [18] W. Koch *et al.*, *Journal of the Chemical Society Perkins Transactions*, **II** 757 [1089].
- [19] P. Longeway, R. Estes and H. Weakliem, *Journal of Physical Chemistry*, **88** 73 [1984].
- [20] P. Haaland and A. Rahbee, *Chemical Physics Letters*, **114** 571 [1985].
- [21] J. Perrin and J. Schmitt, *Chemical Physics*, **67** 167 [1982].
- [22] M. Dillon *et al.*, *Journal of Chemical Physics*, **82** 2909 [1985].
- [23] G. Shulz, *Reviews of Modern Physics*, **45** 279 and 423 [1973].
- [24] W. Goddard and L. Harding, *Annual Reviews in Physical Chemistry*, **29**, 363 [1978].
- [25] H. Schaeffer, *Accounts of Chemical Research*, **15**, 283 [1982].
- [26] P. Ho *et al.*, *Journal of Physical Chemistry*, **89**, 4647 [1985].
- [27] K. Baldridge, *et al.*, *Annual Reviews in Physical Chemistry*, **38** 211 [1987].
- [28] J. Pople *et al.*, **Gaussian 82**. Carnegie-Mellon University, Pittsburgh, PA. [1982].
- [29] J. Pople *et al.*, **Gaussian 86**, Carnegie-Mellon University, Pittsburgh, PA. [1986].
- [30] J. Berkowitz *et al.*, *Journal of Chemical Physics*, **86** 1235 [1987].

- [31] J. Pople and L. Curtiss, *Journal of Physical Chemistry* **91** 155 and 3637 [1987].
- [32] C. Zener, *Proceedings of the Royal Society, London*, **138**, 661 [1932].
- [33] D. Rapp and P. Englander Golden, *Journal of Chemical Physics*, **43** 1464 [1965].
- [34] C. DeJoseph, P. Haaland and A. Garscadden, *IEEE Transactions on Plasma Science*, **ps-14**, 165 [1986].
- [35] R.C. Wetzel *et al.*, *Physical Review*, **A35** 559 [1987].
- [36] W. Koch *et al.*, *Journal of the Chemical Society Perkin Transactions II*, 757 [1986].

æ

# Chapter 4

## Negative Ion Formation

### 4.1 Background

While it is ordinarily presumed that literature whose title includes the phrase *ion chemistry* will be concerned with positively charged species, the formation and reaction of negative ions play important roles in silane containing plasmas. Anion formation modifies the electron transport characteristics by providing a homogeneous loss process that scales differently with gas composition, pressure, and excitation than does electron-cation recombination. Heterogeneous boundary conditions are also changed by attachment, since the ambipolar fields which assist diffusion of charged particles to walls are qualitatively altered by the presence of heavy, negatively charged particles. While electrons and anions have the same charge polarity, their mobilities and characteristic velocity distributions are sufficiently different to permit long residence times for anions in the gas phase. Reflection of anions by sheath electric fields near dielectric boundaries causes their primary loss mechanisms to be homogeneous, in contrast to the situation for cations.

Since noble-gases do not form stable negative ions one need only be concerned with the attachment processes of silane, its radicals, and, under some conditions, molecular hydrogen produced by decomposition of silane. The Koopman's theorem electron affinity <sup>1</sup> of silane is calculated to be -4.5 electron volts. The

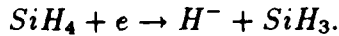
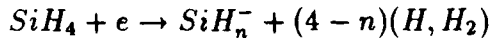
---

<sup>1</sup>Defined as the binding energy of the lowest, unoccupied molecular orbital of the neutral. The sign convention is chosen so that positive electron affinities refer to anions which are bound with respect to the process  $X^- \rightarrow X + e^-$ .

calculated <sup>2</sup> enthalpy difference between optimized geometries of silane and its molecular anion is:



Silane's unambiguously negative electron affinity and the requirement for conservation of energy in low-pressure attachment collisions imply that attachment of electrons to silane is dissociative:



The earliest measurements of silane attachment were reported in 1964 by Ebinghaus *et al.*[1] and five years later by Potzinger and Lampe as summarized in table 4.1. Neither group identified a molecular anion, and the relative cross-sections for production of  $SiH_n^-$  were comparable. Ebinghaus reported a large uncertainty for the magnitude of the  $H^-$  cross-section as a consequence of probable vacuum impurities. Although Potzinger and Lampe did not mention  $H^-$ , it may be that the dynamic mass-range of their magnetic-sector spectrometer precluded its detection.

Agreement between the absolute values of  $\sigma_a$  from these two studies is poor; they differ by an order of magnitude. The experimental methods of Ebinghaus are described in an earlier paper by Kraus [7]. Mass analysis was accomplished with a magnetic sector instrument using either Faraday-cup or electron-multiplier ion detectors. Great care was taken in the design of the electron source; a retarding-potential-difference scheme was employed to enhance the energy-resolution of the electron beam. However no mention was made of the method by which gas pressure was determined for calculation of cross-sections. Although error bounds on the appearance potentials were reported, no estimate of uncertainty in the cross-sections was presented.

The early works also differ in the observation of negative ions below 6 eV. The only anion observed by Ebinghaus at low energies (in the 2.8 to 4 eV range) is ascribed to  $H_3CO^-$ , which derived from ethanol, a vacuum-system impurity. Potzinger's data, while obtained with substantially less energy resolution, imply resonant formation of both  $SiH_2^-$  and  $SiH_3^-$  near 2.5 eV.

Although not yet published there have been some preliminary reports of quadrupole mass spectrometry experiments on silane dissociative attachment by

---

<sup>2</sup>MP4 energies, MP2/6-31g\*\* geometries and frequencies.

Ebinghaus			
Species	A.P.(eV)	$\sigma_a(cm^2)$	$\sigma_a/\sigma_{max}$
$SiH_3^-$	$7.0 \pm 2$	$2.0 * 10^{-18} cm^2$	1.00
$SiH_2^-$	$7.7 \pm 2$	$1.0 * 10^{-18}$	.50
$SiH^-$	$7.7 \pm 2$	$7.0 * 10^{-19}$	.35
$Si^-$	$12.5 \pm 2$	$2.0 * 10^{-19}$	.10
$H^-$	$7.9 \pm 2$	...	...
Potzinger			
Species	A.P.(eV)	$\sigma_a(cm^2)$	$\sigma_a/\sigma_{max}$
$SiH_3^-$	6.7	$1.8 * 10^{-19} cm^2$	1.00
$SiH_2^-$	7.7	$6.7 * 10^{-20}$	.37
$SiH^-$	7.7	$4.8 * 10^{-20}$	.26
$Si^-$	12.5	$1.0 * 10^{-20}$	.05

Table 4.1: Dissociative attachment of electrons to silane from the works of Ebinghaus [1] *et al.* and Potzinger [2].

Species	threshold (eV)	$\sigma_a(cm^2)$	$\sigma_a/\sigma_{max}$
$SiH_3^-$	1.92, 6.03	$6.0 \cdot 10^{-19} cm^2$	1.00
$SiH_2^-$	2.02, 5.73	$2.3 \cdot 10^{-19}$	.38
$SiH^-$	1.70, 6.79	$1.9 \cdot 10^{-19}$	.32
$Si^-$	6.55	$4.2 \cdot 10^{-20}$	.07
$H^-$	5.57	$2.2 \cdot 10^{-19}$	.37

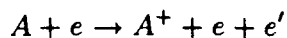
Table 4.2: Dissociative attachment thresholds and cross-sections measured with quadrupole mass spectrometry by Srivastava [3]. Magnitudes refer to the peak intensity associated with the higher threshold processes.

Srivastava [3]. The magnitudes of these cross-sections are between those reported in the earlier studies as summarized in table 4.2. However these recent measurements indicate a substantial channel leading to  $H^-$  from silane, a result which differs from those of Potzinger and Ebinghaus. Low-energy resonances near 2.5 eV for production of  $SiH_n^-$  ( $n = 3, 2, 1$ ) were also observed.

## 4.2 ICR Measurements

### 4.2.1 Experimental Techniques

Wide variation among reported values for the dissociative attachment cross-section of silane motivated a series of pulsed ion cyclotron resonance experiments. Negative ions are measured by FTMS using almost identical techniques to those described earlier for positive ions. Modest differences arise from the need to bias the trap plates negative with respect to the cell center. A negative bias traps both negative ions and low-energy electrons inside the ICR cell. Below the threshold for positive ion formation the number of low-energy electrons in the trap is virtually zero when the incident electron beam is properly aligned and the gas pressure is low. Above threshold the secondary electrons:



generated *in situ* provide a source of low energy electrons in the cell which is difficult to define, both in terms of total flux and energy. Since the attachment processes of silane occur below its ionization threshold the influence of secondary electrons on these measurements is unimportant.

In order to observe negative ions with FTMS one requires the product of electron beam flux, irradiation time, cross-section, and gas density to yield about  $10^4$  ions. Below ten volts the electron beam current density becomes space-charge limited, so that long irradiation times are required to obtain reasonable signal-to-noise ratios in the transformed mass spectra of silicon hydride anions. It is also true that very high energy resolution in the electron beam is not trivial with FTMS. The electron beam energy spread is equal at least to the trap voltage, which must be of order .5 volt to observe ions. However, with appropriate care reasonable spectra can be obtained. Figure 4.1 illustrates a typical silane anion spectrum recorded with  $SiH_3^-$ ,  $SiH_2^-$ , and  $SiH^-$  all in evidence.

### 4.2.2 Results

Since the spectrum in figure 4.1 was obtained with a 2 Tesla magnetic field, the direct observation of  $H^-$  was precluded because its cyclotron frequency is an order of magnitude greater than the digitizer bandwidth (2.667 MHz).<sup>3</sup> However,

<sup>3</sup>A heterodyne experiment would be possible, but requirements for new electronics made reduction of the magnetic field more practical.

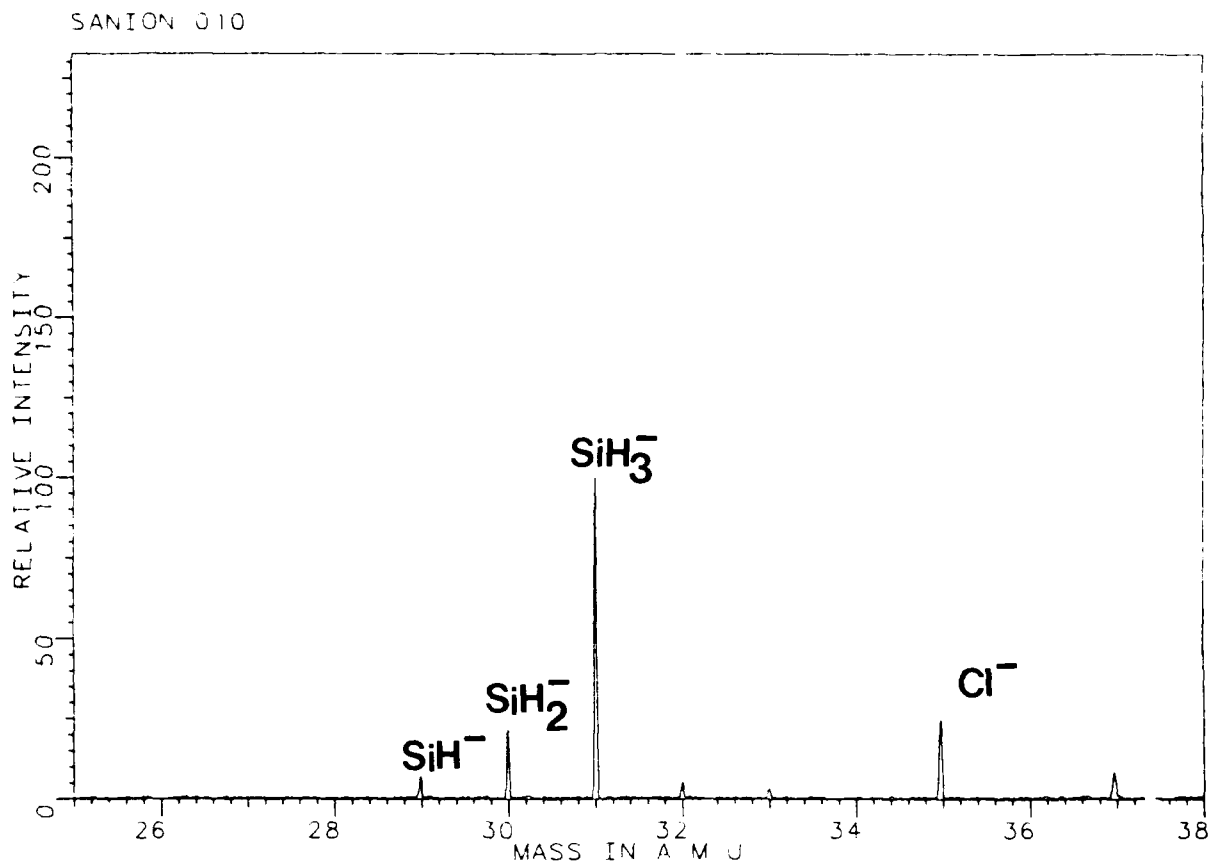


Figure 4.1: Typical silane anion spectrum obtained at  $10^{-7}$  torr with a 1s pulse from a 20nA, 9 volt electron beam.

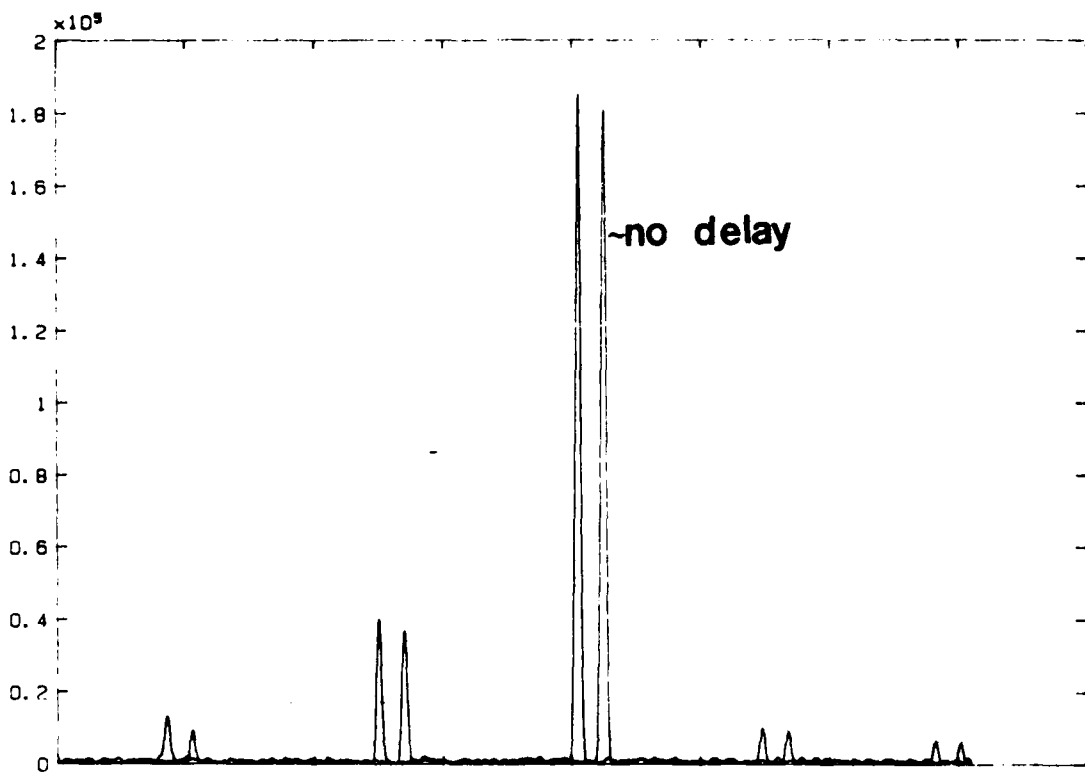


Figure 4.2:  $SiH_n^-$  ions with and without a 500ms reaction delay between formation and detection. The reagent pressure is approximately  $5 \cdot 10^{-7}$  torr, corresponding to 10 e-folding times for the reaction of  $H^-$  with silane.

indirect evidence of  $H^-$  could be obtained by introducing a delay between the formation of the ions and observation of their mass spectrum. The reaction:



has a measured rate constant of  $5.7 \cdot 10^{-10} cm^3 s^{-1}$  [9]. If  $H^-$  were formed in the trap an increase in the absolute and relative intensities of the  $SiH_3^-$  concentration with the introduction of a delay is expected. As can be seen in figure 4.2, no such increases were observed after over ten e-folding times for the reaction of  $H^-$  with silane.

In a separate set of experiments the magnetic field was reduced to 0.15 Tesla, bringing the cyclotron frequencies of  $H^-$  within the bandwidth of the detection electronics. No  $H^-$  was observed over a wide range of pressures (to  $10^{-6}$  torr),

electron beam energies (7-20 eV), and trap potentials (-0.5 to -10.0 V).

The measurements at 2 Tesla were performed at selected electron energies between the thresholds for anion and cation formation. At the upper end of this energy range only  $SiH_2^+$  and  $SiH_3^+$  were observed. This fact permits calibration of the electron energy scale, since the thresholds for formation of  $SiH_n^+$  are 12.2, 11.6, 14.7, and 13.3 eV for  $n = 3, 2, 1$ , and 0 (see Table 3.5). The beam energy is therefore between 12.2 and 13.3 eV. Furthermore, the response of  $SiH_n$  cations and anions to the excitation and detection processes of FTMS are identical. It is therefore possible to relate the ratio of observed cation and anion signals to the ionization cross-section near threshold as reported in chapter 3. Using a total ionization cross-section of  $6 * 10^{-17} cm^2$  for silane at 13 eV one obtains the dissociative attachment cross-sections displayed in figure 4.3. The peak cross-sections inferred in this manner agree best with the results of Potzinger and Lampe. The ICR results have substantially greater uncertainty in the electron-energy scale than those of Ebinghaus or Srivastava, so that a more appropriate comparison is with the integrated cross-sections. The full-width at half-maximum of the cross-sections from both of these studies is 1.5 eV, so that the integrated results for  $SiH_3^-$ ,  $SiH_2^-$ , and  $SiH^-$  are within 20% of Srivastava's most recent<sup>4</sup> values. It is therefore concluded the large, undocumented cross-section magnitudes reported by Ebinghaus are in error and further that  $H^-$  is not formed by dissociative attachment to silane.

## 4.3 Theoretical Aspects

### 4.3.1 $SiH_n^-$

*Ab initio* calculations of the silicon hydride radicals and anions have been performed using the Gaussian 82 program package [10] as introduced in chapter 3. While these calculations provide a reasonable estimate of ionization potentials using Koopman's theorem, the influences of orbital relaxation and correlation combine to yield very poor estimates of electron affinities [18]. In part to provide a uniform level of treatment throughout the present work, the geometries and frequencies of the radical anions have been performed using MP2/6-31g\*\* analytic gradients and MP4 total energies. The electron affinities of the radicals can then be estimated from the Koopman's theorem ionization potential of the anions, or

<sup>4</sup>S. Srivastava, personal communication, 1/88.

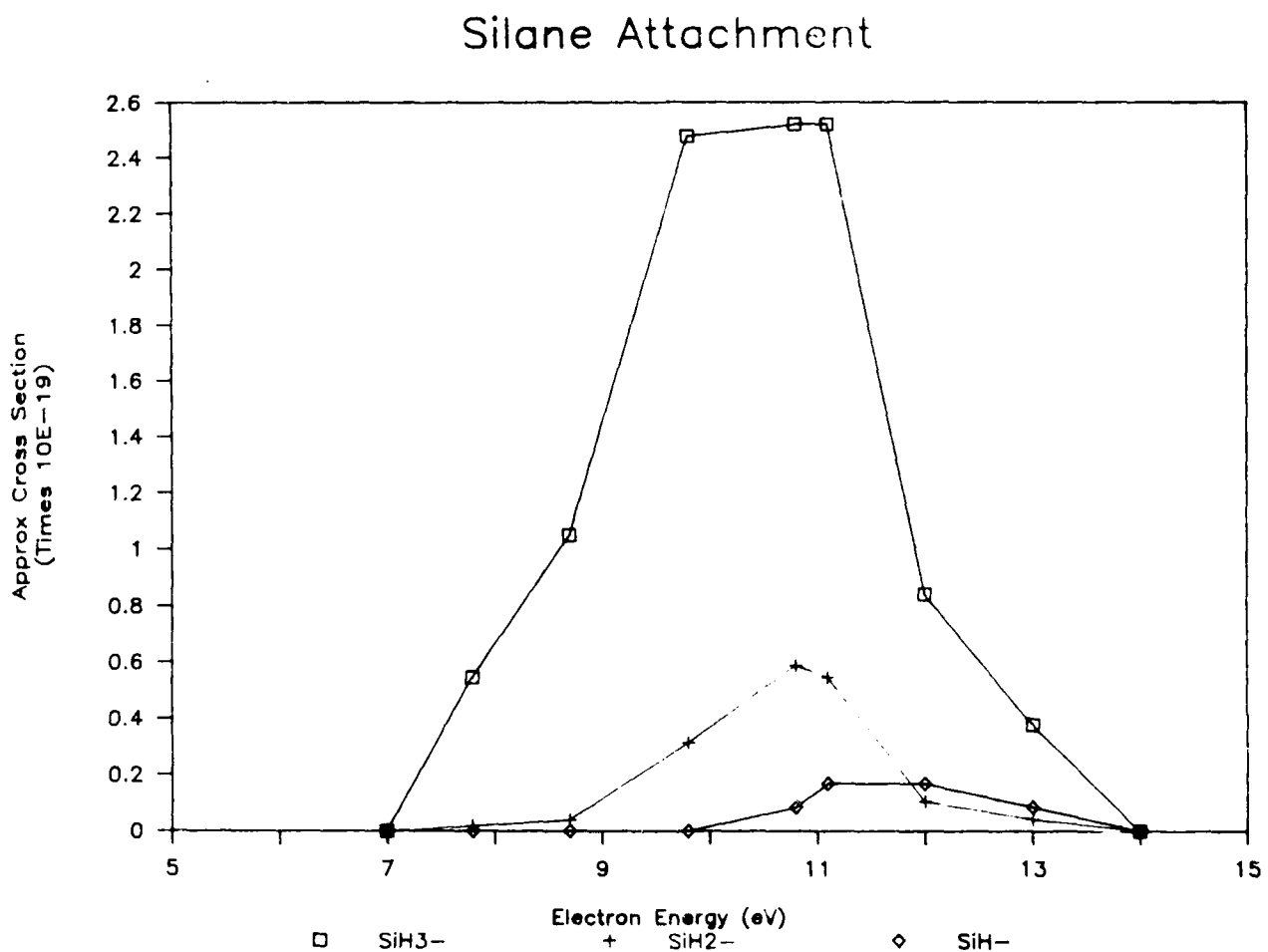


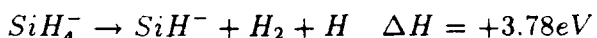
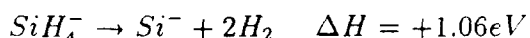
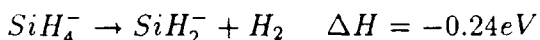
Figure 4.3: Silane dissociative attachment cross-sections as measured by pulsed ion cyclotron resonance mass spectrometry. The absolute uncertainty is  $\pm 15\%$  in amplitude from error in the threshold cross-section for cation formation. Relative ion intensities are good to  $\pm 5\%$  and the energy spread of the electron beam is estimated at 1 eV based on the higher resolution data of Ebinghaus and Srivastava.

Species	$\Delta H$ (eV)	Koopman's	Experimental
$SiH_4$	-2.27	+.07	n.a.
$SiH_3$	0.62	1.41	1.406
$SiH_2$	0.40	.90	n.a.
$SiH$	-0.66	-.46	n.a.
$Si$	0.71	1.20	1.39

Table 4.3: Estimates of silicon hydride radical electron affinities.  $\Delta H$  refers to the enthalpy difference between optimized geometries of radicals and anions. Koopman's reflects the UHF binding energy of the anion's highest occupied molecular orbital.

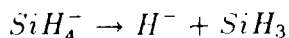
from the calculated enthalpy difference between the neutral free-radical and the corresponding anion. Table 4.3 summarizes the electron affinities of the silicon hydride radicals calculated by these methods.

Like the silane molecular cation  $SiH_4^+$  is Jahn-Teller unstable. The distortion mode which has the steepest potential gradient results in a rearranged geometry (figure 4.4) which is 1.7 eV more stable than the anion whose nuclear configuration is characterized by neutral silane. This optimized structure is similar to that calculated for  $SiH_3^-$  with an extra hydrogen atom located near the  $sp^3$  lone-pair orbital. The dissociation of  $SiH_4^-$  is thermodynamically constrained:



where  $SiH_4^-$  is in its optimized geometry and all products are assumed in their ground electronic and vibrational states. As was the case for  $SiH_4^+$ , the energy associated with the Jahn-Teller distortion, 1.68 eV, provides thermodynamic access to all but the last of these channels if one forms  $SiH_4^-$  in a configuration with identical geometry to the neutral molecule. Figure 4.5 is a schematic correlation diagram which illustrates the thermochemistry of  $SiH_4^-$ .

Thermodynamic analysis of the reaction:



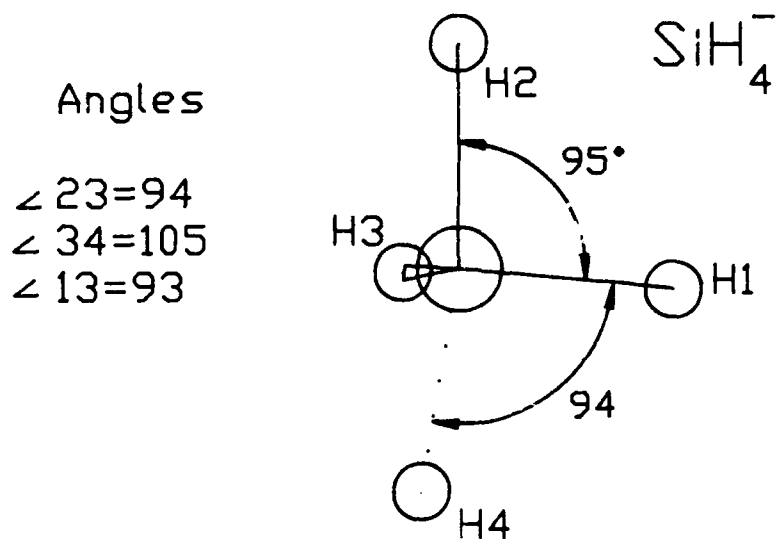


Figure 4.4: Optimized geometry of  $\text{SiH}_4^-$  at the MP2/6-31g\*\* level. This structure is 1.68 eV lower in energy than the  $T_d$  ion with bond lengths of 1.474 Å. This structure is very similar to that calculated for the  $\text{SiH}_3^-$  ion with H4 tacked on.

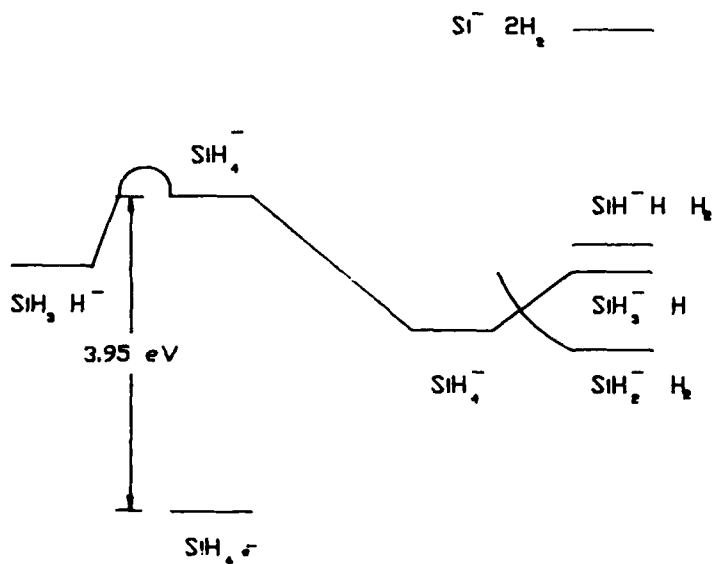
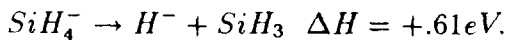


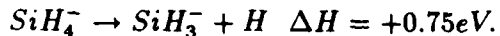
Figure 4.5: Thermochemistry of  $SiH_4^-$  and the products of dissociative attachment to silane from the *ab initio* investigations.

is complicated by the relatively poor description of  $H^-$  which is afforded using the standard 6-31g\*\* basis functions. The electron affinity calculated either by the energy difference between  $H$  and  $H^-$  or from the Koopman's ionization potential of the anion has the wrong sign. The electrons are predicted to be unbound. Increasing the basis by addition of a single diffuse function (6-31++g\*\*) gives the proper sign for the calculated electron affinity using either method, although the results are not in good agreement with the experimental value of 0.754 eV. One faces a dilemma in the *ab initio* treatment of this process; what choice of basis set and correlation treatment give a balanced description of both the negative ions containing silicon and those in which the heaviest element is hydrogen? For thermodynamic comparisons the exact and calculated energies of the hydrogen atom agree within 0.03 eV. Let it be assumed that the total energy of  $H^-$  is equal to the calculated value of the atom minus the experimental electron affinity of hydrogen, or -0.5278 Hartrees. The dissociation into  $H^-$  using these assumptions is calculated to be endothermic from the optimized molecular anion:



The competition between dissociative channels which yield  $H^-$  and  $SiH_3^-$  are

poorly illuminated by the *ab initio* calculations. Using the 6-31++G\*\* basis set the Koopman's theorem ionization potential of the silyl anion is 1.409 eV. The experimental value from photoelectron spectroscopy, 1.406 eV [5], is sufficiently close to suggest that the standard basis sets do a reasonable job of describing negative ions with a heavy center; that is, more than five or six basis functions. Since the experimental electron affinity of hydrogen atoms is only .754 eV, the Born-Oppenheimer approximation argues for negative charge to be concentrated on the  $SiH_3$  radical rather than the  $H$  atom during adiabatic dissociation of  $SiH_4^-$ . However this predilection does not carry over to the calculated thermochemistry using the MP4 energies with MP2 geometries and frequencies. The thermochemical calculations at this level underestimate the electron affinity of  $H$ , failing to resolve a thermodynamic preference among the reactions:



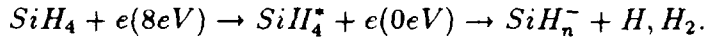
From the difference between the experimental electron affinities of  $H$  and  $SiH_3$  one expects the reaction yielding  $H^-$  to be .655 eV more endothermic than that which yields  $SiH_3^-$ .

The enthalpy difference between the neutral silane molecule and the geometrically identical negative ion at the MP4/6-31g\*\* level is 3.98 eV. The reference point for all of the above thermochemistry is the optimized geometry of  $SiH_4^-$ , which is 1.68 eV more stable than the tetrahedral form, so that corresponding reactions which start with the  $T_d$  anion are 1.68 eV more exothermic. Dissociation of  $SiH_4^-$  from virtual states which correlate with  $SiH_2^-$ ,  $SiH_3^-$ ,  $H^-$  and  $Si^-$  is thermodynamically allowed at thresholds of 2.06, 3.05, 3.09, and 3.36 eV. The production of  $SiH^-$  is predicted to be most endothermic, requiring nearly 6eV on thermodynamic grounds. Ebinghaus observed ions with about one tenth the cross-section of the principal resonances between 2.8 and 4 volts which he ascribed to ethanol impurities. Srivastava has observed similar ion signals which he ascribes to  $SiH_3^-$  and  $SiH_2^-$  near 2.7 eV.<sup>5</sup> His earlier observation of  $SiH^-$  at 2.5 eV violates thermodynamics, according to the calculations. The observation of the di- and tri-hydride anions is consistent with, but not predicted by the calculations. Extension of the pulsed ICR measurements to these low energies is precluded in the present spectrometer configuration. The low-energy processes

<sup>5</sup>S. Srivastava, personal communication, 1/88.

have narrow cross-sections with peak amplitudes which are less than three percent of the main resonances.

The processes which have the largest cross-sections occur at energies in the 8-9 eV range. They must, according to the calculations, involve excited states of  $SiH_4^-$  which correlate with the observed product ions. The mass spectral data by themselves do not reveal whether the product anions and neutrals are in excited vibrational or electronic states. Neither do they indicate the kinetic energy of the fragments. Electron energy loss experiments suggest Rydberg states of silane are formed by electron impact above 7.8 eV [5]. The high thresholds and broad resonances for negative ion formation from silane suggest the relevant interactions are between these Rydberg states and the incident electron, whose velocity has been slowed by the excitation process:



A more precise description of this process utilizes the language of electron-impact spectroscopy, where it is identified as a Feschbach resonance [23].

### 4.3.2 $H^- + SiH_4$

Calculations for the reaction of  $H^-$  with silane were also performed to examine the assumptions which led to the inference that no  $H^-$  was formed in high magnetic field FTMS of silane. Several literature calculations for this reaction [11, 12, 13, 14] have appeared. Calculations were performed with 6-31g\*\* and 6-31++g\*\* basis functions. Geometry optimizations and frequency calculations were carried out with inclusion of correlation using second order Möller Plesset perturbation theory. Single point estimates of correlation energy at the MP4 level were carried out for each of the potential minima. Figure 4.6 summarizes the results of these calculations.

The hydride anion attack on silane converged with no evidence of an enthalpic barrier to the pentacoordinate  $D_{3h}$  anion when starting in  $C_{3v}$ ,  $C_{2v}$ , and  $C_s$  symmetries. The calculated enthalpy difference for this step is very sensitive to the choice of basis set and correlation estimates, as expected, since these are required for reasonable description of the hydrogen anion. Two of the earlier reports were unable to accurately calculate the sign of the hydrogen atom's electron affinity (+.754 eV) with the methods for which results were presented on its reaction with silane [13, 12]. At the MP4/6-31++g\*\* level the enthalpy change for formation

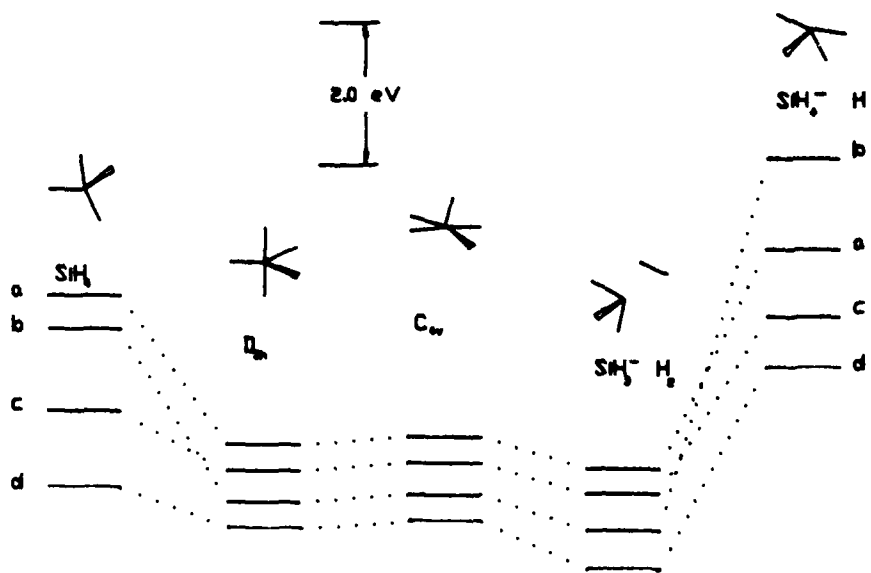


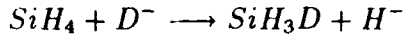
Figure 4.6: Calculated potential energies for the reaction of  $H^-$  with  $SiH_4$ . The zero point energies in eV are at the MP2/631g\*\* level are listed below each configuration. The surfaces labeled a,b,c, and d represent calculations at the MP2/6-31g\*\*, MP4/6-31g\*\*, MP2 6-31++g\*\* and MP4/631++g\*\* level, respectively.

of the pentacoordinate anion is:

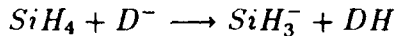


The energy differences between the  $D_{3h}$  local minimum and the  $C_{4v}$  saddle point of  $SiH_5^-$  were relatively insensitive to the basis set and correlation estimates, as were the energy differences for the product channels leading to  $SiH_4^-$  and  $SiH_3^-$ .

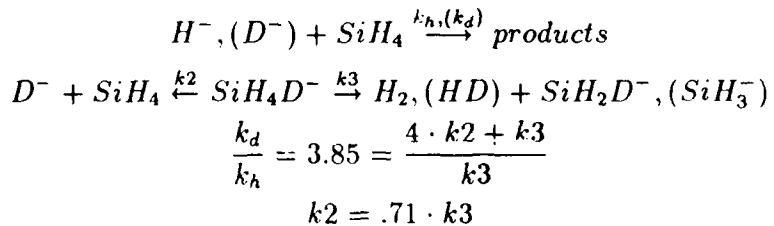
The enthalpy difference between isomers of  $SiH_5^-$  is small compared to the 10.2 kcal/mol potential energy drop in the entrance channel. While orbital symmetry restrictions are used with the calculations of Brandemark and Siegbahn [11] to argue against  $H_2$  elimination from the  $D_{3h}$  anion, the pentacoordinate anion would have  $\approx 10 \text{ kcal/mol}$  of internal (presumably vibrational) energy if formed under low pressure conditions. In the absence of its stabilization by infrared emission or collision,  $SiH_5^-$  would have a fluxional structure that scrambles the axial and equatorial hydrogens [15]. The symmetry arguments against  $H_2$  elimination are therefore waived on timescales which are longer than the tunnelling time for hydrogen ligands. The calculated energy difference between the stationary points corresponding to two stages of the Berry pseudorotation,  $C_{4v}$  and  $D_{3h}$ , is only 2.16 kilocalories per mole. Thus the competition between the displacement reaction:



and the elimination channel:



is reflected in the experimental results of Payzant *et al.* The net loss rate of  $D^-$  was found to be 3.85 times that of  $H^-$  in  $SiH_4$  [9]. The relative roles of  $H_2$  and  $H^-$  elimination from  $SiH_5^-$  can be inferred to first order from this ratio by assuming no kinetic isotope effect in the unimolecular decomposition:



where  $k_2$  indicates the rate at which each hydride ion escapes from the  $SiH_5^-$  complex. For five equivalent hydrogen atoms, the loss of  $H^-$  is about 3.5 times as rapid as the molecular  $H_2$  elimination.

### 4.3.3 Attachment to $H_2$ and $SiH_n$ radicals

The remaining sources of negative ions in silane-containing plasmas arise from decomposition products of silane. The influence of molecular hydrogen will clearly depend on the discharge conditions. Although the dissociative attachment cross-section of  $H_2$  in its vibrational ground state is tiny, (3.8 eV threshold,  $10^{-21} cm^2$ ) vibrational excitation of the molecule results in an enormous increase in its attachment cross-section, for example the threshold and cross-section for dissociative attachment to the seventh vibrational level are .25eV and  $4 \cdot 10^{-15} cm^2$  [16, 17]. A combination of large fractional dissociation of silane and the right electron energy distribution could in principal produce copious quantities of  $H^-$ . However this source of  $H^-$  is balanced by reactive sinks including the rapid reaction with silane and electron impact ionization (detachment) of  $H^-$ .

The final class of negative ion sources is in fact one of the most difficult to measure. Although silane and the noble-gases themselves have negative electron affinities, the radicals  $SiH_3$ ,  $SiH_2$ , and atomic  $Si$  have positive affinities for electrons. The formation of anions by direct or dissociative attachment to these radicals provides a homogeneous electron loss with positive feedback. Initial dissociation enhances attachment, which increases the discharge impedance. The unattached electrons must be driven harder (i.e. higher fields must be applied) to maintain the same discharge current density, so that the dissociation rate, which increases with the mean electron energy, must also increase. The increased dissociation rate feeds back as an increased source of attachers, and so forth.

## 4.4 Conclusions

A combination of FTMS measurements and *ab initio* calculations have been performed to examine the role of negative ion formation processes in silane-containing plasmas.

- The principal anion species formed by dissociative attachment to silane above 7 eV are  $SiH_3^-$  and  $SiH_2^-$ .
- The energy and width of the cross-sections suggest that the attachment process involves interaction of an electronically excited state of silane with an electron which has been slowed by the excitation process. The possibility of vibrationally or electronically excited ion and neutral fragments is strongly suggested from these Feshbach resonances.

- Dissociative attachment to silane has cross-sections which peak in the  $10^{-19} \text{ cm}^2$  range at an electron energy of around nine volts. The integrated attachment cross-section (over all  $\text{SiH}_n^-$ ) is well-represented as a gaussian function peaked at  $10^{-18} \text{ cm}^2$  with a full-width at half-maximum of 1.5 eV.
- $\text{H}^-$  is not formed by dissociative attachment to silane.
- To the extent  $\text{H}^-$  is formed in deposition plasmas from vibrationally enhanced dissociative attachment to  $\text{H}_2$ , one anticipates its rapid removal by reaction with silane to form  $\text{SiH}_3^- + \text{H}_2$ .
- Under conditions where the gas phase contains substantial concentrations of silicon-hydride radicals, the fact that these have positive electron affinities is expected to dominate the negative ion dynamics.

## Bibliography

- [1] Von H. Ebinghaus *et al.*, *Zeitschrift für Naturforschung*, **19a**, 732 [1964].
- [2] P. Potzinger and F. W. Lampe, *Journal of Physical Chemistry*, **73**, 3912 [1969].
- [3] S. Srivastava, *Bulletin of the American Physical Society*, **31** 149 [1986] and personal communications [1987,1988].
- [4] H. Chatham, D. Hils, R. Robertson, and A. Gallagher, *Journal of Chemical Physics*, **81**, 1770 [1984]
- [5] M. R. Nimloos and G. B. Ellison, *Journal of the American Chemical Society*, **108**, 6522 [1986].
- [6] M. Dillon *et al.*, *Journal of Chemical Physics*, **82**, 2909 [1985].
- [7] Von K. Kraus, *Zeitschrift für Naturforschung*, **16a** 1378 [1961].
- [8] J. Morrison and J. Traeger, *International Journal of Mass Spectrometry and Ion Physics*, **11**, 289 [1973].
- [9] J. D. Payzant *et al.*, *Journal of the American Chemical Society*, **98**, 894 [1976].
- [10] J. S. Binkley *et al.*, **Gaussian 82**, Carnegie Mellon Publishing Unit, Pittsburgh, PA 15213.
- [11] U. Brandemark and P. Siegbahn, *Theoretica Chimica Acta*, **66**, 233 [1984].

- [12] D. Wilhite and L. Spialter, *Journal of the American Chemical Society*, **95**, 2100 [1973].
- [13] P. Baybutt, *Molecular Physics*, **29**, 389 [1975].
- [14] M. S. Gordon *et al.*, *Journal of the American Chemical Society*, **108**, 7889 [1986].
- [15] R. S. Berry, *Journal of Chemical Physics*, **32**, 933 [1960].
- [16] A. Garscadden and W. F. Bailey. **Rarefied Gas Dynamics**, **74**, ed. S. Fisher, 1125 [1981].
- [17] M. Allan and S.F. Wong, *Physical Review Letters*, **41**, 1791 [1978].
- [18] A. Szabo and N. Ostlund, **Modern Quantum Chemistry**, New York:Macmillan, [1982].
- [19] G. Turban, PhD. dissertation, University of Nantes, [1980].

æ

# Chapter 5

## Ion Source Kinetics

What is to be done with all of the detailed microscopic information presented in the previous three chapters? One needs a concise representation for the parametric variation of the homogeneous ion sources as the excitation conditions and gas mixture are varied. The first stage of this representation will be concerned with calculation of the nascent ion species distribution. Nascent in the present context describes the distribution of ion species which, having been formed by impact of plasma electrons with neutral species, has not yet had time to be changed by ion-molecule chemistry, diffusion, or further ionization and recombination. The evolution of this nascent distribution by ion-molecule reactions is discussed in chapters six and seven, while the implications of the remaining processes are explored in chapter eight.

### 5.1 Positive Ion Sources

#### 5.1.1 $\mathcal{F}$ and ion formation

At low pressures and modest current densities typical of PECVD reactors the principal source of cations is electron-impact ionization of the reagent gases. The ionization rate and cross-section for each neutral species in the discharge is related to the electron energy distribution,  $\mathcal{F}(\epsilon)$ , by the integral:

$$\frac{dN_i}{dt} = \int \mathcal{F} \cdot \sigma_i \cdot \frac{\sqrt{\epsilon}}{\mu} d\epsilon$$

where both  $\mathcal{F}$  and  $\sigma_i$  are functions of the electron energy,  $\epsilon$  and  $\mu$  is the reduced mass of the colliding pair. Nature determines  $\mathcal{F}$  and the total ionization rates in laboratory discharges self-consistently so that the particle sources and losses are matched to appropriate physical boundary conditions for a particular situation (e.g. wall currents, recombination, total current flow, gas heating, light emission, momentum conservation, ...). Closed, analytic solutions for simple configurations are tractable, for example the cylindrically symmetric positive column of noble-gas discharges has been the subject of numerous treatises [3, 2]. Given a manifold of inelastic losses for electrons colliding with the gas one can calculate the steady-state  $\mathcal{F}$  from an approximate form of the Boltzmann kinetic equation [24]. Optimal calculations of  $\mathcal{F}$  take into account the form of discharge excitation. While the low electric fields typical of the d.c. positive column are amenable to spherical harmonic expansions, radiofrequency reactors are more efficiently described by expansions of  $\mathcal{F}$  in functions which are more naturally asymmetric [3]. The distribution function can also be estimated by Monte-Carlo methods [8].

Introduction of a molecular attaching gas such as silane has significant and nonlinear effects on the coupled plasma equations of motion by introducing negative ions and a manifold of cross-sections which changes with time as the molecular gas is dissociated and excited. One must therefore balance the level of the analytic models to the level of understanding and detail which is possible – or desirable – at the collisional physics level.

Ionization rates are obtained by numerical integration of the above equation if one knows or can estimate the electron energy distribution function  $\mathcal{F}$ . The form of a distribution function whose mean energy is constant but is otherwise unconstrained is Maxwellian:

$$\mathcal{F}(\epsilon) = \frac{1}{kT_e} e^{-\frac{\epsilon}{kT_e}}.$$

Electrons are more easily accelerated by plasma electric fields than ions or neutrals, so that the electron temperature,  $T_e$ , is in general significantly higher than either the gas or the positive ion temperature. Although  $\mathcal{F}$  is rarely Maxwellian due to the complex nature of the inelastic scattering of electrons by molecules, analysis of the ionization rates is facilitated by expressing  $\mathcal{F}$  as a linear combination:

$$\mathcal{F} = \sum_{j=0}^{\infty} \frac{c_j}{kT_j} \cdot (e^{-\frac{\epsilon}{kT_j}})$$

where the  $c_j$ 's are coefficients (not necessarily positive) which may be used as parameters to fit more complicated distribution functions to the easily integrable maxwellians. The total rate for a complex linear combination of  $c_j$ 's is then easily calculated from one set of integrals such as those illustrated in figure 5.1.

Although use of a sufficiently large number of  $c_j$ 's in the previous expansion permits description of an arbitrary distribution function, there are physical situations which provide beam-like energy distributions. A more concise basis for representation of these contributions to  $\mathcal{F}$  is a set of normalized gaussians:

$$\mathcal{F} = \frac{\pi}{\sqrt{\gamma}} \cdot \sum_{j=1}^{\infty} c_j \cdot e^{-\gamma \cdot (\delta - \epsilon)^2}$$

where  $\delta$  is the mean energy of the gaussian beam and  $\gamma$  is a fixed parameter which defines the width of the basis functions.

Since the contributions to  $\mathcal{F}$  are defined above so that the integral of each basis function over energy is unity, the ionization rate for an arbitrary electron energy distribution can be rewritten as:

$$\frac{dN^+}{dt} = \sum_{j=1}^{\infty} k_j \cdot c_j$$

where the  $k_j$ 's are the rates calculated from the integrals:

$$k_j = \int \mathcal{F}(\epsilon) \cdot \sqrt{\epsilon} \cdot \sigma_i(\epsilon) d\epsilon$$

and the  $\mathcal{F}$ 's are the maxwellian and gaussian basis functions described above. The cross-sections for ionization or attachment,  $\sigma_i$ , need be explicitly integrated only once – the variation of the rates with  $\mathcal{F}$  is parameterized by the coefficients  $c_j$ . Recasting the ionization rate in this manner adds no new physics to the analysis but permits a more concise representation of the scaling of ionization with gas mixture and excitation variation from graphs of the basis function integrals such as are shown in figure 5.1.

### 5.1.2 $\mathcal{F}$ estimates

The electron energy distribution function can be inferred from a variety of experimental techniques including electrostatic probe measurements, emission spectroscopy, and optogalvanic or photodetachment spectroscopies[9, 13]. Alternatively, one can attempt to calculate  $\mathcal{F}$  from first principle given a manifold of

elastic and inelastic scattering cross-sections and the excitation conditions (e.g. electric field to gas density ratio) by solving the Boltzmann kinetic equation [7] or applying Monte-Carlo methods [8]. While such calculations may provide guidance on the approximate form of  $\mathcal{F}$ , detailed numerical solutions of electron transport are both beyond the scope of this report and, in the authors view, of limited utility given the uncertainty in the input cross-section manifolds and the variation of gas composition with time in complex molecular mixtures. The present approach therefore will be to describe the scaling of ionization processes with parametric variation of  $\mathcal{F}$  so that the relationship of the ion chemistry to the plasma's excitation may be understood.

It is important to note that the expansion coefficients  $c_j$  can be constrained beyond the normalization condition (i.e.  $\sum_j(c_j) = 1$ ). Quantitative observation of optical emission, for example, can be reexpressed as algebraic constraints on the coefficients which are calculable if the relevant excitation cross-sections are known. Similarly the total electron, cation, and anion densities and fluxes, where measured, constrain the matrix of  $c_j$ 's. The proper approach for a particular set of operating conditions is therefore to synthesize a matrix of  $c_j$ 's which is consistent with observed experimental data but maximally noncommittal in all other senses. Application of these maximum entropy methods to analysis of deposition reactors is the topic of a forthcoming paper [11].

Figure 5.1 illustrates the ionization rates calculated for Maxwellian basis functions using the cross-sections for noble gas and silane ionization reported in earlier chapters. Of the noble-gases silane's ionization rate varies most like that of krypton for Maxwellian  $\mathcal{F}$ 's. Although the ionization thresholds of silane and xenon are most similar, the large magnitude of the xenon ionization cross-section causes its ionization rate to exceed that of silane at all energies. Normalized rates for Gaussian beams are displayed in figure 5.2. As one expects from the energy dependence of the ionization cross-sections, the relative ionization rates for each of the gases changes little when the mean beam energy is above the threshold for ionization.

## 5.2 Anion Sources

The equations which describe negative ion formation are identical to those for cations. However the requirement for conservation of energy and momentum in the attachment collision typically leads to resonant cross-sections, in contrast to

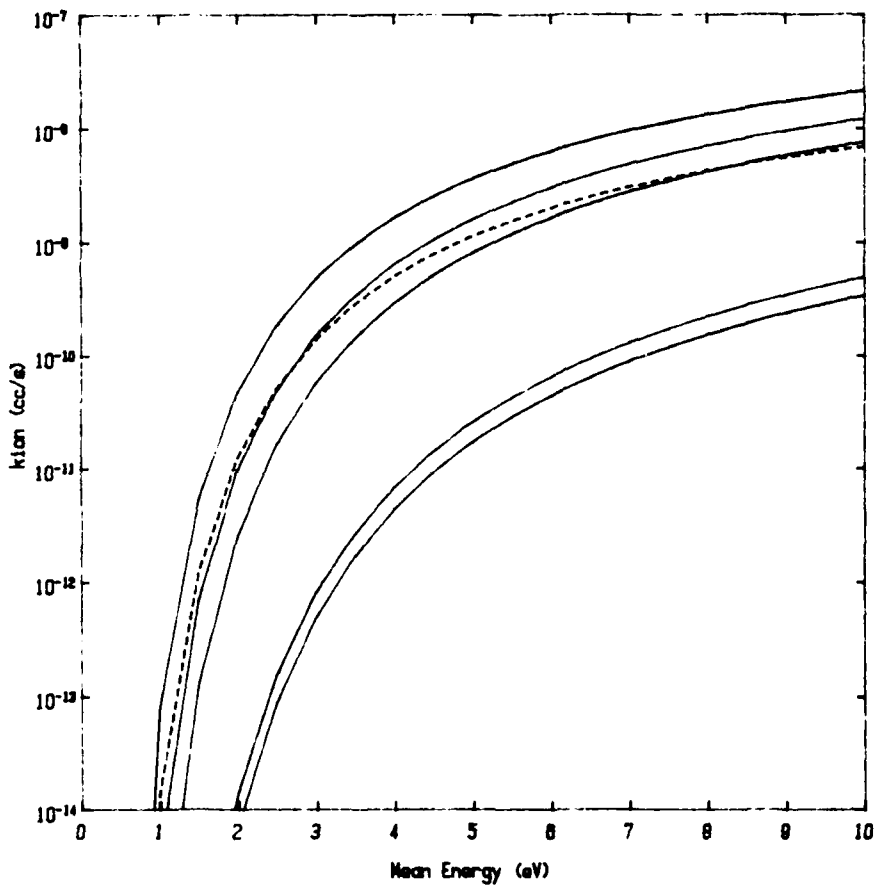


Figure 5.1: Ionization rates for Maxwellian electron energy distributions in pure noble-gases (solid lines) and silane (dashed line). The x-axis is the mean electron energy of the  $\mathcal{F}$  basis function.

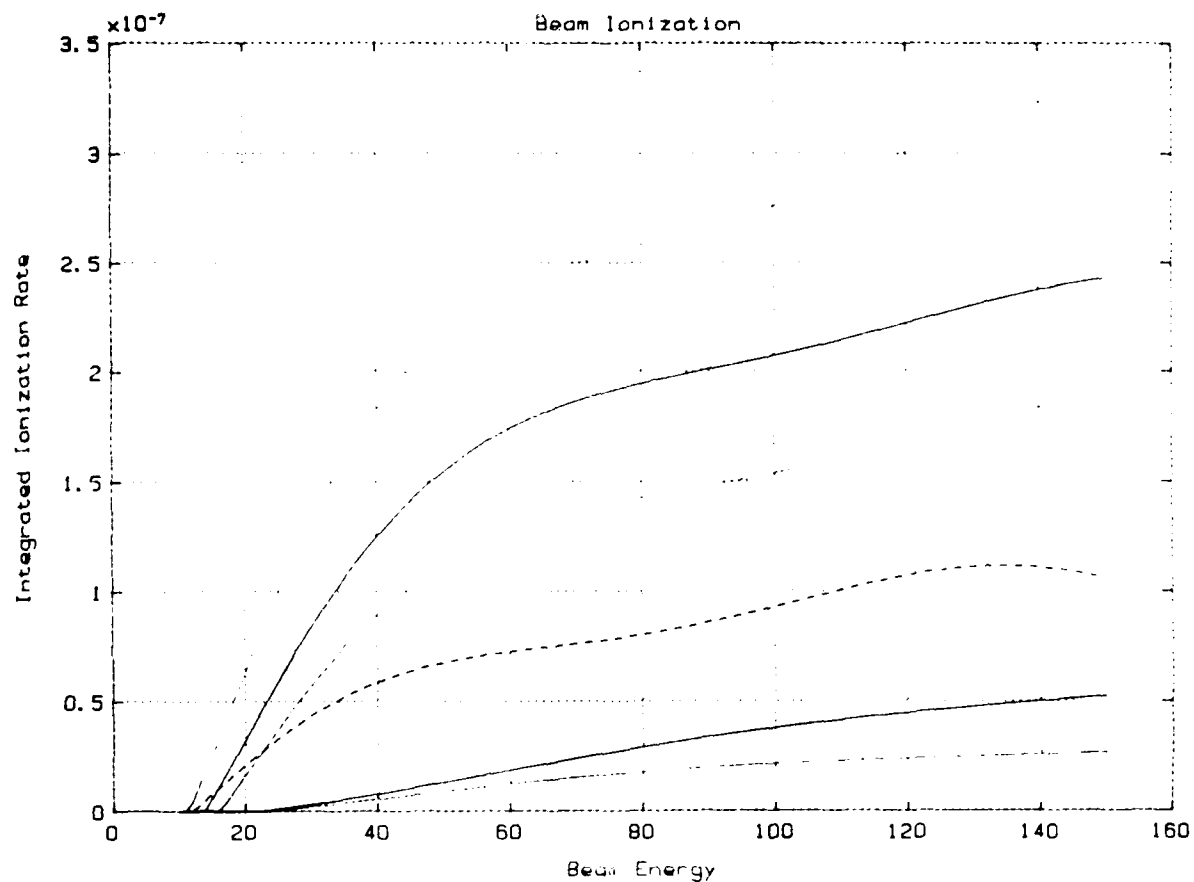


Figure 5.2: Ionization rates for gaussian beam-like energy distributions for the noble-gases (solid lines) and silane (dashed line). Unlike figure 5.1 this graph has a linear y-scale. The calculated ionization rate is relatively constant above threshold, since the electron velocity increases as the cross-sections decrease from 30 to 100 eV.

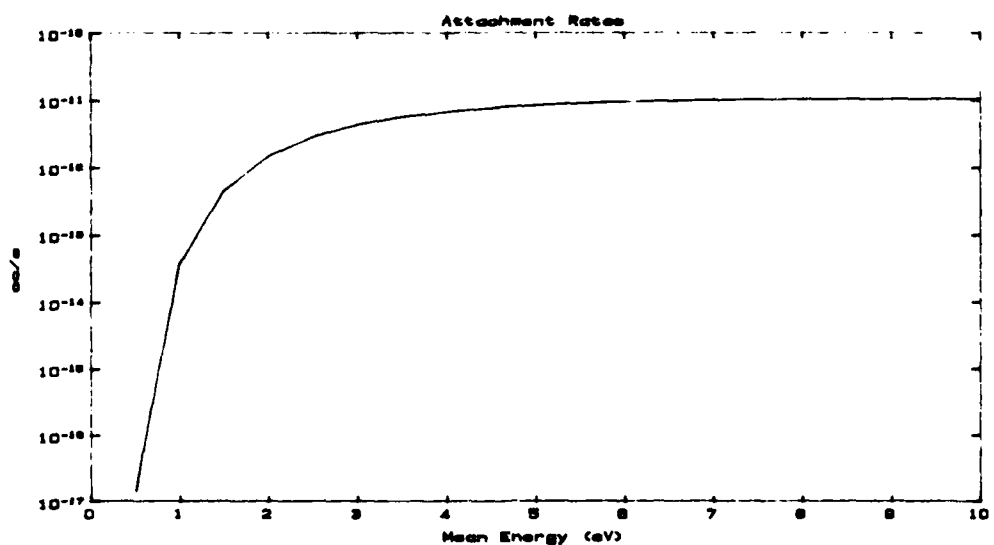


Figure 5.3: Dissociative attachment rate for silane using a gaussian attachment cross-section with 1.5 eV full width at half maximum (c.f. Srivastava and Ebinghaus) centered at 9 eV with an integrated magnitude matched with the experimental FTMS values from figure 4.3. The nascent negative ion formation rates are ordered  $SiH_3^- > SiH_2^- > SiH^-$ .

the case of cation formation where both the primary and secondary electrons are available to carry momentum and energy away from the product ion. Therefore the scaling of attachment with mean energy in the Maxwellian and gaussian basis distribution functions is qualitatively different than that for positive ion generation. Figure 5.3 illustrates the scaling of the total dissociative attachment rate with mean energy for the same distributions as in figure 5.1. Silane's dissociative attachment rate exceeds that of its ionization when the mean energy drops below 2 eV, but the increase of attachment with mean energy is less dramatic than that of ionization over the same range, as expected from the shape of the cross-sections.

The impact of beam-like electrons also scales differently for attachment processes. Gaussian basis functions which have no amplitude in the region of non-zero attachment cross-section will obviously lead to no attachment. Therefore one expects a significant contribution from beam attachment only when beam electrons have kinetic energies in the 8 to 12 eV range. Under these conditions  $\int \sigma_a \cdot v dv$

attains a value of  $4.7 \cdot 10^{-10} \text{ cm}^3 \text{s}^{-1}$  assuming perfect overlap between  $\mathcal{F}$  and  $\sigma_a$ . Such a situation is unlikely in real discharges, since beam electrons at these low energies are rapidly degraded by other processes with large inelastic scattering cross-sections.

## 5.3 Nonlinear Sources

### 5.3.1 Radical Ionization

Given the difficulties associated with the measurement of ionization and attachment cross-sections of stable gaseous species it is not surprising that very little data is available for free radical ionization and attachment. Even if these cross-sections were known with high precision one would still have to understand the competition between the radicals' homogeneous and surface reactions and electron-impact processes in order to define their contribution to electron transport.

However the properties of the radical species, including their ionization and attachment properties, can be estimated using *ab initio* electronic structure calculations and analogy with their parent molecule. Ionization of the silicon-hydride radicals ought to occur at significantly lower thresholds than that of silane or the noble gases as reflected in the calculated ionization potentials summarized in table 3.6. One plausible-but arbitrary-form for the ionization potential of the  $\text{SiH}_3$  radical would have  $d\sigma_i/d\epsilon$  near threshold equal to that for dissociative ionization of silane and a constant magnitude comparable to that for silane ionization ( $\approx 1.6 \cdot 10^{-16} \text{ cm}^2$ ) at energies well above threshold. Obviously, the assumed form of the cross-section implies substantially greater ionization rates for the Maxwellian basis functions, as summarized in figure 5.4.

In early 1988 Hayes *et al.* reported cross-sections for the ionization of the  $\text{SiF}$  free radical using the same crossed-beam technique that was used for their noble ion measurements [12]. The threshold for generation of  $\text{SiF}^+$  (7 eV) as well as the shape and peak magnitude ( $6.2 \text{ \AA}^2$ ) argue for the validity of the approximate form for the ionization cross-sections of the silicon-hydride radicals using the *ab initio* calculations and analogies described above.

The inference that the radical ionization rates exceed those for silane under conditions of monotonically decreasing  $\mathcal{F}$  has important implications for one's interpretation of the nature of depositing species. For example Turban *et al.* [1] claimed that the observation of total silane depletion in a radiofrequency

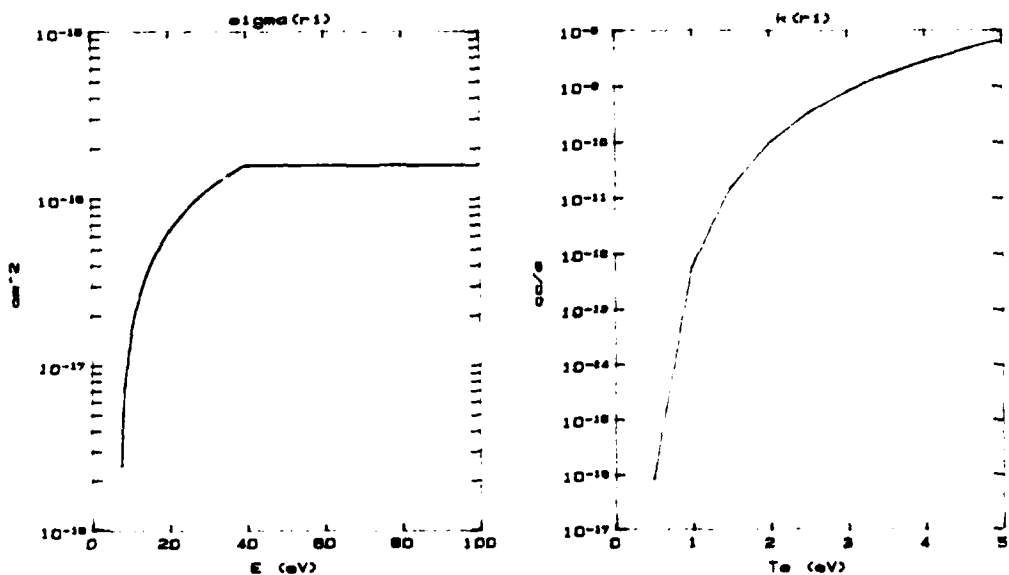


Figure 5.4: Estimated ionization rates of the silicon-hydride radicals calculated for Maxwellian  $\mathcal{F}$  and cross-sections analogous to those of silane but displaced to the calculated ionization threshold.

silane:helium discharge proved that uncharged free radicals were primarily responsible for film deposition since the cross-section for neutral dissociation exceeds that for silane ionization at all energies. This assertion is true for radicals if they have a sticking coefficient of order unity, since the diffusion time under Turban's experimental conditions (one millisecond) is short compared with the gas residence time (one second). On the other hand, the time constant for radical ionization is about ten milliseconds, so that radicals would be more likely ionized than deposited if the sticking coefficient was less than 0.1. Note that the sticking coefficient of the OH radical, a very reactive species, is only of order  $10^{-4}$  on untreated pyrex [14].

### 5.3.2 Radical Attachment

The situation for attachment to the radicals produced by electron-silane collisions is somewhat more difficult. Unlike their parent silane the radicals  $SiH_3$ ,  $SiH_2$  and  $Si$  all have positive electron affinities. In addition, the first two of these can satisfy energy and momentum conservation in an attachment collision

by dissociation, infrared emission, or formation of vibrational states which are subsequently stabilized by heavy particle collisions. These attachment processes are most probably resonant with energy thresholds substantially below the silane dissociation threshold, implying interaction with a region of  $\epsilon$  in which  $\mathcal{F}$  is relatively large under many discharge conditions. Therefore even modest attachment cross-sections can yield very high attachment rates for the dissociated fragments. At the same time, the relatively weak binding energy of the electron in the negative ions and the trapping of these species by electrostatic wall sheaths suggests a competing, non-resonant process of electron-impact detachment



The actual role of free-radical attachment is determined in detail by the balance between these two processes and the reactive sinks for intermediate free radicals in the vapor phase and at the reactor walls.

Experimental evidence of radical attachment has been reported based on microwave interferometric electron density measurements in pulsed silane:helium plasmas [14, 15]. Indeed these authors concluded that, "... attachment is due mainly to a product of the dissociation of silane and is not due to silane itself." This conclusion is fully consistent with the interpretation of the *ab initio* calculations of electron affinities as well as the silane dissociative attachment cross-sections measured and discussed in chapter 4. It should be noted that the large reported attachment rates are in part a consequence of the low electron temperature which characterized the authors' afterglow. Under steady-state or driven conditions attachment and ionization of the negative ion are competitive, so that the negative ion density may be quite low indeed. This topic will be revisited in chapter 8.

The absence of quantitative data on radical ionization, wall reaction, attachment, and homogeneous chemistry make predictions about the role of processes that scale superlinearly with discharge current (or power) for a constant electron energy distribution function extremely speculative. However, one can, by appeal to the *ab initio* calculations, qualitatively estimate the relative importance of these processes as pressures, reactor dimensions, and power are scaled by methods in which  $\mathcal{F}$  is integrated with estimated cross-sections for relevant intermediate species.

## 5.4 Conclusions

A convenient form for the parametric analysis of ionization rates of silane and the noble gases has been introduced which involves convolution of the measured cross-sections with a family of Maxwellian and Gaussian basis functions. Measurement, inference or calculation of the electron energy distribution function,  $\mathcal{F}$ , permits rapid estimation of the nascent ion species distribution using figures 5.1, 5.2, 5.3, and 5.4, in which integrated rates for the normalized basis functions are presented. An approximate form for the ionization cross-sections of the silicon-hydride radicals has been synthesized by analogy with the silane ionization cross-section and the *ab initio* radical ionization potentials reported in chapter 3. Assuming this form implies the lifetime of a silicon-hydride radical to ionization is often less than that of the parent silane, so that radical densities and fluxes to the walls are governed by a balance between the wall sticking probability and the radical ionization rate for relatively long gas residence times.

The measured dissociative attachment cross-sections for the ground electronic and vibrational state of silane reported in chapter 4 have been subjected to a similar analysis. The attachment rate for silane is calculated to be substantially less than its ionization rate under most discharge conditions, with an upper bound to this direct negative ion source of  $\approx \mathcal{N} \cdot 4.0 \cdot 10^{-10} \text{ cm}^3 \text{s}^{-1}$  where  $\mathcal{N}$  is the number of electrons in the seven to ten electron volt range. While measurements of the radical attachment cross-sections have not been made, *ab initio* calculations suggest an important role for attachment to the  $\text{SiH}_2$  and  $\text{SiH}_3$  radicals.

The analytical tools developed in this chapter permit estimates of the distribution of ion species produced by electron collisions. The relaxation of this species distribution through ion-molecule reactions and diffusion are the next logical steps in the development of a paradigm for ion kinetics in semiconductor deposition discharges and thus the topics of the remaining three chapters.

# Bibliography

- [1] R. Franklin **Plasma Phenomena in Gas Discharges**, (Oxford:Clarendon Press) [1976].
- [2] A. Von Engel **Ionized Gases**, (Oxford:Clarendon Press), [1965].
- [3] L. Friedland and H. Eizenkiet, *Physical Review*, **A 36**, 1351 [1987].
- [4] B. Smirnov, **Physics of Weakly Ionized Gases**, (Moscow:Mir) [1981].
- [5] L. Overzet and J. Verdeyen, *Applied Physics Letters*, **48**, 695 [1986].
- [6] C. Fledderman, J. Beberman and J. Verdeyen, *Applied Physics Letters*, **58**, 1344 [1985].
- [7] A. Garscadden, G. Duke and W. Bailey, *Applied Physics Letters*, **43** 1012 [1983].
- [8] M. Kushner, *IEEE Transactions on Plasma Science*, **PS-14**, 179 [1987].
- [9] f. Kampas and R. Griffith, *Journal of Applied Physics*, **52**, 1285 [1981].
- [10] J. Perrin and J. Aarts, *Chemical Physics*, **80**, 351 [1983].
- [11] P. Haaland, manuscript in preparation [1988].
- [12] T. Hayes *et al.*, *Journal of Chemical Physics*, **88**, 823 [1988].
- [13] G. Turban, Y. Catherine and B. Grolleau, *Thin Solid Films*, **60**, 147 [1979].

- [14] J. Margitan, *Gas Phase Reactions of OH Radicals Studied by Molecular Resonance Fluorescence*, PhD Thesis, University of Pittsburgh, [1971].

æ

# Chapter 6

## Ion Kinetics

### 6.1 Introduction

The nascent distribution of ion species produced by electron impact on a specific gas mixture evolves in time as a result of both homogeneous chemistry and wall reactions fed by diffusion. The important roles of electron-ion and ion-ion recombination as well as diffusion will be deferred to chapter 8. This chapter will focus on experimental results from investigation of reactions between noble or silicon hydride cations and silane. *Ab initio* electronic structure calculations will be described in the next chapter which assist in the interpretation of an unusual reactivity trend for the reactions of noble cations with silane.

Rapid reactions of ions with neutral species have been well documented. The starting point for most treatments of charge transfer chemistry is the classic 1905 work of Langevin in which the capture cross-section for an ion by a spherically symmetric molecule is derived in terms of the molecule's electronic polarizability: [1]

$$\sigma_L(\epsilon) = \pi \sqrt{\frac{2\alpha e^2}{\epsilon}}$$

where  $\sigma_L$ ,  $\alpha$ ,  $e$ , and  $\epsilon$  are the Langevin cross-section, the molecule's polarizability, the electronic charge, and kinetic energy respectively. Eyring *et al.* first applied this result to the analysis of rate constants, leading to an energy independant rate constant which is commonly called the Langevin rate: [2]

$$k_L = 2\pi \cdot e \sqrt{\frac{\alpha}{\mu}}$$

where  $\mu$  is the reduced mass of the colliding pair. The analytical trajectories which result from Langevin's approach represent an important theoretical benchmark against which experimental rate constants must be compared. Since the one key parameter for the present systems, the polarizability of silane, is poorly defined in the literature, a brief experimental digression is in order before returning to the question of ion-molecule reaction chemistry.

## 6.2 Silane Polarizability

Diverse values for the polarizability of silane may be gleaned from the literature. Maryott and Buckley report a value of  $5.44 \text{ \AA}^3$  in a 1953 circular [28]. A pathetically sparse table in a 1969 monograph edited by Hill [8] contains a chapter entitled, "The Permittivity of Liquids," in which Price reports a molar refrac-tion for silane of  $4.50 \cdot 10^{-24} \text{ cm}^3$  [6]. There is no mention of the experimental method, sample purity, or error bounds other than the reporting of three significant figures. In a recent calculation of electron scattering by silane Jain needed to normalize his *ab initio* polarizability to this 'experimental' value in order to obtain plausible cross-sections at low impact energies [3]. In a 1972 paper Bowers and Elleman assumed that the polarizability of methane ( $2.6 \text{ \AA}^3$ ) and silane were equal for calculation of the limiting rates [26]. Another extant but nebulous value for silane's polarizability may be inferred as  $4.33 \cdot 10^{-24} \text{ cm}^3$  from the Langevin rate constants reported by Chatham *et al.* [7]. In short, the present definition of silane's polarizability is rather poor.

In a recent thesis Ralph Keeling has designed and built a very stable inter-ferometer for precise measurement of the oxygen mole fraction in air which exploits the refractivity ratio of nitrogen to oxygen at two wavelengths [4]. The experimental technique, which is also described in reference [5], infers the partial pressures of a two component gas mixture by exploiting their different, known refractive indices at 435.956 and 253.727 nanometers. Silane's refractive index can therefore be inferred from examination of silane mixed with another gas whose absolute refractivity is known. A 1:19 mixture of silane in helium was selected for study since the refractive index of helium is small and very well defined while that of silane is roughly 20 times larger. The use of a dilute mixture also simplified handling of the gas as concentrated silane mixtures are pyrophoric and produce sand in oxygenated pump oil.

Results of Keeling's measurements are summarized in table 6.1. The principal

$\lambda_{vac}$	$(1-n) \cdot 10^4$	error
4359.56 Å	8.49	$\pm 1\%$
2537.27 Å	9.80	$\pm 1\%$
$\frac{n_{2537}-1}{n_{4360}-1}$	$1.3131 \cdot 10^{-4}$	$\pm .02\%$

Table 6.1: Silane refractivity results.

source of uncertainty in the absolute refractive index measurements arises from the gas mixture tolerances. The gas was a gravimetric mixture with a certified composition of  $5.0\% \pm .05\%$  [9]. The ratio of the refractive indices, however, is independent of this error and is thus defined to within two parts in ten thousand.

The electronic polarizability is estimated from the measured refractivity through the Lorentz-Lorenz relation [14]:

$$\frac{4}{3}\pi N\alpha = \frac{n^2 - 1}{n^2 + 2}$$

where  $\alpha$ ,  $N$ , and  $n$  are the polarizability, number density, and refractive index, respectively. To obtain the infinite wavelength or d.c. polarizability from which Langevin's rates are calculated one must extrapolate the normal dispersion using the Cauchy form for the refractive index variation with frequency:

$$(n_\lambda^2 = n_\infty^2 + \frac{b}{\lambda^2})$$

Simple algebra leads to a value of  $4.62 \pm .10 \text{ \AA}^3$  for the d.c. polarizability of silane. The sources of uncertainty in this value are twofold. First, the  $\pm 1\%$  experimental uncertainty in the measured refractive indices propagated through the calculation of  $\alpha$  using the Cauchy and Lorentz-Lorenz relations is summarized in table 6.2. The second source of error is associated with the approximate form of the optical dispersion. The Cauchy form is valid only away from absorption resonances, a condition which is satisfied for the selected wavelengths [11, 12]. Also, the Cauchy expansion systematically underestimates  $\alpha$  by approximately one percent due to neglect of the contributions of nuclear motion, that is infrared absorption. Measurements at many frequencies would be desirable to better determine the legitimacy of the Cauchy expansion, however error associated with the infinite wavelength extrapolation is likely to be of the same order as the experimental error for the present data [6].

$\alpha$	8.41	8.49	8.57
9.70	4.59	4.66	4.73
9.80	4.56	4.62	4.70
9.90	4.53	4.60	4.67

Table 6.2: Error propagation in calculation of the d.c. polarizability from the refractive index data of Keeling using the Lorentz-Lorenz and Cauchy forms (see text). The refractive indices used labeled as  $10^4(1 - n)$  along the top and right side; the calculated polarizabilities are in units  $\text{\AA}^3$ .

Species	Basis	$\alpha_{\text{calc}} \text{\AA}^3$	$\alpha_{\text{expt}}$
He	6-31g**	.06	.205
Ne	6-31g**	.18	.396
Ar	6-31g**	.73	1.641
<i>SiH</i> <sub>4</sub>	6-31g**	3.18	4.62
<i>SiH</i> <sub>4</sub>	6-31++g**	3.60	4.62

Table 6.3: Calculated polarizabilities using Gaussian 86 with second order MP perturbation theory for electron correlation and the specified bases at the tetrahedral geometry (1.474  $\text{\AA}$  Si-H distance).

As a complement to the experimental measurements several *ab initio* calculations of silane's polarizability were performed. Using the Gaussian 86 [10] program package polarizabilities were obtained for silane at its equilibrium geometry with the results summarized in table 6.3. As one might expect the calculated polarizabilities using standard bases are ordered properly ( $\text{SiH}_4 > \text{Ar} > \text{Ne} > \text{He}$ ) but substantially underestimate the experimental values. More sophisticated calculations such as the complete active space studies of Siegbahn *et al.* come substantially closer to the experimental polarizabilities; these authors calculate neon's static polarizability to within 1% of the experimental value [15]. Interest in calculated polarizabilities stems not from systems for which  $\alpha$  is easily probed with experiment, but rather from species such as free radicals whose polarizabilities would be prohibitively difficult to measure. The polarizability of the  $\text{SiH}_2$  radical, for example, has been recently calculated using *ab initio* methods by Bauschlicher [16] and could serve as the basis for calculating a Langevin rate for reaction of ions with the radical.

Summarizing the results of this digression the literature values for silane's

polarizability, while plausible, are completely undocumented. The preferred value of  $4.62 \pm 10 \text{ \AA}^3$  has been inferred from careful refractive index measurements at 253 and 435 nm and Cauchy's form for optical dispersion in the measured region, far from any absorption features.

### 6.3 Silicon Hydride Cation Reactions

The effective potential energy of a singly charged ion and silane is

$$V(r) = \epsilon \frac{b^2}{r^2} - \frac{\alpha e^2}{2r^4}$$

where  $\epsilon$  is the relative kinetic energy at infinite separation and  $b$  is an impact parameter related to the pair's angular momentum  $L = 2mvb$  [13]. This effective potential is plotted for  $b = 0$  in figure 6.1. The Langevin rate, calculated with the polarizability presented in the last section, is  $5.0 \cdot 10^{-9} \frac{1}{\sqrt{\mu}} \text{ cm}^3 \text{ s}^{-1}$  where  $\mu$  is the reduced mass of the ion-silane collision pair in atomic mass units.

While early papers concerned with the mass spectrometry of silane [17] hinted at the charge transfer reactions which occur, the first quantitative work on the kinetics of these reactions appeared in 1972. In one of these reports Yu *et al.* examined the dependence of a magnetic sector mass spectrometer's ion signal as a function of ion source pressure up to .5 torr [19]. These authors also examined the reactions of each hydride cation with silane at collision energies in the 1-10 eV range using a tandem quadrupole mass spectrometer. The second key paper, by Henis *et al.*, employed conventional ion cyclotron resonance mass spectrometry to probe the  $\text{SiH}_n^+$  reactions with silane [20]. A summary of the results from these studies is presented in table 6.4.

No clear trends are apparent from the data in table 6.4. In order to better establish the role and mechanism of charge transfer in the silicon hydride ion silane reactions a series of pulsed ICR measurements were performed. In particular, the capability of forming an ensemble of a particular ion and unambiguously elucidating the kinetically preferred products was exploited to provide new qualitative insight into this class of reactions.

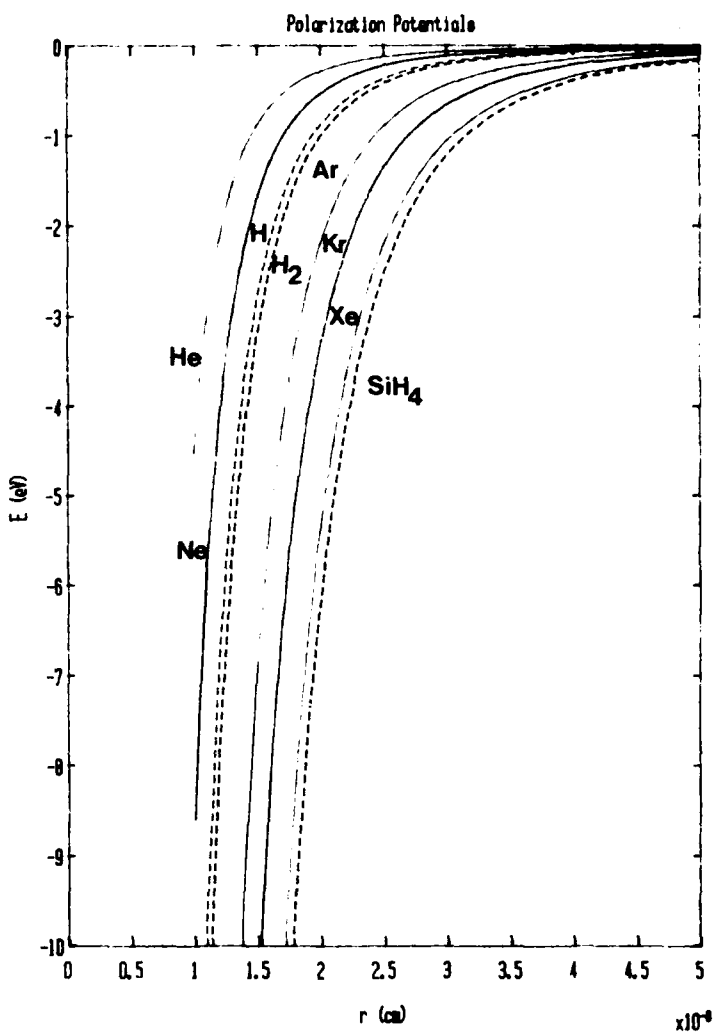
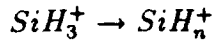


Figure 6.1: Calculated polarization potentials for interaction of various molecules with a point charge for head-on ( $b = 0$ ) collisions. For ( $b > 0$ ) the potentials have a centrifugal contribution  $V_{eff}(r) \propto \mu b^2 r^{-2} + V(r)$ .

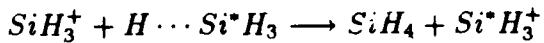
Reactant Ion	Product Ion	k (Yu)	k(Henis)
$SiH_3^+$	$SiH_3^+$	...	13.50
$SiH_3^+$	$Si_2H_5^+$	0.07	0.24
$SiH_3^+$	$Si_2H_3^+$	...	0.07
$SiH_2^+$	$SiH_3^+$	2.50	10.70
$SiH_2^+$	$Si_2H_5^+$	.08	...
$SiH_2^+$	$Si_2H_4^+$	1.10	2.50
$SiH_2^+$	$Si_2H_2^+$	.31	.55
$SiH^+$	$Si_2H_3^+$	2.00	2.80
$SiH^+$	$Si_2H_2^+$	0.30	...
$SiH^+$	$Si_2H^+$	...	0.70
$SiH^+$	$SiH_3^+$	0.60	...
$Si^+$	$Si_2H_3^+$	0.40	...
$Si^+$	$Si_2H_2^+$	3.20	4.80

Table 6.4: Dissociative charge transfer rates reported by Yu and Henis in units of  $10^{-10} cm^3 s^{-1}$ . Yu's data are from tandem quadrupole mass spectrometry (collision energy  $\approx 1 eV$ ) while those of Henis are from ICR experiments (collision energy  $\approx .02 eV$ .)

### 6.3.1 $SiH_3^+$ Reactions



Langevin's limiting rate for capture of  $SiH_3^+$  by silane is  $1.26 \cdot 10^{-9} cm^3 s^{-1}$ . The symmetric hydride transfer reaction:

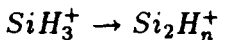


occurs with a near-Langevin rate as was demonstrated by the double resonance ICR experiments of Henis *et al.* (Their reported rate constant has an uncertainty of  $\pm 37\%$ .) These spectra showed that the ions of mass 32,  $^{29}SiH_3^+$  and  $^{30}SiH_2^+$ , arose from the interaction of species at both mass 30 and 31, that is  $SiH_3^+$  and  $SiH_2^+$ , with silane. It was suggested that the reactions involve hydride ion rather than hydrogen atom transfer [20]. Although no rate constant for the reaction is reported by Yu,  $SiD_3^+$  was observed as a product of the reaction between  $SiH_3^+$  and deuteriosilane [19].

Evidence supporting the hydride transfer mechanism was obtained in a simple pulsed ICR experiment. Figure 6.2 illustrates the fate of  $^{30}SiH_3^+$  after its collisions with silane, whose principal isotopic component (92%) is  $^{28}SiH_4$ . A sample of  $^{30}SiH_3^+$  was formed from electron impact on silane followed by resonance ejection of all of the other cations. Programmed delays between ion formation and excitation/detection evinced rapid decay of the  $^{30}SiH_3^+$  at  $m/e=33$  and the correlated emergence of the lighter trihydride cation isotope  $^{28}SiH_3^+$  at  $m/e=31$ . A mechanism in which a hydrogen atom is transferred from silane to yield an excited  $^{30}SiH_4^+$  which dissociates to either  $^{30}SiH_2^+$  or  $^{30}SiH_3^+$  is precluded by the results of figure 6.2.

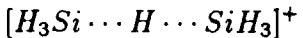
Hydride transfer is intuitively reasonable on the basis of *ab initio* electronic structure calculations which show that electron density is localized about silane's hydrogen atoms<sup>1</sup> and that its highest ( $t_2$ ) molecular orbital is involved in Si-H  $\sigma$  bonding. The approach of the planar  $SiH_3^+$  to silane permits favorable overlap between the empty p-orbital of the cation and electron-rich hydride ligands, with the result being a thermoneutral hydride transfer. This very rapid reaction has the important consequence that  $SiH_3^+$  which has acquired translational kinetic energy (from plasma electric fields for example) will be rapidly thermalized in the presence of silane gas.

<sup>1</sup>typical Mullikan overlap populations of 1.10-1.16 around H.



Both Yu and Henis agreed that the production of  $Si_2H_5^+$  is the second major channel for reaction of  $SiH_3^+$ . While it is plausibly claimed [20] that this reaction is exothermic only if the neutral product is molecular hydrogen, there is generally a tendency in the literature to overstate the reliability of thermochemical arguments in low pressure ion reaction experiments. Specifically, the internal vibrational and electronic energy of ions produced by electron impact may vary with electron energy, ionizer pressure and current, and ambient electric fields. Similarly, the internal energy and geometric isomer of the products are not rigorously known. The inference of formation enthalpies for reactants and products on the basis of appearance potential data is similarly suspect since potential energy surfaces of ions need not generally parallel those of the neutral molecule's ground state.

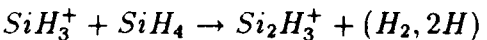
The mechanism of  $Si_2H_5^+$  formation may be viewed as a result of competition between the hydride transfer channel and insertion into a silicon hydrogen bond followed by  $H_2$  elimination from an ion-molecule complex:



If the complex were formed at the Langevin rate one would expect no dependence of the reaction rate on ion kinetic energy. It is not possible to say whether the factor of three difference between the rate constants of Yu and Henis are a result of different ion kinetic energies. The experiments of Yu were conducted with about 1eV of ion kinetic energy, while those of Henis involved reactant ions at roughly thermal energies.

The reactions of  $SiH_3^+$  with silane were examined at thermal energies using an earlier pulsed ICR experiment with 5% silane in argon [18]. The argon buffer enhances thermalization of the  $SiH_3^+$  ions formed by 15 eV electron impact prior to resonance ejection of all other ions. After a three second delay at a silane pressure of approximately  $10^{-7}$  torr<sup>2</sup> the only appreciable disilicon hydride ion observed was  $Si_2H_5^+$  (Figure 6.3). The observed conversion of  $SiH_3^+$  ( $.09s^{-1}$ ) implies a rate of  $\approx 3 \cdot 10^{-11} cm^3s^{-1}$ , in good agreement with Henis' value of  $2.4 \cdot 10^{-11} cm^3s^{-1}$ .

The other condensation reaction:




---

<sup>2</sup>uncorrected ionization gauge reading in a standard Nicolet FTMS-1000 instrument.

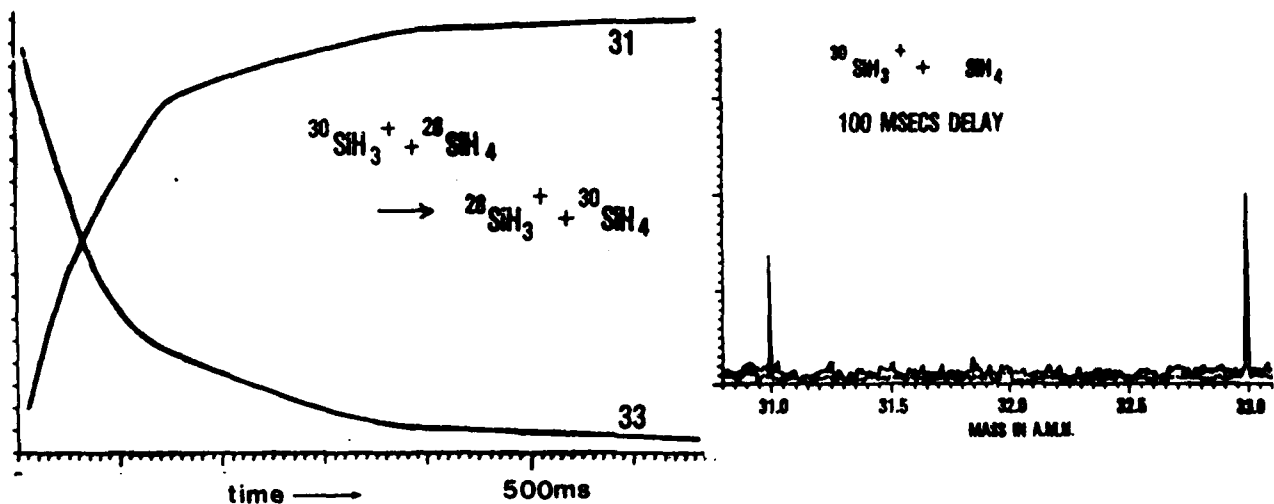
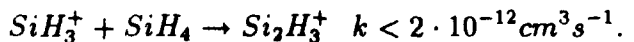
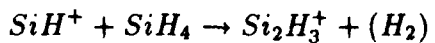


Figure 6.2: Reaction of  $^{30}\text{SiH}_3^+$  with silane.

should show a mass spectral peak at  $m/e=59$  which is 30% of that at  $m/e=61$  according to the relative rates for formation of  $\text{Si}_2\text{H}_5^+$  and  $\text{Si}_2\text{H}_3^+$  reported by Henis. Its very weak intensity in figure 6.3 implies that  $\text{Si}_2\text{H}_3^+$ , if formed by thermal collisions of  $\text{SiH}_3^+$  with silane, does so at a rate less than one twentieth of that which results in  $\text{Si}_2\text{H}_5^+$ :



Although few  $\text{SiH}^+$  ions were formed at 15 eV, production of  $\text{Si}_2\text{H}_3^+$  by the fast reaction:



during resonant ejection is precluded in the present experiments by the absence of  $m/e=29$  and 59 in the spectrum with no delay. Reactant ions were formed at higher electron energies (22 eV) and pressures ( $2 \cdot 10^{-6}$  torr) in the experiments of Henis *et al.*, which may account for their inference that this reaction is nearly as facile as that which forms  $\text{Si}_2\text{H}_5^+$ .

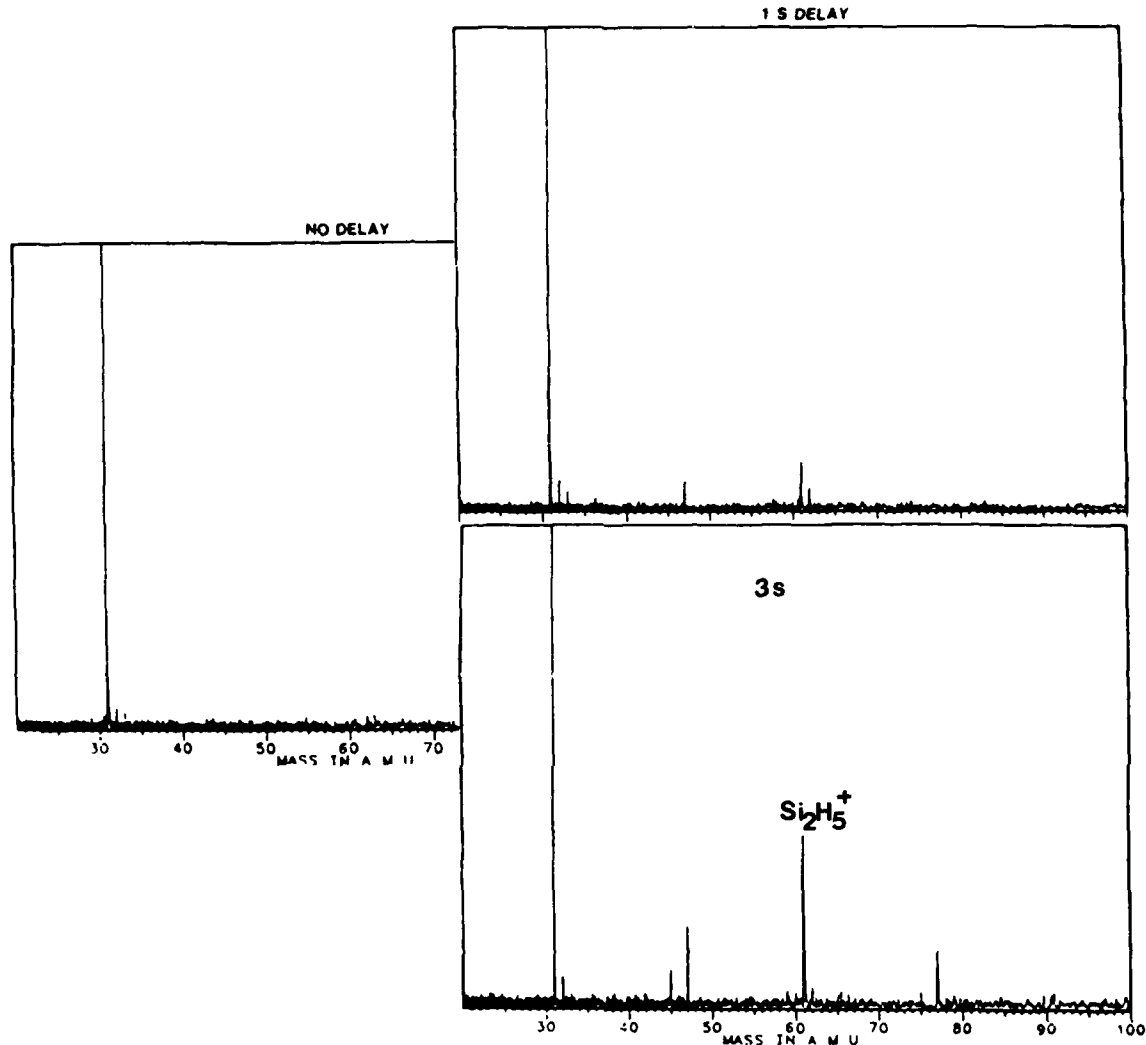
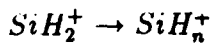


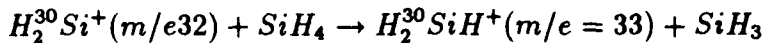
Figure 6.3: Reactions of  $^{28}\text{SiH}_3^+$  after one and three seconds comingling with  $2 \cdot 10^{-6}$  torr of 5% silane in argon. Reactant ions were formed by near-threshold electron impact with resonant ejection of  $\text{SiH}_2^+$ . Species at  $m/e=45, 47$ , and  $77$  are a consequence of background water vapor ( $p < 10^{-9}$  torr). The absence of a significant signal at  $m/e=59$  demonstrates the unimportance of the condensation product  $\text{Si}_2\text{H}_3^+$  at thermal energies.

### 6.3.2 $SiH_2^+$ Reactions



Reactions of  $SiH_2^+$  with silane are considerably more diverse than their trihydride counterparts. Its most rapid reaction results in the formation of  $SiH_3^+$  as observed both by Henis and Yu. Henis concluded that it was not possible to differentiate between hydride anion and hydrogen atom transfer based on his experimental data.

The reaction was therefore probed using pulsed ICR of the naturally abundant silicon isotopes. An ensemble of ions at  $m/e=32$  was formed by resonance ejection of all other species. Contributions from  $^{29}SiH_3^+$  and  $^{30}SiH_2^+$  were resolved. Introduction of a programmed delay yielded only  $^{28}SiH_3^+$ , as illustrated in figure 6.4. Hydrogen atom transfer from silane to the dihydride cation:



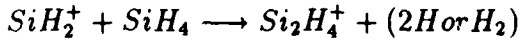
would result in correlated changes in the ion intensity at nominal  $m/e=33$ , which were not observed. Furthermore, the decay of the trihydride  $^{29}SiH_3^+$  and dihydride  $^{30}SiH_2^+$  ions occurred with comparable rates, as was confirmed by a similar study using only  $^{30}SiH_3^+$  as the reactant ion (figure 6.2). The conclusion from these experiments is that a hydrogen nucleus and two electrons:



are transferred to the reactant ion  $SiH_2^+$ .



In contrast to the analogous trihydride cation reaction the process:



is quite rapid. At thermal energies Henis reports this reaction accounts for between 6 and 22% of the  $SiH_2^+$  loss while Yu finds, at 1eV energy, that this process absorbs 30% of the available dihydride cations. Pulsed ICR experiments performed as part of the present work indicate a branching ratio for production of  $Si_2H_4^+$  of one third at thermal energies (Figure 6.5). The rate of  $Si_2H_2^+$  generation was observed to be one fifth that of  $Si_2H_4^+$  from the dihydride cation silane reaction, in accordance with the observations of Yu and Henis.

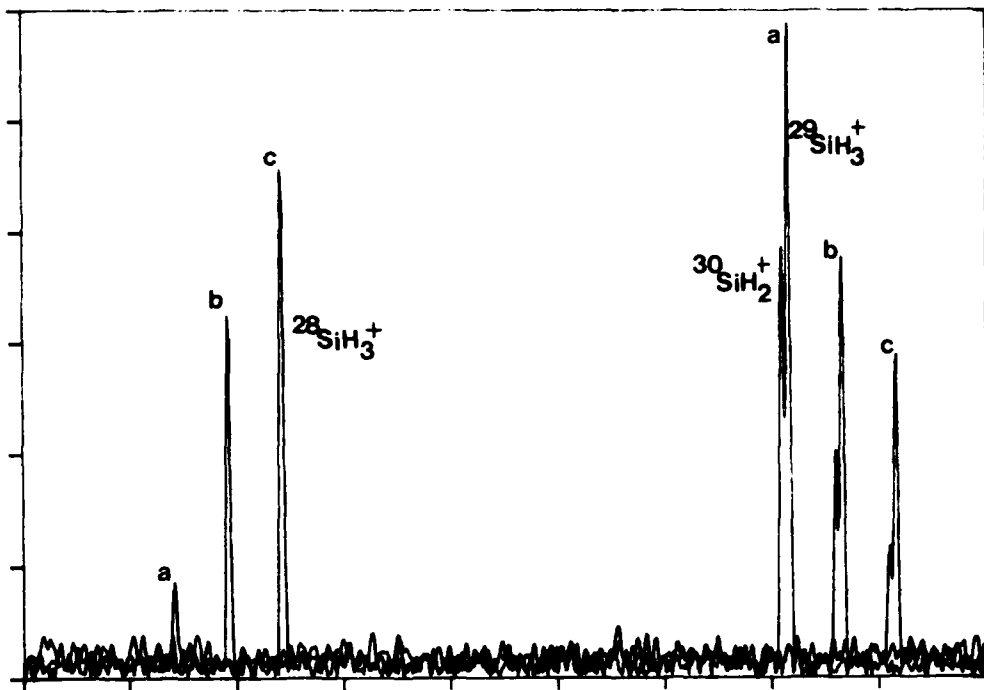


Figure 6.4: Hydride transfer from silane to  $^{29}\text{SiH}_3^+$  and  $^{30}\text{SiH}_2^+$ .

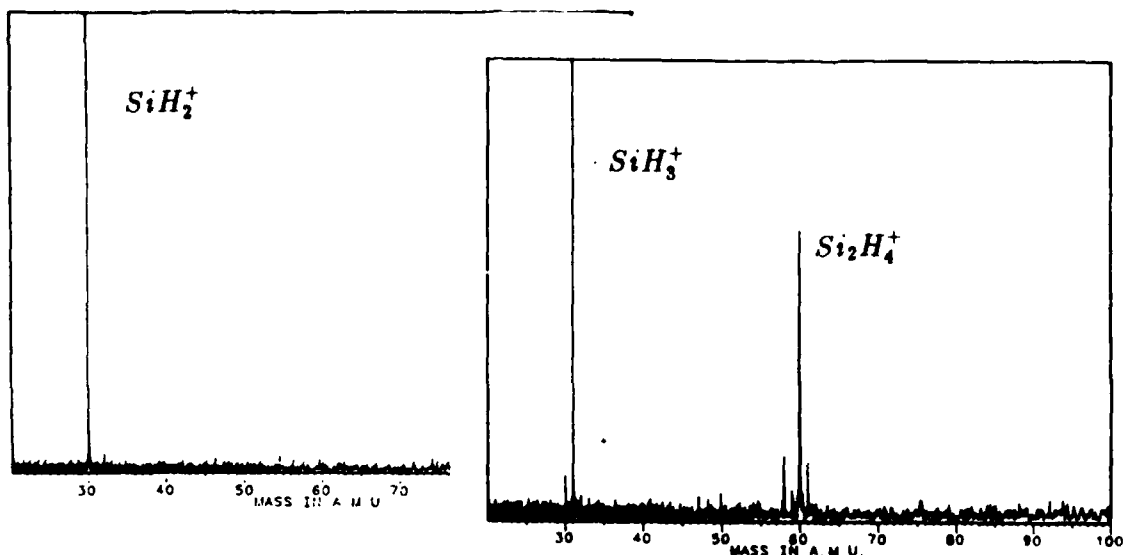
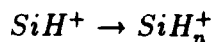
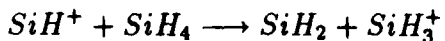


Figure 6.5: Branching of  $\text{SiH}_2^+$  + silane products observed from 18 eV electron impact in sample of 5% silane in helium.

### 6.3.3 $\text{SiH}^+$ Reactions



Although not observed by Henis, the hydride transfer reaction:



was observed to have one third the rate of the condensation reaction at 1 eV in the tandem experiments of Yu. Pulsed ICR measurements indicate that the hydride transfer reaction is more rapid than the condensation channels at thermal energies as illustrated in figure 6.6. The plotted spectrum is the point-by-point difference between the FTMS observations with and without a 100 millisecond delay between  $\text{SiH}^+$  formation and pulsed excitation-detection.

Estimates of thermochemistry associated with the hydride transfer reactions from silane to the  $\text{SiH}_n^+$  cations were obtained using *ab initio* electronic structure calculations whose results are summarized in table 6.5. Optimized geometries and frequencies from which zero point energies were calculated were performed using second order Möller Plesset perturbation theory and the 6-31g\*\* gaussian basis. Some authors empirically correct vibrational frequencies by arbitrary factors of

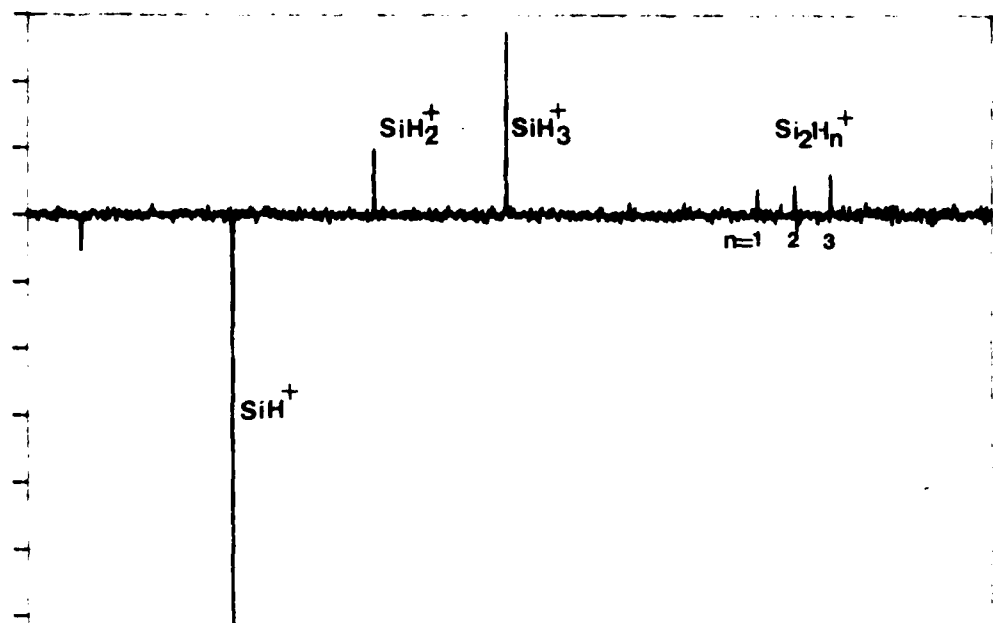


Figure 6.6: Difference mass spectrum resulting from  $\text{SiH}^+$  interaction with silane after a 100 millisecond delay at  $\approx 5 \cdot 10^{-8}$  torr of silane. The fastest reactions yield  $\text{SiH}_3^+$  and  $\text{SiH}_2^+$  rather than disilicon hydride cluster ions  $\text{Si}_2\text{H}_n^+ n = 1, 2, 3$ .

about 10%; no such correction has been applied here to retain validity of the description *ab initio*. Enthalpies were then calculated from the MP4/6-31g\*\* total energies obtained at the MP2/6-31g\*\* optimized geometry using MP2 frequency calculations to estimate the zero point energies.

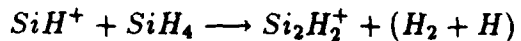
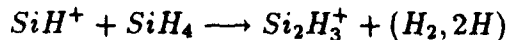
The failure of Henis to observe the hydride transfer to  $\text{SiH}^+$  is most probably a consequence of the relatively weak contribution of its ion to the double resonance spectrum of  $\text{SiH}_3^+$  compared to those of the  $\text{SiH}_2^+$  and  $\text{SiH}_3^+$  ions. Nevertheless the FTMS results demonstrate what the thermochemistry suggests: facile reactions which form  $\text{SiH}_3^+$  and  $\text{SiH}_2^+$ . Indeed the experiments show that these reactions must be significantly faster than the condensation reactions at thermal kinetic energies. The reactant ion was formed by 18 eV electron impact to prevent production of electronically excited  $\text{SiH}^+$ . Following resonance ejection of all other ions the principal products were observed to be  $\text{SiH}_3^+$  and  $\text{SiH}_2^+$ , that is net hydride ion and hydrogen atom transfer from silane, respectively.

Reactant Ion	Products	$\Delta H$ eV
$^1SiH_3^+$	$SiH_3^+, SiH_4$	0.00
$^2SiH_2^+$	$SiH_3^+, ^2SiH_3$	-0.03
$^1SiH^+$	$SiH_3^+, ^1SiH_2$	-1.23
$^1SiH^+$	$SiH_2^+, ^2SiH_3$	-0.35
$^2Si^+$	$SiH_3^+, ^2SiH$	+0.99
$^2Si^+$	$SiH_2^+, ^1SiH_2$	+1.72
$^2Si^+$	$SiH^+, ^2SiH_2$	+0.72

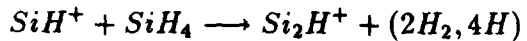
Table 6.5: Hydride transfer thermochemistry inferred from *ab initio* electronic structure calculations. Calculations apply to the ground electronic and vibrational states of all species. Superscripts refer to the spin multiplicity of the ground states.



The condensation reactions:

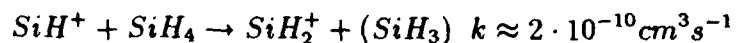


and

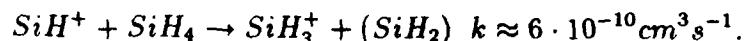


were reported by either Yu or Henis. All three reactions were also observed in the pulsed ICR spectra of figure 6.6 but at rates much slower than the hydride transfer reactions. Note that the most rapid clustering reaction yields an unsaturated product,  $Si_2H_3^+$  with loss of two hydrogens, although it is not possible to say experimentally whether these depart as atoms or a molecule.

The reported rates for  $Si_2H_n^+$  formation can be used with the relative intensities from the ICR results to estimate the rate of the hydride transfer reactions:



and



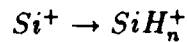
Note that the total rate for  $SiH^+$  loss by these two reactions is almost two thirds of the Langevin limiting rate,  $1.3 \cdot 10^{-9} \text{ cm}^3 \text{s}^{-1}$ . The present data support

Reactant	Products	$\Delta H(\text{eV})$
$^4\text{Si}^+$	$^1\text{SiH}_3^+$ , $^2\text{SiH}$	-3.93
$^4\text{Si}^+$	$^2\text{SiH}_2^+$ , $^1\text{SiH}_2$	-3.21
$^4\text{Si}^+$	$^1\text{SiH}_2^+$ , $^2\text{SiH}_2$	-1.99

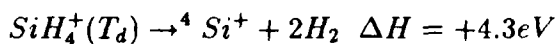
Table 6.6: *Ab initio* enthalpies for reaction of the quartet atomic silicon ion with silane correlated with the lowest energy  $\text{SiH}_n^+$  products. The production of higher spin multiplicity products is also possible.

the conclusion that reactions of  $\text{SiH}^+$  result in both mono and disilicon hydride cations, with the former being kinetically preferred; sixty percent of the reacted  $\text{SiH}^+$  fails to form new silicon-silicon bonds. Taken together these two classes of reactions consume  $\text{SiH}^+$  at nearly the Langevin limiting rate.

### 6.3.4 $\text{Si}^+$ Reactions



The difference mass spectrum for reaction of the atomic silicon ion with silane is shown in figure 6.7. As was the case for the reactions of  $\text{SiH}^+$  the formation of monosilicon hydride product ions is evident. However the calculated thermodynamics suggests that each of these reactions is endothermic. The enthalpies presented in table 6.5 were for reactant ions in their ground electronic and spin states. The calculated energy separation of the ground and  $^4P$  ion states is 4.91 eV using the 6-31g\*\* basis and MP4 correlation estimates. From the same calculations the enthalpy change for the process:



suggests that this ion is formed only by impact of electrons with energy above 15.3 eV. The relatively small cross-section for generation of  $\text{Si}^+$  near threshold required use of electron energies above this value for production of ample atomic ion. The ions produced in the experiments of Yu and Henis also were formed well above threshold. It is therefore not possible, on the basis of the present data, to determine which spin state of atomic silicon cation is undergoing reaction. However the calculated thermochemistry supports the idea that some  $^4\text{Si}^+$  is involved in production of  $\text{SiH}_n^+$ , as summarized in table 6.6.

The reaction of  $\text{Si}^+$  with silane also yields  $\text{Si}_2\text{H}_2^+$  as reported by both Yu and Henis. Traces of  $\text{Si}_2\text{H}_3^+$  are apparent in the difference mass spectrum, however

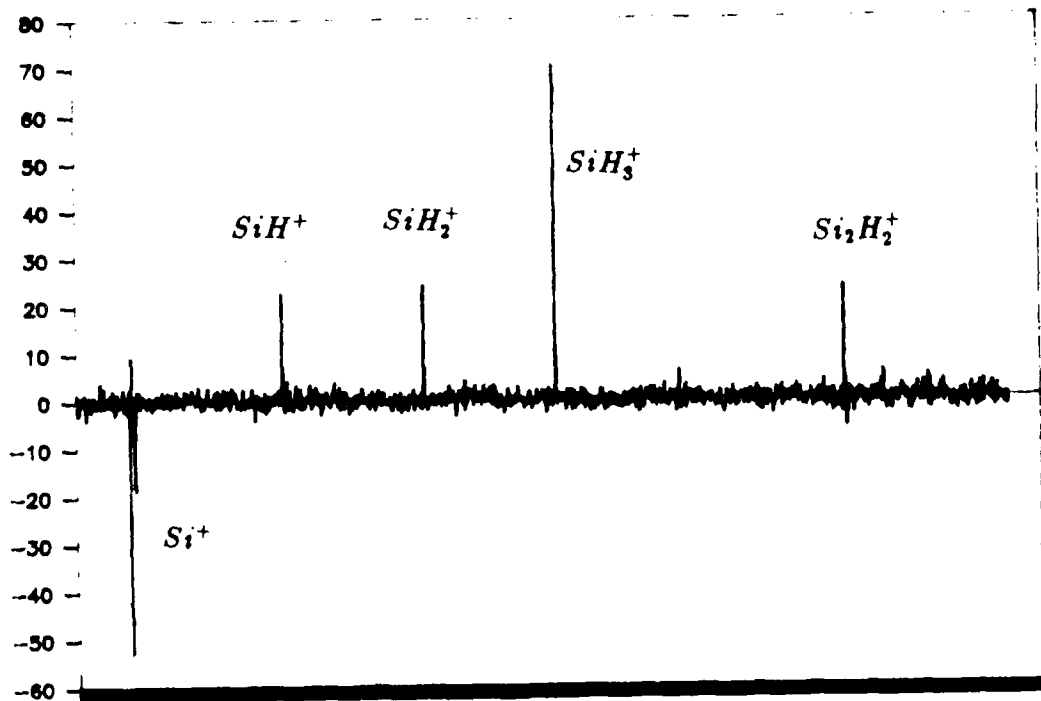
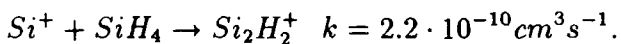
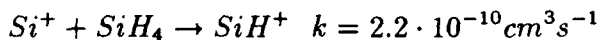
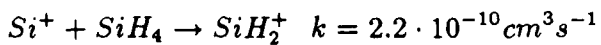
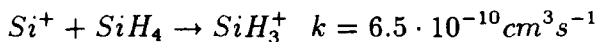


Figure 6.7: Difference mass spectrum of  $Si^+$  with and without a 100 ms delay between ion formation and excitation/detection.

the rapid formation of  $SiH^+$  makes it difficult to unambiguously correlate this ion with the reactant  $Si^+$ . As was the case for the quartet atomic ion, the excited  $4p^2P$  state of  $Si^+$  produced by electron impact is not prevented from hydride abstraction on thermodynamic grounds. However the cross-section for its formation from silane by electron impact is less than  $10^{-19} cm^2$  below 70 volts, which is three orders of magnitude less than the total  $Si^+$  formation cross-section [22].

Assuming that the total reaction rate of  $Si^+$  is equal to the Langevin value,  $1.3 \cdot 10^{-9} cm^3 s^{-1}$ , an estimate of the rates at which each product is formed is possible using observed branching ratios:



While this approach leads to a value for the production of new silicon-silicon bonds which is somewhat below that of Yu, Henis, and the very recent reports of Mandich [29], the present results were obtained under rigorously single collision conditions. The dissociation modes of the ion-silane complex, ( $Si \cdots SiH_4^+$ ), are expected to favor the monosilicon hydride products in the absence of collisional stabilization, since the line-of-centers kinetic energy obtained from the polarization potential is correlated with the Si-Si vibrational motion.

### 6.3.5 Summary of $SiH_n^+$ reactions.

The silicon hydride ions formed by dissociative ionization of silane are extremely reactive towards their parent molecule. While several papers on the kinetics of these reactions have appeared, no systematic explanation for the reported reactivity trends has emerged. This is in no small part due to the difficulties associated with handling silane, since it irreversibly effects ionizer filaments by the deposition of thin silicon films. As a pyrophoric compound it has a proclivity for production of undesirable silicon oxides in partially oxygenated vacuum pump oil. In addition, the near-Langevin rates which, it has been shown, characterize these reactions make it difficult to establish reactant-product correlations. Even at silane pressures of  $2 \cdot 10^{-6}$  torr the e-folding time for of an ion reacting at the Langevin rate is only 7 milliseconds.

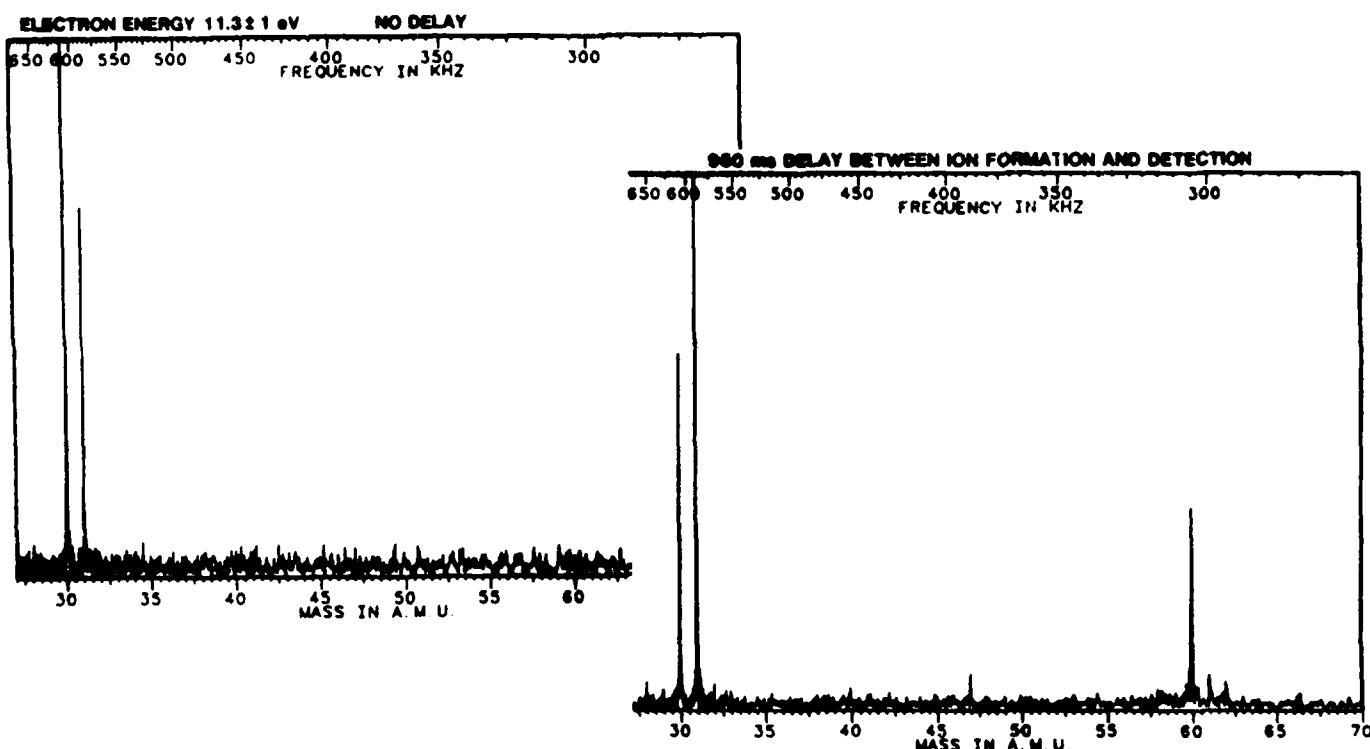
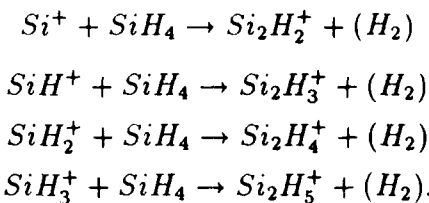


Figure 6.8: Evolution of  $SiH_3^+$  and  $SiH_2^+$  in 5% silane: argon. The nascent ion species distribution evolves rapidly to one dominated by  $SiH_3^+$  and  $Si_2H_4^+$ .

None of the mass spectrometry studies of these reactions, including the present work, identifies the vibrational or electronic state of the reactant ion. Neither is the conformation of the disilicon hydride clusters experimentally measured. Given these problems, of what use are rate constants with three significant figures of accuracy? The approach in the present work has been to probe the reactions of those ions formed by electron impact as close to the threshold for their formation by dissociative ionization as possible, since such are the conditions under which ions are most commonly formed in low pressure plasmas. One summary of the results is illustrated in figure 6.8, in which the temporal evolution of the  $SiH_2^+$  and  $SiH_3^+$  formed by near threshold electrons (no resonant ejection) is mapped. The trihydride reacts only slowly to form  $Si_2H_5^+$ . Three eighths of the dihydride cation forms  $Si_2H_4^+$ , while the remainder is bottled up by hydride transfer in  $SiH_3^+$ .

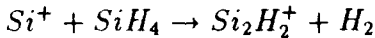
As the electron energy is increased, the possibility of forming  $Si^+$  and  $SiH^+$  in significant quantities arises. They are formed at slower rates than  $SiH_2^+$  and  $SiH_3^+$  according to chapter five, and approximately 80% of these ions yield  $SiH_3^+$  after only two Langevin collision times. However the remaining 20% include ions which are sufficiently unsaturated to continue reacting with silane. The general proclivity with which the relatively unreactive  $SiH_3^+$  is formed by reaction of silane's with  $SiH_n^+$  is a new result. It has important consequences for the evolution of the nascent ion species distribution to be described in chapter eight.

The second general observation on these reactions is that disilicon hydride cation formation is preferred for conditions which result in loss of two hydrogen atoms. It seems plausible but is unproven that this loss is as a hydrogen molecule. The fastest clustering reactions for each of the  $SiH_n^+$  ions have been shown to be:

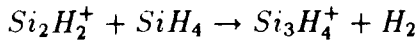


These products bear no obvious relationship to the ion spectrum produced by electron impact on disilane (Figure 6.9.) It is interesting to note that no monosilicon-hydride ion products were observed in the dissociative ionization of disilane, despite the fact that the silicon-silicon bonds are putatively weaker than their silicon-hydrogen counterparts [27]. The qualitative kinetic data presented in this section illustrate the competition between hydride transfer, resulting in  $SiH_3^+$ , and insertion of the ion into the silicon-hydrogen bond of silane followed by elimination of molecular  $H_2$  from the complex. More quantitative examination of this mechanistic competition using deuterated silane, disilane, and selected waveform inverse fourier transform resonance ejection are planned as a series of future experiments.

In the February 1988 issue of the *Journal of Chemical Physics* two articles on the reactions of  $Si^+$  with  $SiD_4$  appeared. The first of these, by Raghavachari [30], describes some *ab initio* calculations for the reaction



and subsequent insertion of the unsaturated products into silane:



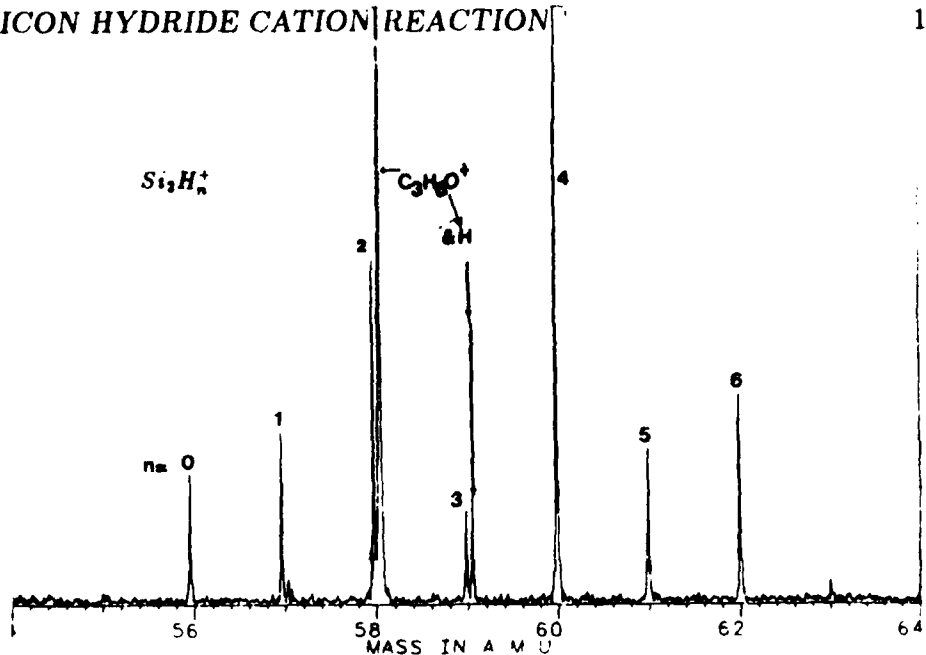
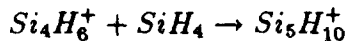
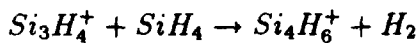


Figure 6.9: 25 eV electron impact mass spectrum of disilane. The right-hand isotopic peaks at  $m/e$  58 and 59 are from background acetone in the vacuum system. The relative peak intensities are roughly independent of electron energy above 20 volts.



The second paper, by Mandich *et al.* [29], reports some FTMS measurements of these reactions studied with  $^{29}Si^+$  generated from a pulsed, laser-initiated plasma and  $SiD_4$  as the neutral reagent. The first three steps, leading to  $Si_4D_6^+$ , are relatively rapid. However a kinetic bottleneck was identified with the formation of the  $Si_5H_{10}^+$  ion, which has a calculated geometry which restricts elimination of molecular hydrogen:  $(SiH_3)_3SiH^+$ .

Each of the  $SiH_n^+$  ions formed by electron impact below twenty volts react at nearly Langevin rates. A simple flow chart which illustrates the fate of the various ions as they interact with silane for the first few Langevin periods is shown in figure 6.10. Application of these data is straightforward, for example at a silane pressure of 10 millitorr the Langevin period is about 2 microseconds. After six microseconds 62% of the  $SiH_2^+$ , 79% of the  $SiH^+$  and 77% of the  $Si^+$  will have reacted to form the  $SiH_3^+$  cation. Those ions whose fate is not to become  $SiH_3^+$

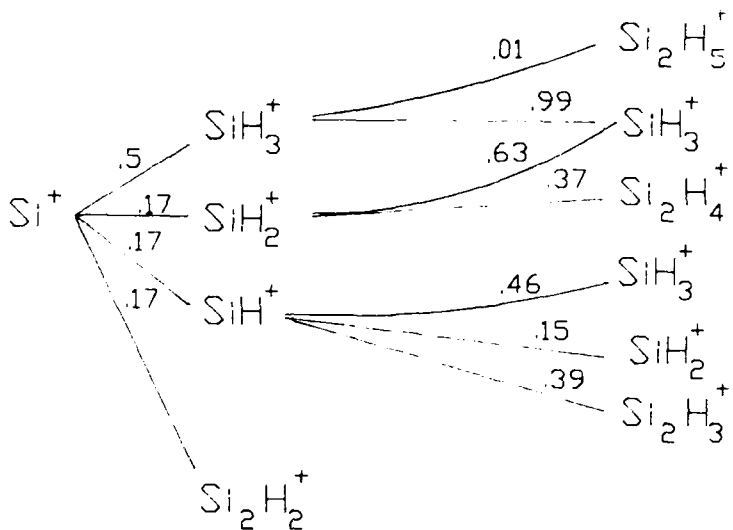
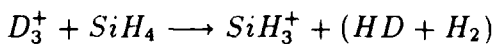


Figure 6.10: Flow chart illustrating the fate of  $\text{SiH}_n^+$  in their reactions with silane. The statistical fate of each ion per Langevin collision with silane is indicated above each channel.

form ions with new silicon-silicon bonds, some of which are sufficiently reactive to insert again into silane.

## 6.4 $\text{H}_3^+$ Reaction

The reaction of  $\text{H}_3^+$  with silane is analogous in many ways to the other hydride abstraction reactions. The very rapid process:



was first examined by Allen *et al.* in 1977 using tandem quadrupole mass spectrometry. At 1eV in the center of mass frame the cross-section for this reaction was observed to be  $34 \text{ \AA}^2$ , which implies a near-Langevin reaction rate. In order to examine the reaction of thermal  $\text{H}_3^+$  with silane several experiments using pulsed ion cyclotron resonance mass spectrometry were performed. The selectivity for production of  $\text{SiH}_3^+$  by this reaction is really quite remarkable. Figure 6.11 demonstrates the absence of hydrogen scrambling in the reaction of  $\text{D}_3^+$  with

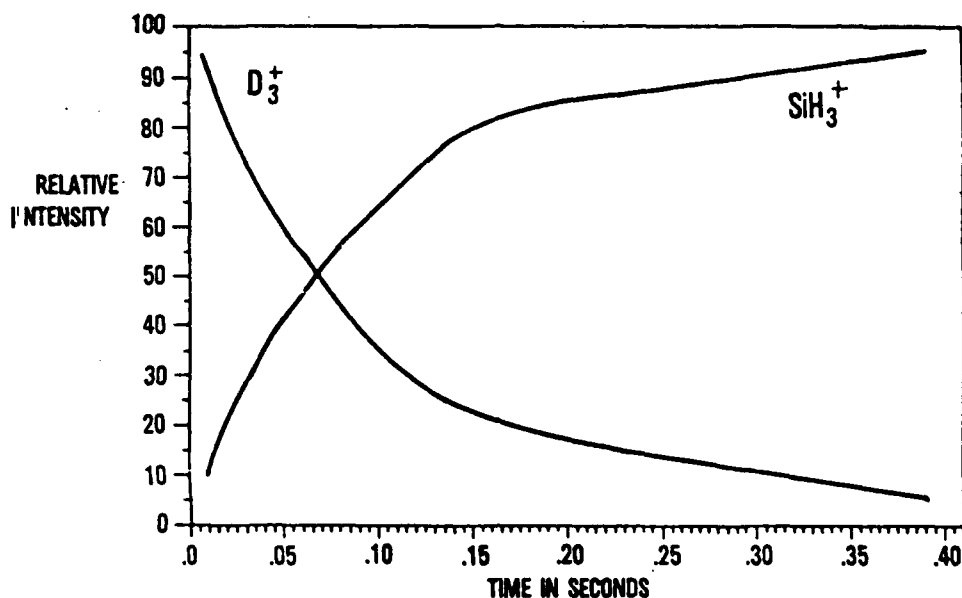
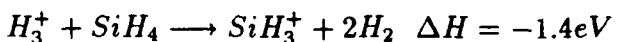


Figure 6.11: Reaction of  $D_3^+$  with silane. The absence of deuterated silicon hydride cations in the product mass spectrum demonstrates hydride transfer is preferred to elimination of  $H_2$  from an ion complex.

silane.  $H_3^+$  (or  $D_3^+$ ) is formed at low pressures by the reaction of the molecular  $H_2^+$  ( $D_2^+$ ) ion with the corresponding neutral at low, ( $10^{-7}$  torr), pressures. While the vibrational state of the trihydrogen cation is not measured in these experiments, hydride transfer from silane is exothermic even for the ground vibrational state of  $H_3^+$ .

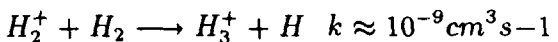
The enthalpy of reaction can be estimated from the careful *ab initio* studies of  $H_3^+$  by Michels [24]:



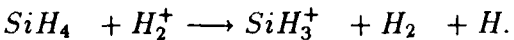
where the reactants and products are assumed to be in their vibrational ground states. Extension of the thermochemistry to vibrationally excited reactants is straightforward; the vibrational spacing in  $H_3^+$  is about .39 eV [25].

From a molecular orbital point of view the  $H_3^+$  ion is remarkably similar to  $SiH_3^+$ . Both reactant ions have  $D_{3h}$  symmetry and positive character (electron density deficiency) along the  $C_3$  symmetry axis. Of course the  $H_3^+$  reaction coordinate is asymmetric in enthalpy and entropy, so that the sign of the free energy change for the reaction is unambiguously negative.

There were two motivations for having a look at this reaction. First, hydrogen is sometimes chosen as a buffer gas in silane deposition plasmas. Even if hydrogen is not a chosen reagent, dissociation of silane in the reactor generates roughly two equivalents of hydrogen gas per silane (some is incorporated into the growing film). The fate of hydrogen molecular ions formed in a hydrogen:silane mixture is illustrated in figure 6.12. Rapid conversion to  $H_3^+$  by the reaction



is followed by hydride transfer from silane to yield an overall transformation:



Maintenance of plasma conductivity under conditions which generate lots of  $H_2^+$  (e.g. beam ionization, high  $[H_2]$ ) will therefore limit formation of polysilicon hydride cation clusters by channeling charged particles into the  $SiH_3^+$  reaction pathway. Second, the extreme selectivity for hydride transfer from silane in this reaction provides a critical test of the quantum chemistry paradigm for silane ion-molecule reactions that forms the topic of chapter 7.

## 6.5 Noble-Gas Ion Reactions

Reactions of noble-gas ions with silane are of engineering importance since most deposition reactors operate with noble buffer gases. In particular He and Ar are often used with silane in the production of silicon films by glow discharges. While noble buffers facilitate handling of pyrophoric silane, no chemical role for these 'inert' species has been proposed. On a more fundamental level one's understanding of the reactivity trend down the eighth period, where chemical and physical properties such as mass, ionization potential, and polarizability vary monotonically, provides a test of paradigms for dissociative charge transfer.

The noble-gas ion reactions with silane were first examined by Bowers and Elleman using conventional ICR experiments in 1972 [26]. Total reaction rates for depletion of the ions of He, Ne, Ar, Kr, and Xe were reported without observation of the product silicon hydride ions and are summarized in table 6.7. The only other earlier work on these reactions was reported by Chatham *et al.* in 1983. Rate coefficients for the reactions of helium, neon, and argon cations with silane were examined with a drift tube:quadrupole mass spectrometer apparatus [7]. The rate constants were found to be independant of collision energy over the

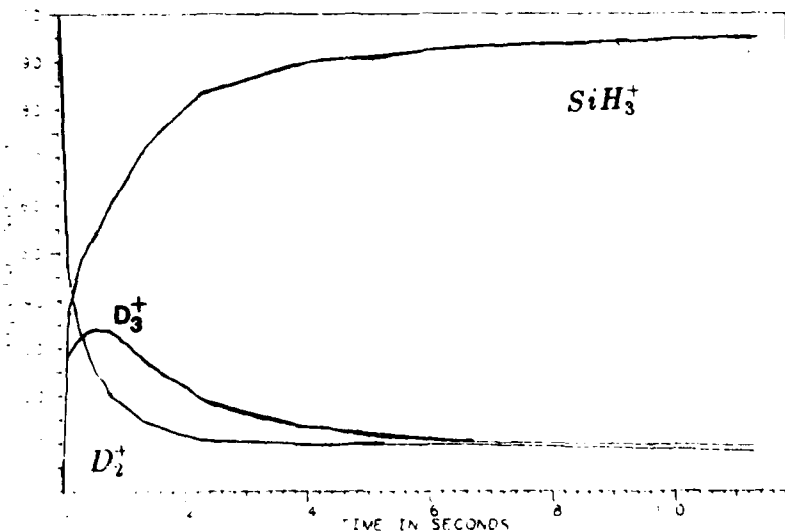


Figure 6.12: Reactions of  $D_2^+$  in a  $D_2$  silane mixture. The end result is conversion to  $SiH_3^+$  with a very short time constant.

range from .01 to 1 eV in the center of mass frame, as suggested by the form of the Langevin rate. However the ratio of the observed reaction rates to Langevin's limiting value varied remarkably from He to Ar. Table 6.7 summarizes their results.

Classically these ions all approach silane along the same potential energy surface. In each case electron transfer to the noble-gas is strongly favored on thermodynamic grounds. In order to probe this reactivity trend a series of pulsed ICR experiments was undertaken to examine in detail the thermal rate constants and product distributions for each of the noble-gas cation silane reactions.

### 6.5.1 $He^+$ Reactions

The total rates for  $He^+$  neutralization by silane reported both by Chatham and Bowers are in plausible agreement and within 20% of the Langevin rate. The products of reaction found by Chatham *et al.* were in descending order  $Si^+$ ,  $H^+$ ,  $SiH^+$ , and  $SiH_2^+$ .

Pulsed ICR spectrometry of helium:silane mixtures requires operation at low magnetic field to bring the  $He^+$  cyclotron frequency into the bandwidth of the

Reagent Ion	$k_{Chatham}$	$k_{Bowers}$	$k_L$
He	2.4	2.18	2.65
Ne	0.85	0.85	1.41
Ar	0.017	0.10	1.18
Kr	...	0.85	1.03
Xe	...	0.84	0.99

Table 6.7: Total charge transfer rate constants for rare gas ion reactions with silane reported by Chatham, Bowers, and calculated from Langevin's expression using the measured polarizability.

excitation and detection electronics. A steady flow of helium was passed through the spectrometer at a pressure of  $\approx 10^{-7}$  torr. The silane reagent pressure was calibrated using pulsed valves and the spinning rotor gauge as described in chapter 2.  $He^+$  ions were formed in their ground electronic state by 35 volt electron impact and all other ions were swept from the cell by resonance ejection. Programmed delays between ion formation and detection were then introduced to permit examination of the temporal evolution of the reactant and product ions which is summarized in figure 6.13. Rate constants are calculated from the decay of the parent ion as shown in figure 6.14, and product species are observed *in situ*. The total rate of charge transfer observed is  $1.6(\pm 0.2) \cdot 10^{-9} cm^3 s^{-1}$  with the partitioning among charged products,  $Si^+$  and  $SiH^+$ , of about 2:1. No proton production was observed, nor was the  $H_2^+$  cation in evidence in these experiments. Trapping potentials of as much as ten volts failed to yield evidence of either of these species by  $He^+$  charge transfer, in contrast to the conclusions of Chatham *et al.*

### 6.5.2 $Ne^+$ Reactions

Chatham observed the same products for the  $Ne^+$  reaction as were found for the  $He^+$  charge transfer process, but with a different ordering at low collision energies:  $SiH^+ > H^+ > Si^+ >> SiH_2^+$ . The total charge transfer rates of Chatham and Bowers are in remarkable agreement at  $8.5 \cdot 10^{-10} cm^3 s^{-1}$ .

Pulsed ICR measurements for the neon ion reaction were performed as described in the last section. The dominance of  $SiH^+$  over  $Si^+$  was confirmed, although again no evidence for direct production of the other ionic products  $H_n^+$ ,  $SiH_3^+$ , or  $SiH_2^+$  was observed. A total charge transfer rate of  $6.7(\pm 2.0) \cdot$

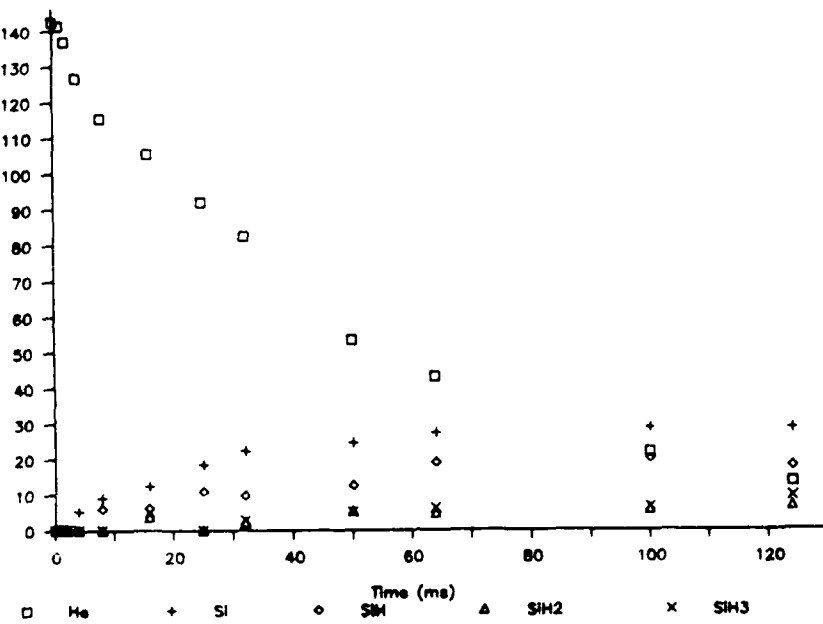


Figure 6.13: Products of the  $\text{He}^+ + \text{SiH}_4$  reaction.  $\text{Si}^+$  and  $\text{SiH}^+$  are the kinetic products. The formation of  $\text{SiH}_2^+$  and  $\text{SiH}_3^+$  is largely, if not totally, due to further reaction of  $\text{Si}^+$  and  $\text{SiH}^+$ . The e-folding time for their reactions with this silane pressure is  $\approx 50\text{ms}$ .

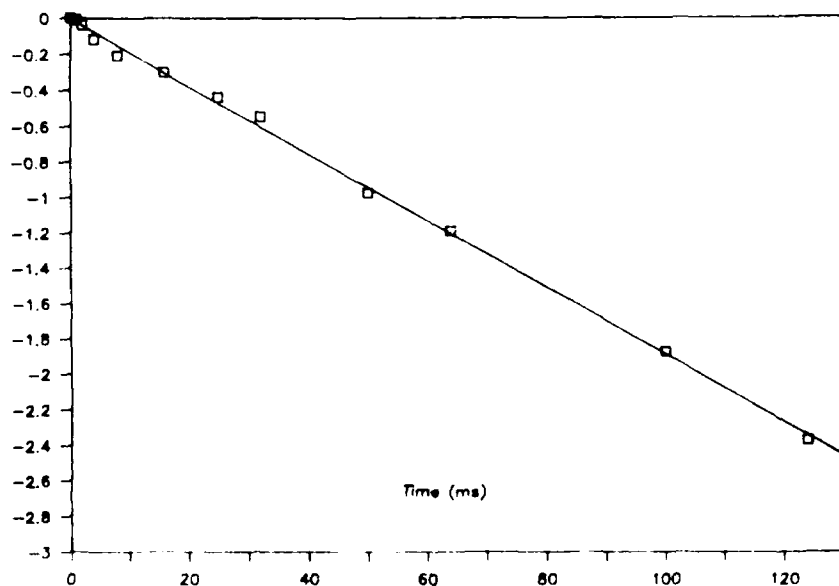


Figure 6.14: Plot of  $d \ln[\text{He}^+]/dt$  as a consequence of its reaction with silane.

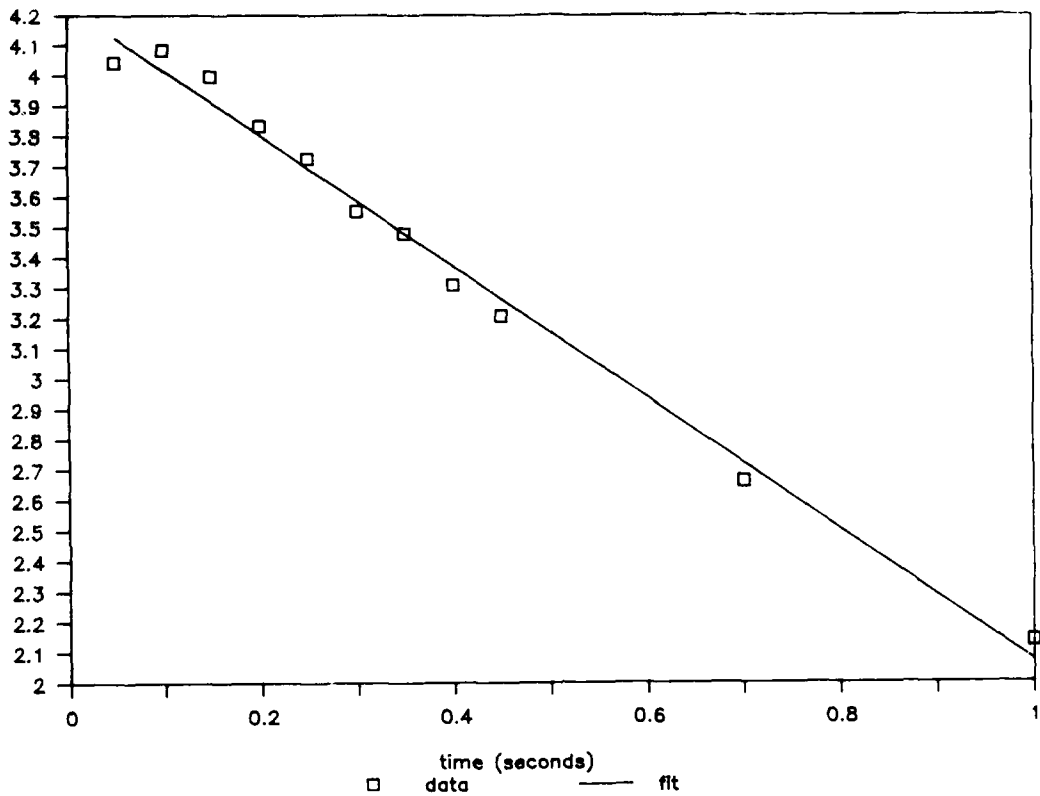


Figure 6.15: Semilog plot of  $Ne^+$  versus interaction time with  $1(\pm.3) \cdot 10^{-7}$  torr silane observed by pulsed ICR mass spectrometry. Inset is the difference mass spectrum between zero and 50 ms reaction time.

$10^{-10} cm^3 s^{-1}$  was obtained, a value which agrees with the earlier work within the combined experimental errors. Figure 6.15 summarizes the experimental data for the neon ion dissociative charge transfer reaction.

### 6.5.3 $Ar^+$ Reactions

Both Chatham and Bowers have found that the reaction of  $Ar^+$  with silane occurs at substantially less than the Langevin rate. The tentative product distribution reported by Chatham found  $Si^+ > SiH^+ > SiH_3^+ > SiH_2^+$ . Pulsed ICR measurements of the reaction of thermal  $Ar^+$  with silane clearly show that the charge transfer proceeds exclusively into  $SiH_3^+$ . The observed rate is  $8.0(\pm 2.7) \cdot 10^{-11} cm^3 s^{-1}$ , in good agreement with the earlier ICR measurement of Bowers.

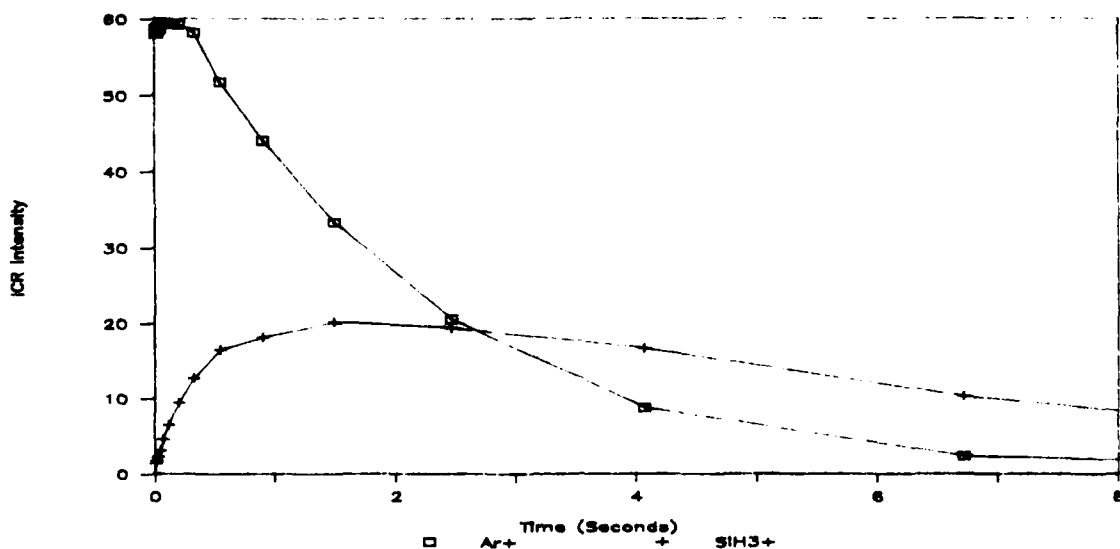
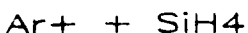


Figure 6.16:  $\text{Ar}^+$  reaction with silane as observed by FTMS. The product  $\text{SiH}_3^+$  reacts only slowly with silane to yield  $\text{Si}_2\text{H}_5^+$  (not shown).

As illustrated in figure 6.16, no species other than  $\text{SiH}_3^+$  were observed in the product ion mass spectrum.

#### 6.5.4 $\text{Kr}^+$ Reactions

Examination of the krypton ion reaction was motivated by the quest for a trend down the noble-gas period. No obvious trend emerges, since the rate of charge transfer to the krypton ion returns to nearly the Langevin limiting value. Although this reaction was not probed by Chatham, the rate reported by Bowers,  $8.5 \cdot 10^{-10} \text{ cm}^3 \text{s}^{-1}$  is just below the presently observed value of  $1.2(\pm .35) \cdot 10^{-9}$  and equal to the Langevin value within experimental error. Although thermodynamically accessible, neither  $\text{Si}^+$ ,  $\text{SiH}_2^+$  nor  $\text{SiH}^+$  were observed as products of this reaction. (Figure 6.17) shows the first order decay of the noble ion and the observed product,  $\text{SiH}_3^+$ .

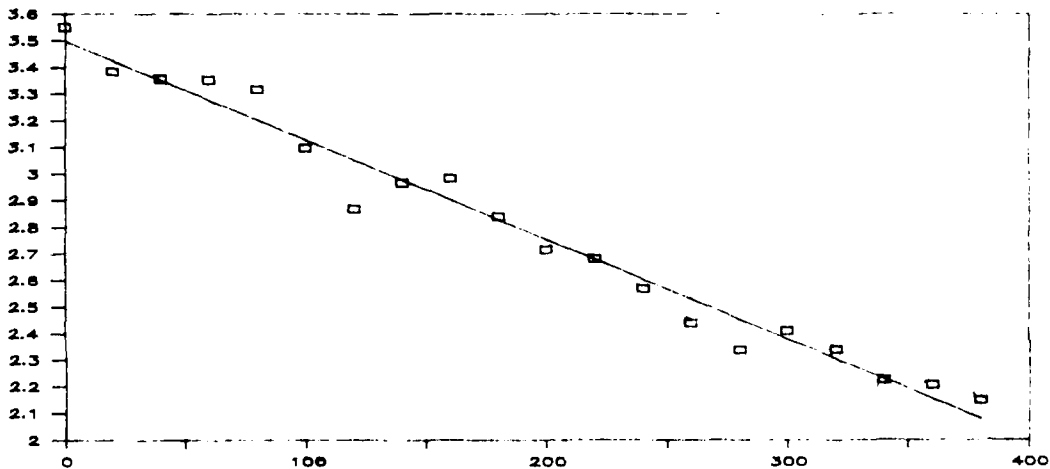
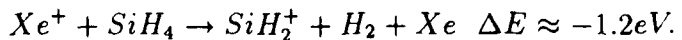
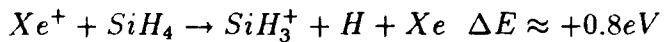


Figure 6.17: Semilog plot of  $Kr^+$  decay under the same conditions as were reported for the neon and argon reactions. Only  $SiH_3^+$  is observed in the product mass spectrum.

### 6.5.5 $Xe^+$ Reactions

The reaction of the xenon ion provides an especially interesting result. The total rate of xenon ion neutralization by silane obtained by FTMS is  $5.1 \cdot 10^{-10} cm^3 s^{-1}$ , which is within the combined error of this and Bowers' rates and roughly half of the Langevin limiting value. Unlike the krypton and argon ion reactions, the principal product was  $SiH_2^+$  (Figure 6.18). The fact that the appearance potential of  $SiH_3^+$  from silane exceeds the ionization potential of Xe may account for the failure to form the trihydride cation. Using the average experimental appearance potentials from chapter 3 one estimate of the energetics can be formed:



Evidence of branching to a bound complex containing silicon and the noble-gas was also obtained, but not under sufficiently reproducible conditions to warrant extensive discussion. The mass spectrum corresponding to a mixture of

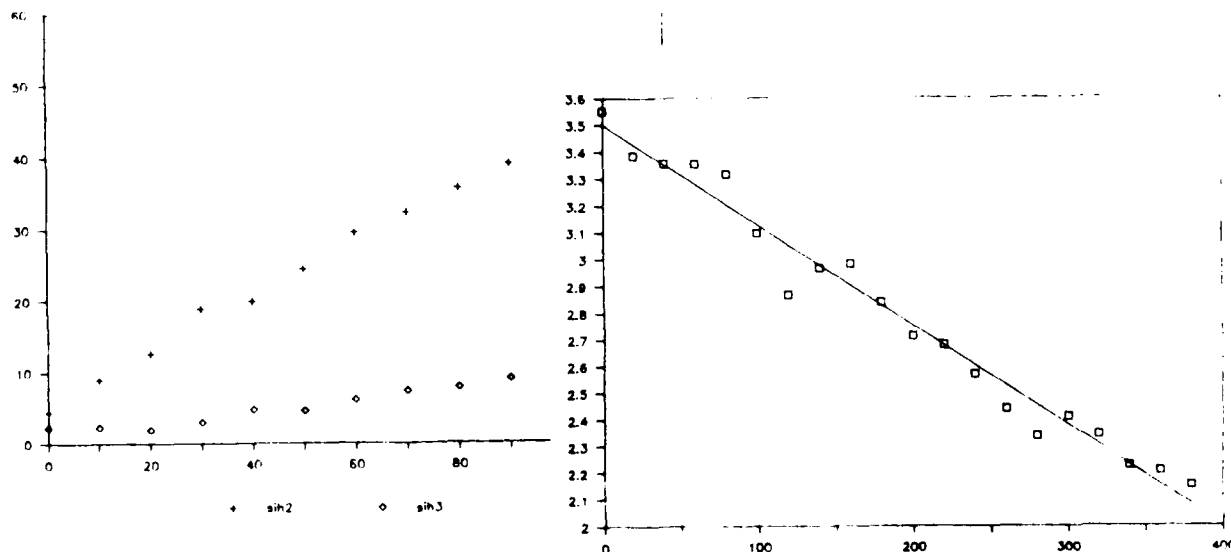


Figure 6.18:  $Xe^+$  reaction with silane showing the evolution of  $\text{SiH}_n^+$  for  $n = 2, 3$ . Most, if not all, of the trihydride may be accounted for by the rapid hydride transfer from silane to  $\text{SiH}_2^+$ .

the species  $Xe\text{SiH}_2^+$  and  $Xe\text{SiH}_3^+$ , and an integrated intensity of a few percent relative to that of the monosilicon hydride product (Figure 6.19).

## 6.6 Conclusions

The production of positive ions by electron impact provides the mechanism of electron current amplification by which the conductivity of semiconductor deposition plasmas is maintained. This chapter has examined in detail the chemical fate of these ions as they interact with the neutral gas mixtures from which they were formed. The Langevin limiting reaction rate has been presented based on a careful optical measurement of silane's polarizability and is found to be  $5 \cdot 10^{-9} \frac{1}{\sqrt{\mu}} \text{ cm}^3 \text{s}^{-1}$  where  $\mu$  is the reduced mass of the ion-silane pair. Pulsed ion cyclotron resonance mass spectrometry techniques have been used to measure reaction rates and product distributions for the reactions of helium, neon, argon, krypton, xenon,  $\text{SiH}_n$  and  $\text{H}_3$  ions with silane. The theoretical implications of these kinetic observations, summarized in table 6.8 and figure 6.10, will form the

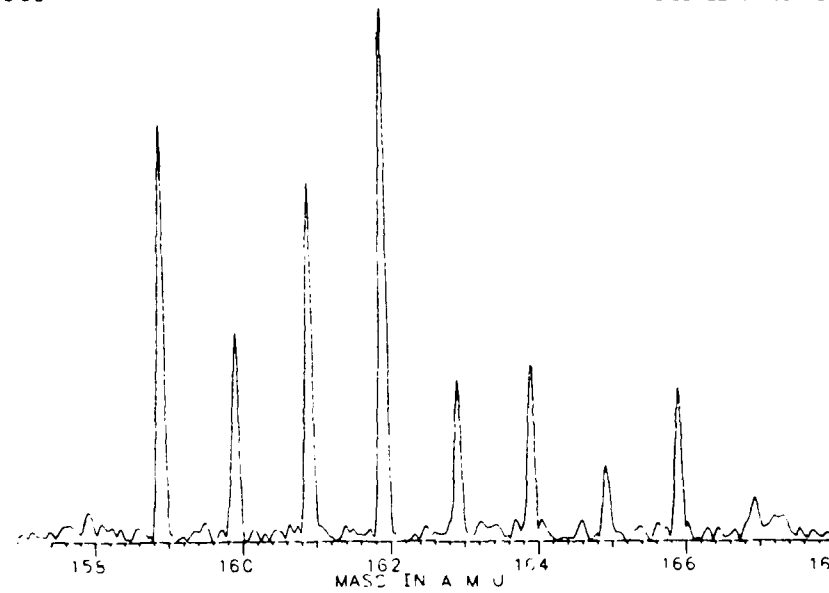


Figure 6.19:  $Xe^+$  reaction with silane showing the production of condensation products  $XeSiH_n^+$  for  $n = 2, 3$ .

central theme of the next two chapters.

Reagent Ion	$k_{FTMS}$	$k_{FTMS}/k_L$	Product Ions
$He^+$	1.6	0.6	$Si^+, SiH^+$
$Ne^+$	0.67	0.5	$SiH^+, Si^+$
$Ar^+$	0.08	0.07	$SiH_3^+$
$Kr^+$	1.2	1.	$SiH_3^+$
$Xe^+$	0.54	0.55	$SiH_2^+$
$H_3^+$	1.7	0.57	$SiH_3^+$

Table 6.8: Total charge transfer rate constants and observed products for rare gas ion reactions with silane measured in the present work and compared to Langevin's limiting rate using  $\alpha(SiH_4) = 4.62 \cdot 10^{-24} cm^3$

## Bibliography

- [1] M. Langevin, *Annales de Chimie et de Physique*, **8**, 245 [1905].
- [2] H. Eyring, J. Hirschfelder and H. Taylor, *Journal of Chemical Physics*, **4**, 479 [1936].
- [3] A. Jain, *Journal of Chemical Physics*, **86**, 1289 [1987].
- [4] R. Keeling, *Development of an Interferometric Probe for Determination of the Oxygen Mole Fraction in Air*, PhD thesis, Harvard University Division of Applied Sciences [1987].
- [5] R. Keeling, personal communication, [1987].
- [6] A. Price, *The Permittivity of Liquids* in N. Hill ed., **Dielectric Properties and Molecular Behaviour**, (New York:Van Nostrand) [1969] pp. 232-279.
- [7] H. Chatham *et al.*, *Journal of Chemical Physics*, **79**, 1301 [1983].
- [8] N. Hill ed., **Dielectric Properties and Molecular Behaviour**, (New York:Van Nostrand) [1969].
- [9] Scott Specialy Gases, South Plainfield N.J. cylinder number 15-7889 project number 196240, 16 October 1987.
- [10] J. Pople *et al.* Carnegie Mellon University, [1986].
- [11] Y. Harada, J. Murrell and H. Sheena, *Chemical Physics Letters*, **1**, 595 [1968].
- [12] U. Itoh *et al.*, *Journal of Chemical Physics*, **85**, 4867 [1986].

- [13] J. Dugan and J. Magee, *Advances in Chemical Physics*, **21**, 209 [1971].
- [14] J. Hirschfelder, C. Curtiss and R. Bird, **Molecular Theory of Gases and Liquids**, (New York:Wiley), 827 [1954].
- [15] C. Nelin, *et al.*, *Journal of Chemical Physics*, **77**, 3607 [1982].
- [16] C. Bauschlicher and P. Taylor, *Theoretica Chimica Acta*, **bf 71** 263 [1987].
- [17] G. Hess and F. Lampe, *Journal of Chemical Physics*, **44**, 2257 [1966].
- [18] P. Haaland and A. Rabee, *Chemical Physics Letters*, **114** 571 [1984].
- [19] T. Yu, *et al.*, *Journal of Physical Chemistry*, **76**, 3321 [1972].
- [20] J. Henis *et al.*, *Journal of Chemical Physics*, **57**, 389 [1972].
- [21] J. Henis *et al.*, *Journal of Chemical Physics*, **58**, 3639 [1973].
- [22] J. Perrin and J. Schmitt, *Chemical Physics*, **67**, 167 [1982].
- [23] W. Allen, T. Cheng and F. Lampe, *Journal of Chemical Physics*, **66**, 3371 [1977].
- [24] H. Michels and R. Hobbs, Dissociative Recombination of  $e + H_3^+$ . An Analysis of Reaction Product Channels, Appendix A in UTRC report P83-339, United Technologies Research Center, Hartford, CT. [1983].
- [25] I. Hamilton, *Journal of Chemical Physics*, **87**, 774 [1987].
- [26] M. Bowers and D. Elleman, *Chemical Physics Letters*, **16**, 486 [1972].
- [27] R. Walsh, *Accounts of Chemical Research*, **14**, 246 [1981].
- [28] A. Maryott and F. Buckley, **NBS Circular 537**, (Washington:National Bureau of Standards), [1953].
- [29] M. Mandich, W. Reents and F. Jarrold, *Journal of Chemical Physics*, **88**, 1703 [1988].
- [30] K. Ragavachari, *Journal of Chemical Physics*, **88**, 1688 [1988].

# Chapter 7

## Theory for Charge Transfer

### 7.1 Introduction

The sequence of dissociative charge transfer reactions between the noble-gas ions and silane vigorously challenges chemical notions which provide a basis for predictions of reaction kinetics. All five reactions have the same interaction potential ( $\propto \alpha(SiH_4) \cdot r^{-4}$ ) at long range. All are exothermic. All but one involve the collision of a  $^2P$  ion with  $^1A_1 SiH_4$ . ( $He^+$  is  $^2S$ .) Successful charge transfer yields an unreactive noble-gas in its ground electronic state; in other words a filled valence shell. Reduced masses, polarizabilities, spin-orbit coupling parameters, and ionization potentials all vary monotonically down the eighth period of Mendeleev's table.<sup>1</sup> How then is one to understand the peculiar reactivity trend detailed in the last chapter and summarized in table 7.1?

### 7.2 Classical Features

It is quite obvious that there is no correlation between the total reaction rate and the reaction free energy change. Simple symmetry arguments also run aground, as the reactant ions are all of the same shape and, with the exception of helium, lack a single valence p electron. Benson's modification of the Langevin picture for exothermic charge transfer with no activation barrier predicts that

---

<sup>1</sup>Actually, Mendeleev's original table had no eighth period, since noble-gases were discovered twenty years later. However the last column of the modern table that bears his name contains all of the noble-gases.

Reagent Ion	$\Delta H$ (eV)	$k_{expt}$	$k_{expt}/k_L$
He	-13.9	$1.6 \cdot 10^{-9} \text{ cm}^3 \text{s}^{-1}$	0.60
Ne	-10.9	0.67	0.5
Ar	-5.1	0.08	0.07
Kr	-3.3	1.2	1.0
Xe	-1.4	0.54	0.57

Table 7.1: Total charge transfer rate constants measured by FTMS,  $k_{expt}$  and their relationship to the Langevin limiting rate,  $k_L$ .

Reagent Ion (eV)	$k_{expt}$	$k_{Benson}$	Ratio
He	$1.6 \cdot 10^{-9} \text{ cm}^3 \text{s}^{-1}$	$0.56 \cdot 10^{-9} \text{ cm}^3 \text{s}^{-1}$	2.7
Ne	0.67	0.42	1.6
Ar	0.08	0.71	0.11
Kr	1.2	0.76	1.6
Xe	0.57	0.92	0.62

Table 7.2: Charge transfer rates estimated using Benson's thermochemical kinetics artifice.

rates should correlate with the polarizability of the product neutral. In other words, he suggests that charge transfer is facile between reactants at large distances and that the actual reaction rate is limited primarily by requirements of energy and momentum conservation in the product channel. For the reaction of  $H_2^+$  with methane, for example, it is suggested that the thermal cross section should scale with  $\alpha(H_2)$  [1]. Application of this approach to the rare-gas ion : silane reactions results in the predictions summarized in table 7.2. There is no correlation between these thermochemical kinetic predictions and the observed reaction rates.

Unlike the radical-radical and radical-molecule reactions considered in some detail by Benson, charge transfer reactions have as a common feature an interaction potential which is strongly attractive in both the reactant and product channels. The strength of the attractive potential between  $SiH_n^+$  and noble-gases increases by a factor of twenty from He to Xe. A plot of these classical potential curves, as well as the polarization potentials for molecular and atomic hydrogen, is illustrated in figure 7.1. Successful charge transfer must leave enough kinetic energy in the relative motion of the rare-gas and silicon-hydride ion to overcome

the attractive polarization potential. If charge transfer occurs at a distance  $r_1$  then the relative kinetic energy must change by an amount equal in magnitude but opposite in sign to the instantaneous change in the polarization potential, or  $(\alpha(SiH_4) - \alpha(Rg)) \cdot r_1^{-4}$ . This quantity is always greater than zero since the polarizability of silane is larger than that of all the other species here considered, so the binary pair is expected to dissociate after successful charge transfer. As a refinement on the classical potentials in the products one may consider the kinetic energy constraints on the hydrogen atoms or molecules which result from some dissociative ionization channels. The kinetic energy derived from an instantaneous change in the rare-gas - silane polarization potential need not stay in one vibrational mode, it may be channeled into modes which couple atomic or molecular hydrogen to the binary encounter complex. Table 7.3 summarizes the electronic potential energy changes, while the polarization potentials which constrain dissociation into products are calculable for any value of  $r_1$  by the formula:

$$\sum_i \frac{\alpha_i}{r_1^4} \leq \frac{\alpha(SiH_4)}{r_1^4}$$

where the index  $i$  runs over all of the dissociative charge transfer products including hydrogen atoms and molecules. The inequality must be satisfied if the polarization forces on the products are insufficient to hold the complex together following charge transfer. If it is not satisfied, the possibility of a very long lived ion-molecule complex in which charge is delocalized arises. The total changes in the polarization energy which characterize reactant and product ensembles are estimable graphically from figure 7.1 for values of  $r_1$  between one and five angstroms. The kinetic energy available for dissociation is just the difference between the sum of the product curves, *e.g.*  $Ar + H$ , and the reactant potential,  $V(r) \propto \alpha(SiH_4)$ .

In other words, conservation of energy and the separation of nuclear motion from electronic rearrangement (the Born-Oppenheimer approximation) constrains the reactive collision. Since  $\alpha(SiH_4) > \alpha(Rg)$ , successful electron transfer from silane to the noble-gas produces an ion-molecule pair which dissociates adiabatically. The additional potential energy of the departing hydrogen atoms and molecules qualitatively influences only the  $Xe^+$  reaction, since  $\alpha(Xe) + (\alpha(H_2) \text{ or } \alpha(H)) \approx \alpha(SiH_4)$ .

Rg	$SiH_3^+, H$	$SiH_2^+, H_2$	$SiH^+, H, H_2$	$Si^+, 2H_2$
He	-12.4	-13.0	-9.9	-11.3
Ne	-9.4	-10.0	-6.9	-8.3
Ar	-3.6	-4.2	-1.1	-2.5
Kr	-1.8	-2.4	+0.7	-0.7
Xe	+0.1	-0.6	+2.6	+1.2

Table 7.3: Total free energy changes in eV for the reactions  $Rg^+ + SiH_4 \rightarrow$  calculated from the average appearance potentials of the silicon hydride (see table 3.5) and noble-gas ions.

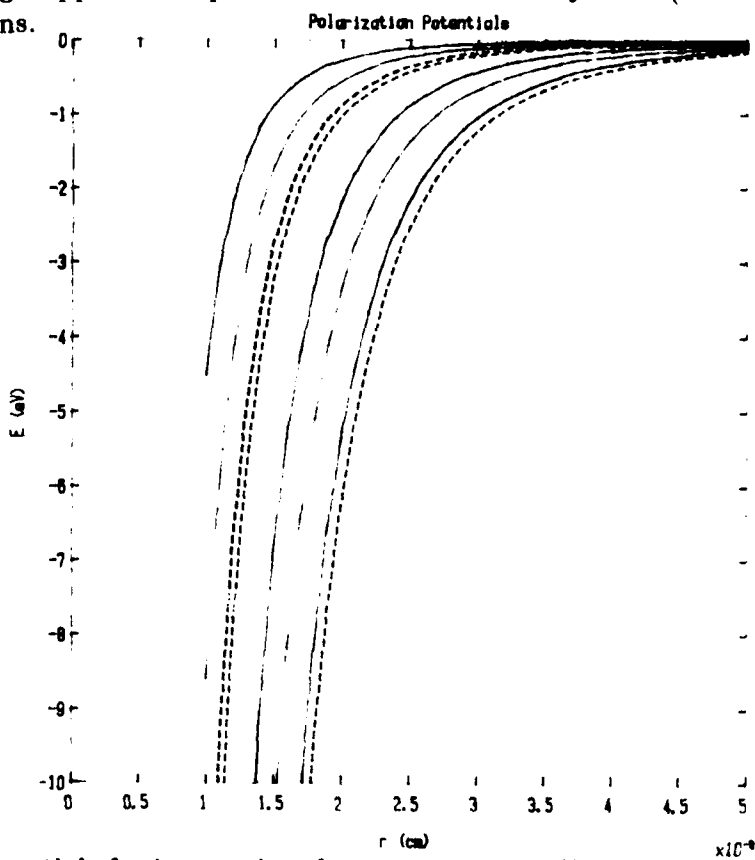


Figure 7.1: Polarization potentials for interactions between ions and (from left to right)  $He, Ne, H, H_2, Ar, Kr, Xe$ , and  $SiH_4, H_2$  with impact parameter  $b = 0$ . These classical potentials,  $\propto \frac{a}{r^4}$ , illustrate the magnitude of the change in kinetic energy of the  $Rg^+ \cdots SiH_4 \rightarrow Rg \cdots SiH_4^+$  complex required by total energy conservation as a function of the separation at which charge transfer occurs.

### 7.3 Electronic Structure

The monotonic variation of physical properties for the series of noble-gases He, Ne, Ar, Kr, and Xe is unlike the trend observed for the corresponding ion-silane reaction rates. If on no other grounds than a principal of correspondance, one expects the long-range dynamical interactions to be essentially classical for these systems. The approach to the 'argon anomoly' has therefore been to probe for the existence of constraints on electron transfer from silane to the incoming noble cation. In the course of these investigations very many *ab initio* electronic structure calculations were performed with a view to identifying such a barrier.

The electronic structures of silane and its cations have already been discussed in chapter 3. Silane has a triply degenerate ( $t_2$ ) highest occupied molecular orbital with a calculated binding energy of 13.1 eV. The next occupied level is of  $a_1$  symmetry and is bound by 19.9 eV using the 6-31++g\*\* gaussian basis functions and the optimized  $T_d$  geometry with a Si-H bond distance of 1.474 Å. On ionization all of the electronic eigenvalues shift to lower energy by an average of just over 7 eV, as expected from the increased average nuclear charge experienced by each electron. As one is concerned in the case of silane with dissociative ionization, one should consider the family of silicon hydride cation eigenvalue spectra. A schematic view of these binding energies for all of the  $SiH_n^+$  ions with  $n=0$  to 4 is displayed in figure 7.2.

Similar calculations can be made for helium, neon, and argon with the results listed in table 7.4. Krypton and xenon are not amenable to these simple approaches; their high nuclear charge makes non-relativistic treatment of core electrons and separation of spin and orbital angular momenta unrealistic. Although techniques are available for treatment of these wavefunctions in an approximate way, the error introduced by discontinous *ab initio* treatment of the noble-gases was thought likely to mask any anomolous trend in the calculated electronic properties down the eighth period. Therefore appeal was made to spectroscopic information from which binding energies of the highest occupied orbitals in the noble-gases and their cations were tabulated as continuum limits or ionization thresholds.

In the case of silane one can also infer the eigenvalues associated with the  $t_2$  and  $a_1$  orbitals from experimental photoelectron spectra. Potts and Price [2] observed continuum limit vertical ionization thresholds from these orbitals of 12.82 and 18.17 eV in silane's He(I) photoelectron spectrum. As one expects for the Jahn-Teller unstable  $^2T_2$  ion formed by removal of an electron from the

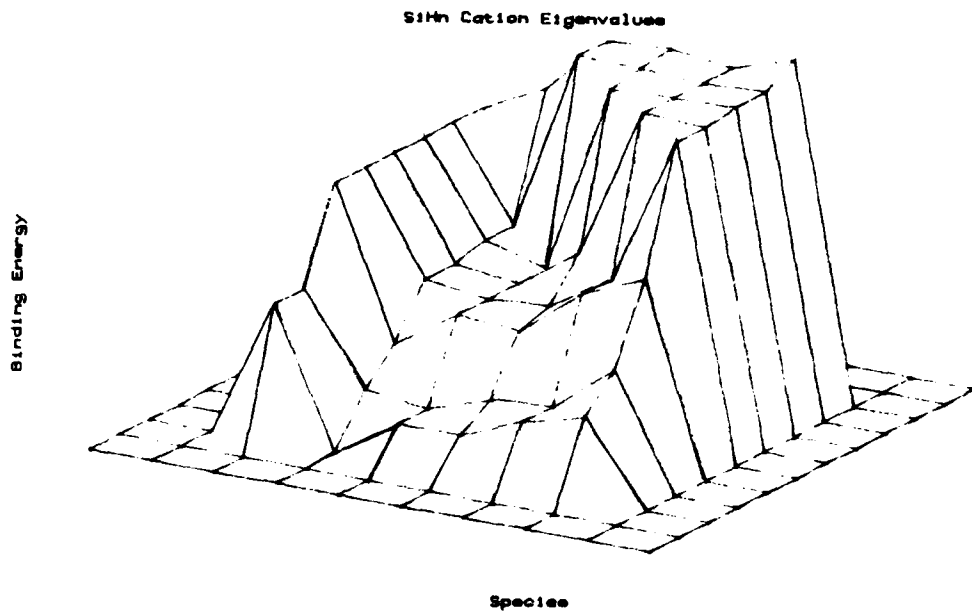


Figure 7.2: UHF eigenvalue spectra for the silicon hydride cations using geometries optimized at the MP2/6-31g\*\* level. Vertices correspond to one electron binding energies. The flat base is at an energy of  $-30\text{ eV}$ . From left to right the ridges correspond to  $\text{SiH}_4$ ,  $\text{SiH}_n^+$   $n = 4, 3, 2, 1, 0$ . Recall that the  $\text{SiH}_4t_2$  and  $a_1$  orbitals are at  $-13.1$  and  $-19.9\text{ eV}$ , respectively. Highest occupied molecular orbitals, indicated by circles, of  $\text{SiH}_n$  for  $n=4,3$ , and 2 are lower in energy than those for  $n=0,1$ .

Species	I1 calc	I1 spect	I2 calc	I2 spect
He	24.8	24.6	54.1	54.4
Ne	22.5	21.6	42.0	41.1
Ar	16.0	15.8	27.6	27.7
Kr	...	14.0	...	26.4
Xe	...	12.1	...	21.1
$SiH_4(t_2)$	13.1	12.8	20.2	...
$SiH_4(a_1)$	19.9	18.2	25.1	...

Table 7.4: Binding energy of highest occupied orbitals of noble-gases (I1) and their ions (I2) as estimated using *ab initio* calculations with Pople's standard 6-31g\*\* basis set and literature spectroscopic data.

highest occupied molecular orbital, the  $t_2$  photoelectron spectrum is broadened substantially.

The orbital energies shown in table 7.4 become transparently relevant when one considers a simple correlation diagram for the charge transfer reactions, as illustrated in figure 7.3. The highest occupied orbitals of  $He^+$  and  $Ne^+$  remain lower in energy than the  $a_1$  orbital of silane as they are neutralized. The remaining noble-gas ions' highest occupied orbitals become less stable than the silane  $a_1$  on their way to the neutral noble-gas with energies approaching the silane  $t_2$  level more closely as one goes from Ar to Kr to Xe. On the basis of simple perturbation theory [3] one expects the interaction of two wavefunctions to scale inversely with their energy difference. Therefore the strongest interaction between helium or neon and silane is expected to be with the  $a_1$  orbital of silane. Furthermore, the eigenvalues associated with the neutral helium and neon atoms are lower in energy than the highest occupied orbital of either the silicon hydride ions displayed in figure 7.2 or hydrogen atoms and molecules. Therefore electron transfer to helium or neon from the  $a_1$  orbital of silane occurs irreversibly, in the sense that the energetics prevent electron transfer from  $Rg$  to  $SiH_n^+$  across the entire correlation diagram.

By contrast extraction of an electron from the  $a_1$  orbital of silane by an argon ion is resonant at some point along the reaction coordinate. On the product side of the correlation diagram the neutral argon orbitals are higher in energy than the highest occupied orbitals of the hydride cations. Further, a monotonic change of the orbital associated with the argon nucleus never gets closer than 3 eV to the silane  $t_2$  orbital. Similar consideration of the krypton ion leads to the same

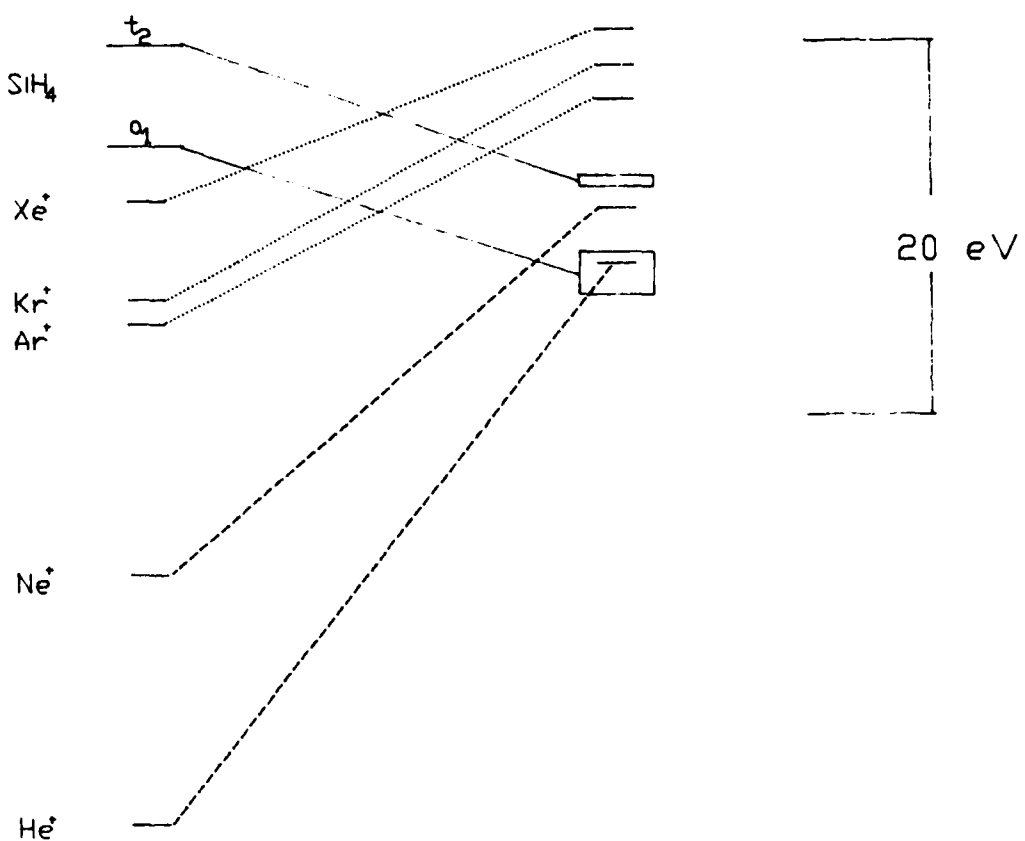


Figure 7.3: Orbital correlation diagram illustrating the massive electronic reorganization required for successful electron transfer from silane to noble-gas cations. Shown at left are the eigenvalues corresponding to the rare-gas ions and neutral silane's  $a_1$  and  $t_2$  orbitals. The right-hand side of the diagram shows the eigenvalues associated with the noble-gas neutral atoms and silicon-hydride ions.

observations with respect to the  $a_1$  orbital, but krypton comes within 1.2 electron volts of the  $t_2$  orbital in neutral silane. Charge transfer from xenon is almost symmetric in the sense that the orbital energy associated with the xenon nucleus changes from 21.1 to 12.1 while that of silane moves from 12.8 to 20.2. Again, only loss of an electron from the silane  $t_2$  orbital is anticipated. The emerging picture from this simple correlation discussion is thus that electron transfer to helium and neon should occur from the  $a_1$  orbital and yield common hydride cation products. Xenon, krypton, and argon, by analogy, should be neutralized from the silane  $t_2$  orbital and yield products different—at least in theory—from those of the helium and neon reactions.

An alternative way of formalizing these interactions borrows the language of the Stark effect [4]. Clearly, the wavefunctions of silane will be influenced by the enormous electric field of the noble cations as they approach. The ordinary WKB<sup>2</sup> expansion method for solution of ionization by an electric field should be modified by the condition of a stationary solution centered on the noble-gas following charge transfer. Instead of an infinite sum of plane waves as a product wavefunction, solution of the wave equation for the transferred electron around the noble-gas assumes a range of energy values as charge is transferred and the effective nuclear charge with which the valence electrons are bound decreases from  $Z_{eff}(Rg^+)$  to  $Z_{eff}(Rg)$ . This quasi-continuum is coupled to the dynamic solutions of the electrons bound to silane as its nuclear charge changes from  $Z_{eff}(SiH_4)$  to  $Z_{eff}(SiH_n^+)$  in the reaction. Although the magnitude of the classical electric field generated at silane by the incoming cations, and therefore the field ionization rate, is the same for all of the noble-gases, the eigenfunctions of the product neutrals constrain electron transfer. First-order perturbation theory suggests that the interaction of the orbitals centered on silicon and those around the noble-gas nucleus is inversely proportional to their energy difference. On the reactant side of figure 7.3 all of the half-filled ion orbitals are below the silane  $a_1$ , suggesting  $a_1 \rightarrow Rg^+$  electron transfer with efficacy decreasing in the order  $Xe > Kr > Ar > Ne > He$  as the primary charge transfer mechanism. However as Xe, Kr, and Ar are neutralized their highest occupied orbital moves to energies above that of the  $a_1$ , so that electron transfer is expected to occur back to the silicon center. Transfer of a silane  $t_2$  electron to  $Ar^+$ ,  $Kr^+$ , and  $Xe^+$  is still anticipated by these arguments, with decreasing facility from Xe to Ar based on the orbital energy differences.

<sup>2</sup>Wentzel Kramers Brillouin wavefunctions are described in any quantum mechanics text including, for example, reference [3].

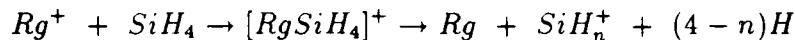
The next question concerns expectations about the products of charge transfer reactions. What difference is anticipated for reactions which proceed via  $t_2$  and  $a_1$  electron abstraction? As was shown in chapter 3, loss of a  $t_2$  electron from silane leads to substantial reorganization of the molecule's electronic structure, resulting in a Jahn-Teller distortion of the nuclear configuration which adiabatically dissociates the molecular cation into  $SiH_3^+$  and  $H$  or  $SiH_2^+$  and  $H_2$ . The role of hydrogen tunneling, arguably important in the electron impact and photoionization processes, is expected to be qualitatively changed by the relatively long time constants ( $\approx 200$  times slower than electron impact) associated with heavy particle motion in ion-molecule reactions. Whether electron transfer from silane to an ion is characterized as slow, encouraging adiabatic motion of the nuclei, or fast, paralleling photoionization, will clearly depend on the time rate of change of electron density as the transferred electron 'moves' from silicon to the noble-gas nucleus.

By contrast removal of an  $a_1$  electron yields an excited ion state which is not orbitally degenerate. The Jahn-Teller distortion is not expected for this  $^2A_1$  ion, a prediction for which experimental evidence is found in the photoelectron spectrum of silane [2]. To first order one expects the influence of the  $a_1$  orbital electron loss to affect Si-H bonding symmetrically, that is it should change all four bound hydrogens equally. The  $^2T_2 \leftarrow ^2A_1$  transition is optically allowed in all three polarizations, so that common products resulting from  $a_1$  and  $t_2$  electron removal are not precluded by these arguments. One therefore expects differences in the product distributions for  $a_1$  and  $t_2$  electron loss to reflect competition between optical emission from and dissociation of the  $^2A_1$  ion state. That this competition is not totally one-sided is again suggested by the photoelectron spectrum of silane, where vibrational structure corresponding to a series of Rydberg levels which correlate with a bound  $^2A_1$  ion state is observed between 16 and 18 eV [8].

A report of  $SiH^+$  ( $X^1\Sigma \leftarrow A^1\Pi$ ) emission produced from the reaction of thermal helium cations with silane recently appeared [12]. The authors estimate that 25% of the  $SiH^+$  produced by helium charge transfer is in the excited A state. The appearance potential for  $SiH^+(A^1\Pi)$  from electron impact on silane was found by Perrin to lie at  $19 \pm .5$  eV [13], in remarkable agreement with the calculated binding energy of the  $a_1$  silane orbital. This provides an experimental intimation that the  $a_1$  orbital is playing a role in the  $He^+ + SiH_4$  reaction.

In addition to the kinetic energy arguments summarized in the last section,

the entropy increase in the dissociative charge transfer reactions:



suggests that the reactions occur in a single collision. With the exception of xenon, one does not expect long lifetimes for the complex ion surrounded by brackets. If charge is not transferred, the classical trajectory runs into a repulsive wall and rebounds to reactants. If charge is transferred, the total free energy change on moving to products ( $\Delta G = \Delta H - T\Delta S$ ) is unambiguously negative, so that without non-classical barriers the dissociation is spontaneous. Therefore the operative question for the reactivity trends concerns the probability of electron transfer in a single, binary encounter between the noble-gas ion and silane.

## 7.4 Quantum Constraints

Having reviewed features of the electronic structure of silane and the noble-gases in the last section one is now in a position to pose the question: are there quantum mechanical constraints on electron transfer in the ion-silane reactions which account for the non-monotonic trend of reactivity down the eighth period?

While the correlation diagram of figure 7.3 is suggestive, it is only intended to be schematic. Consider first the influence of the electric field associated with a point charge (the noble cation) on the wavefunction of a single electron in a potential. In very weak electric fields, corresponding to large ion-silane separations, non-hydrogenic wavefunctions and eigenvalues are not influenced by the field to first order in perturbation theory. Second order perturbation theory yields an energy change (*i.e.* the quadratic Stark effect) :  $\Delta E \approx \frac{-\alpha}{2} \cdot E^2$  where  $\alpha$  is the polarizability ([4] § 76; [7] § 52). As the electric field is increased the probability of tunneling through the potential barrier increases. In fact, closed analytic solutions to the ionization rate of a hydrogen atom were presented in 1928 by Oppenheimer [6] and also in 1930 by Lanczos [5]. The essential feature of these calculations involved description of the ionized product as a properly normalized superposition of plane waves with a continuum of energy eigenvalues. The main result of these analyses is that quantum mechanical barrier penetration of an electron wave increases with the applied field which mixes the bound state with the continuum of 'ionized' states in which the electron propagates irreversibly to the anode. For excellent discussions of the mathematics the interested reader is referred to the original paper of Oppenheimer [6] and also the texts by Landau [4] or Bethe [7].

As mentioned in the last section, ion-molecule reactions do not involve coupling of a unique bound electronic state to a continuum. The coupling is rather to a restricted continuum of bound states corresponding to binding of electrons to the reactant ion. The approach here will closely parallel that described in two elegant papers written in the early 1930's by Zener<sup>3</sup> [9, 10] which considered non-adiabatic potential crossing and predissociation. A precis of the original argument follows. Consider two potential energy surfaces, one of which is bound, which intersect at some distance  $R_0$  (Figure 7.4). If the system is initially in state  $|1\rangle$  what is the probability of finding it not in  $|1\rangle$  as a function of time and the characteristics of the potentials? The desired transition probability is :

$$|\int U_1(r) < 1|H_1|2 > U_2(r)|^2 dr$$

where the U's are vibrational wavefunctions and the matrix element describes the mixing of the two electronic states by an external perturbation,  $H_1$ . The U's are, for the case at hand, unbound vibrations whose effective frequencies are determined by the magnitude of the polarization potential between  $Rg^+$  and silane in the case of  $U_1$  and  $SiH_n^+$  and  $Rg$  for  $U_2$ . Evaluation of this integral using WKB approximate wavefunctions leads to a transition rate of:

$$P_{12} = 1 - \exp\left(-\frac{4\pi^2 \epsilon_{12}^2}{h\nu|s_1 - s_2|}\right)$$

where  $\epsilon_{12}$ ,  $s_k$  and  $\nu$ , are defined as  $< 1|H_1|2 >$  and  $\frac{dV_k}{dr}$  evaluated at the curve crossing  $R_0$ , and  $\sqrt{2(E - V_0)/m}$ , respectively. For the case at hand  $V_1$  corresponds to the eigenvalue of a particular bound eigenfunction of silane and  $V_2$  to that of the incoming noble cation. Recall that the  $t_2$  and  $a_1$  orbitals were bound by 12.8 and 18.2 eV, respectively. As the  $Rg^+ \cdots SiH_4$  distance decreases to some value,  $r_i$ , the wavefunctions associated with an incoming noble-gas ion will interact with silane, giving rise to a matrix element  $< 1|H_1|2 >$  which can be related to the separated wavefunctions and eigenvalues by first order perturbation theory:

$$|m\rangle^{(1)} = \sum_{n \neq m} \frac{< m|H_1|n >}{\Delta E_{mn}} \cdot |n\rangle$$

<sup>3</sup>The method was first described by Landau in *Phys. Z. Sowjetunion*, 1, p.88 [1932] but a copy could not be located.

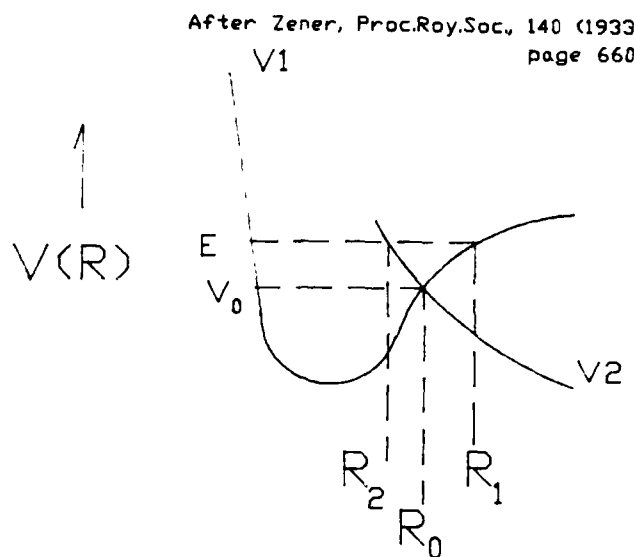


Figure 7.4: Potential energy surfaces and reference points for the tunneling calculation after the treatment of Zener (see text).

where all but the term on the left hand side refer to unperturbed wavefunctions. That the first order variation of the perturbed wavefunction, and therefore the second order correction to the total energy, scale inversely with the energy difference between the eigenvalues at infinite  $r$  means that orbital mixing is most effective for cases where the silane and noble cation orbitals are close in energy. In other words, if one assumes that the perturbed Hamiltonian for the noble-gas ion silane reactions have the same form, *e.g.* Stark mixing of bound and continuum orbitals on silane, then the matrix element needed for the tunneling calculation,  $\epsilon_{12}$ , should also vary with the inverse of the energy difference between the eigenvalues associated with the noble-gas ion and silane. This is the essential result.

It is now possible to estimate trends as one moves down the periodic table for reactions of noble ions with silane. The internuclear potential will be approximated as an  $\alpha \cdot r^{-4}$  interaction truncated by a steep, repulsive wall at some critical radius  $r_c$ . Assuming negligible relative velocity at infinite  $r$  one can rewrite the potential energy as velocity using total energy conservation and the reduced mass of the ion-silane pair,  $\mu$ . The probability of ionization of silane is then just the integral of  $P_{12}$  over time:

$$\frac{1}{2}\mu v(r)^2 = \frac{\alpha}{r^4}$$

$$v(r) = \frac{1}{r^2} \sqrt{\frac{2\alpha}{\mu}}$$

$$\int P_{12}(t)dt = \int \frac{dr}{v} \cdot P_{12}(r)$$

$$\int P_{12}(t)dt = \sqrt{\frac{\mu}{2\alpha}} \int_{\infty}^{r_c} P_{12}(r) r^2 dr$$

The total probability of electron transfer increases with the square root of the reduced mass, as expected due to the increased interaction time of the binary pair. Similarly, the transfer probability drops with increasing polarizability, since a stronger potential increases the colliding velocity and therefore decreases the interaction time.

When  $V_1$ , that is the binding energy of the silane electron, and  $s_k$ , the potential gradients at  $r$ , are assumed the same for all of the noble-gases, only  $\epsilon_{12}(r)$  governs the scaling of the integrated tunneling probability. Indeed the lower bound on the integral should be replaced by that value of  $r = r_i$  for which  $\epsilon_{12}$  first becomes non-zero. As described above, for a general perturbative treatment the interaction  $\epsilon_{12}(r)$  will scale with the reciprocal of the energy difference between the separated states. Rewriting  $\epsilon_{12}(r)$  with this feature explicit and parameterizing the  $r$  dependence of the matrix element as  $f(r)$  yields the equation:

$$\int P_{12}(r)dr = \sqrt{\frac{\mu}{2\alpha}} \cdot \frac{1}{\Delta E_{mn}} \int_{r_i}^{r_c} f(r) r^2 dr.$$

While  $f(r)$  may in general be a complicated function for arbitrary reactant species, its variation down the series of noble-gases is of subsidiary importance. The essential point is that, to second order in perturbation theory, the integrated tunneling probability scales with the inverse of  $\Delta E_{mn}$  for the same  $f(r)$ .

There is one remaining element in the consideration of quantum constraints on charge transfer. In real systems the value of  $\Delta E_{mn}$  changes as charge is transferred. In other words, as the electron which starts in potential  $V_1$  develops a finite probability density in  $V_2$  the effective potentials  $V_1$  and  $V_2$  change as a consequence of the new effective nuclear charge which characterize these potentials.

The range of values which are taken by  $V_1$  and  $V_2$  are limited by the first and second ionization potentials of the species involved in the charge transfer reaction. For transfer of an electron from the silane  $t_2$  to a krypton ion, for example,  $V_1$  runs from -12.8 to -20.2 electron volts while  $V_2$  changes from -26.4 to -14.0 eV. A self-consistent solution of the charge transfer probability therefore requires inclusion of this reaction-dependant  $\Delta E_{mn}$ . One can see by inspection that this is precisely what is required to understand the anomolous reactivity of  $Ar^+$  with silane.  $\Delta E_{mn}$  for the  $Ar^+$  ion and the silane  $a_1$  is less than for the helium and neon analogues. However as electron density is transferred to the argon nucleus its highest occupied orbital moves through the energy of the  $a_1$  on its way to ground state  $Ar$  (15.8 eV). The singularity in the electron transfer probability when  $\Delta E_{mn} = 0$  shows that the electron transfer rate is expected to be large at resonance. However, as the electron density associated with the argon nucleus increases further  $\Delta E_{mn}$  becomes negative, implying a reversal of the charge transfer process. Electron density is driven back to the silicon center. To the extent that  $\frac{df(r)}{dr}$  is small over a narrow range of  $r$ , that is in the Born-Oppenheimer approximation, the integrated tunneling probability is expected to be small since  $P_{12}$  changes sign with  $\Delta E_{mn}$ .

The increasing closeness of the krypton and xenon ion orbitals to the silane  $a_1$  suggests a large probability of  $a_1 \rightarrow Rg^+$  electron transfer. However as was argued for the argon case, reduction of  $Z_{eff}$  on  $Kr^+$  and  $Xe^+$  is energetically unfavorable. By the same arguments their interaction with the silane  $t_2$  is expected to decrease with increasing  $\Delta E_{mn}$  in the order  $Xe > Kr > Ar$ . Considering only the reactant orbital interactions leads to the erroneous inference that the reaction rates would decrease monotonically from xenon to helium. The existence of two sets of silane orbitals at energies which are between those of the noble-gases and their ions gives rise to a slightly more complicated picture as summarized in table 7.5. It has been argued on kinematic grounds that successful charge transfer results in adiabatic dissociation. Unsuccessful electron transfer, by conservation of energy, precludes formation of a long-lived complex ion. Therefore the redistribution of electron density must occur on the time-scale of a single collision, or about  $10^{-14}$  seconds. While interaction between orbitals of the ion and molecule in the entrance channel has been shown to enter into the reaction probability, it is not the whole story. Reorganization of the electrons to accomodate the changing effective nuclear charges associated with the ion and molecule block transfer of silane  $a_1$  electrons to argon, krypton, and xenon ions. Left only with the option of abstracting a  $t_2$  electron, the  $Ar^+$  wavefunctions start farther away in energy

Ion	$\sqrt{\mu}$	$\Delta E_{mn}^{-1}a_1$	$\Delta E_{mn}^{-1}t_2$	$\Delta E p1_{mn}^{-1}$	$\Delta E p2_{mn}^{-1}$
He	1.89	0.028	0.024	1.67	0.244
Ne	3.51	0.044	0.035	-.417	0.909
Ar	4.22	0.105	0.067	-.122	-.213
Kr	4.81	0.122	0.074	-.100	-.154
Xe	5.08	0.345	0.120	-.084	-.119

Table 7.5: Calculated values for prefactors in the integrated electron tunneling probabilities (see text).  $\Delta E_{mn}a_1$  and  $\Delta E_{mn}t_2$  refer to the  $Rg^+$  and  $SiH_4$  reactant orbitals, while  $\Delta E p1_{mn}$  and  $\Delta E p2_{mn}$  refer to orbitals on neutral  $Rg$  and a hypothetical,  $SiH_4^+ T_d$  product characterized by its highest ( $E p1$ ) or second highest ( $E p2$ ) occupied molecular orbitals.

than either krypton or xenon ions, and so react more slowly.

## 7.5 Comments

The picture which emerges from consideration of the quantum constraints on charge transfer demonstrates a mechanistic shift in the dissociative charge transfer reactions of noble-gas ions with silane. While various arguments based on the classical ion motion or conventional thermochemical kinetics fail to account for the 'argon anomaly', an approximate formulation of the quantum mechanics which may be applied using only spectroscopic values for the first and second ionization potentials of the species concerned is shown to describe the reactivity trend satisfactorily.

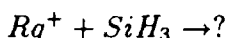
In a low-pressure ion molecule reaction the reactant state may be bound for many vibrational periods if, for example, some of the potential energy of the reactants' polarization interaction is partitioned into vibrational modes of the system other than the 'reaction coordinate'. Under these conditions the analogy with the Landau-Zener formalism for treatment of predissociation is transparent and useful. However accurate numerical rate constants from analysis such as that proposed in the last section involves calculation at a level of detail well beyond the scope of the present investigation. The stabilization of the ion-molecule complex by radiation and internal conversion, vibronic coupling, and tunneling calculations for the non-classical motion of silane's hydrogen atoms would be required to quantitatively assess the lifetime of the bound complex and the probability of

its dissociation to other than reactants.

However the present paradigm is viewed as an improved description of the ion kinetics for two reasons. First, it provides a plausible explanation for the relatively slow reaction rate of argon ions with silane. Second, the shift in product distributions is also rationalized by the model, since loss of the  $a_1$  electron to  $He^+$  and  $Ne^+$  yields the more dissociated silicon hydride ion products  $Si^+$  and  $SiH^+$ . Conversely, the reactions of the remaining ions, which are predicted to proceed via  $t_2$  electron transfer, produce only  $SiH_3^+$  and  $SiH_2^+$  as charged products, species which are expected on the basis of the Jahn-Teller distortions associated with the  $^2T_2$  molecular ion and which are observed in the threshold ion mass spectrum.

Given the first and second ionization potentials of an arbitrary reactant ion, the model permits prediction of both the products of the reaction with silane and the possibility that the rate is substantially less than that predicted by the Langevin-Eyring model. For example the reaction of  $H_3^+$  fits in nicely with the predictions of the model in the observation of a near Langevin rate and exclusively  $SiH_3^+$  as the charged product.

Extension of the model to other trends in the dynamics of dissociative charge transfer is straightforward. Indeed it is precisely predictions of unmeasured reaction rates and product distributions which provide the most vigorous test of any model. For example, refinement of the Langevin picture for ion-radical reactions such as



is elementary using the *ab initio* calculations for orbital eigenvalues of the radical as input. Such reactions would be very difficult to characterize experimentally, but may nevertheless play a role in the kinetics of plasma deposition reactors.

# Bibliography

- [1] S. Benson, **Thermochemical Kinetics**, 2<sup>nd</sup> edition, (New York:Wiley) [1976].
- [2] A. Potts and W. Price, *Proceedings of the Royal Society, London, A* **326**, 165 [1972].
- [3] E. Condon and G. Shortley, **The Theory of Atomic Spectra**, (Cambridge University Press:London) [1935].
- [4] L. Landau and E. Lifshitz, **Quantum Mechanics (Non Relativistic Theory)**,(Pergamon Press:New York) [1977].
- [5] Von C. Lanczos, *Zeitschrift für Physik*, **68** 204 [1931], **65** 431 [1930], and **62** 518 [1930].
- [6] J. Oppenheimer, *Physical Review*, **13**, 66 [1928].
- [7] H. Bethe and E. Saltpeter, **Quantum Mechanics of One and Two Electron Atoms**, (Plenum: New York) [1977].
- [8] T. Heinis, K. Borlin, and M. Jungen, *Chemical Physics Letters*, **110**, 429 [1984].
- [9] C. Zener, *Proceedings of the Royal Society, London*, **137** 697 [1932].
- [10] C. Zener, *Proceedings of the Royal Society, London*, **140** 661 [1933].
- [11] J. Berkowitz *et al.*, *Journal of Chemical Physics*, **86**, 1235 [1987].
- [12] S. Yamaguchi *et al.*, *Journal of Chemical Physics*, **86**, 4952 [1987].
- [13] J. Perrin and J. Aarts, *Chemical Physics*, **80**, 351 [1983].

[14] J. Burdett, **Molecular Shapes**, (New York:Wiley) [1980].

æ

# Chapter 8

## Films and Ions?

In the preceding chapters those microscopic quantities which define the ion kinetics of silane plasmas, the cross-sections and rate constants, have been analyzed with theory and experiment. The present chapter applies these results to the macroscopic deposition reactors. For commercially useful operating conditions it will be argued that the silicon hydride cations,  $SiH_n^+$ , are the most plausible precursors of amorphous silicon films in PECVD.

### 8.1 Ions or Radicals?

To illustrate application of the ion kinetic data to real reactors consider the account by Turban *et al.* published in 1979 entitled *Reaction Mechanism of the Radiofrequency Glow Discharge Deposition Process in Silane-Helium*. The authors employed radiofrequency (13.6 MHz) excitation of a 5% mixture of silane in helium [1]. The electron density in the central volume of the tubular reactor was measured by free space microwave interferometry, the deposition rate as a function of distance from the gas injector was presented, and the extent of silane decomposition was probed with quadrupole mass spectrometry. At a total pressure of 0.2 torr the observed power dependence of the electron density and deposition rate are summarized in table 8.1. Neither the electron temperature nor the distribution of electron energies were measured, but an estimate of the former, inferred from the observed depletion of silane and an analogy with methane's dissociation cross-section [2], is reported as 3.5 eV.

Suppose, as did the authors, that the electron energy distribution is roughly Maxwellian with a temperature of 3.5 eV. From table 5.1 one obtains ionization

Power (Watts)	$N_e \cdot 10^9 \text{ cm}^{-3}$	$\Gamma \cdot 10^{14} \text{ cm}^{-2} \text{ s}^{-1}$
10	3	8.3
20	5	10.3
50	8	13.3
100	11	14.4
200	15	15.2

Table 8.1: Electron densities  $N_e$  and silicon deposition rates  $\Gamma$  reported by Turban *et al.* for a radiofrequency discharge in 0.2 torr of 5% silane in helium.

rates for silane and helium of  $2.9 \cdot 10^{-10}$  and  $1.7 \cdot 10^{-12} \text{ cm}^3 \text{ s}^{-1}$  respectively. The rate for dissociative attachment to silane (from figure 5.3) is  $5.6 \cdot 10^{-12} \text{ cm}^3 \text{ s}^{-1}$ . Multiplying by the relevant neutral densities one obtains the homogeneous ion sources at small fractional silane dissociation <sup>1</sup>:

$$\frac{d[SiH_n^+]}{dt} = 1.02 \cdot 10^5 \cdot N_e$$

$$\frac{d[He^+]}{dt} = 1.1 \cdot 10^4 \cdot N_e$$

$$\frac{d[SiH_n^-]}{dt} = 2.0 \cdot 10^3 \cdot N_e.$$

From chapter 6 it was learned that the rate of dissociative charge transfer from helium to silane is very rapid. The e-folding time for helium ion conversion to  $SiH_n^+$  in 10 millitorr of silane is 1.4 microseconds, enough time for a 1 eV helium ion to travel less than one centimeter. Clearly, thermal helium ions, whose energy is of order 0.03 eV, will react with silane more rapidly than they are lost to the walls. For this mixture of helium and silane one therefore expects silicon-hydride ion concentrations to exceed those of  $He^+$ .

Diffusion of charged species in plasmas is qualitatively altered from that of their neutral counterparts by the stiffness of Poisson's equation. Specifically, the enormous electric fields which arise from small charge imbalances require the electron and ion densities to be equal in the body of the plasma. Poisson's equation also requires a balance between electron and ion fluxes to any dielectric

<sup>1</sup>fractional dissociation  $0 < f < 1$  defines the relationship between the reagent stoichiometry of the input gas and that in the actual plasma. It is governed by the interplay of gas residence time and the total dissociation rate of silane.

Power (Watts)	$\Gamma_i \cdot 10^{14} \text{ cm}^{-2} \text{ s}^{-1}$	$\Gamma \cdot 10^{14} \text{ cm}^{-2} \text{ s}^{-1}$
10	3.5	8.3
20	5.9	10.3
50	9.4	13.3
100	12.9	14.4
200	16.5	15.2

Table 8.2: Ion fluxes,  $\Gamma_i$ , inferred from Turban's electron density measurements, an assumed temperature of 3.5 eV, and the Bohm criterion and silicon deposition rates  $\Gamma$  reported by Turban *et al.* for a radiofrequency discharge in 0.2 torr of 5% silane in helium.

boundary, so that a steady wall potential is maintained. Electrons are  $\approx 10^4$  times less massive than ions. Their free diffusion is thus more rapid, so that an electric field or sheath is formed at the plasma boundaries which accelerates ions and repels electrons. This ambipolar diffusion of electrons and ions is discussed in elementary plasma physics texts. In the absence of heavy anions ambipolar diffusion implies a wall flux of cations which is related to the *electron* temperature according to the Bohm criterion [3]:  $\Gamma_i = \frac{1}{4} \cdot N_i \cdot c_i$  where  $c_i$  is the ion velocity at the plasma's electron temperature and  $N_i$  is the ion number density. In the absence of negative ions the electron and  $\text{SiH}_n^+$  concentrations in the bulk plasma are equal. (Negative ions cause  $N_i > N_e$ ). Calculation of ion wall fluxes at each of the discharge powers of table 8.1 is straightforward if one assumes that  $N_i = N_e$  and  $c_i$  is inferred from Turban's estimate of the electron temperature, 3.5 eV. The results of this first-order analysis are summarized in table 8.2.

The calculated ion fluxes are of course only applicable for small fractional dissociation of silane. If silane is dissociated and deposited as silicon film more rapidly than new silane is flowed into the reactor, the change in gas composition feeds back into the electron transport characteristics, raising the mean electron energy and thereby perturbing the nascent ion species distribution. This effect, which is a direct consequence of the large, low-energy, inelastic, electron scattering cross-sections of silane, has also been observed in direct current discharges of silane argon mixtures [23].

As a consistency check on this simple model it is easy to show that the homogeneous source of ions is of the same order as their diffusive loss. At twenty watts the measured electron density is  $5 \cdot 10^9 \text{ cm}^{-3}$  so the total ionization rate is

$$(1.02 + .11) \cdot 10^5 N_e \Omega = 5.7 \cdot 10^{14} \Omega \text{ s}^{-1}$$

where  $\Omega$  is the reactor volume. The loss to the walls by ambipolar diffusion is just

$$1.05 \cdot 10^{15} \cdot A s^{-1}$$

where  $A$  is the total wall area. In Turban's reactor the ratio of volume to surface area,  $\frac{\Omega}{A}$ , is 1.75 cm. The dimensionless ratio of the  $SiH_n^+$  sources and wall losses is:

$$\frac{5.5 \cdot 10^{14} \Omega}{1.05 \cdot 10^{15} A} = 0.91$$

a result which is considered excellent in view of the crude assumptions employed.

Summarizing, the experimental results of electron density and film deposition rate reported by Turban have been used in conjunction with the present data to argue the plausibility of silicon hydride ions as the depositing species in PECVD reactors. These estimates of ion fluxes are of the right order to account for the observed deposition rates. Before further refining the homogeneous ion chemical kinetics, it is necessary to consider the fate of these ions as they approach the reactor boundaries.

## 8.2 The Wall

While the results of the last section are plausible, Turban *et al.* reached the remarkable conclusion [1]:

Since the generation rate of neutral radicals for glow discharges in diatomic gases is much higher than the ionization rate, the experimental observation of a total conversion (of silane to film) leads us to assume that mass transport is mainly due to activated neutral species.

As was shown in chapter 3, all ionizing collisions with silane are dissociative, so that the total dissociation rate must be greater than or equal to the ionization rate. However, the extent to which neutrals are formed is difficult to quantify. The cross-section for electron-impact dissociation of silane,  $\sigma_d$ , while not measured directly, has been inferred from infrared diode laser absorption measurements of the observed dissociation rate under properly diagnosed plasma conditions [4]. The proposed cross-section increases from a threshold at 7.8 eV to a maximum value of  $5 \cdot 10^{-16} cm^2$  at 16 eV. More recent electron energy loss experiments with silane [5] confirm the 7.8 eV threshold and suggest modest variation of the total scattering amplitude above ten volts energy loss. One component of this

$T_e(eV)$	$k_d \cdot 10^{-9} cm^3 s^{-1}$	$k_i \cdot 10^{-9} cm^3 s^{-1}$	$\frac{k_i}{k_d}$
1.5	0.13	0.00089	0.007
2.5	1.59	0.032	0.020
3.5	5.09	0.17	0.033
4.5	10.01	0.48	0.048

Table 8.3: Estimated rates for total dissociation  $k_d$  and dissociative ionization  $k_i$  using the approximate cross-sections shown in figure 8.1 and maxwellian  $\mathcal{F}$ 's with the stated mean energies,  $T_e$ .

$\sigma_d$  arises from dissociative ionization as reviewed in chapter three. While the rate of change of the ionization cross-section with electron energy is only one eighth that of  $\sigma_d$ , it would comprise one third of the dissociative processes at forty volts if  $\frac{d\sigma_d}{d\epsilon} \approx 0$  for  $\epsilon > 16\text{ eV}$ . Between the thresholds for  $\sigma_d$  and  $\sigma_i$  only neutral fragments are possible from dissociative collisions. This 3.2 eV threshold difference and the inference that  $\frac{d\sigma_d}{d\epsilon} \approx 10 \cdot \frac{d\sigma_i}{d\epsilon}$  below 16 eV confirms the premise of Turban's argument:

$$\int \sigma_{dn}(\epsilon) d\epsilon > \int \sigma_{di}(\epsilon) d\epsilon$$

where the subscripts *dn* and *di* on  $\sigma$  refer explicitly to those dissociative channels which yield neutral and positively charged products, respectively.

The relative rates at which free-radicals and ions are formed by electron impact can be estimated from approximate forms for the corresponding cross-sections, as illustrated in figure 8.1, from the integral

$$\int_0^\infty \mathcal{F}(\epsilon) \cdot \sigma_d \cdot \epsilon^{1/2} d\epsilon.$$

As one expects, this integral is larger for the neutral channel when  $\mathcal{F}$  is maxwellian, as summarized in table 8.3. When  $T_e$  is several eV, only a few percent of the total dissociation is occurring into ions. If this is so, how is it argued that ions rather than neutrals are responsible for deposition?

Two central elements are missing from the analysis of Turban. First, no attempt is made to consider the ionization (or dissociation) of the free radicals by the plasma electrons. As was shown in chapter 5, the silicon hydride radicals have ionization potentials which are well below the 11 eV threshold for ionizing silane directly. Thus the same arguments applied to the relationship between dissociation versus ionization also apply to free radical versus silane ionization.

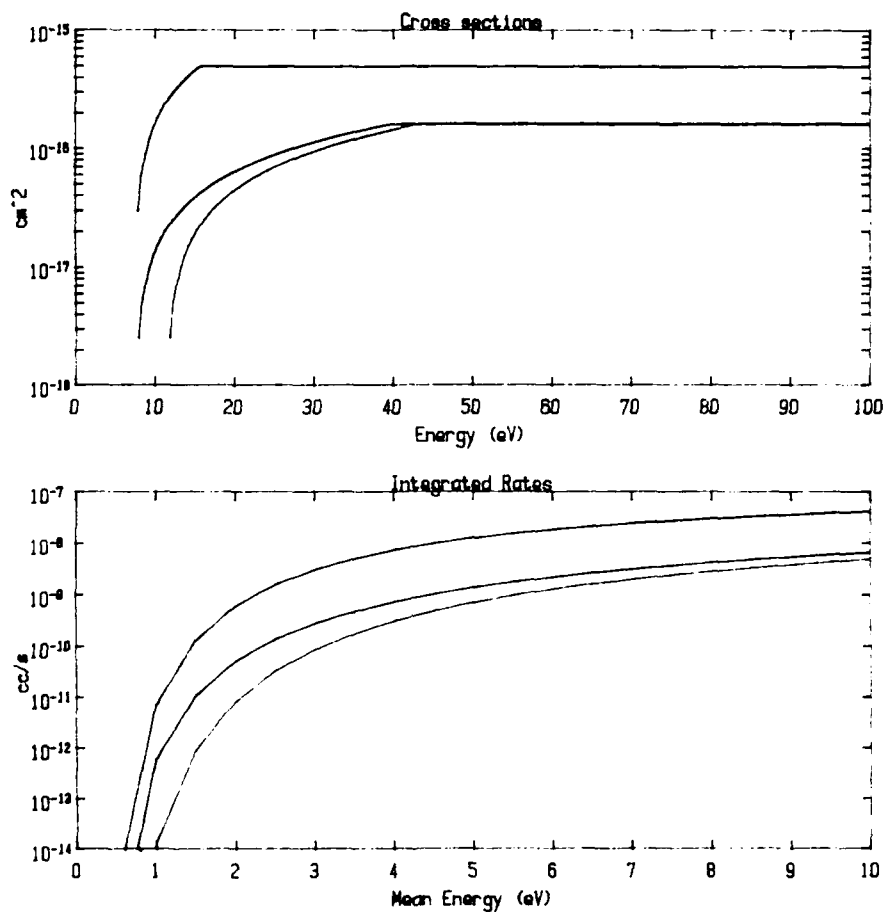
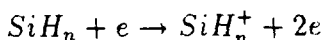


Figure 8.1: Approximate form for the total dissociation cross-section,  $\sigma_d$ , the dissociative ionization cross-section,  $\sigma_i$ , and the silyl radical ionization cross-section,  $\sigma_{ri}$ . On a linear scale the cross-sections have constant  $\frac{d\sigma}{dE}$  from threshold to their respective maxima at 16, 40, and 37 eV. Inset are the integrated rate constants for Maxwellian  $\mathcal{F}$ 's using these cross-sections.

Suppose for example that  $\sigma_i(SiH_n)$  is similar in shape and magnitude to that observed for silane itself, but is displaced to the appropriate threshold (8 eV see table 3.6). From this cross-section one calculates a large radical ionization rate :



of  $4.8 \cdot 10^{-10} cm^3 s^{-1}$  when  $T_e \approx 3.5$  eV. At an electron density of  $10^{10} cm^{-3}$  this implies a lifetime of 200 milliseconds-significantly shorter than the gas residence time of one second. Assuming  $N_e \approx N_i$ , the Langevin rate for ion-radical charge transfer,  $1.3 \cdot 10^{-9} cm^3 s^{-1}$ , also suggests a short lifetime for neutral radicals, about 77 milliseconds. The principal competitor of these homogeneous processes is radical diffusion. Assuming a perfectly absorbing wall the time constant for diffusion in the fundamental mode of Turban's reactor,  $t_d = \frac{\Lambda^2}{D} \approx 1ms$ . ( $D = 2425 cm^2 s^{-1}$  at .2 torr using the Chapman-Enskog approximation, a collision cross-section of  $23 \text{ \AA}^2$  and a temperature of  $300^\circ K$ ). If the radicals stick to the walls with probability  $\gamma$  then the continuity equation for radicals is:

$$\frac{[SiH_n^\cdot]}{dt} = k_d N_e [SiH_4] - [SiH_n^\cdot] (k_{ri} N_e + k_L N_i + \gamma \cdot D \Lambda^2)$$

where  $k_{ri}$ ,  $k_L$ ,  $N_e$ , and  $\Lambda$  are the radical ionization rate, the Langevin ion-molecule reaction rate, the electron density and the characteristic reactor dimensions, respectively. For  $N_e = N_i = 5 \cdot 10^9 cm^{-3}$  and the rate constants of  $a \approx 3.5 eV$  maxwellian  $\mathcal{F}$  as described above the steady-state solution of this equation becomes:

$$25.5 [SiH_4] = [SiH_n^\cdot] (2.4 + 6.5 + \gamma \cdot 5136)$$

so that

$$\frac{[SiH_n^\cdot]}{[SiH_4]} = \frac{25}{(8.9 + 5136\gamma)}$$

which varies dramatically with the sticking probability  $\gamma$  as illustrated in figure 8.2. Characterization of the competition between ionization and deposition of radicals is therefore critically dependent on one's assumptions about the radical's sticking probability. When chemisorption is certain at every collision only 0.2% of the radicals are ionized. If the sticking coefficient is 0.002, then the probability of a radical's ionization equals that of its sticking to the walls. The implicit treatment of all  $SiH_n$  radicals together in this discussion obviates consideration of dissociation of the free-radicals since the dissociation processes

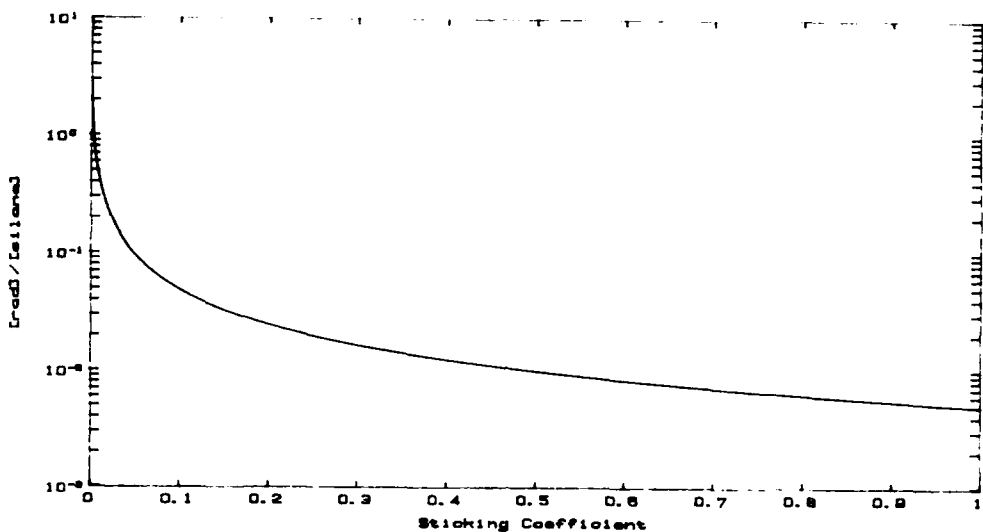


Figure 8.2: Steady-state free-radical concentrations as a function of the sticking probability,  $\gamma$ , for Turban's reactor conditions: 5%  $\text{SiH}_4$  in He at 0.2 torr, 20 Watts rf power.

$\text{SiH}_n + e \rightarrow \text{SiH}_{(n-m)} + mH + e$  conserves the total number of easily ionized (i.e. silicon-containing) radical fragments.

The second critical element missing from Turban's analysis concerns the interaction of the impinging radical or ion with the silicon surface. In a very concise dissertation by Otting [6] the quantum mechanics of electron transfer between a metal and an impinging atom was worked out. The essential result is that electron transfer between the solid and incoming gas are calculated to occur on a timescale which is short compared to that of the wall collision. Indeed this is not surprising, it is simply a restatement of the Born-Oppenheimer approximation in terms of the metal's work function  $\Phi$  on one hand and the molecule's ionization potential or electron affinity on the other. The appropriate quantities for the  $\text{SiH}_n^+$  ions are the ionization potentials of the corresponding radicals, as summarized in table 3.6. These ionization potentials,  $IP(\text{SiH}_n) = 8.15, 7.91, 9.15$ , and 8.01 eV for  $n = 0, 1, 2$ , and 3 respectively, are all greater than the work function of crystalline silicon <sup>2</sup>, 4.8 eV [7]. According to the Otting model electron transfer from the silicon surface to the incoming ion is facile. Therefore one expects the

<sup>2</sup>The work function of the amorphous film may deviate slightly from this value

$SiH_n^+$  ions which strike the surface are reduced to  $SiH_n$  radicals on a timescale which is short compared to the kinematic timescale of the collision.

The same general approach to electron transfer in the gas phase which was described in chapter 7 might actually be extended to treat the wall neutralization problem, however the band structure of the semiconductor film seriously complicates quantitative aspects of the argument. An important difference between noble gas and silyl ion neutralization has been already mentioned. Noble gas ions reduced by the surface have filled valence shells and thus are at most physisorbed to it. As they arrive with substantial kinetic energy obtained from the sheath electric field, it is possible that they participate in chemical or physical modifications of the surface [20]. However their inability to form chemical bonds with the growing film suggests that their residence time on the surface is short. By contrast, the exclusively dissociative ionization of silane requires that reduction of  $SiH_n^+$  ions at the surface yield only free-radicals. Unlike their noble counterparts, these open-shell species have an opportunity to form chemical bonds with the surface.

If the  $SiH_n$  free radicals chemisorb to the wall following their generation by electron impact on silane then so must the corresponding ions. The converse of this statement is not necessarily true, however. Ions impinging on the growing film arrive at the wall with substantial kinetic energy, of the order of the electron temperature, due to their acceleration by the sheath electric field which balances ion and electron wall fluxes. Although they are converted chemically to neutral free radicals by electron transfer from the surface, impinging ions arrive with enough translational energy to overcome kinetic and thermodynamic barriers to surface reaction which would preclude successful incorporation of free radicals that diffuse from the body of the plasma and strike the surface with thermal kinetic energies. Recall that a typical  $2eV$  radical has an equivalent temperature of  $\approx 22,000^\circ K$ , well above the temperature required for pyrolysis of silane under single-collision conditions.

The extent to which the free radicals are reflected from a wall is obviously a pivotal quantity. If the sticking probabilities of the radicals are near unity and the plasma boundary conditions arranged so that their diffusion and loss at the walls is more rapid than their ionization, attachment, or homogeneous reaction then radicals are justifiably invoked as the film precursor. Ion deposition is still calculable given the total plasma density and electron temperature, since effective sticking of the free radicals implies effective sticking of the ions. Very little experimental information on radical sticking coefficients is available, although

heuristic guidelines have been proposed by Winters [8]. Recently Perrin and Broekhuizen have reported a sticking coefficient for thermal  $SiH_3$  of between 0.1 and 0.2 using photolysis of mercury doped silane as the radical source [9]. While their inference that  $SiH_3$  is the only radical present may be tenuous, they observe that over 60% of the radicals that stick form disilane rather than being incorporated into their slowly growing film.

Chemisorption of  $SiH_2$  has also been proposed as the primary deposition process. However the modest spatial gradients and low concentrations of the  $SiH_2$  radical in silane and disilane plasmas measured using frequency modulated absorption spectroscopy by Jasinski [13] argue against this mechanism. The nail in its coffin is the observation that the  $SiH_2$  densities were a factor of two less in disilane than in silane plasmas while the film growth rate from the former is approximately twenty times that of the latter.

Free-radical densities may exceed those of ions in plasmas, but the combination of imperfect sticking, relatively slow transport to the walls by thermal diffusion, and a lack of total energy for the enhancement of surface kinetics make them unlikely precursors for the deposition of films in PECVD reactors. If neutral radicals were the primary precursor, one would expect wider variation in the reported deposition rates than is found in the literature. There have also been reports that spatial variation of the deposition rate is caused by external magnetic and electrostatic fields [14], which is clearly impossible for uncharged species.

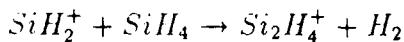
In sum, a variation of the Born-Oppenheimer theme, as described in 1956 by Otting, implies that if neutral silicon hydride radicals formed by electron impact dissociation of silane stick to reactor walls then so do the corresponding ions. The converse is not necessarily true, since ions arriving at the wall do so with kinetic energy of the order of several electron volts, which provides kinetic and thermodynamic access to reactive channels which are closed for radicals impinging with thermal velocities. That the enthalpy of silicon-silicon and silicon hydrogen bonds and the kinetic energy of impinging ions are comparable, about 3 eV (70 kcal/mol), may only be coincidence. However consideration of the surface chemistry and a more detailed description of homogeneous radical losses by ionization and charge transfer suggest that deposition results primarily from directed ion fluxes which, by analogy with the homogeneous ion chemistry described in chapter 6, can either incorporate silicon into the film or remove excess hydrogen from it by rapid hydride transfer.

### 8.3 Clusters and Dust

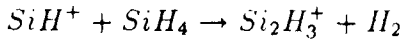
Numerous investigators have observed the formation of undesirable silicon dust, normally under conditions of high silane concentrations or fractional decompositions [1]. The presence of particles imposes radically new boundary conditions on the plasma's electrical characteristics, in addition to offering enormous opportunities for heterogeneous processes. The very rapid reactions of cations with silane provide a natural candidate for the nucleation process which leads to these silicon dusts.

Consider first a pure silane discharge. As was demonstrated in chapter six, the most rapid reactions of  $SiH_n^+$  with silane result in hydride transfer. The ionization cross-sections of silane imply a nascent silicon hydride ion composition which decreases in the order  $SiH_2^+ > SiH_3^+ > Si^+ > SiH^+$ , although the detailed ratios depend on  $\mathcal{F}(\epsilon)$ . If the argument concerning ion deposition at the walls is correct, then the relevant parameters to consider for cluster formation are the reactor dimensions  $\Lambda$  and the reactive mean free path of the ions  $\lambda$ . At silane concentrations for which  $\Lambda > \lambda$  the nascent ion distribution formed by electron impact will be that which strikes the walls. As the concentration of silane is increased, that is as  $\lambda \approx \Lambda$ , the ion distribution which arrives at the substrate evolves to one dominated by  $SiH_3^+$ , since it is formed in rapid reactions but reacts only slowly to yield the almost fully saturated  $Si_2H_5^+$ . This change in sampled ion composition has been observed by ion extraction in the multipole reactor studies of Perrin [11] and also in a later study of radiofrequency plasmas in silane helium mixtures by Turban [12].

The evolution of the ion distribution to  $SiH_3^+$  occurs over only a limited range of pressures and excitation conditions. Reactions which lead to unsaturated disilicon hydride cations such as:



and



are accessed when the silane pressure is further increased. The reaction of these disilicon hydride ions with silane can lead to trisilicon hydride cations, and so on. As the ions become heavier their diffusive flux drops as the square root of the ion mass, so that positive feedback drives the formation of heavier clusters in the sense

Reactant	Product	$\frac{\lambda}{\Lambda}$
$SiH_2^+$	$Si_2H_4^+$	.148
$SiH_2^+$	$SiH_3^+$	.036
$SiH_3^+$	$Si_2H_5^+$	1.478
$SiH_3^+$	$SiH_3^+$	.025
$Si^+$	$Si_2H_2^+$	.076
$SiH^+$	$Si_2H_3^+$	.132
$SiH^+$	$SiH_3^+$	.616

Table 8.4: Ratio of reactive mean free path for ions with thermal ( $\approx 0.03eV$ ) velocities in 0.05 torr silane to the characteristic dimension,  $\Lambda$  of Turban's cylindrical reactor. Small values of the ratio indicate likely reaction prior to wall loss.

that the mean residence time of a cluster ion formed in the gas phase increases as its mass increases, which in turn favors further reaction over diffusive wall loss. Turban [1] observed the onset of particle formation at 1 torr of 5 % silane in helium, which corresponds to  $\frac{\lambda}{\Lambda}$  for the ion-molecule reactions as summarized in table 8.4. Small values of this ratio imply that a reaction is kinetically favored over wall loss. The competition between reactions which form unsaturated disilicon hydride ions and diffusion starts to favor the former near the threshold silane concentration above which Turban reported particulate formation. Note that the total  $Si_2H_n^+$  sources must consider the relative concentrations of the monosilicon hydride ion reactants.  $SiH_3^+$  and  $SiH_2^+$  are the dominant ion species in the nascent distribution due to their relatively large cross-sections. The onset of unsaturated polysilicon ion formation may be estimated with a simple nomograph such as is shown in figure 8.3, where the logarithm of the reactive mean free paths for typical charge transfer reactions are plotted versus silane partial pressure.

Discharges in dilute mixtures of silane and noble-gases provide an interesting variation on the scaling of cluster formation. As was described in chapters six and seven, helium and neon ions react with silane to produce mainly  $Si^+$  and  $SiH^+$ . Even when  $\mathcal{F}$  is Maxwellian, larger concentrations of noble gas with a higher ionization threshold can lead to significant  $Rg^+$  formation by electron impact. In helium and neon this results in enhancement of the homogeneous sources of  $Si^+$  and  $SiH^+$ , both of which produce unsaturated disilicon hydride cations more rapidly than their di- and tri-hydride counterparts. The generation of heavier ions is further enhanced by the presence of beam-like components in the

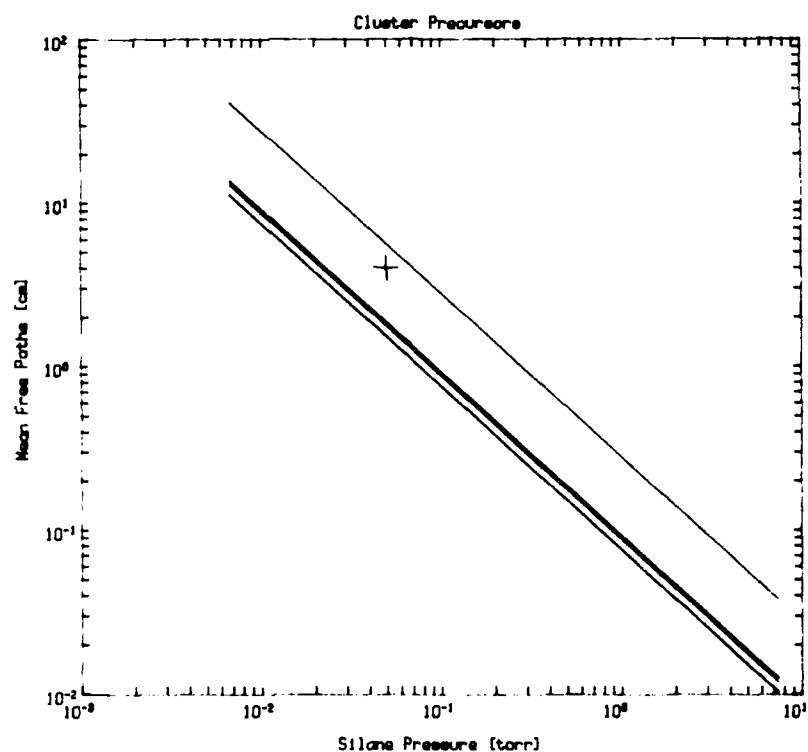


Figure 8.3: Nomograph for estimating the onset of parasitic cluster formation. Shown is the relationship of the silane pressure to the mean free path for cluster nucleation initiation via unsaturated polysilicon hydride cation generation. Lines represent, from left to right, the reactions of  $SiH_n^+ \rightarrow Si_2H_m^+$  for  $n = 0, 1, 2$ , and  $3$ . The  $+$  indicates the position at which Turban observed cluster formation.

electron energy distribution functions, as illustrated in figure 5.4. These ionizing electrons, which may contribute significantly to ionization in commercially useful radiofrequency reactors [15], favor silane over buffer ionization to a lesser extent. The relative contributions of noble gas and silicon hydride ions in the nascent distribution then scales sensitively with the gas mixture than is the case for a Maxwellian  $\mathcal{F}(\epsilon)$ .

In contrast to helium and neon, ionization of argon, krypton, and xenon by plasma electrons shifts the evolution of the nascent ion distribution away from cluster precursors.  $Ar^+$  and  $Kr^+$  in particular produce  $SiH_3^+$  with greater selectivity even than 15 eV electron impact. This simple description of the ion chemistry predicts that silane plasmas with helium and neon buffers will yield undesirable particulates at lower silane concentrations than plasmas buffered with the other noble gases for similar  $\mathcal{F}(\epsilon)$ 's. In addition the helium and neon discharges will perform less well under excitation conditions where energetic, beam-like electrons increase the ratio of noble gas to silane ionization.

## 8.4 Negative Ions

Negative ions formed in silane-containing discharges have qualitatively different behavior since their polarity is the same as the much less massive plasma electrons. The sheath field which develops at plasma boundaries reflects rather than accelerates anions. Thus although the generation of negative ions by electron impact is substantially slower than that of cations, the absence of a heterogeneous loss permits densities to build well beyond what would be suggested by the relative formation rates. In the limit of no electron density, the sheath field collapses and cation and anion fluxes to walls become equal, but this is a trivial case applicable only to afterglow plasmas since the mechanism for maintenance of plasma conductivity and current involves acceleration of plasma electrons by the applied field.

One can estimate the steady-state concentration of negative ions by considering only attachment and detachment collisions. Let the latter, which correspond to ionization of the anion, have cross-sections of similar shape and magnitude to that for  $SiH_4$  ionization but shifted in energy to the calculated thresholds presented in table 4.4. Assuming no heterogeneous loss and constant electron

density  $N_e$  one can relate the anion and silane concentrations at steady state:

$$\frac{d[SiH_n^-]}{dt} = 0 = N_e \cdot (k_a \cdot [SiH_4] - k_d \cdot [SiH_n^-])$$

so that

$$\frac{[SiH_n^-]}{[SiH_4]} = \frac{k_a}{k_d}.$$

For a 3.5 eV maxwellian  $\mathcal{F}(\epsilon)$  and the assumed form for the detachment cross-section the attachment and detachment rates are  $5.6 \cdot 10^{-12}$  and  $4.9 \cdot 10^{-9} \text{ cm}^3 \text{s}^{-1}$ , yielding a steady state anion concentration of 0.1%. The gross imbalance between creation and loss rates for negative ions, both of which scale with  $N_e$ , means that the approach to this steady state would be slow. The ratio  $\frac{k_a}{k_d}$  for maxwellian basis functions is outlined in figure 8.4. Beam ionization at higher energy clearly tilts the balance further in favor of detachment, since dissociative attachment is a resonant process. However, as outlined in chapter four, there are nonlinear sources of negative ions from attachment to the free radicals  $SiH_n$  for  $n = 3, 2, 0$ . Interferometric measurements of electron density decay in pulsed silane-helium afterglows by Verdeyen *et al.* [16, 17] clearly demonstrate the attaching nature of silane, however the authors argue persuasively that this attachment is due to dissociated fragments of silane generated by the plasma. The estimated lower bound for attachment to these fragments is reported as  $2.65 \pm .19 \cdot 10^{-10} \text{ cm}^3 \text{s}^{-1}$ . Neither the electron temperature nor  $\mathcal{F}(\epsilon)$  were reported, so that the scaling of this radical attachment with the plasma electrical characteristics cannot be addressed.

The role played by negative ions in semiconductor deposition discharges arises primarily from the change in discharge electrical conditions caused by attachment. Since they are reflected by wall sheaths, negative ions should not participate directly in deposition of silicon film. However attachment causes an increase in plasma impedance, so that the mean electron energy,  $\int \epsilon \mathcal{F}(\epsilon) d\epsilon$ , must increase to maintain constant current density in the plasma. According to the Bohm criterion, an increase in wall flux is anticipated for increased electron temperature. Note that Poisson's equation only constrains only the sum of negative ion, positive ion, and electron densities. The measured electron densities therefore represent a lower bound on the positive ion concentrations. In short, attachment enhances the positive ion wall fluxes both through an increase in the ratio  $\frac{N_i}{N_e}$  and through modification of the Bohm velocity, which increases as  $\sqrt{T_e}$ . Elegant treatises have been written on the part played by negative ions in electrical discharges [18], and

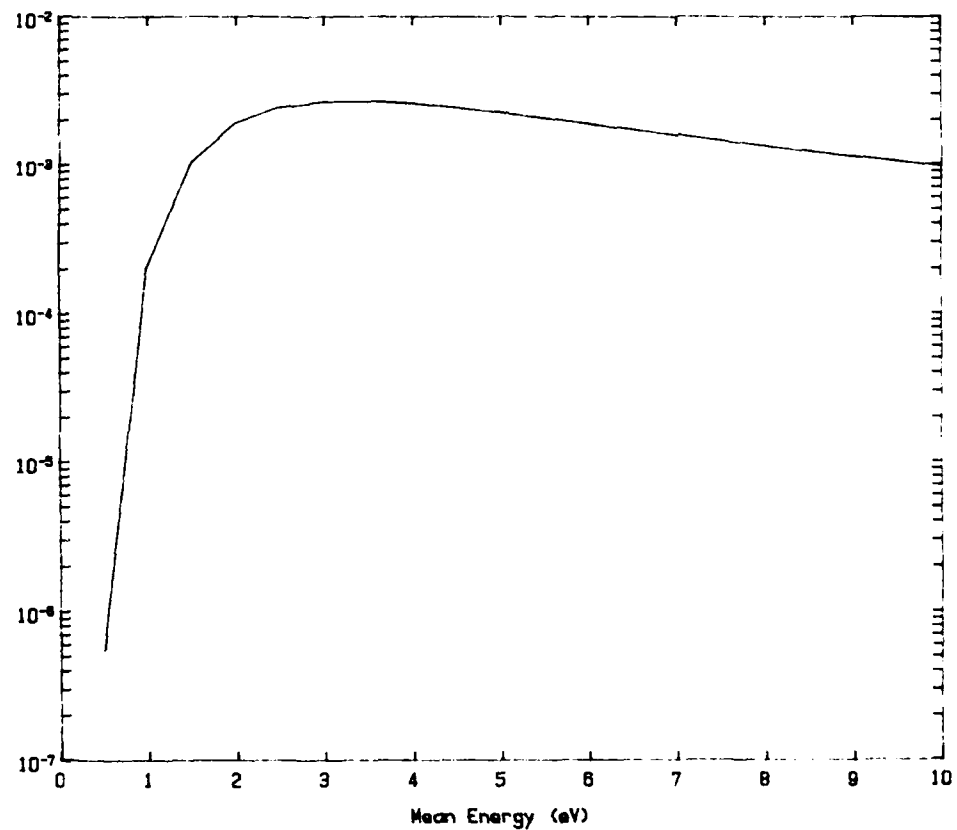


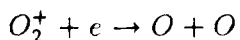
Figure 8.4: Ratio of rates calculated for dissociative attachment to silane and detachment of the negative ions assuming the latter have a cross section whose energy dependence and magnitude are the same as silane's ionization cross-section whose threshold has been shifted to 1eV.

the various perturbations to the plasma transport equations are too complex to elaborate here. Concise discussions for the simple positive column of a direct current discharge by Edgely and von Engel [19] and Franklin [3] are excellent starting points for a detailed consideration of negative ion transport.

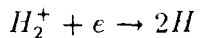
In PECVD reactors the possibility for generation of negative ion densities which approach or exceed the electron density is considered to be remote since the calculated detachment rate is so large. Further, the decomposition of silane and its deposition as thin film occur rapidly, cutting off access to negative ion forming channels. For example, radicals which are generated by dissociation of silane and detachment of anions can, by the arguments of the last section, be ionized and deposited quite rapidly. Therefore it is expected that negative ion formation enters into the plasma dynamics in an experimentally meaningful way only at high pressures, where it has already been shown that undesirable clustering occurs.

## 8.5 Homogeneous Ion Losses

The preceding sections have failed to account for homogeneous processes such as electron-ion and ion-ion recombination. First consider electron cation recombination. The two body recombination of electrons and noble gas ions is radiative and therefore very slow, having rate constants for room temperature Maxwellian  $\mathcal{F}(\epsilon)$  in the  $10^{-12} \text{ cm}^3 \text{ s}^{-1}$  range [24]. However recombination of an electron with  $\text{SiH}_n^+$  can be dissociative, a process which is typified by very rapid rate constants. Although experimental examination of dissociative recombination are not available for silicon hydride ions, the rate for the process:



is very fast. Decay of a room temperature electron swarm occurs with a rate constant of  $2 \cdot 10^{-7} \text{ cm}^3 \text{ s}^{-1}$  [21]. However one expects the cross-section for dissociative recombination to decrease strongly with the electron energy, as has been recently calculated for molecular hydrogen [25]. These careful calculations suggest a dissociative recombination rate for molecular hydrogen which decreases with mean electron energy  $T_e$  as  $\frac{0.086}{T_e}^{0.29}$ . For the reaction:



the recombination rate drops by a factor of four, from  $1.7 \cdot 10^{-8}$  to  $3.7 \cdot 10^{-9} \text{ cm}^3 \text{ s}^{-1}$ , on increasing the electron temperature from 300 K to 3 eV. By analogy one

estimates that the homogeneous loss for silicon hydride cations is of order  $10^{-8}$ .  $N_e \cdot N_i \approx 10^{-8} N_e^2$  so that the lifetime of an ion to dissociative recombination at an electron density  $N_e = 10^{10} \text{ cm}^{-3}$  is roughly 10 milliseconds.

The principal competition for dissociative recombination is thermal ion diffusion. From the Chapman-Enskog approximation the free diffusion coefficient of silicon hydride ions in helium may be estimated using a collision cross-section<sup>3</sup> of  $23 \text{ \AA}^2$  to be  $0.64 \text{ cm}^2 \text{ s}^{-1}$  [26]. For comparison the measured diffusion coefficient for silicon atoms in argon [22] is  $0.56 \text{ cm}^2 \text{ s}^{-1}$ . However ion diffusion is constrained by Maxwell's equations, so that the ambipolar diffusion coefficient is related to the electron temperature:

$$\mathcal{D}_a = \mathcal{D}_i \left(1 + \frac{T_e}{T_i}\right)$$

where the  $\mathcal{D}$ 's are the ambipolar and free ion diffusion coefficients and the  $T$ 's are the electron and ion temperatures. For a 3 eV electron temperature and a room temperature ion ensemble this makes  $\mathcal{D}_a = 3.97 \text{ cm}^2 \text{ s}^{-1}$  at 1 atmosphere. In a radial configuration the ion diffusion time constant for the fundamental mode is:

$$\tau = \frac{P_0 \Lambda^2}{\mathcal{D}_a}$$

where  $\Lambda = R/2.405$  is the characteristic dimension of a cylindrical reactor and  $P_0$  is the total pressure in atmospheres. Ions diffuse in about 140 microseconds at 0.2 torr in a 3.5 cm cylinder, a time which is very short compared to the dissociative recombination time estimated in the last paragraph.

The homogeneous loss for electrons and ions has a similar effect on the plasma balance equations as does attachment, so that the mean electric field required to maintain finite conductivity is increased compared to a plasma for which this process is forbidden. Radicals produced by electron cation recombination are amenable to the same arguments with respect to deposition as those produced by electron impact on silane itself. While the detailed influence on the ion fluxes which deposit silicon depend on the recombination rates of the ions and the ionization rates of the radicals produced, the total ion wall currents are still coupled to the electron density by Maxwell's equations. The dominance of dissociative over radiative recombination suggests that electron- $\text{SiH}_n^+$  recombination followed by radical ionization, a process which scales with  $N_e^3$ , will permit access to clustering

<sup>3</sup>Estimate based on the sum of covalent radii

by production of reactive  $Si^+$  as described in the previous section. These contributions are best avoided by employing discharges with low electron densities, that is, modest powers.

The problem of ion-ion recombination is much less complex. While measured rates of cation-anion recombination for atmospheric species at 300 K lie in the  $4 - 10 \cdot 10^{-8} cm^3 s^{-1}$  range, low anion concentrations are predicted for useful deposition reactor conditions. Even at enormous negative ion concentrations of  $10^{10} cm^{-3}$  the time constant for this process,  $\approx 25ms$ , is two orders of magnitude slower than positive ion diffusion. Ion-ion recombination just adds another homogeneous loss for negative ions, yielding free radicals which may be rapidly ionized and deposited as film. Clearly, the competition between anion detachment and cation-anion dissociative recombination is determined by two unmeasured quantities, so argument over their relative roles is, at present, purely speculative.

## 8.6 Optimal Conditions

If monosilicon hydride ions are indeed responsible for thin film deposition what are the optimal conditions for film growth predicted on the basis of the present work? Helium and neon buffers are to be avoided, as parasitic cluster formation is predicted to occur at lower silane concentrations due to the channeling into unsaturated disilicon hydride cations *e.g.*:



Argon and krypton are optimal from a clustering point of view. Although argon is commercially popular, the present results suggest that krypton would be more effective since the rates of forming  $Kr^+$  are faster than for  $Ar^+$ , as is the chemistry which leads to exclusively  $SiH_3^+$ . While concrete predictions of deposition rates depend sensitively on the modification of the electron transport characteristics by different noble gases as well as the change in ion chemistries, parametric control of the ion species and the rate at which they strike the wall is possible by tuning the buffer gas mixture for a fixed reactor geometry and excitation source.

In general, the roles of radical ionization, anion detachment, and electron ion recombination have been considered only in an approximate way. However the scaling of these processes with the plasma electron density,  $N_e$ , is such that optimal reactor conditions are expected to occur for lower rather than higher electron

densities. These may be obtained by beam-like ionization in radiofrequency discharges or by employing a buffer gas with a low ionization potential (such as a xenon containing mixture).

The final prediction for efficient film deposition concerns the reactor dimensions. Since one is continually dealing with competition between homogeneous ion reaction and wall loss, conditions should be chosen so that the reactor dimensions maximize the monosilicon hydride ion flux. For dilute silane noble gas mixtures one wants the silane mean-free path to be of the same order as the reactor dimension, so that the nascent ion distribution evolves to  $SiH_n^+$  following a few reactive collisions.

## 8.7 Conclusions

Returning to the original theme of the introduction, the enormous range of operating parameters for which successful production of thin silicon films by PECVD is observed suggest an important role for ion chemistry in the deposition process. The present chapter has elaborated on this intuitive conclusion by assessing the kinetics of ion formation and deposition. It is argued that ions are the principal depositing species under typically employed reactor conditions, that is low fractional silane dissociation, modest pressure, and low electron density. Logical arguments for the relative roles of radical and ion deposition based both on consideration of the surface chemistry and the correlation of observed deposition rates and calculated ion fluxes support the argument that ions are the principal film precursor.

While configurations which vary the concentrations of various radicals are sensitive to unquantifiable details, calculation of the nascent ion distribution and its evolution by reaction and diffusion is shown to be possible using the data presented here. Estimates for the relationship between total silane pressure, reactor dimensions, gas residence time and the formation of parasitic clusters are also possible. It is hoped that the present approach provides a framework for concrete predictions of thin film reactor performance characteristics thereby facilitating extension of plasma-enhanced chemical vapor deposition to new materials.

## Bibliography

- [1] G. Turban, Y. Catherine and B. Grolleau, *Thin Solid Films*, **60**, 147 [1979].
- [2] H. Winters, *Journal of Chemical Physics*, **63**, 3462 [1975].
- [3] R. Franklin, **Plasma Phenomena in Gas Discharges**, (Oxford:Clarendon Press) [1976].
- [4] C. DeJoseph, A. Garscadden and D. Pond, *Proceedings of the International Conference on Lasers '82*, 738 [1982].
- [5] M. Dillon *et al.*, *Journal of Chemical Physics*, **82**, 2909 [1985].
- [6] W. Otting, Jr., **Electron Transfer Between a Metal and a Gas Molecule**, (PhD thesis, Catholic University of America) [1956].
- [7] R. Weast, ed. **CRC Handbook of Chemistry and Physics**, (Cleveland:CRC Press), 58th edition, [1978].
- [8] H. Winters, *Elementary Processes at Solid Surfaces Immersed in Low Pressure Plasmas* in **Topics in Current Chemistry**, **94** (New York:Springer Verlag) [1982].
- [9] J. Perrin and T. Broekhuizen, *Applied Physics Letters*, **50**, 434 [1987].
- [10] P. Potzinger *et al.*, *Journal of Physical Chemistry*, **81**, 1543 [1977].
- [11] J. Perrin *et al.*, *International Journal of Mass Spectrometry and Ion Processes*, **57**, 249 [1984].
- [12] G. Turban, Y. Catherine and B. Grolleau, *Thin Solid Films*, **67**, 309 [1980].

- [13] J. Jasinski, *Applied Physics Letters*, **44**, 1155 [1984].
- [14] B. Drevillon *et al.*, *Applied Physics Letters*, **42**, 801 [1983].
- [15] A. Garscadden, *Spectroscopic Diagnostics and Kinetics of Low Pressure Processing Plasmas*, Proceedings of the Materials Research Society, Boston [1986].
- [16] C. Fledderman *et al.*, *Journal of Applied Physics*, **58**, 1344 [1985].
- [17] L. Overzet *et al.*, *Applied Physics Letters*, **48**, 695 [1986].
- [18] H. S. W. Massey, **Negative Ions**, (Cambridge: University Press) [1976].
- [19] P. Edgley and A. von Engel, *Proceedings of the Royal Society, London, A* **370**, 375 [1980].
- [20] K. Emeleus and J. Coulter, *International Journal of Electronics*, **59**, 65 [1985].
- [21] D. Smith and N. Adams, **Ion Ion Neutralization**, USAF report AFOSR-77-3260E, 31 May 1982.
- [22] K. Tachibana *et al.*, *Journal of Physics D: Applied Physics*, **15**, 177 [1984].
- [23] G. Nolet, *Journal of the Electrochemical Society*, **122**, 1030 [1975].
- [24] S. Brown, **Basic Data of Plasma Physics**, (New York: Wiley) [1959].
- [25] K. Nakashima *et al.*, *Journal of Chemical Physics*, **86**, 726 [1987].
- [26] B. Smirnov, **Physics of Weakly Ionized Gases**, (Moscow: Mir), [1981].